Master Thesis, Department of Geosciences

Basin modelling of the south-west Barents Sea

Peter Anthony Hansford

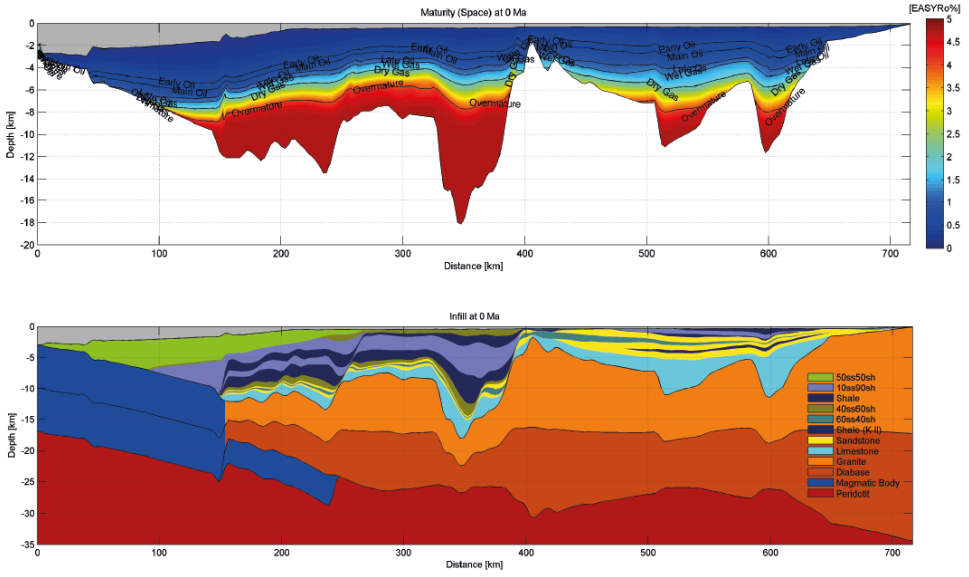

UNIVERSITY OF OSLO

FACULTY OF MATHEMATICS AND NATURAL SCIENCES

Basin modelling of the south-west Barents Sea

Peter Anthony Hansford

Master Thesis in Geosciences

Discipline: Geology

Department of Geosciences

Faculty of Mathematics and Natural Sciences

University of Oslo

December 2014

© Peter Anthony Hansford, 2014

This work is published digitally through DUO – Digitale Utgivelser ved UiO

http://www.duo.uio.no

It is also catalogued in BIBSYS (http://www.bibsys.no/english)

All rights reserved. No part of this publication may be reproduced or transmitted, in any form or by any means, without permission.

Abstract

The south-west Barents Sea is an epicontinental platform consisting of N- to NNE-oriented basins separated by basement highs. It is underlain by thick sequences of Upper Paleozoic to Cenozoic sediments and Caledonian metamorphosed basement. The basins were formed during four distinct rift-phases in the Carboniferous, late Permian, Late Jurassic-Early Cretaceous, and Paleocene-Eocene. Progressive rifting culminated in continental breakup and seafloor spreading along the North Atlantic axis approximately 55 Ma.

This study explores the structural and thermal evolution of the south-west Barents Sea. The thermal and isostatic history of basins within the south-west Barents Sea is constrained through time-forward basin modelling along two profiles, building on the earlier work of Clark et al. (2014) and the PETROBAR project. Automated basin reconstructions are applied to the two profiles using the TecMod basin modelling toolbox. The effect of continental breakup and potential near-margin underplating below the Vestbakken Volcanic Province is estimated by comparing a reference case which neglects the effect of breakup and near-margin underplating with a series of scenarios which progressively integrate both (1) continental breakup and (2) continental breakup together with magmatic underplating. Both free-air and bouger gravity anomalies are extracted from the lithospheric density distribution within a new integrated routine in TecMod. Basin models are calibrated against well data and free-air and bouger-corrected gravity anomaly data. The results imply that both breakup and underplating alter the thermal and isostatic history of sediments along the margin. The hydrocarbon potential of source rocks modelled along the margin suggest breakup has a permanent thermal effect on the present-day sediments promoted by lateral heat flow, while heat conduction by underplating is more diffuse, inhibited to some degree by deeply-buried, low-conductivity shales and limestones. The likelihood of serpentinization reactions below the deep (exceeding 15km) Bjørnøya and Tromsø basins during Jurassic-Cretaceous time is tested within all basin models, concluding that the amount of crustal stretching is too low, and syn-rift sedimentation rates too high to permit embrittlement of the entire crust and hydration of the mantle.

Some recent oil and gas discoveries close to the modelled profiles are investigated within the context of the calculated maturation history, validating both the models and the extent of the

petroleum systems. Some assumptions are made within the basin modelling workflow and sensitivity tests are performed to scale the uncertainty inherent in the models.

Acknowledgements

I would like to kindly thank my supervisors, Prof. Dr. Jan Inge Faleide and Dr. Sébastien Gac for providing a very interesting project to work with and their invaluable support during the course of this study. Sébastien and Jan Inge have always been available over the past 18 months for discussions and guidance and I am very grateful for their time and effort.

For the PETROBAR-07 dataset, answering countless questions about its intricacies, and some great advice regarding basin modelling, I sincerely thank Dr. Stephen (Stoney) Clark for his assistance.

Dr. Daniel Schmid is thanked for providing the new version of TecMod v2014.1 and for some interesting discussions regarding TecMod and this project.

My family has been a big support during the course of my study. They have been a source of motivation and I am indebted to their patience. Thanks Gro Marita and Magnus, and the rest of the clan back in Australia.

GeoModelling Solutions are acknowledged for providing TecMod2D academic licenses to UiO.

Table of Contents

1. Introduction

The Barents Sea is an epicontinental basin on the northwestern part of the Eurasian continental shelf. It is bounded to the south by the Norwegian and Russian landmasses, to the north by the Arctic Ocean, to the east by Novaya Zemlya, and to the west by the North Atlantic Ocean (specifically the Norwegian-Greenland Sea). The area extends from approximately 70°N to 82°N latitude and 10°E to 50°E longitude. The south-west Barents Sea (where this study is focused) is characterized by a series of NNE-SSW oriented rift basins (up to 18 km in depth) filled with (clastic/carbonate) sediments separated by basement highs, formed by multiple deformational events since the collapse of the Caledonian Orogeny in Devonian time. Rifting culminated into seafloor spreading and continental breakup along a sheared to transtensional margin conjugate to East Greenland (Wandel Sea Basin) throughout the Eocene (Rønnevik, 1981; Faleide et al., 1984, 1993b, 1996, 2008, 2010; Gabrielsen et al., 1990; Dengo & Røssland, 1992; Gudlaugsson et al., 1998). Breakup was followed by subsequent passive margin development which continues to this day. Extensional and transtensional stress regimes have been predominant throughout the history of the basin. However, compressional events are also recorded, evidenced by fault reactivation, salt migration, and inversion structures (Gabrielsen, 1984; Gabrielsen et al., 1993; Faleide et al., 2010). From an economic perspective, the basins are highly prospective for hydrocarbons, but are immature in comparison to the North Sea. Despite 99 wildcat exploration wells drilled to date and countless seismic surveys, only 2 fields have been developed (Snøhvit and Goliat).

The maturation of hydrocarbons is dependent on the thermal history of the sedimentary basin infill. In order to reduce exploration risk, it is important to constrain the thermal history of sediments. The basin modelling approach estimates the thermal and burial history of basins. Basin modelling is based on the assumption that the formation of sedimentary rift basins is directly related to lithospheric extension. Far-field extensional forces trigger local thinning of the crust and mantle lithosphere resulting in surface subsidence. Once extension has ceased, the thinned lithosphere cools, providing additional subsidence through thermal contraction (McKenzie, 1978; Jarvis & McKenzie, 1980). Basin modelling tools (such as TecMod; Rüpke et al., 2008) help to estimate crustal and mantle thinning factors. Assuming thermal properties for sedimentary, crustal and mantle rocks, the thermal and burial history

of sediments can then be modelled. Two basin modelling approaches are generally used; backstripping and time-forward modelling. In backstripping, sedimentary layers are removed and decompacted one-by-one. At each time step, horizons are restored to paleo-water depths. Tectonic subsidence is computed by removing the isostatic subsidence (due to sediment and water load) from the total subsidence. It is assumed tectonic subsidence results from lithospheric stretching and the thinning factor (β) is determined by trial-and-error to reproduce this subsidence. Time-forward modelling is based on a different approach. Assuming initial arbitrary values for the crust and mantle thinning factors, a synthetic stratigraphy is modelled then compared to the observed input stratigraphy. The misfit is reduced by adjusting paleo-water-depths and β factors through an inversion scheme and iteratively forward modelling (Rüpke et al., 2008).

Using the basin modelling approach, Clark et al. (2014) and Glørstad-Clark et al. (2011a) evaluated the thermal history of basins along 2-D seismic reflection profiles cross-cutting the structural grain of the south-west Barents Sea. They assumed 4 discrete rifting episodes, and examined the implications on thermal and subsidence history. Their work was comprehensive. However, there remain uncertainties and questions that require further investigation. For example, factors affecting the thermal evolution of the south-west Barents Sea basins such as continental break-up together with seafloor spreading, potential near-margin underplating, and/or serpentinization of the upper mantle lithosphere were ignored in previous studies. Continental breakup along the Barents Sea margin was associated with volcanism in the Vestbakken Volcanic Province. Faleide et al. (1991) identified a high-amplitude seismic marker within the lower crust of the Vestbakken Volcanic Province, postulating the presence of a high-density magmatic underplate. A study of the isostatic and thermal implications of magmatic underplating and continental breakup with seafloor spreading along the Barents Sea margin is therefore warranted. Serpentinization beneath deep Jurassic-Cretaceous basins in the south-west Barents Sea was proposed by Lundin & Doré (2010) upon recognition of elevated levels of crustal stretching from this time period in addition to observable velocity anomalies in the lower crust. These events are expected to have significant implications on the thermal history of the sediments within the Barents Sea.

This study extends the work of Clark et al. (2014). The goal of this thesis is to evaluate the thermal history of sediments in the south-western Barents Sea, based on modelling of depth-converted 2-D seismic reflection profiles. The effects of tectonic events such as continental break-up, magmatic underplating, and serpentinization are investigated. The input data

consists of a series of regional seismic lines recorded perpendicular to the structural grain in the south-west Barents Sea, across the ocean-continent boundary (OCB), and into the North Atlantic Ocean (figure 1.1). Stratigraphic interpretation of the seismic lines (adapted from Clark et al. 2014; Glørstad-Clark et al. 2011a; and the author) are presented and input into a commercial 2-dimensional forward thermotectonostratigraphic model (TecMod; Rüpke et al. 2008) which can solve thermal and subsidence histories of the basin. The tectonic evolution of the basin is evaluated based on the modelled outputs. The isostatic and thermal implications of magmatic underplating and continental breakup with seafloor spreading are explored and quantified within different models. The likelihood of mantle serpentinization under the thinned crust of deep Late Jurassic – Early Cretaceous basins is discussed in the context of forward models which quantify the competing effects of syn-rift strain rate and sedimentation rate on sub-Moho temperatures. The validity of each model is tested by comparing the results with independent well data and potential field data, including gravity data. And finally, the sensitivity of the model to changes in some poorly constrained geological assumptions, such as (1) the initial pre-rift crustal thickness and (2) the inclusion of known sedimentary horizons older than late Carboniferous, is tested.

The following thesis describes (1) the geological setting and history of the south-west Barents Sea; (2) concepts in modern basin modelling and analysis; (3) modelling results; (4) a discussion of the thermal and isostatic history of the south-west Barents Sea, focused on the effect of continental breakup, potential magmatic underplating and mantle serpentinization, together with a review of some important recent hydrocarbon discoveries in the context of the modelled source rock maturity, and a sensitivity analysis; (5) a summary and conclusion of the study.

Figure 1.1. (next page). Bathymetric chart of the Arctic (Jakobsson et al. 2012) with the location of the study area outlined in white (above) and tectonic basemap of the south-west Barents Sea (below). The PETROBAR-07 profile (red line; Clark et al., 2014) ties-in with the HB-3-96A seismic reflection line (orange line) near the COB, extending the profile westward to the Knipovich Ridge. The regional seismic line of Glørstad-Clark et al. (2011a) is shown as a magenta line. Major faults are shown as black lines (Faleide et al., 2008). Local highs shown as dashed black lines. Well locations are labelled in white. MR: Mohns Ridge, KR: Knipovich Ridge, COB: continent–ocean boundary, HFZ: Hornsund Fault Zone, SFZ: Senja Fracture Zone, VVP: Vestbakken Volcanic Province, BB: Bjørnøya Basin, LH: Loppa High/Selis Ridge, SH: Stappen High, TB: Tromsø Basin, OB: Ottar Basin, HB: Hammerfest Basin, NB: Nordkapp Basin, FP: Finnmark Platform, VP: Varanger Peninsula. Figure modified after Clark et al. (2013).

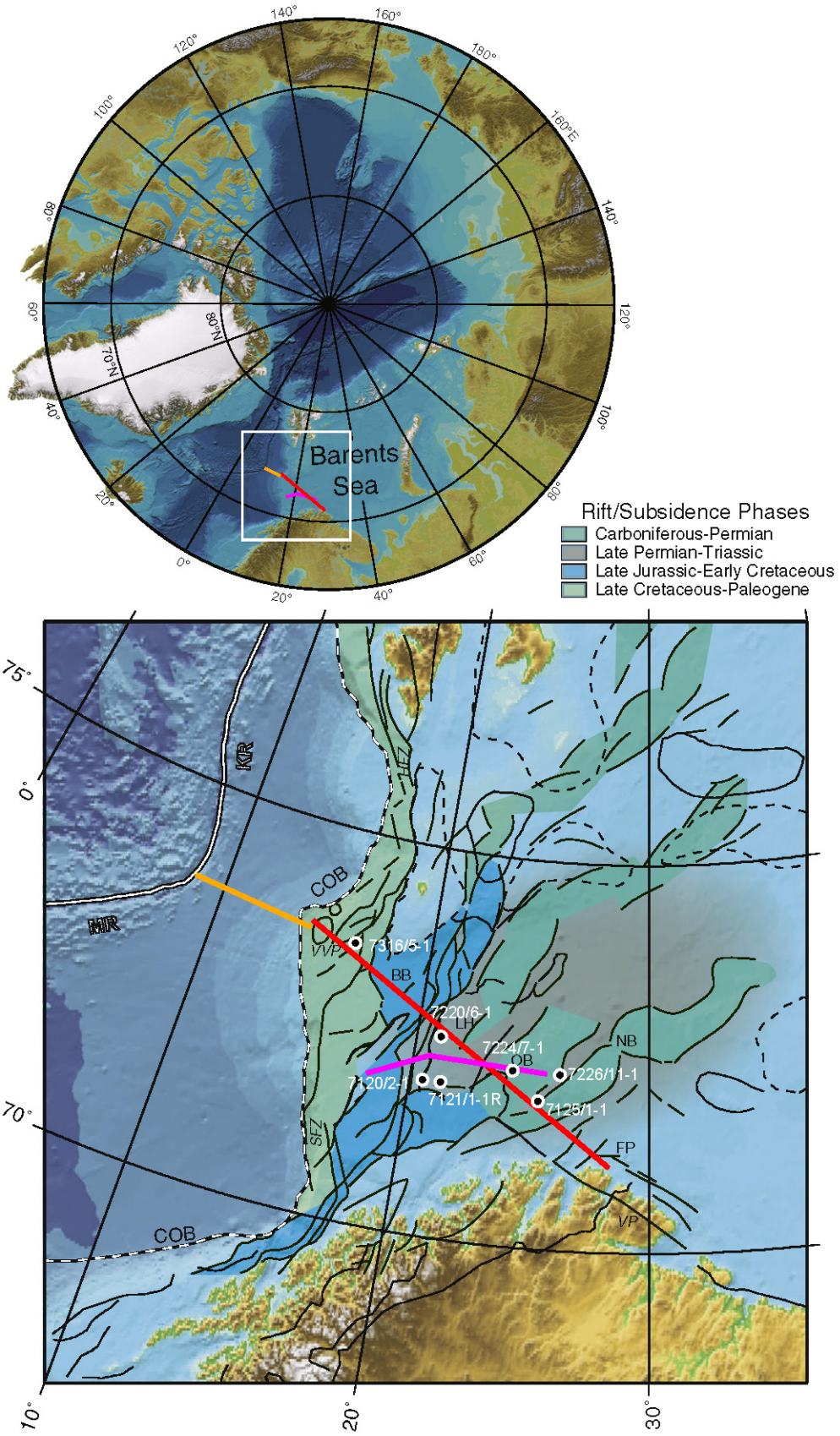
Barents Sea
Rift/Subsidence Phases
Carboniferous-Permian
Late Permian-Triassic
Late Jurassic-Early Cretaceous
Late Cretaceous-Paleogene
KR
HR
COB
VVP
7316/5-1
BB
7220/6-1
LH
7224/7-1
NB
OB
7226/11-1
7120/2-1
7121/1-1R
7125/1-1
SFZ
FP
VP
COB

2. Geological Framework

The Barents Sea is an epicontinental basin forming part of the north-west continental shelf of Eurasia. It was formed in response to discrete periods of extension and lithospheric thinning following gravitational collapse of the Caledonian Orogeny. It is bound to the west and north by passive margins that developed in response to opening of the Norwegian-Greenland Sea and the Eurasian Basin respectively. To the east, the width of the Barents Sea is limited by the northernmost extension of the Ural Mountains - the Novaya Zemlya archipelago (Faleide et al., 1984, 2010; NASA, 2014). The Barents Sea has been separated into three distinct areas in the peer-reviewed literature record; east (Russian Barents Sea), central (former disputed-zone between Norway and Russia), and west (Norwegian Barents Sea). There appears to be some consensus regarding this naming convention (Figure 2.1; Johansen et al., 1992; Smelror et al., 2009; Henriksen et al., 2011a; Klett & Pitman, 2011). The eastern Barents Sea features a broad, regional (1500 km long, 300-600 km wide), very deep basin (~20 km deep) trending NNE that may have formed by lithospheric shortening/buckling processes, primarily in response to the Uralian orogeny in Permian-Triassic time (Gac et al., 2012, 2013, 2014). The central Barents Sea features a regional basin high (sometimes referred to as the Central Barents Arch or Central Barents Monocline) separating the genetically different eastern and western sectors of the Barents Sea basin. The western Barents Sea features a series of discrete, relatively narrow rift basins (up to 18 km deep) and intermittent highs formed by lithospheric stretching and crustal thinning processes.

The western Barents Sea is the focus area for this study, and exhibits an almost complete succession of thick early Paleozoic to Cenozoic sedimentary sequences which constitute three distinct regions (figures 2.1 and 2.2). (1) The Svalbard Platform (north of 74°N) is covered by a relatively flat-lying succession of late Paleozoic and Mesozoic, mainly Triassic strata. (2) A basin province (south of 74°N and east of the Loppa High) between the Svalbard Platform and the Norwegian coast is characterised by a number of sub-basins and highs with an increasingly accentuated structural relief westward. Jurassic-Cretaceous, and in the west Paleocene-Eocene sediments are preserved in the basins. (3) The continental margin (west of the Loppa High) consists of three main segments: (a) a southern sheared margin along the Senja Fracture Zone; (b) a central rifted complex southwest of Bjørnøya (Bear Island) associated with volcanism and (c) a northern, initially sheared, later rifted margin along the Hornsund Fault Zone (Faleide et al., 2008; Faleide et al., 2010; Glørstad-

Clark et al., 2010). The continent-ocean transition along the western margin occurs over a narrow zone over the line of early Cenozoic break-up, covered by a late Cenozoic sedimentary wedge of predominantly glacial-derived deposits (Breivik et al., 1999).

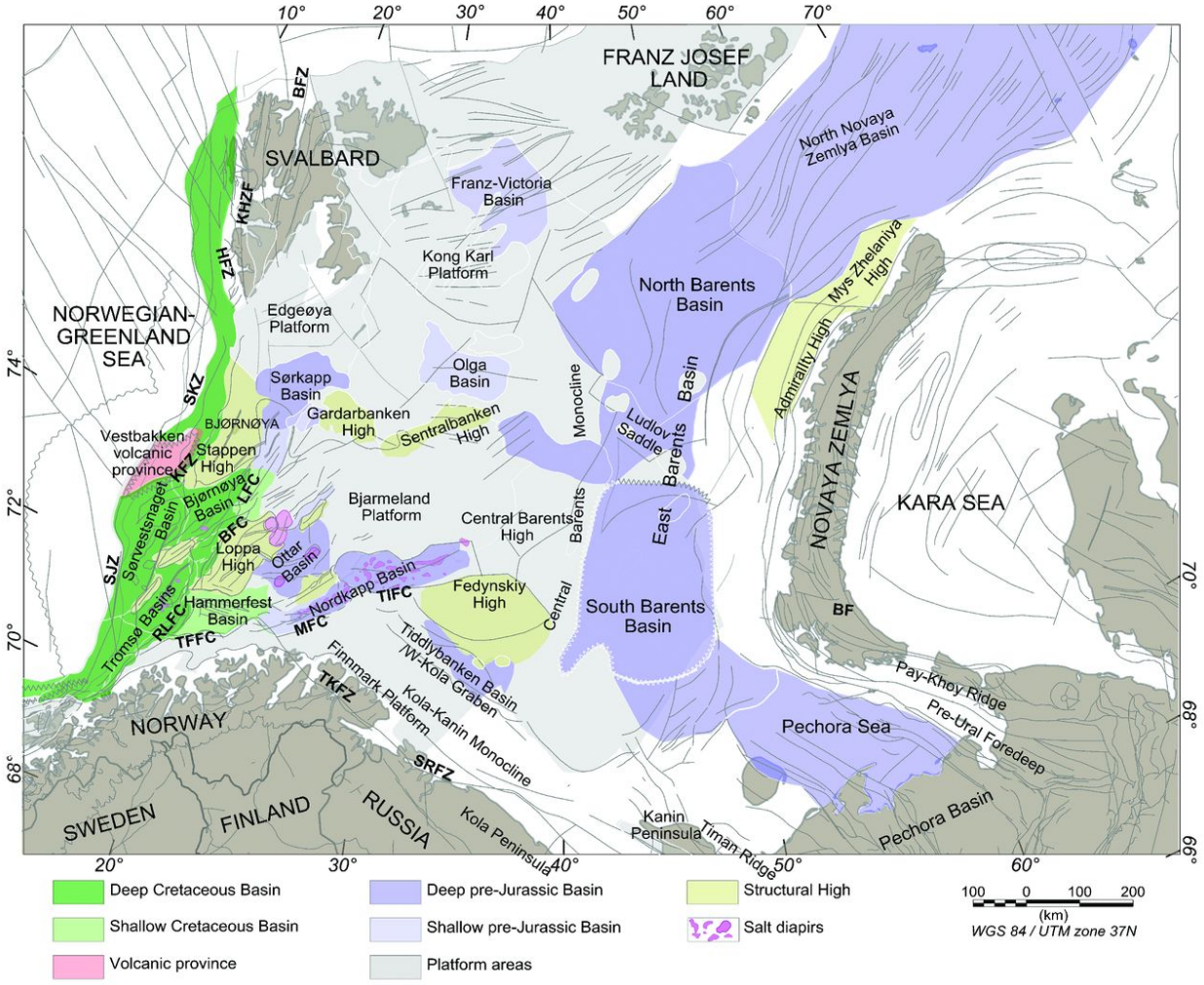

Figure 2.1. Geological setting of the Barents Sea, including the western, central, and eastern domains. The abbreviations denote to the major fault complexes: BF, Baidsratsky Fault Zone; BFC, Bjørnøyrenna Fault Complex; BFZ, Billefjorden Fault Zone; HFZ, Hornsund Fault Zone; KFZ, Knølegga Fault Zone; KHFZ, Kongsfjorden–Hansbreen Fault Zone; LFC, Leirdjupet Fault Complex; MFC, Måsøy Fault Complex; RLFC, Ringvassøy–Loppa Fault Complex; SJZ, Senja Fracture Zone; SKZ, Sørkapp Fault Zone; SRFZ, Sredni–Rybachi Fault Zone; TIFC, Thor Iversen Fault Complex; TFFC, Troms–Finnmark Fault Complex; TKFZ, Trollfjorden–Komagelva Fault Zone (Marello et al., 2013).

2.1 Major structural elements of the south-west Barents Sea

The major structural elements of SW Barents Sea, discussed throughout this thesis, sorted from occurrence west to east, are summarized below. The data, unless otherwise indicated, is collated from Gabrielsen et al. (1990). See figures 2.1 and 2.2 for locations.

Finnmark Platform:

Stable area bounded to the south by Caledonides of the Norwegian mainland. Its western and northwestern bounderies are defined by the Troms-Finnmark Fault Complex and the Nordkapp Basin. The platform is underlain by Paleozoic and Precambrian rocks that have structural features associated with the Caledonian Orogeny.

Nordkapp Basin:

A deep Paleozoic basin with a general NE-SW trend but central part of the basin has an E-W orientation and is more than 300 km long and 30-80 km in width. It is associated with gravity low and its central part is deformed by numerous salt structures.

Troms-Finnmark Fault Complex:

Comprised of individual faults trending NNW-SSW, NE-SW and ENE-WSW. It represents a major structural division between the Finnmark Platform in the south and southeast and the basinal area (Harstad Basin, Tromsø Basin and Hammerfest Basin) to the north and northwest. It is characterized by listric normal fault geometries accompanied by hanging-wall roll-over anticlines and antithetic faults.

Ottar Basin:

Upper Paleozoic graben with large accumulations of unmobilized salt (up to 2.4 km thick), buried beneath flat-lying Mesozoic strata (Breivik et al., 1995).

Maud Basin:

Interpreted as part of the primary rim syncline of the Svalis Dome.

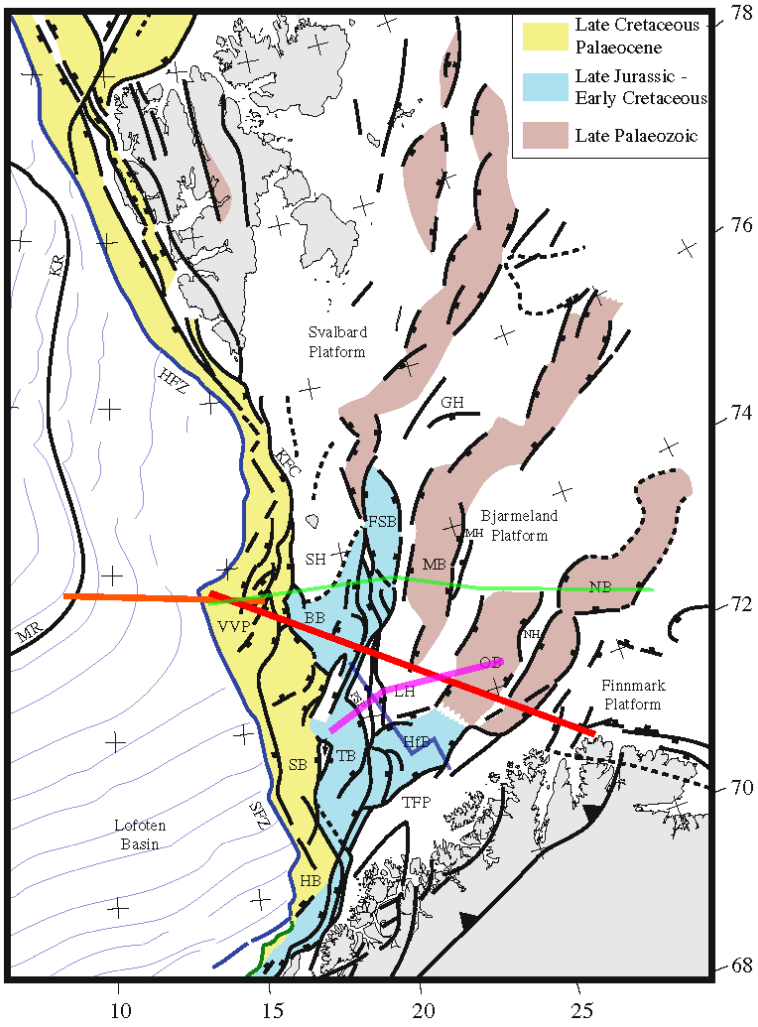

Figure 2.2. Geological setting of the western Barents Sea and adjacent areas. The thick red line represents the PETROBAR-07 transect, the thick orange line represents the HB-3-96A seismic line. These two lines make up the input stratigraphy (derived from Clark et al., 2014 and the author's work) for the first basin model run. The thick magenta line represents the transect used for stratigraphy input (derived from Glørstad-Clark et al., 2011a) within the second basin model run. The thin green line and thin blue line show the location of the profile in figure 2.5 and figure 2.6 respectively. Abbreviations: BB = Bjørnøya Basin; FSB = Fingerdjupet Sub-basin; GH = Gardarbanken High; HB = Harstad Basin; HfB = Hammerfest Basin; HFZ = Hornsund Fault Zone; KFC=Knølegga Fault Complex; KR = Knipovich Ridge; LH = Loppa High; MB = Maud Basin; MH = Mercurius High; MR = Mohns Ridge; NB = Nordkapp Basin; NH = Nordsel High; OB = Ottar Basin; PSP = Polheim Sub-platform; SB = Sørvestsnaget Basin; SFZ = Senja Fracture Zone; SH = Stappen High; SR = Senja Ridge; TB = Tromsø Basin; TFP = Troms-Finnmark Platform; VH = Veslemøy High; VVP = Vestbakken Volcanic Province (modified from Faleide et al., 2010).

Bjarmeland Platform:

Stable area between Hammerfest and Nordkapp basins to the south and southeast, and the structural highs of the southern Svalbard Platform to the north, and the Loppa High to the west. The structural pattern within the platform is mainly related to halokinesis and weak extension.

Hammerfest Basin:

Relatively shallow basin with an ENE-WSW structural trend. It is separated from the Finnmark Platform to the south by the Troms-Finnmark Fault complex and from the Loppa High to the north by the Asterias Fault complex. The general structure follows a gentle central dome paralleling the basin axis with an internal fault system trending E-W, ENE-WSW and WNW-ESE. The Hammerfest Basin has been interpreted as a failed rift within a triple junction and as a remnant of an older rift system.

Loppa High:

The Loppa High is situated north of the Hammerfest Basin and southeast of the Bjørnøya Basin, bounded to the south by the Asterias Fault Complex, and on the east and southeast by a monocline towards the Hammerfest Basin and the Bjarmeland Platform. To the west, it is bounded by Ringvassøy-Loppa and Bjørnøyrenna Fault Complex. The Svalis Dome and the Maud Basin marks the north-eastern limit of the high. It occurs as a major basement high, but was a major depocentre in the Triassic to middle Jurassic, but the area has subject to long periods of uplift and erosion during at least four distinct times since the Devonian. Recent literature separates two phases of platform high development in this area into the Selis Ridge (pre-Triassic) and the Loppa High (post-Jurassic), with markedly different geometries (Glørstad-Clark et al., 2011a).

Selis Ridge:

An old, relict structural high underlying the western parts of present-day Loppa High. Its presence is thought to have evolved during extension and uplift in the Late Carboniferous, with the primary uplift phase occurring during the Late Permian. It is also commonly referred to as the palaeo-Loppa High, but a separate definition was proposed by Glørstad-Clark et al. (2011a) due to its narrow geometry trending north-south and its prevalence during the late Carboniferous to middle Triassic.

Svalis Dome:

The Svalis Dome is located at the north-eastern margin of the Loppa High. It has a sub-circular cross-section in map view with a diameter of approximately 35 km, and occurs as a major salt structure, with a salt pillow geometry. The salt is interpreted to be of late Carboniferous age.

Bjørnøyrenna Fault Complex:

Situated between 72°N, 19°E and 73°15'N, 22°E and trending NE-SW direction. It defines the boundary between the Loppa High and the deep Bjørnøya Basin in the southwest and in the northeast it separates the Loppa High from the shallow Fingerdjupet Subbasin. In general, the complex is characterized by normal faults with large throws.

Fingerdjupet Subbasin:

Shallow, northeastern part of the deep Bjørnøya Basin. Separated from the Bjørnøya Basin by the Leirdjupet Fault Complex. The Loppa High and Bjarmeland Plaform define its southeastern and eastern boundaries. Consists of horst and graben structures following NNE-SSW trending fault blocks, with the western margin acting as the horst.

Bjørnøya Basin:

The Bjørnøya Basin is divided by the Leirdjupet Fault Complex into a deeper, westerly component and a shallow easterly component (the Fingerdjupet Subbasin). The basin is bounded to the south-east by the Bjørnøyrenna Fault Complex and the northwestern boundary is a faulted slope dipping down from the Stappen High towards the basin. It is a very deep half-graben, with a sedimentary succession downfaulted to 18 km depth (Clark et al., 2014).

Stappen High:

The Stappen High, trending N-S, is bounded to the west by Knølegga Fault, to the south by the Bjørnøya Basin and to the east by the Sørkapp Basin. The southern part of the high is strongly affected by NNE-SSW trending faults.

Veslemøy High:

The Veslemøy High is a complex NE-SW trending structural high. Bounded by the deep Bjørnøya Basin and the Sørvestsnaget Basin to the north and north-west and the Tromsø Basin to the south. Underlain by a basement high, with associated positive gravity anomaly, but separated from the Senja Ridge by the Bjørnøyrenna Fault Complex.

Tromsø Basin:

Located north of the city of Tromsø, bordered by the Senja Ridge to the west and the Ringvassøy-Loppa Fault complex to the east. To the south-east, it terminates against the Troms-Finnmark Fault complex. In the north, it is separated from the Bjørnøya Basin by the Veslemøy High. The Tromsø Basin has a NNE-SSW trending axis enhanced by a series of salt diapirs and is associated with a system of detached faults.

Harstad Basin:

The Harstad Basin is located north of Andøya, close to the shelf edge with a NNE-SSW trending axis. Its eastern boundary is defined by the southernmost part of the Troms-Finnmark Fault Complex whereas the western limit coincides with the Continent-Ocean Transition.

Senja Ridge:

Structural high which runs subparallel to the continental margin and defines the western limit of the Tromsø Basin. Underlain by a basement high, with associated positive gravity anomaly.

Sørvestsnaget Basin:

The Sørvestsnaget Basin is located adjacent to the Barents Sea shelf and is composed of thick succession of Cretaceous and Tertiary sediments. The Sørvestsnaget Basin represents the structural continuation of the Bjørnøya Basin from which it is separated by a normal fault system of Tertiary age. The northern limit of the basin is defined by the lavas of the Vestbakken Volcanic Province and by the NE-SW trending fault complexes on the southern part of the Stappen High. The basin is bounded by the Senja Ridge and Veslemøy High in the southeast.

Vestbakken Volcanic Province:

A pull-apart basin situated south and west of Bjørnøya. Formed in response to extension between present-day Greenland and northern Norway along the releasing bend of a transform margin. Significant volumes of volcanics and intrusions are observed in seismic

and the well 7316/5-1 associated with continental breakup in Eocene time. Huge submarine fans of Quaternary glacial-derived sediments present along western parts.

Continent-Ocean Transition:

A primarily sheared margin, which varies in width considerably from north to south. Separated into two sheared segments in the north and south; the Hornsund Fault Zone (north), and Senja Fracture Zone (south). A rifted margin due to pull-apart tectonics is present along the northern periphery of the Vestbakken Volcanic Province (Breivik et al., 1999).

Barents Shelf, Continental Rise and Abyssal Plain:

Development began in Eocene time due to seafloor spreading, characterised by thick deposits of glacial-derived sediments towards the mid-ocean ridge along a series of submarine fans. These fans complexes include the Storfjorden Fan (between Svalbard and Bjørnøya), and the Bjørnøya Fan (south of Bjørnøya) (Hjelstuen et al., 1996, 2007).

2.2 Geological Evolution of the western Barents Sea

The basins of the western Barents Sea were formed in response to three major rift phases, late Devonian?-Carboniferous, Late Jurassic-Early Cretaceous, and early Cenozoic (Faleide et al., 2008). An inferred late Permian rift event (probably also affecting the earliest Triassic) is also recognized, though poorly defined due to a lack of resolvable widespread rift-faulting. Following orogenic collapse of the Caledonides in the Early Devonian, the western margin of Baltica (including the western Barents and Vøring margins) acted as a transfer zone linking extension occurring in the present-day North Atlantic and Arctic regions (Ziegler, 1988; Doré, 1991; Gudlaugsson et al., 1988; Clark et al., 2014).

The lithostratigraphy of the western Barents Sea is shown in figure 2.3 together with the timing of discrete rifting periods.

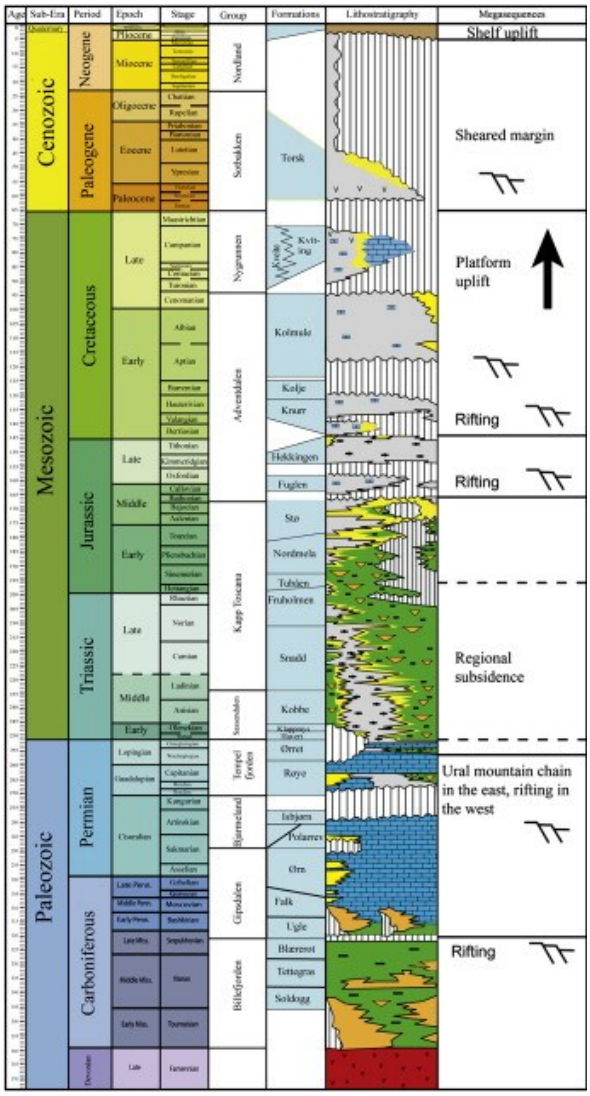

Figure 2.3. Schematic diagram of the lithostratigraphy in the western Barents Sea. The lithostratigraphy is modified from Nøttvedt et al. (1993) and Larssen et al. (2002). Time scale is from Gradstein et al. (2004). Formation names are from Mørk et al. (1999) (after Glørstad-Clark et al., 2010).

The crystalline basement of the western Barents Sea probably consists of igneous and metamorphic rocks associated with the Caledonian Orogeny. This assumption is based on mostly indirect evidence from geophysical data (e.g. Ritzmann & Faleide, 2007; Gernigon & Brönner, 2012; Marello et al., 2013; Gernigon et al., 2014). Caledonian rocks were formed from an Archean to Proterozoic protolith during subduction associated with the closure of the Iapetus Ocean and oblique continental collision of Baltica and Laurentia between Ordovician to early Devonian time (Roberts & Gee, 1985; Roberts, 2003). The deformation associated with the Caledonian Orogeny resulted in nappe imbrication along NE-SW trending thrusts and sutures in northern Norway. Five distinct crustal units can be identified; including four allochthons or nappe complexes (Lower, Middle, Upper, Uppermost), and

Precambrian autochthonous basement. The allochthonous crustal units (nappe complexes) consist of marine metasedimentary rocks from the Baltica continental margin (Lower-Upper Allochthon) and obducted supracrustal rocks (including both metasedimentary and magmatic rocks) derived from outboard of Baltica margin - most likely of Laurentian origin (Uppermost Allochthon). Nappe complexes are stacked along sutures which have facilitated hundreds of kilometres of strain along a NE-SW structural grain (Roberts, 2003). This prevalent grain has had a profound effect on subsequent basin development following the collapse of the Caledonian orogeny and extension within discrete rifts in the western Barents Sea (Faleide et al., 1984, 1993a,b; Dengo & Røssland, 1992; Gudlaugsson et al., 1998; Breivik et al., 2002; Ritzmann & Faleide, 2007).

During the late Devonian?-Carboniferous rift event, most of the Barents Sea was affected by crustal extension. Interconnected half-grabens separated by highs were created with fan-shaped configurations along a N to NE trend (Faleide et al., 1984; Rønnevik & Jacobsen, 1984; Gabrielsen et al., 1990; Dengo & Røssland, 1992; Gudlaugsson et al., 1998). The post-rift phase consists of late Carboniferous to early Permian platform strata covering the structural relief, specifically evaporates and shallow water carbonates (Faleide et al., 1984). Significant volumes of hydrocarbons have recently been identified in these carbonates along the Loppa High at the Gohta and Alta prospects (Carstens, 2013). The clastic input of basin fill increased throughout the Permian. Later stretching events compartmentalized extension further into well-defined rift basins, with basin development progressively migrating westward since the Late Paleozoic (see figure 2.2). Strike-slip faults accommodating lateral displacement in the north are synchronous with these later extensional phases.

The inferred late Permian rift event, poorly defined due to a lack of rift-faulting, is focused along a localized N-S axis adjacent to the Selis Ridge (paleo-Loppa High). Uplift of the Selis Ridge is observed in the Early and Middle Triassic, evidenced by widespread erosional surfaces. Islands along the ridge inhibited sediment progradation westward. The subsidence from this inferred rift event provides the accommodation space required for large volumes of clastic sedimentation observed in the rock record of both basin (throughout the entire Triassic) and high areas (confined to the Late Triassic) around the Selis Ridge. The Ural orogenic belt, the Baltic Shield, and other locally uplifted areas are considered to be the source of clastic sediments (Faleide et al., 2010; Glørstad-Clark et al., 2010; Glørstad-Clark et al., 2011b). As thermal subsidence waned through the middle Triassic, the south-west Barents Sea basin shallowed considerably from predominantly marine depositional

conditions to continental and deltaic conditions. In the central and northern parts of the western Barents Sea, distal to the primary clastic source regions, marine conditions persisted. The organic-rich marine shales of Early-Middle Triassic age (e.g. Top Klappmys and Top Kobbe formations) may act as a source rock across the western Barents Sea. The latest Triassic was characterised by a marine regression and erosion, quite possibly the result of reduced accommodation space on a basin-scale due to minimal thermal subsidence and far-field effects related to mantle plume activity in the central Atlantic (Hallam, 2001; Faleide et al., 2010).

Clastic sedimentation continued into the Jurassic, with Early-Middle Jurassic sandstones found over the entire western Barents Sea. These sandstones have high porosity and permeability and act as a primary hydrocarbon reservoir (e.g. Snøhvit field). A major rift event is recorded from the Middle Jurassic to Early Cretaceous. The event is characterised by two rift pulses from Middle-latest Jurassic and latest Jurassic-Early Cretaceous (Faleide et al., 1984; Faleide et al., 1993a; Faleide et al., 1993b). In deeper water environments, contemporaneous with the rift event, organic-rich shales were deposited during the Late Jurassic which are considered excellent potential source rocks (Hekkingen Formation). Deep water shales deposited in the Cretaceous form very thick successions in the deep basins of the south-west Barents Sea (Ryseth et al., 2003). Salt tectonics (halokinesis) induced by thermal subsidence of the Tromsø Basin was prevalent in the Late Cretaceous.

A widespread unconformity marks the boundary between the Cretaceous and Paleogene sediments. Rapid Paleocene subsidence in the west resulted in the deposition of clays across an open to deep marine shelf. Dextral oblique slip along the proto-breakup margin – the De Geer Zone – accommodated Paleocene-Eocene extension, and produced pull apart basins in the Wandel Sea (present-day western Greenland) and the western Barents Sea (Vestbakken Volcanic Province), though this process may have started in the Late Cretaceous (Faleide et al., 2008). This is illustrated in the Cenozoic plate reconstruction presented in figure 2.4. The De Geer megashear zone, which linked the Norwegian- Greenland Sea with the Eurasia Basin in the south, consisted of 2 wrench-faulted segments; the Hornsund Fault Zone in the north (between Bjørnøya and Svalbard) and the Senja Fracture Zone in the south, separated by a releasing bend where rifting dominated. Continental breakup and seafloor spreading occurred along this predominantly sheared margin at approximately 55-54 Ma (Faleide et al., 2008). The different components of the De Geer system had different breakup histories. The

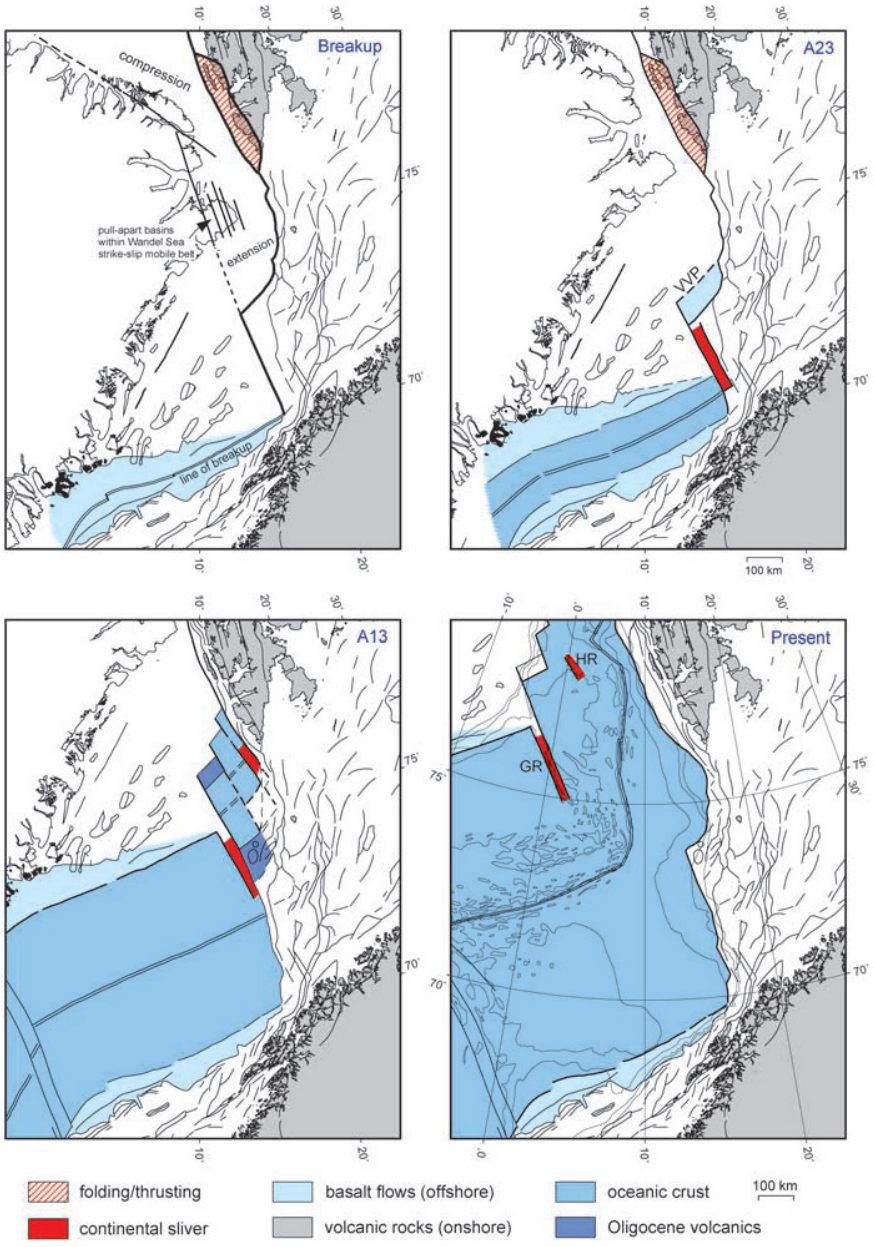

Figure 2.4. Cenozoic plate tectonic evolution of the Norwegian-Greenland Sea following continental breakup from the Eocene (55-54 Ma) (Faleide et al., 2008).

Senja Fracture Zone developed by continent-continent shear followed by continent-ocean shear. It has a clearly identifiable Continent-Ocean Boundary, and has been passive since earliest Oligocene time. Breakup-related magmatism and partly associated uplift is recorded in the Vestbakken Volcanic Province from Palaeocene to Eocene, and was followed by down-faulting and deposition of thick Eocene strata. The Hornsund Fault Zone experienced oblique continent-continent and partly continent-ocean shear with both transtensional and transpressional components during the Eocene (Faleide et al., 2008). At the end of the Eocene, a narrow oceanic basin existed between the western Barents Sea and NE Greenland

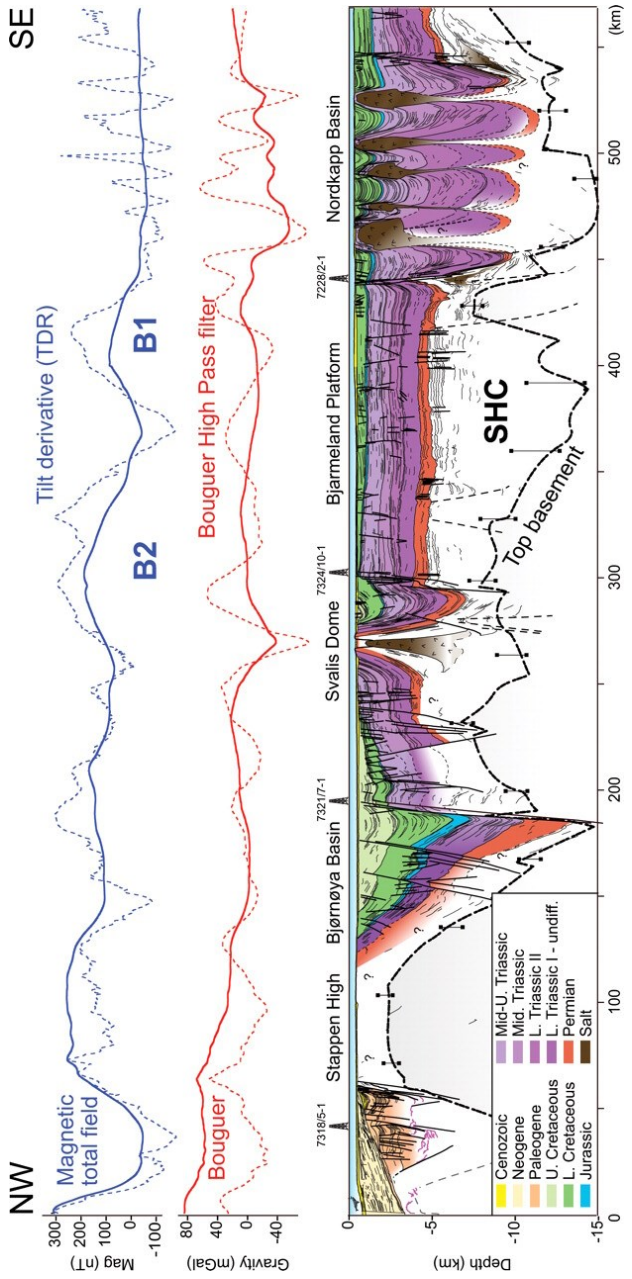

Figure 2.5. WNW-ESE basin-wide cross section through the western Barents Sea. The black dashed line and vertical error bars in the lower part of the figure indicate the depth estimation (and its uncertainties) to crystalline basement obtained from potential field modelling. The Magnetic Field data (solid blue) and tilt derivative (dotted blue) reflect the deep (pre-Permian) basement highs. The Bouger Gravity (solid red) and Bouger High-Pass filter (dotted red) reflect density variations in the sediments and basement. Note the influence of salt on the structure of the Svalis Dome and the Nordkapp Basin and their associated gravity lows . Profile location marked with green line in figure 2.2 (Gernigon & Brönner, 2012).

continental margins. A plate reorganization event in the early Oligocene caused Greenland to move in a more westerly direction with respect to Eurasia, and reactivated faults and renewed magmatism in the Vestbakken Volcanic Province. By the Miocene, a deep water gateway between the North Atlantic and Arctic was established, with significant implications for palaeo-oceanography and climate in the region (Engen et al., 2008; Faleide et al., 2008).

Reactivation of faults and uplift is recorded in the middle to late Cenozoic. In the late Miocene, a tectonic uplift event (unrelated to later glacial periods) is recorded with increasing amplitude from west to east in the Vestbakken Volcanic Province (Jebsen & Faleide, 1998). Over the entire shelf, this uplift event had severe consequences for the petroleum systems of the Barents Sea, with significant redistribution of hydrocarbons due to tilting beyond the spill point and depressurization of reservoirs, re-organization of migration pathways, and removal of some source-sink areas from the oil window (Ohm et al., 2008). Following the Neogene uplift, global climate change at 2.6 Ma brought about the Northern Hemisphere glaciation, marked by a basin-wide unconformity. Glacial erosion exacerbated by Plio-Pleistocene uplift removed kilometer-thick layers of Cenozoic sediments from the shelf and deposited huge prograding wedges of sandy/silty muds along the western margin (Laberg & Vorren, 1996; Faleide et al., 1996; Knies et al., 2009). Disruption of petroleum systems stability therefore continued following the Neogene event and throughout the Plio-Pleistocene glaciation. Massive submarine slides can be identified along the distal western margin, evidence of sediment instability related to excess depositional rates and elevated pore pressure (Hjelstuen et al., 2007). Debate continues, however, in the peer-reviewed literature regarding the relative contribution to the total Cenozoic erosion budget of the Neogene uplift and the Quaternary glaciations. Nyland et al. (1992) and Rodrigues Duran et al. (2013) advocate the Neogene uplift as the primary contributor to total erosion compared to the Quaternary glaciations (with an erosion magnitude ratio of 2:1) based on Apatite Fission Track analysis and 3-D modelling through the Hammerfest Basin. Cavanagh et al. (2006), on the other hand, support Quaternary glaciations as the primary influence over total Cenozoic erosion based on 2-D modelling across the Hammerfest Basin.

2.3 Petroleum Systems of the southwestern Barents Sea

Source rocks

Source rocks ranging from Carboniferous to Cretaceous have been identified within the south-west Barents Sea. Potential for Cenozoic source rocks along the western margin is also contemplated by some workers based on results from other Arctic basins (e.g. Spencer et al., 2011), but this has yet to be confirmed by drilling. The five main source rock groups within the south-west Barents Sea include the early-middle Carboniferous, late Permian, Triassic, Late Jurassic, and Early Cretaceous (Henriksen et al., 2011a). Their petroleum potential

based on vitrinite reflectance and geochemical analysis of well-core data is summarized in table 2.1.

Table 2.1. Petroleum potential derived from analyses of core data from wells drilled in the western Barents Sea. Rock-Eval Pyrolysis (T_{max} – thermal maturity indicator), Total Organic Carbon (TOC), and petroleum content measurements form the basis of these evaluations (Pedersen & Karlsen, 2005).

Source Rock Interval	Petroleum Potential
Early-Middle Carboniferous	Fair to Good
Late Permian	Fair to Good
Triassic	Good
Late Jurassic	Excellent
Cretaceous	Not quantified

Gas-prone coals and mudstones from the early Carboniferous Billefjord Group are known as potential source rocks within the south-west Barents Sea. Oil discovered on the Finnmark Platform and on Svalbard is known to originate from these rocks (van Koeverden et al., 2011).

Oil prone late Permian carbonaceous mudstones and limestones of the Tempelfjorden Group are known source rocks. The oil and gas discovered recently at the Gohta and Alta prospects on the Loppa High is derived from these sediments (Carstens, 2013). The organic content of these shales and limestones are higher on and to the east of the Loppa High, whereas to the south and west of the Loppa High the sediments of late Permian age are dominated by organic-poor siliclastic siltstones and sandstones (Larssen et al., 2002).

Oil and gas prone Triassic marine shales along the western parts of the Barents Sea (including the Loppa High, Bjarmeland Platform, and Svalbard) are known source rocks. The Triassic source rock intervals are generally patchier in distribution compared to the more prolific Late Jurassic source rocks, and are associated with marine anoxia during periods of maximum flooding and/or condensation (Ohm et al., 2008; Henriksen et al., 2011a). These flooding events correspond to the following ages: Early Norian (Top Snadd Formation), late Anisian-early Ladnian (Top Kobbe Formation), late Olenekian-early Anisian (Top Klappmys Formation), Olenekian (Top Havert Formation), and early Induan (Base Havert Formation). Oils from the Obesum discovery (non-commercial) on the Bjarmeland Platform are derived from middle Triassic shales, with a minor component from Early Triassic shales (Henriksen et al., 2011a). Some of the oil from the lower reservoir

(Kobbe Formation) of the Goliat field is thought to be derived from Early and Middle Triassic shales (NPD, 2012).

Oil and gas prone Late Jurassic shales of the Hekkingen Formation are the best source rocks, with very high Petroleum to Total Organic Carbon (TOC) weight ratios (Pedersen & Karlsen, 2005; Ohm et al., 2008). Most of the discovered oil and gas fields in the western Barents Sea are related to source rocks from Middle to Late Jurassic. These include the Snøhvit, Johan Castberg, and the upper reservoir of the Goliat field (NPD, 2012).

Cretaceous source rocks with significant proportions of organic material may occur within the Vestbakken Volcanic Province and Sørvestsnaget Basin. However, the large volumes clastic sedimentation both during and following lithification in the Cretaceous and Early Cenozoic may have inhibited the development of a substantial petroleum system (Henriksen et al., 2011a). The only well that has been drilled in the Vestbakken Volcanic Province was a gas discovery, but 97% of the trapped methane was reported to be of biogenic in origin (Knutsen et al., 2000). The recent 7319/12-1 Pingvin gas discovery in the Bjørnøya Basin may derive from Cretaceous source rocks, but the results are yet to be published. So an effective Cretaceous petroleum system is yet to be proved.

Source rock maturation and hydrocarbon migration

Source rocks in the western Barents Sea were probably generating oil in the deepest basins (e.g. Bjørnøya and Tromsø basins) by the Middle Triassic, peaking in the Cretaceous. Some of the source rock intervals, for example the Late Jurassic shales in the Hammerfest Basin, are in the oil window at present and therefore form an active petroleum system (Henriksen et al., 2011a). Migration pathways are often up-dip along permeable sandstone or fractured limestone and through faults into traps. These migration pathways can occur over long distances. The Hekkingen Formation is mature approximately 30-40 km north and west of the Snøhvit field, whereas the Goliat field is 100 km from mature Late Jurassic source rocks (see figure 2.6).

Traps

Potential reservoirs are distributed across several stratigraphic levels from Devonian to Tertiary and comprise both sandstone and carbonate lithologies. Jurassic sandstones are the main proven reservoir but hydrocarbons have also been found in sandstones of Triassic and

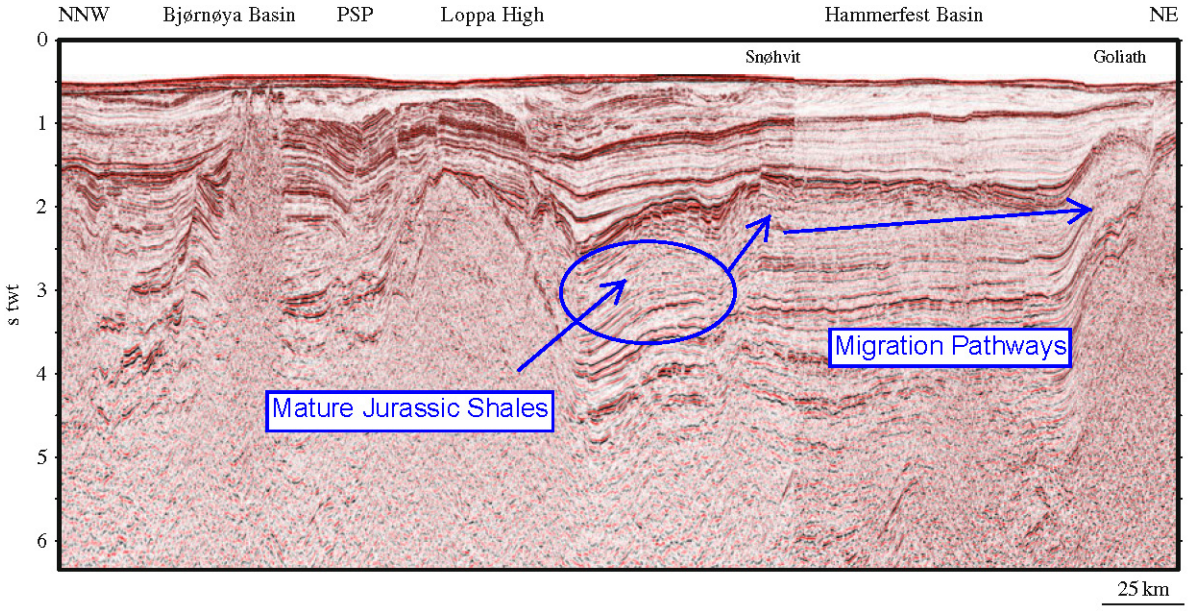

Figure 2.6. Seismic line illustrating the common features within petroleum systems of the southwest Barents Sea. Late Jurassic source rocks in the western, deeper portions of the Hammerfest Basin feeding the Snøhvit and Goliat fields are mature significant distances from the traps. This petroleum system may not have been active without substantial Cenozoic uplift and tilting. Seismic profile oriented in a NNW-SSE direction, looking ENE. Location shown on map in figure 2.2. Figure adapted from Faleide et al. (2010).

Cretaceous age (Faleide et al., 2010). A number of trap types including faulted domes, tilted fault blocks and roll-over anticlines exist on the Bjarmeland and Finnmark Platforms. Numerous tilted fault-blocks and extensional horsts occur along the western margin (Henriksen et al., 2011a). Salt structures in the Nordkapp Basin, and stratigraphic pinchouts towards platform-highs also provide traps for hydrocarbon accumulations (Faleide et al., 2010).

Cenozoic uplift and erosion

The Cenozoic uplift and erosion associated with (1) continental breakup; (2) North Atlantic Neogene uplift; (3) Plio-Pleistocene glaciations have resulted in the removal of up to 2 km sedimentary overburden. This has had a profound effect on all petroleum systems in the Barents Sea (Doré & Jensen, 1996; Ohm et al., 2008). Depressurization of reservoirs resulted in gas expansion and exsolution of gas from oil, expelling large volumes of oil from the traps, evidenced by residual oil columns in a number of wells (Nyland et al., 1992). Uplift and tilting of traps led to seal breaching and spillage (Doré & Jensen, 1996). While significant volumes of hydrocarbons may have been percolated up to seabed during the uplift and tilting, reducing the total hydrocarbon budget of the Barents Sea, it also provided the necessary dip in permeable sandstones and limestones for hydrocarbon migration over 100

km into new traps at Goliat and Snøhvit. The failure of seals through hydraulic fracture may also be relevant following uplift. Cooling of source rocks was also an inevitable consequence of uplift, resulting in cessation of hydrocarbon generation in some areas (Ohm et al., 2008). A positive contribution of uplift and erosion is that uplifted reservoirs inhibit biodegradation by sterilization of hydrocarbon-degrading organisms (Wilhelms et al., 2001). In summary, while Cenozoic uplift and erosion has certainly caused leakage and loss of hydrocarbons from the Barents Sea sediments to the seafloor, it has also contributed to redistribution of oil and gas to more accessible traps at higher stratigraphic levels and sterilized some reservoirs from the deleterious effects of biodegradation.

3. An introduction to the principles of basin modelling

Quantifying the hydrocarbon maturation in source rocks is crucial for assessing the viability of a petroleum system. Hydrocarbon maturation is controlled by the thermal history of source rocks which is in turn controlled by various interacting processes such as sediment deposition and compaction, sea level variations (Makhous & Galushkin, 2005) and lithospheric processes associated with basin formation.

Basin modelling aims to simulate fundamental sedimentary and lithospheric processes in order to quantify the thermal and burial history of sediments in a specific sedimentary basin. Basin models are built on the assumption that sedimentary rift basins are the result of extension within the lithosphere due to far-field tectonic forces (McKenzie, 1978).

3.1 Lithospheric extension theory

Subsidence histories of many sedimentary rift basins can be explained by extension in both the crust and mantle lithosphere. This extension leads to a disruption of the hydrostatic equilibrium between the extended and thinned lithosphere and the adjacent undeformed lithosphere, and a compensating rise of the asthenosphere ensues to restore equilibrium. Hydrostatic equilibrium in the lithosphere is defined by the concept of isostasy (Allen & Allen, 2013).

3.1.1 Isostasy and flexure

The term isostasy, comes from the Greek words “iso” and stasis” meaning “equal standing” (Watts, 2001). The isostasy concept describes the stress balance in the lithosphere. The lithosphere tends to approach gravitational equilibrium. At isostatic equilibrium it is assumed that the weight of any lithospheric column overlying the fluid-like asthenosphere is equal to the weight of a reference lithospheric column (generally the non-deformed continental lithosphere). Stretched lithosphere (including sedimentary basin infill and water) will tend to settle at an elevation above the weaker asthenosphere to achieve equal gravity

with the reference column. Historically, three models of isostasy have been used to explain density-depth distributions in the lithosphere and asthenosphere (figure 3.1):

1. The Airy (1855) Model
2. The Pratt (1855) Model
3. Flexural Isostasy Model (Vening Meinesz, 1941)

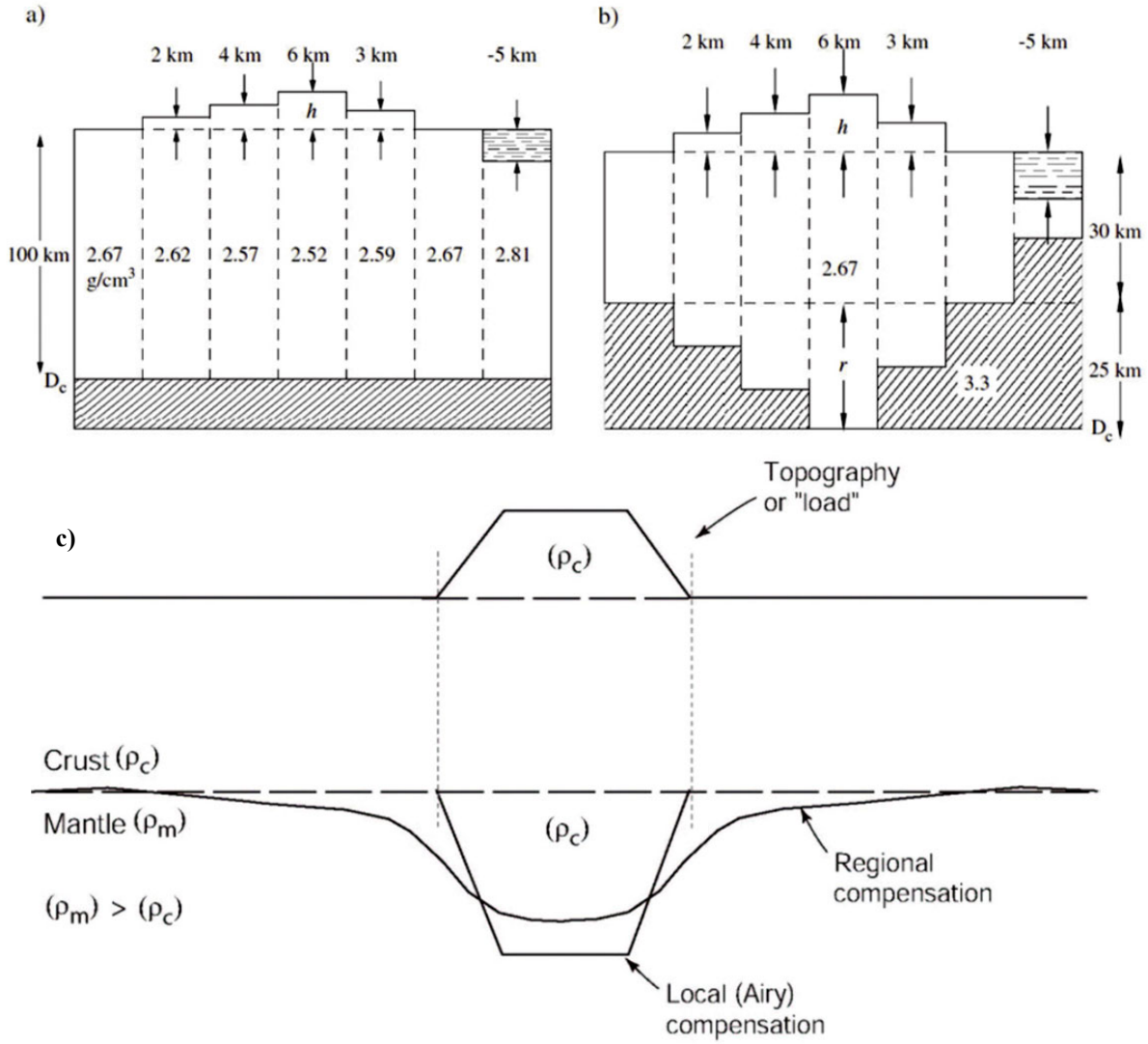

Figure 3.1. The three different models for isostasy. (a) Pratt model consists of a crust with heterogeneous density, with adjacent columns balancing on a uniform Moho – the height of each column is dictated by its density. (b) Airy model consists of a crust with homogeneous density, with adjacent columns balancing on a viscous mantle (with variable Moho) at a height related to their thickness. (c) Flexural isostasy model relates loading of the mantle to regional bending of the lithosphere. While Airy and Pratt models are compensated locally, Flexural isostasy models are compensated regionally (Watts, 2001).

The Airy model assumes topographic variation along the earth's surface is a response of varying thicknesses of adjacent lithospheric columns. The Pratt model assumes that varying density of adjacent lithospheric columns explains the observed topography. These two

models are locally-compensated, in that the isostatic response of each lithospheric column is solved independently, and have no effect on adjacent movements. With the advent of seismology and velocity inversion in the mid 20th century, significant density differences through the crustal structure of the continents were not observed, and the Pratt model deemed invalid, despite its popularity in North America (Watts, 2001). In the Flexural Isostasy model it is assumed that the lithosphere behaves like an elastic plate characterized by an elastic thickness T_E. This model incorporates the effect topographic loads have on the regional displacement of the lithosphere (a simple analogy of a continuous plate subject to a point-load can be invoked) and is therefore not locally compensated.

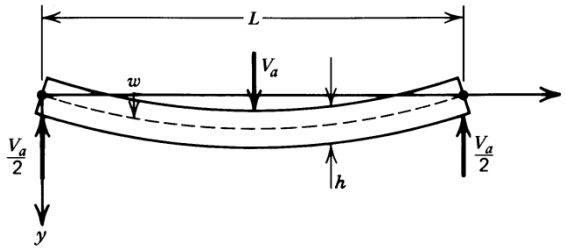

$$D = \frac{ET_E{}^3}{12(1-\nu)^2}$$

Figure 3.2. Thin plate of length L, and thickness h (analogous to T_E) bending under an applied load V_a, with a measurable deflection w. In this example, due to the symmetry of the plate, the applied load V_a is supported by 2 vertical line forces $V_a/2$ at each end. The flexural rigidity of the plate describes the bending moment divided by its curvature (in essence, the strength of the plate), and is a function of the effective elastic thickness (Turcotte & Schubert, 2002).

3.1.2 Lithospheric stretching models

McKenzie (1978) proposed a two-phase model: a rift-phase and a post-rift phase (sag phase), to explain the evolution of sedimentary basins. According to McKenzie, during rifting, the crust and mantle lithosphere are stretched and thinned, and isostatic compensation is provided by uplift of the Moho (with hot asthenosphere replacing cooler lithosphere) together with subsidence (or sometimes uplift if the crust is very thin compared to the lithosphere) at the surface (figures 3.3 and 3.4a). This stretch event is assumed to occur instantaneously. McKenzie & Jarvis (1980) later showed that this assumption is sufficient provided that the duration of mechanical rifting ceases within a time frame of at least 15 Ma. This is a valid assumption for most continental rift scenarios. The stretching factor (β) is a geometric concept relating the initial pre-rift width of the basin (defined by 'l_0' in figure 3.3) with the stretched post-rift width of the basin ('$l_0\beta$').

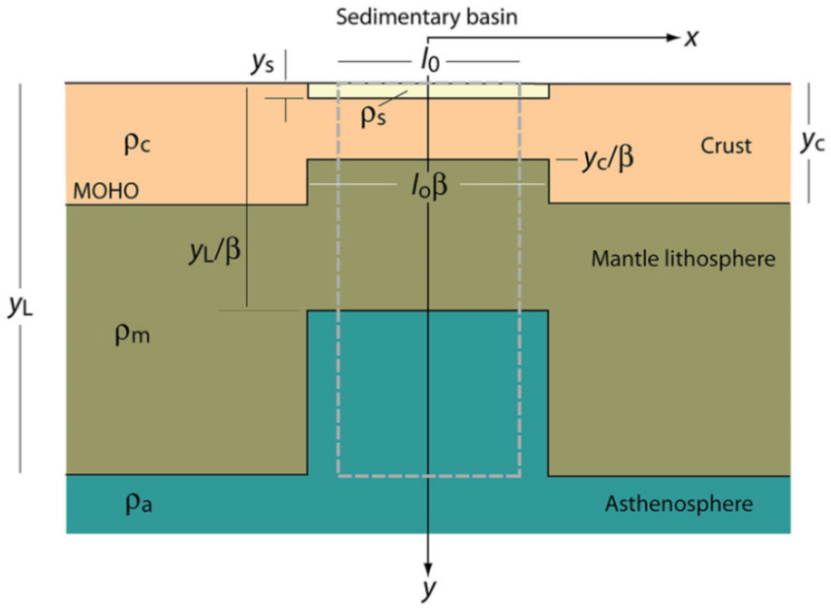

Figure 3.3. Setup for the reference uniform stretching model (McKenzie, 1978). The crust and subcrustal lithosphere stretch horizontally and thin vertically, uniformly with depth. Sediment, crustal, mantle and lithospheric densities are ρ_s, ρ_c, ρ_m, and ρ_a. The crust and lithosphere have an initial thickness of y_c and y_L, the zone of stretching has an initial width l_0. The crust and subcrustal (mantle) lithosphere stretch uniformly by a factor β (Allen & Allen, 2013).

After the instantaneous rift-phase, slow cooling of the thermal anomaly beneath the stretched lithosphere describes the sag phase. As upwelled asthenosphere cools, densification of the upwelled material follows and the Moho subsides. Contemporaneous basin subsidence and heat flux evolution in the sag phase follow a negative exponential function, and can span over a period of 60 My until thermal and isostatic equilibrium are achieved (Allen and Allen, 2013). The McKenzie (1978) model assumes the homogeneous lithosphere is stretched uniformly to create a symmetric basin. This requires no solid body rotation. Such a scenario is described by pure shear deformation. However, some basins have a pronounced asymmetry. To account for this asymmetry, Wernicke (1985) proposed large-scale detachment faults linking the brittle upper crust to the lower ductile lithosphere and asthenosphere based on observations in the Basin and Range Province of western USA. This scenario involves significant solid body rotation and is described by simple-shear deformation (figure 3.4b). The main difference between these two end-member models lies within how basin-scale extension is facilitated: through uniform stretching of the lithosphere (McKenzie, 1978), or through large-scale asymmetric detachment faulting (Wernicke, 1985). Most basins worldwide provide evidence of both these processes occurring during extension.

The Wernicke (1985) model is predominantly qualitative, based on field observations, and is difficult to quantify specifically due to the asymmetric disconnect between the thermal anomaly and the stretched/rotated lithosphere. Pure-shear and simple-shear may affect different epochs of rift evolution, and the primary deformation mechanism may be a function of crustal thickness, with pure-shear affecting relatively thick crust, while simple shear dominating in thin crustal sections like hyperextended margins. Because of this temporal evolution problem, and the simplicity of pure-shear solutions, variants of the McKenzie (1978) model, including those which incorporate simple shear deformation in the upper crust directly above the thermal anomaly (e.g. the Flexural-Cantilever model of Kusznir et al., 1987 and Kusznir et al., 1991 in figure 3.4c) are certainly the most popular methodologies for quantitative basin analysis.

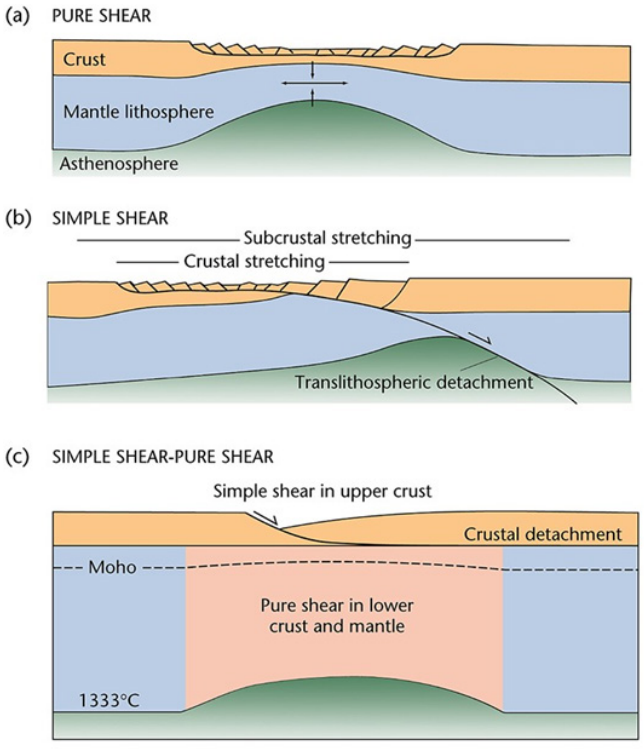

Figure 3.4. Lithospheric shear models derived from pure shear, simple shear, and combined shear mechanisms. (a) Pure shear geometry with an upper brittle layer overlying a lower ductile layer, producing a symmetrical lithospheric cross section with the initial fault-controlled subsidence spatially superimposed in the thermal subsidence. The ductile stretching may be accompanied by dilation due to the intrusion of melts. (b) Simple shear geometry with a through-going low-angle detachment dividing the lithosphere into an upper plate or hangingwall, and a lower plate or footwall. Thinning of the lower lithosphere is relayed along the detachment plane, producing a highly symmetrical lithospheric cross-section. Initial fault-controlled subsidence is spatially separated from the thermal subsidence. (c) Hybrid model of simple shear in the upper crust on listric or planar fault planes, and pure shear in the ductile lower crust and mantle lithosphere (Allen & Allen, 2013).

Variations of the uniform stretching model of McKenzie (1978) have been proposed to explain (1) syn-rift uplift observed in many rifted-basin flanks (e.g. eastern Canadian shelf, East African Rift, and the Red Sea); and (2) the extension measurable from observed normal faults is far less than that required to produce the observed stretching of the whole crust and/or lithosphere (Allen and Allen, 2013). These are presented in figure 3.5. In McKenzie's uniform stretching model, crustal uplift occurs only within the region of stretching, and then only when the ratio of crustal thickness (y_c) to lithospheric thickness (y_L) is less than 0.2. Royden & Keen (1980) and later Rowley & Sahagian (1986) used depth-dependent stretching to explain uplifted rift shoulders, as well as the extension discrepancy related to normal faulting. Royden & Keen (1980) introduced a depth-dependent stretching concept whereby initial basin flank uplift occurs when $\beta_{mantle} > \beta_{crust}$, and is a consequence of the replacement of dense lithosphere by warmer, less dense asthenosphere below relatively less-stretched crust. The requirements of this model include: (1) a marked structural discontinuity within the lithosphere, usually taken to be the base of the crust; (2) a reasonable mechanism by which the mantle is detached and stretched more than the overlying crust; (3) most importantly, space problems resulting from greater stretching of the mantle lithosphere than of the overlying crust. These requirements, particularly the space problems, led Rowley & Sahagian (1986) to suggest that the crust is stretched uniformly and the mantle is stretched by the same amount but over a wider area, with the bounding surface of stretching widening with depth. This geometric approach resolves the space issues. It is widely accepted that depth-dependent stretching exists, especially where the unroofing of continental mantle rocks occurs along the continent-ocean transition of hyperextended margins (e.g. Iberia-Newfoundland conjugate margin described in Huismans & Beaumont, 2008). However, the debate regarding the nature, validity, importance, and widespread applicability of depth-dependent stretching models to rifts and rifted-margins continues. Indeed, some camps consider uplift and extension discrepancies to be the result of (1) poor seismic resolution of normal-fault extension within the sediments and upper crust and (2) neglect of the changes in flexural behaviour within the lithosphere during loading and unloading (e.g. Reston, 2007).

3.1.3 Flexural models

More sophisticated lithospheric stretching models are based on a flexural isostasy approach. An important parameter of flexural models is the 'depth of necking'. The 'depth of necking' refers to the theoretical level within the crust that remains horizontal during thinning in the

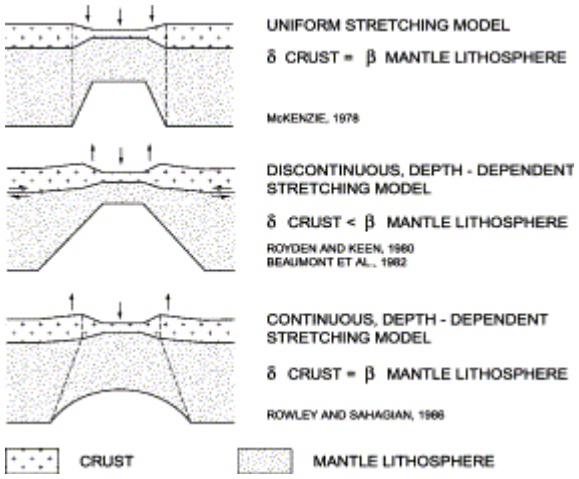

Figure 3.5. Lithospheric stretching models (Ziegler & Cloetingh, 2004).

absence of isostatic forces, and determines the ratio between thinning of the crust (where crustal material is replaced by sediments, water, air, or a combination of these factors), and thinning of the mantle lithosphere (where lithosphere is replaced by upwelling asthenosphere). In models based on Airy isostasy, such as the reference uniform reference stretching model (figure 3.1; McKenzie, 1978), the 'depth of necking' is zero, since crustal thinning is accommodated solely by uplift of the Moho. The mutual effect of necking depth and T_E has been explored by Fjeldskaar et al. (2004). As shown in figure 3.6, based on a simple 3-layer sedimentary basin and formed by 2 consecutive rift-phases, different combinations of necking depth and T_E values results in different basin geometries. Furthermore, setting the necking depth to 0 km generally leads to underestimation of lithospheric strength, and overestimation of thinning (β) factors. Necking depth values at intermediate crustal levels gives results comparable to observations. 'Depth of necking' approximations almost certainly vary temporally and spatially, which introduces uncertainty when applying them to model scenarios. Common 'depth of necking' estimates for rift basins are approximately 15 km, and around 5-15 km for T_E estimates (Fjeldskaar et al., 2004; Clark et al., 2014). However, T_E estimates in oceanic lithosphere are thought to follow a particular temperature-controlled isotherm (e.g. the 450^0C isotherm; Watts, 2001). Values of T_E and 'depth of necking' are not directly observable and are therefore difficult to constrain. Nonetheless, as can be seen in figure 3.6, their input has a large influence on basin structure and therefore on other derived modelled parameters. As such, necking depth and T_E need to be considered within a quantitative basin analysis context.

The equation describing the vertical deflection of the top of the crust, w, due to flexural isostasy is (after Turcotte & Schubert, 2002):

$$\frac{\partial^2}{\partial x^2}\left(D\frac{\partial^2 w}{\partial x^2}\right) + (\rho_m - \rho_s)g(w+s) = q$$

Where x, D, ρm, ρs, g, and s are the horizontal coordinate, the flexural rigidity, the average density of the lithospheric mantle, the average density of the basin infill (compacted sediments), the acceleration due to gravity and the kinematic deflection due to necking. The differential load, q, represents differences in the load relative to the load in the equilibrium state. The kinematic deflection, s, i.e. the surface depression that results from stretching and not isostatic compensation, is calculated using crustal thinning factors and the depth of necking (Watts, 1990; Rupke et al., 2010).

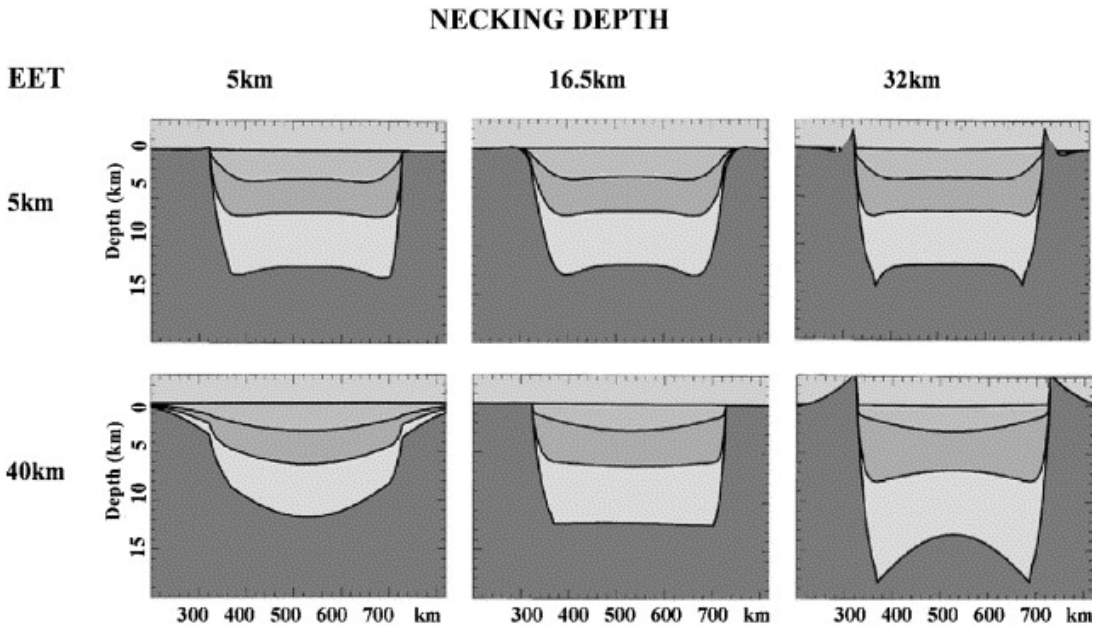

Figure 3.6. The effect of necking depth and EET on basin configuration in the context of a synthetic cross-section with two rifting phases (at 100 and 50 Ma). Results are shown for EET of 5 km (upper part) and 40 km (lower part), versus a necking depth of 5 km (left), 16.5 km (middle) and 32 km (right). The synthetic sedimentary layers are indicated by different shading (Fjeldskaar et al., 2004).

To summarize, the creation of accommodation space by rifting (e.g. rift-basins), flexure (e.g. foreland-basins), and subsequent sediment filling are the consequence of isostasy. The sediment infill itself is a load that further encourages subsidence through flexure, and sediment compaction results in increasing the bulk density of sedimentary strata with burial – affecting local and (to a lesser degree) regional isostasy. The concept of isostasy is crucial

to understanding the dynamics of sedimentary basins, and predicting basin evolution through modelling.

3.2 Basin Modelling Workflows

3.2.1 Backstripping

Traditionally, basin reconstruction is performed by either a time-reverse or time-forward modelling approach. Reverse models start from the present basin configuration and go back in time through the backstripping and decompaction of individual stratigraphic layers along normal faults. Backstripping is performed by removing each stratigraphic unit (layer-by-layer removal of the sedimentary load, from the latest deposited unit to the earliest) and decompacting the sediments below to a level consistent with the assumed palaeo-water depth by following pre-defined porosity versus depth relationships. Porosity-depth curves based on well data and seismic-velocity analysis are available for a number of basin provinces and follow a general exponential decay (e.g. Sclater & Christie, 1980 – North Sea; Schmoker & Halley, 1982 – South Florida; Ehrenberg, 2004 – Barents Sea). The effect of variance in porosity-depth distributions on reverse model outputs is summarized in Marcussen et al. (2010). Erosion is readily accounted for at each time step by removing eroded thicknesses from affected areas. Normal fault slip between each time step is restored using vertical simple shear (Clark et al., 2014). Figures 3.7 and 3.8 summarize the backstripping approach, based on the principle that a subsiding basin along a series of time steps results in compaction and reduction in sediment thickness.

Watts & Ryan (1976) first proposed to extract the tectonic subsidence contribution by removing the effect of sediment loading. This is conducted within a backstripping workflow by subtracting the isostatic subsidence changes in the sediment/water load through time from the total observed subsidence (figure 3.8). Assuming the tectonic subsidence is a result of instantaneous, pure-shear stretching of the lithosphere, β-factors can be estimated (usually through trial-and-error) by fitting the degree of lithospheric stretching to the tectonic subsidence (Sclater & Christie, 1980; Watts et al., 1982). Common basin modelling workflows which employ backstripping techniques for basin reconstruction include BMT (Basin Modelling Toolbox; Fjeldskaar et al., 2004) and Petromod (Al-Hajeri et al., 2009).

The drawbacks of the backstripping methodology are well understood. Reverse basin models separate the structural from the thermal solution because heat diffusion is not readily modelled backward in time. This produces inconsistencies in the results (Rüpke et al., 2008).

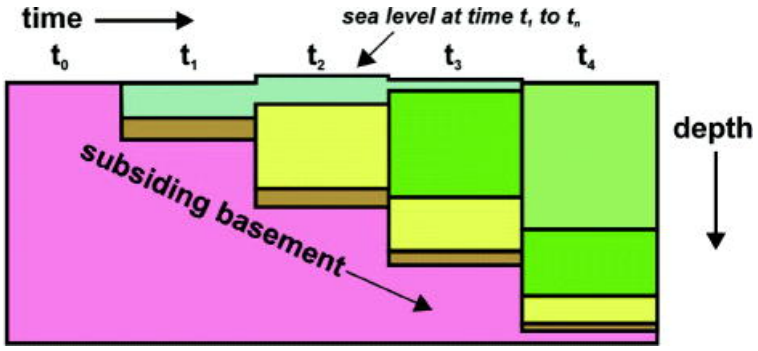

Figure 3.7. Time slices in the subsidence history of a basin. Water depth, sedimentation rate, and compaction all vary with time. Each increment of sediment is compacted beneath the weight of successive increments. Backstripping (time-reverse modelling) removes the effect of compaction for each time slice from time $t_4 \rightarrow t_1$ by following established porosity-depth relationships. Time-forward models start with an initial configuration prior to rifting (t_1), and try to reproduce the current stratigraphy (t_4) through rifting and sediment compaction (after Miall, 2010).

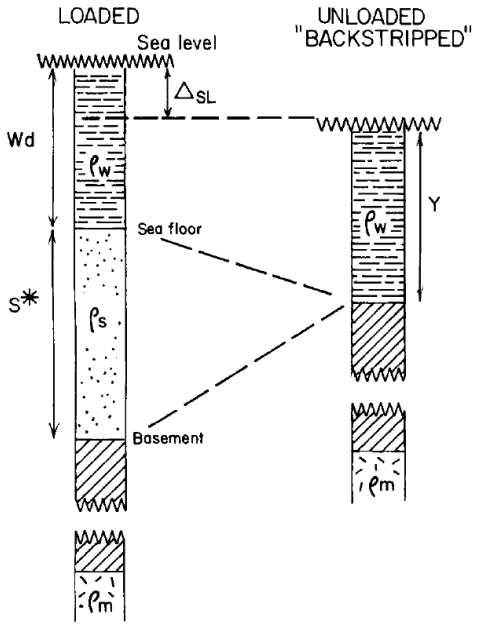

Figure 3.8. Principle of estimating tectonic subsidence by backstripping. The present-day (loaded) column consists of sediment layer thickness S overlain by water layer thickness Wd. It is assumed that pre-extensional (unloaded) crust is at a sea-level which differs from the present day by Δ_{SL}. Wd is estimated from paleoenvironmental analysis of benthic formanifera. S* is the uncompacted sediment thickness as it existed at some former time (though any datum can be chosen). Decompaction calculations are based on exponential porosity-depth curves (e.g. Sclater & Christie, 1980). Backstripping involves the removal of sediment loads and also water loads due to changes in sea-level. Tectonic subsidence (Y) is the depth to basement in the absence of surface loads. ρw, ρs, and ρm represent water, sediment, and mantle densities. The isostatic compensation depth is most often taken to occur at the lithosphere/asthenosphere boundary (after Steckler & Watts, 1978).

They do not account for the blanketing effect of sedimentation, which produces cooler upper crust and elevated sub-moho mantle temperatures when considered (Wangen et al.. 1995; Theissen & Rüpke, 2009). Reverse models also do not compensate for the thinning of sediments related to subsequent stretching events, because thinning can only occur locally through faulting, which is often under-represented (Reston, 2007; Theissen & Rüpke, 2009).

3.2.2 Forward models

Time-forward models start from an initial configuration prior to rifting, requiring substantial *a priori* knowledge of the basin, and try to reproduce the present basin configuration. This involves solving simultaneously for lithospheric thinning, sediment deposition and compaction, temperature, and isostatic compensation forward in time. This has substantial advantages over backstripping, since the structural and thermal solutions are coupled, the blanketing effect of sedimentation is taken into account, and the thinning of sediments is considered. Unfortunately, thinning factors, sedimentation rates, fault locations, and paleo-bathymetry have to be known beforehand, limiting the applicability of standard forward models for full-scale basin reconstructions (Rüpke et al., 2008).

TecMod

TecMod is a basin modelling software package that automates sedimentary basin reconstruction in 2-D. It is based on an algorithm which couples a forward model based on pure shear stretching to an inverse scheme, whereby after each of a series of forward iterations are run, the inverse scheme automatically updates crustal- and mantle-stretching factors (δ and β respectively) and paleo-water depth until the input stratigraphy is fitted to desired accuracy (generally within 5-10% error) (Rüpke et al., 2008; Rüpke et al., 2010). Details of the TecMod algorithm and its application to basin modelling are discussed in Rüpke et al. (2008); Theissen & Rüpke (2009); Rüpke et al. (2010); Rüpke et al. (2013); and Hartz et al. (2013).

All models within this study were generated using TecMod v2014.1. The general workflow of basin reconstruction modelling using TecMod can be summarized in the following steps (GeoModelling Solutions, 2014):

- Load an Input Stratigraphy
- Specify rift phases

- Adjust the inverse modeling parameters
- Adjust the forward parameters
- Start the Automated Reconstruction

TecMod – Forward Model

The 2-D forward model resolves simultaneously differential thinning, flexural isostasy, heat transfer, sedimentation, erosion, compaction, and hydrocarbon maturity on a Lagrangian finite-element mesh. The general modelling strategy is that the structural and thermal solutions are in equilibrium after every simulation time step. During each time step, the entire computational (Lagrangian) mesh is deformed with pure shear stretching/thinning factors, new sediment packages are deposited and become part of the computational domain, and flexural isostasy is ensured by further movement of the mesh in the vertical direction (Rüpke et al., 2010). Heat transfer occurs by diffusion and advection, based on deformation of the langrangian mesh (pure shear velocities in vertical and horizontal directions), and constrained by material property quantities (density, specific heat, thermal conductivity, radiogenic heat production rate). Water and sediments are included into the thermal solver to account for the effects of sediment blanketing (Theissen & Rüpke, 2009). Lithospheric flexure can be applied for modelling purposes using the general flexural equation described on page 30, with boundary conditions available to differentiate different lithospheric strengths at the periphery of the input stratigraphy. Extra features within the forward model that can be applied for specific scenarios include: (i) Sedimentation (forced deposition) and erosion; (ii) Generalized igneous events to model the thermal and structural effects of underplating, extrusive flows, and sill intrusion; (iii) Load events can simulate foreland basins, glaciations, and out-of-plane erosion; (iv) Multiple continental breakups, spreading ridges, and formation of new oceanic crust; (v) Influence of crustal and mantle phase transitions on the density distribution and following isostatic response; (vi) Sub-Moho serpentinization reactions and their effect on the density, isostasy, and temperature history of the basin (Rüpke et al. 2010).

TecMod – Inversion Model

The inversion process is fully automated, but can be optimized to obtain a better fit. An initial guess of the water depth when rifting starts (W_{rift}) is required. After each iteration,

TecMod minimizes the misfit between the modelled and input stratigraphies (called the goal function) by updating stretching factors and paleo-water depths (GeoModelling Solutions, 2014). The relative importance of the update of these model parameters is controlled by a series of Inversion Control Parameters (δ_{up}, β_{up}, W_{up}). Usually the highest weight is assigned to the crustal stretching factors (δ_{up}) since they have a direct response in the sediments, followed by the mantle stretching factors (β_{up}) which are characterized by post-rift sequences, and finally the paleo-water depth (W_{up}), which is often difficult to determine. The relationship between the crustal thinning required to create a certain amount of subsidence within a basin is defined by δ_{coeff}. Values greater than 1 imply less stretching is required to create a specific amount of subsidence, while values less than 1 imply more stretching is required.

TecMod fits the modelled stratigraphy to the input stratigraphy through the inversion scheme in two ways (controlled by the W_{weight} weighting parameter). Either the sedimentation rates through time are updated, so that the thickness of individual layers is accurately modelled ($W_{weight} = 0$), or the paleo-water depths are updated ($W_{weight} = 1$), which mainly helps to control the depth of each horizon. TecMod uses both methods simultaneously by assigning a user-defined W_{weight} value between 0 and 1. Low values of W_{weight} generally provide better fits, and more realistic paleo-water depths (GeoModelling Solutions, 2014).

Paleo-water depth and mantle stretching factors can be smoothed (W_{smooth}, β_{smooth}) to remove unrealistic sharp gradient change (this is expected in the crust however due to the prevalence of brittle deformation) (GeoModelling Solutions, 2014). Unfortunately, given the number of physical processes involved and the range of parameters, the evolution of sedimentary basins cannot be uniquely reconstructed. Nonetheless, using a targeted approach, with reasonable initial guess/control parameter inputs that reflect the current understanding of the basin history, a good fit to the present-day stratigraphy can be achieved.

3.2.3 Model Calibration

Basin models should be calibrated based on all available independent data. Common calibration sources include the input stratigraphy, crustal structure, and well data (including bottom-hole temperature, vitrinite reflectance, and paleo-bathymetry estimates based on paleoenvironmental studies). It needs to be emphasized that although these calibration points provide a methodology for quality control of a model, they too have a range of uncertainties

associated with them. Bottom-hole temperature in a well is measured by logging-while-drilling or wireline tools. It is a measurement of the temperature of the drilling fluid at bottom of the well, not the formation temperature (wireline measurements are naturally more accurate because the drilling fluid is in a static state for an extended period of time and therefore equilibrates with the formation temperature to a degree). Vitrinite reflectance (R_o) is a semi-quantitative measurement of the reflectivity of organic macerals within sediments through a microscope. The measurements taken from samples of drilled well cuttings can vary depending on the operator, the light source, the angle of incidence/reflection upon the macerals among other things. Within most modern basin modelling solutions, the vitrinite relectance is calculated synthetically from the thermal solution based on the EASY%R_o algorithm of Burnham & Sweeney (1989) based on the kinetics of 20 chemical reactions, but is not sensitive to the actual chemical composition of source rocks (Rüpke et al., 2008). Paleo-bathymetry estimates are entirely qualitative and are based on paleoevironmental studies of the water depths which different micro-organisms may have potentially tolerated and were likely to reside. Benthic formanifera are often used for this purpose (Steckler & Watts, 1978). Considering most of these species have evolved into other forms over the millions of years since sediment deposition and fossilization, these bathymetry estimates have often considerable ranges of uncertainties.

Within this study, free-air corrected and Bouger-corrected gravity anomaly data from satellite altimetry and ship track sources are used for model calibration. An integrated routine within TecMod allows calculation of the free-air and Bouger gravity anomaly based on the reconstructed density profile. This provides an extra source of calibration not often used in basin modelling studies.

4. Data and methods

The geological and geophysical data used in this study of the south-west Barents Sea margin include: published, interpreted depth-converted seismic profiles (Clark et al., 2014; Glørstad-Clark et al., 2011a); a conventional 2-D seismic reflection line (NPD survey code: HB-3-96A), well data (collected from the Norwegian Petroleum Directorate); average seismic velocities (Clark et al., 2013; Libak et al., 2012a; Fiedler & Faleide, 1996); 1'x1' bathymetric grid data (IBACO, Jakobsson et al., 2012); rock properties (Clark et al., 2014); erosion estimates (Clark et al., 2014); and free-air gravity anomaly and bouger-corrected gravity data (Kenyon et al., 2008; Olesen et al., 2010).

4.1 Data

4.1.1 2D Seismic Profiles

In order to evaluate the geological history of the south-west Barents Sea through modelling, a series of depth-converted 2D seismic profiles were required as input. The first studied profile was sourced primarily from the PETROBAR-07 onshore-offshore seismic reflection/refraction transect detailed in Clark et al. (2013) and Clark et al. (2014) (figure 4.1). The PETROBAR-07 profile utilized extends from the coastline near the Varanger Peninsula in Finnmark in the south-east to within 14 km of the continent-ocean boundary inside the Vestbakken Volcanic Province in the north-west (location map in figures 1.1 and 2.2). In order to explore the effects of continental breakup and magmatic underplating within the Vestbakken Volcanic Province, and understand the nature of the continent-ocean transition, horizon and fault interpretation of the HB-3-96A 2D multi-channel seismic reflection profile was conducted and depth-converted by the author to extend the input stratigraphy from the PETROBAR-07 study (Clark et al., 2014) into the oceanic crustal domain toward the Knipovich Ridge.

The second studied profile, located further south, was sourced from an unpublished manuscript by Glørstad-Clark et al. (2011a), detailed in the PhD thesis of Glørstad-Clark (2011): "Paper 3 – Basin Dynamics of the Loppa High area, SW Barents Sea: A history of complex vertical movements in an epicontinental basin". The stratigraphy was compiled

from 3 connected 2D multi-channel seismic reflection surveys recorded by Fugro and TGS Nopec, and depth-converted by Glørstad-Clark et al. (2011a), following the velocity model of Clark et al. (2013). The profile is 262 km long running in an approximate east-west direction from the Norsel High in the east to the Tromsø Basin in the west. Backstripping analysis of the profile using the BMT software package was discussed by Glørstad-Clark et al. (2011a), focusing on the post-orogenic evolution of the Loppa High (and the Selis Ridge). The depth-converted stratigraphy detailed in Glørstad-Clark et al. (2011a) was digitized by the author for input directly into forward modelling software (TecMod).

Seismic Data: Profile 1 – Extension of PETROBAR-07 profile

The 2-D seismic survey line HB-3-96A was part of a broader collection of six seismic surveys over the Barents Sea continental margin and out towards the Knipovich and Mohns Ridge called NPD-HB-96. The 'HB' is an abbreviation for 'Havretts Bjørnøya Vest'. The data set was compiled on behalf of the Norwegian Petroleum Directorate in 1996 to study the extent of the Barents Sea continental shelf and support Norway's maritime border claim in accordance with the UN Convention on the Law of the Sea. The position of the HB-3-96A seismic reflection line is presented in figures 1.1 and 2.2. The post-stack HB-3-96A seismic line data was loaded from .segy TWT (ASCII) format into the seismic-to-simulation software package Petrel for interpretation by constraining the dataset to the ED50-UTM31 co-ordinate reference system (as defined in the post-stack processing log file). The 7316/5-1 well drilled by Norsk Hydro in 1992 along the eastern margin of the seismic profile (within the Vestbakken Volcanic Province) was tied-in to the seismic data and was used to calibrate horizon interpretations. This is the only well drilled within the Bjørnøya Vest sub-area (NPD licensing map) and is located approximately 4.8 kilometres north of the HB-3-96A seismic line.

Seismic Interpretation

A total of 7 horizons were identified within the HB-3-96A seismic line and interpreted across the profile (figure 4.2). The ages of these horizon range from 0-55 Ma (Seabed – Base Eocene). These horizons are listed in table 4.1. The horizons were picked based on well formation tops from the 7316/5-1 and a series of published references based on work along the continental margin. Unfortunately, the resolution of the data below the Top Basalt/Base Eocene marker is very poor due to the strong acoustic impedance of the basaltic volcanics

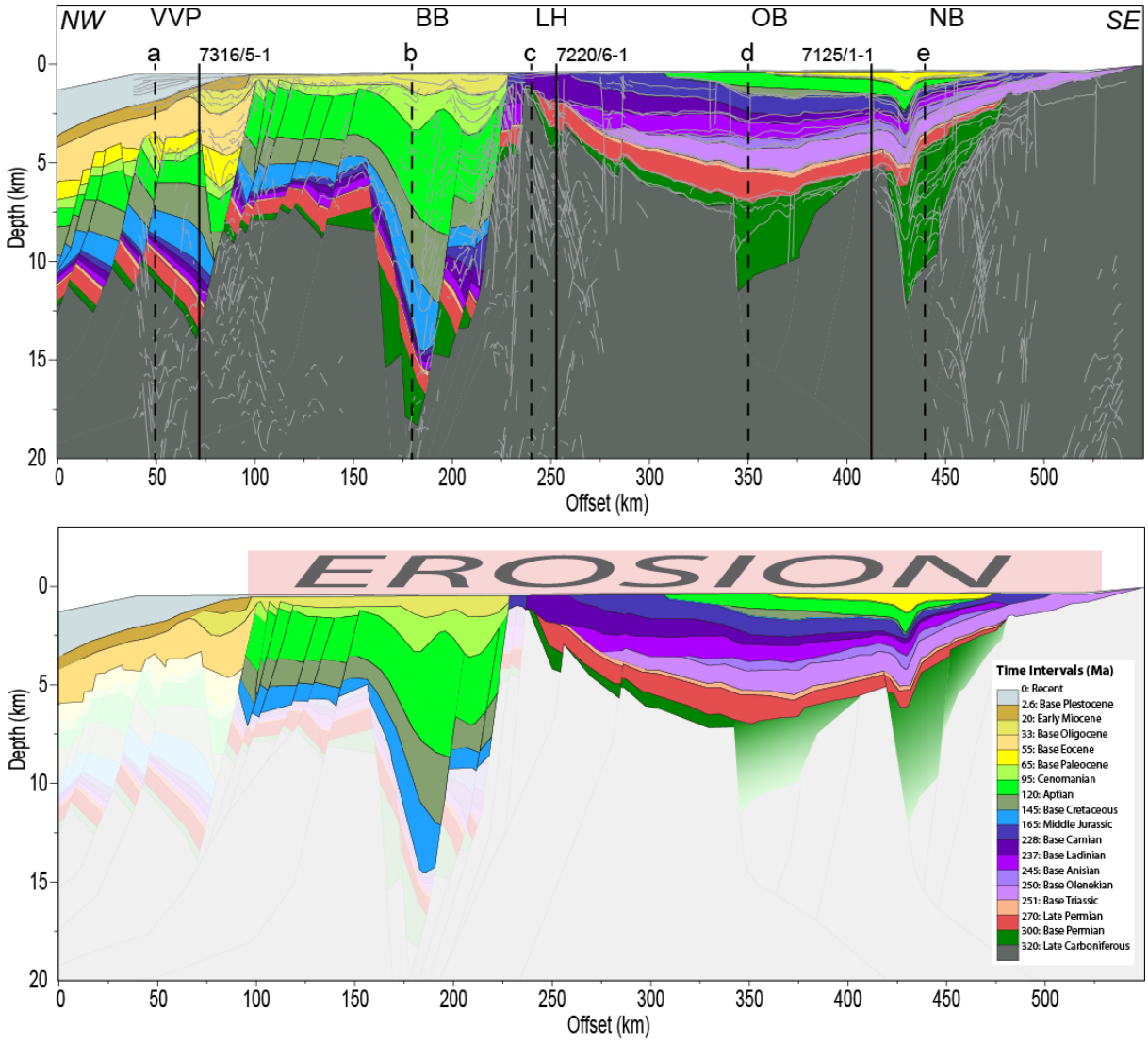

Figure 4.1. Interpreted, depth-converted cross-section along PETROBAR-07 profile from Clark et al. (2014). The upper panel shows the input stratigraphy for the BMT reverse model and TecMod inversion in their study. A depth-converted seismic line-drawing interpretation from co-incident profiles is overlain in light grey (Breivik et al., 1995; Ritzmann & Faleide, 2007). Some locations of 1D modelling results are shown as dashed lines (a-e); wells within the vicinity of the profile are indicated by solid lines. VVP – Vestbakken Volcanic Province; BB – Bjørnøya Basin; LH – Loppa High; OB – Ottar Basin; NB – Nordkapp Basin. The lower panel shows well-constrained portions of the model in bright colours and poorly constrained portions in faded colours. Eroded stratigraphy is also shown and is poorly constrained. The legend in the lower panel also applies to the upper panel.

and shallow intrusions, inhibiting seismic wave propagation and transmission to rock units below. As a result, further interpretation below 55 Ma was aborted. Clark et al. (2014) mapped horizons down to 320 Ma in this area close to the continent-ocean transition by integrating the HB-3-96A multi-channel seismic reflection data with wide-angle seismic refraction data from the PETROBAR-07. They did, however, recognize the high-degree of uncertainty with such an interpretation (see figure 4.1, lower panel).

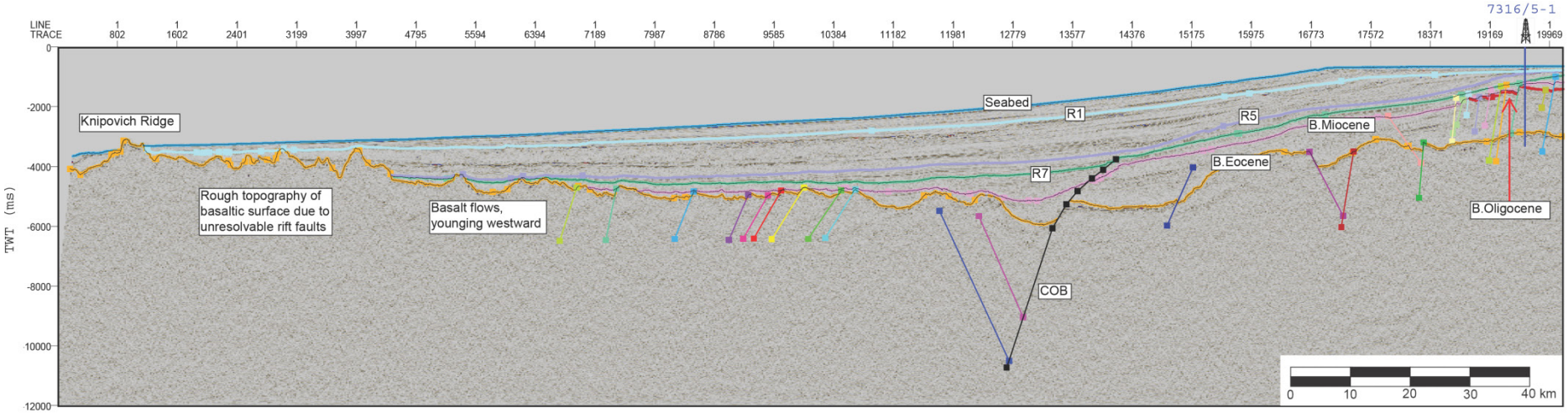

Figure 4.2. Seismic Interpretation of 2-D line HB-3-96A in two-way-time (ms).

Table 4.1. Seismic Horizons mapped along the HB-3-96A seismic line with their general corresponding amplitude polarity and matching well tops from well 7316/5-1 drilled by the rig Polar Pioneer (RKB elevation 23 m) for Norsk Hydro in 1987. TVDSS (True Vertical Depth Subsea) refers to the vertical distance between the interpreted horizon and mean sea level.

Seismic Horizon	Polarity (colour)	Well Tops
Seabed	Peak (red)	Seabed
R1	Peak (red)	-
R5	Peak (red)	-
Base Pleistocene	Peak (red)	Torsk Formation (922 mTVDSS)
Early Miocene	Peak (red)	Intra Lower Miocene (ILM) unit in Eidvin et al. (1998) at 937 mTVDSS
Base Oligocene	Peak (red)	Bottom of Base Oligocene (BO) unit in Eidvin et al. (1998) at 1067 mTVDSS
Top Basalt/Base Eocene	Peak (red)	Eocene/Paleocene transition in the 7316/5-1 Completion Log (NPD/Norsk Hydro, 1987) at 3277 mTVDSS

Important references used during the seismic interpretation exercise are highlighted here. Detailed stratigraphic analysis of the shelf sediments drilled in well 7316/5-1 is detailed in Eidvin et al. (1994) and Eidvin et al. (1998), and provided a solid starting point for understanding the nature of the Cenozoic sedimentation along the western Barents margin and mapping the horizons precisely. Regional interpretations by Faleide et al. (1996) along profiles of similar orientations to the HB-3-96A line were also used for calibration of interpreted horizons. Ryseth et al. (2003) describe the Paleogene-Neogene stratigraphy of the nearby Sørvestsnaget Basin. Libak et al. (2012b) and Solbu (2013) discussed the nature of the continent-ocean transition along the HB-3-96A seismic line, which for the most part agree with the interpretation presented in this work. The input stratigraphy of Clark et al. (2014) was based on interpretation of the HB-3-96A line supplemented by refraction data from the PETROBAR-07 study to within 14 kms of the continent-ocean transition. Hjelstuen et al. (2007) describes the nature and timing of glacial-derived submarine fan deposition and mega-slides along a series of profiles (including the HB-3-96A profile) including the continental shelf, slope, and rise.

The shelf and slope sediments are characterized by shallowly west-dipping reflectors, dominated by glacial-derived submarine fans from the Plio-Pleistocene boundary (2.7 Ma) to present. Within this package, seven different sequence boundaries can be identified, based on changes in seismic reflector configuration and orientation. These have been assigned the codes of R1-R7 spanning from 0.2-2.5 Ma (introduced by Faleide et al., 1996; revised by Hjelstuen et al., 2007). In order to assist in the depth-conversion of the seismic line

(discussed later), the R1 and R5 horizons were interpreted across the profile. They were not used as input for basin modelling.

Interpretation Workflow

The seven horizons of interest were mapped along the 2-D HB-3-96A profile from the shelf to the mid-ocean ridge by a combination of a well-tie in the east, and following major reflector trends over the continent-ocean transition and across the continental rise and abyssal plain to the west. Guided autotracking and seeded autotracking along distinct seismic reflectors was employed to map each horizon across either the entire extent of the seismic profile or to where the horizon terminates. The Top Basalt/Base Eocene unit, representing the top of the basaltic extrusives and shallow intrusives, was mapped across the profile and over the Knipovich Ridge. It should be noted however that technically the rocks at or below this horizon west of the Continent-Ocean transition are much younger than Early Eocene age, and probably represent oceanic crust. Indeed, the basalts at the Knipovich Ridge are very young, probably < 0.1 Ma. So the Base Eocene label as a chronostratigraphic descriptor is most relevant for sediments and volcanic/igneous rocks within the vicinity of the Continent-Ocean transition and rocks to the east. This is convenient since the basin modelling workflow limits the stratigraphic extent of the pre-breakup sediments to the boundary between continental and oceanic crust. To the west, in the oceanic crustal domain, it is simply the Top Basalt horizon, a boundary between submarine sedimentary fan deposits and basaltic volcanics and shallow intrusions of the upper oceanic crust, with the surface younging in age to the west. This younging of the mapped Top Basalt surface westwards reflects the opening of the North Atlantic Ocean with respect to time.

Horizon characteristics and diagnostic reflection configurations

The seabed is a distinct, strong, positive reflection across the HB-3-96A line. The seabed follows the shelf in the east, the continental rise around the centre of the profile (above the continent-ocean transition), and the abyssal plain to the west before abruptly intersecting the vent zone of the mid-ocean ridge. Reflections within the Quaternary sediments underlying the seabed are predominantly parallel, but do include some chaotic patterns (approximately 250 ms below the R1 horizon on the abyssal plain) where submarine mega-slides of enormous scale have collapsed and settled (detailed in Hjelstuen et al., 2007). The R1 horizon, a widespread unconformity, represents a change from erosion to accumulation and aggredation of the outer shelf (Faleide et al., 1996). Chaotic reflection patterns are also

identified directly above the R5 horizon, and relate to a marked increase in sediment supply from the east. The R5 horizon represents an erosional unconformity, truncating older sediments on the shelf (Faleide et al., 1996). The Base Pleistocene unconformity marks the onset of glacial erosion and outbuilding of sedimentary fans towards the shelf.

Reflections are predominantly parallel below the Base Pleistocene (R7) unconformity, with some sporadic progradational clinoforms from the east. The Base Oligocene unconformity pinches out at the Early Miocene unconformity within the Vestbakken Volcanic Province. Significant normal faulting with rotated fault block geometries can be identified throughout the Vestbakken Volcanic Province up to the Early Miocene and Base Pleistocene horizons, primarily in response to thermal contraction of the mantle lithosphere following continental break-up and opening of the North Atlantic Ocean in the Cenozoic. Below the Early Miocene horizon, reflections are parallel and often strong within downfaulted areas, with some prograding clinoforms in the upper layers. However, reflections in the horsts below the Early Miocene horizon have less structure and could be due to significant amounts of reworking associated with the Neogene uplift period.

The Top Basalt/Base Eocene horizon represents the top of volcanic sequences associated with continental breakup. This horizon is an uneven marker characterized by a strong acoustic impedance contrast. The volcanics were probably deposited flat-lying near surface. Extension and subsidence associated with breakup formed a westward downfaulted terraced surface with a change in depth of over 1 km from the eastern high down to the COB. Evidence of erosion on fault crests is also seen due to hangingwall uplift in some areas. The extension-related faulting clearly post-dates the main volcanic event. Horizons below the Top Basalt/Base Eocene horizon could not be identified with any confidence due to low signal to noise ratio. It is postulated that most of the acoustic energy of the incident wave is reflected along the Top Basalt/Base Eocene marker due to a marked velocity/density contrast between the Mid-Cenozoic sediments above and the volcanics and intrusives directly beneath. This, in turn, masks considerably any reflectors below the Base Eocene horizon.

Fault Interpretation

A series of steeply west-dipping synthetic faults with occasional east-dipping antithetic faults dominate the interpreted section below the Base Pleistocene horizon (coloured fault sticks, figure 4.2). These geometries are directly related to the pre- and syn-breakup extension together with the significant post-breakup thermal subsidence which the western

margin has been subjected during the Cenozoic. Faulting in the post-rift cooling stage (sag phase) is normally minor, but in the Vestbakken Volcanic Province there was considerable faulting associated with the complex opening history of the North Atlantic and Arctic realms through Eocene-Oligocene times (e.g. Engen et al., 2008). The thermal subsidence following breakup around the COB probably ceased 5-10 Ma within the Vestbakken Volcanic Province, and this is why the no faults can be identified intersecting the Base Pleistocene horizon and affecting the glacial-derived submarine fan deposits. The rough topography of the basaltic surface close to the Knipovich Ridge is thought to be the result of rift faulting along an ultraslow spreading ridge (Macdonald, 1982; Bruvoll et al. 2009; Kvarven et al. 2013). Unfortunately the faults close to the ridge are not resolvable along the HB-3-96A seismic line and have are therefore not marked on the interpretation line (figure 4.2).

Continent-Ocean Transition

The transition between the continental platform in the east and oceanic crust in the west is defined by large, deep, steeply west-dipping fault (marked black in figure 4.2). This interpretation is in agreement with the work of Faleide et al. (1996); Libak et al. (2012b); and Clark et al. (2013). The middle of the COB fault is located approximately 152 km east of the Knipovich Ridge along the HB-3-96A profile.

Velocity Model and Depth Conversion

By comparing the TWT horizon intersections on the HB-3-96A seismic line with formation tops identified in the 7316/5-1 well (Eidvin et al., 1998), an estimate of average velocities between each horizon identified in the HB-3-96A survey was made. Calibration of the velocity model was conducted by comparing my results with those derived from the PETROBAR-07 study (Clark et al., 2013, 2014), the BIN-2008 study (Libak et al., 2012a), the BIS-2008 study (Libak et al., 2012b), and Barents Sea continental margin seismic refraction compilations (Fiedler & Faleide, 1996). These velocity estimates provided a foundation for the depth conversion process, and are listed in table 4.2.

The broad range of average velocities calculated (1970-2400 m/s) between the seabed and the Base Pleistocene (R7) highlights the need for differentiation within Quaternary glacial sediments and why the R1 and R5 horizons were required to reduce error margins during the depth conversion process. Velocity models utilizing linear velocity gradients instead of discrete average velocities (shown in table 4.2) were also run, however the results were

spurious and it was decided that the average velocities listed in table 4.2 provided the accuracy required for depth conversion.

Table 4.2. Average velocities estimated along the HB-3-96A seismic line derived from comparing formation tops from well data with TWT horizon intersections. The velocity models of Clark et al. 2013; Libak et al. 2012a; and Fiedler and Faleide, 1996 were used for velocity model calibration.

Seismic Interval	Average velocity (m/s)
Datum - Seabed	1500
Seabed – R1	1970
R1 – R5	2160
R5 – R7 (Base Pleistocene)	2400
R7 – Base Miocene	2700
Base Miocene – Top Basalt/Base Eocene	2950

Each horizon was converted to depth in metres and exported as text files. The data was adjusted to tie-in with the western limit of the PETROBAR-07 interpretation of Clark et al. (2014), as shown in figures 1.1 (map view) and 4.6 (section view). Two sections were created (figure 4.6a, b), together with the original PETROBAR-07 reference section (figure 4.1).

4.1.2 Gravity Data

In conjunction with the input stratigraphy from the PETROBAR-07 and Loppa High profiles used for basin modelling, free-air gravity data from satellite altimetry (Kenyon et al., 2008) were used to compare the modelled gravity anomalies from TecMod with observed gravity anomalies along each profile. Bouger-corrected gravity data along the PETROBAR-07 extended profile (Olesen et al., 2010) were also used to eliminate the gravity anomaly effect of the bathymetry and focus on the lateral density variations in the sediments, crust and upper mantle following breakup and potential underplating. The location of the two profiles along a contoured free-air gravity anomaly map (Olesen et al., 2010) is provided in figure 4.3a. The 5'x5' free-air gravity anomaly data set from the Arctic Gravity Project (Kenyon et al., 2008) was utilized to extract a free-air gravity profile for (1) the PETROBAR-07 extended line (solid black line; figure 4.3b) and the (2) the Loppa High line (figure 4.3c) using an in-house Matlab script. The PETROBAR-07 Bouger-corrected data (dashed black line; figure 4.3b) was digitized from a figure published in Clark et al. (2013).

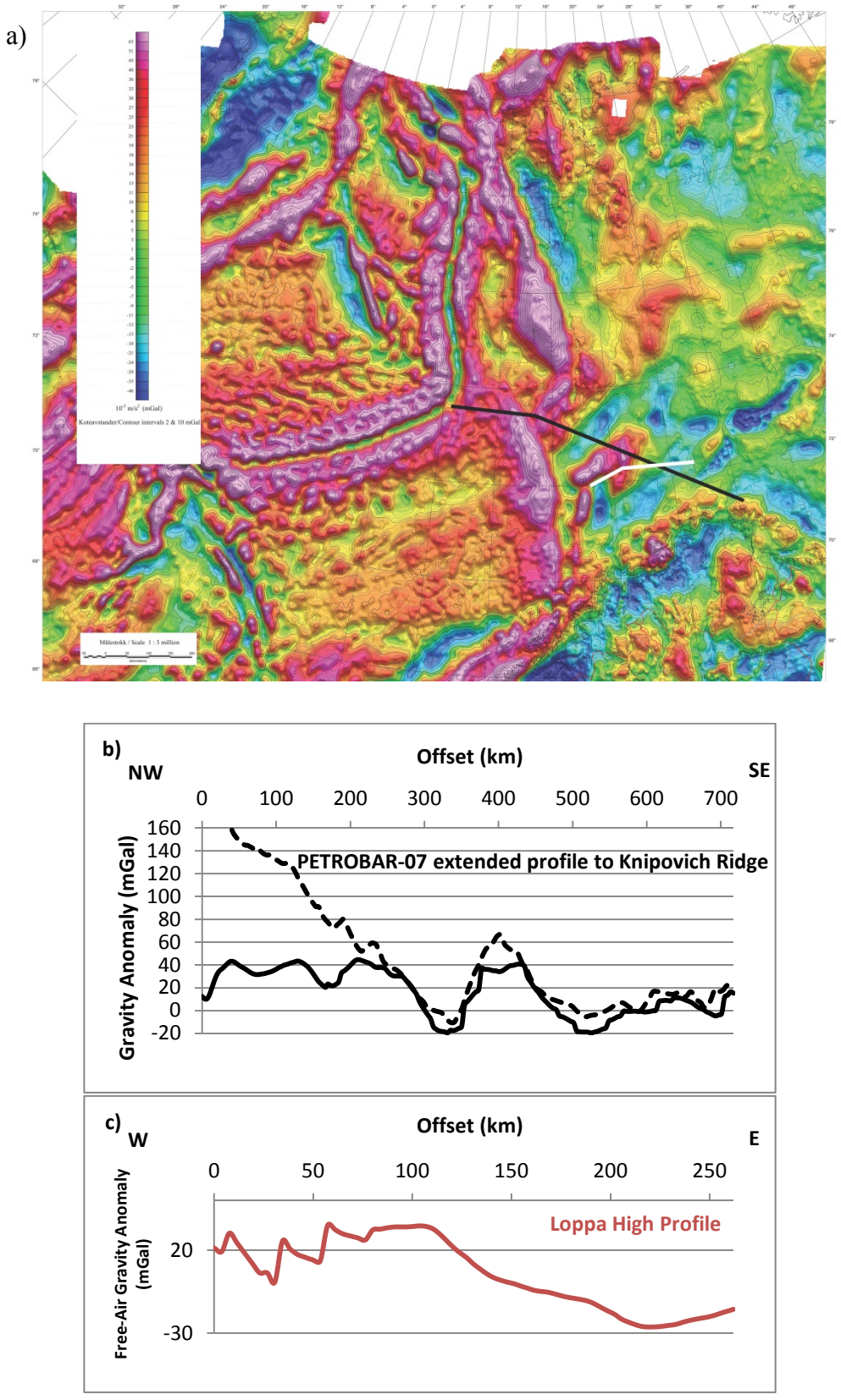

Figure 4.3. Free-air gravity data from the Barents Sea. a) Contoured 2 x 2 km free-air gravity map derived from ship track data with position of the extended Petrobar-07 profile (black line) and the Loppa High profile (white line; Olesen et al., 2010). Free-air gravity anomaly data along (b) Extended Petrobar-07 profile (black solid line), and (c) Loppa High profile from satellite altimetry data (Kenyon et al., 2008). 2200 kgm^{-3} Bouger-corrected gravity data along extended PETROBAR-07 shown in (b) as black dashed line (Olesen et al., 2010).

Gravity anomalies are calculated by measuring the gravitational attraction over the surface of the Earth and subtracting this from a value predicted by a specific Earth model, most often a reference ellipsoid. While the gravity associated with the reference ellipsoid accounts for the flattening of the Earth due to centrifugal forces (bulging at the equator), the free-air correction applied to marine areas removes the effect of satellite altimeter elevation above the Earth's mean sea level (the geoid) (Fowler, 2005). The Bouger-correction removes the effect of topography by accounting for the excess mass above a specific datum (e.g. geoid); or bathymetry by accounting for the mass deficiency below a mean sea-level.

Gravity anomalies are caused by lateral variation in the gravitation acceleration of the Earth. This variation is a direct consequence of non-uniform density distributions within the subsurface, and therefore provides important information about the structure and properties of the lithosphere and mantle. Three primary sources of gravity anomalies exist in marine areas: density contrasts and structure at (1) the seabed; (2) within the underlying sedimentary succession and crust; (3) the lower crust/mantle interface. Gravity anomalies from deep sources (e.g. along the Moho) have long wavelengths, while gravity anomalies from shallow sources (e.g. seabed and basement) have short wavelengths. Where large changes in bathymetry are not accompanied by large changes in the gravity anomaly, the subsurface structures must be isostatically compensated (Fowler, 2005).

The free-air gravity anomaly data extracted from the density distribution in TecMod is calculated by taking the left side of the profile as reference. Stüwe (2007) suggests that the mid-ocean ridge (MOR) is a good reference column to use in gravity modelling because it represents asthenosphere, without contamination from crustal sources. So, along the PETROBAR-07 profile, modelled gravity profiles incorporating breakup and breakup+underplating are used as a reference. All modelled gravity profiles along the PETROBAR-07 profile which do not have a MOR as part of the input are shifted by a correction factor of -43.4 mGal such that the right-side of all gravity anomaly profiles are equal. The right-side of all profiles should be the same along the PETROBAR-07 profiles, because this represents continental crust (without overlying sediments). No corrections are made to the modelled gravity profile from the Loppa High profile because no MOR is included in any of the models to provide a reference column.

Comparison between the observed free-air gravity from satellite altimetry and modelled free-air gravity from the density distribution within TecMod can then be easily made. The

Bouger-corrected data along the PETROBAR-07 extended profile involves replacing the seawater with an infill density of 2200 kgm^{-3}, consistent with Olesen et al. (2010). With respect to the basin models produced in this study, where the modelled and observed free-air gravity signatures show a high degree of correlation, confidence in the validity of the basin model can be asserted. Where this is not the case, and the trends in the modelled and observed free-air gravity signatures are significantly different, the model requires further analysis and interrogation to determine why a discrepancy exists.

4.1.3 Bathymetry data

Bathymetric data along the PETROBAR-07 profile (figure 4.4a) was derived from depth-conversion of seismic data by Clark et al. (2014) within the continental domain and the author along the HB-3-96A profile. Along the Loppa High profile (figure 4.4b), the present-day bathymetric profile was extracted from the IBACO Bathymetric Chart of the Arctic Ocean (version 3.0) 500 m spaced grid (Figure 1.1; Jakobsson et al., 2012), using the GIS software package ArcMap.

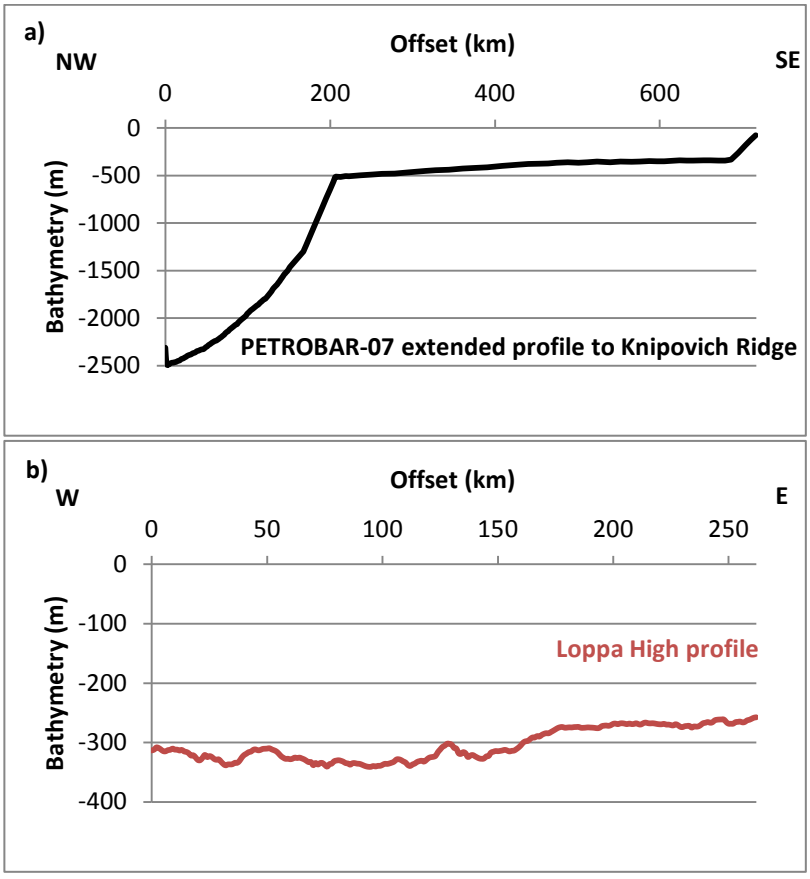

Figure 4.4. Bathymetric profiles along the (a) PETROBAR-07 extended profile toward the Knipovich Ridge (Clark et al. 2014; and this thesis), and (b) the Loppa High profile (Jakobsson et al., 2012).

4.2 Methods: Basin modelling

4.2.1 Input Stratigraphy for TecMod modelling

Profile 1 – PETROBAR-07 extended into the oceanic crustal domain

The PETROBAR-07 profile data (Clark et al., 2014) was checked before loading into TecMod. A feature was observed within the original dataset whereby late Triassic – Early Jurassic sediments west of the Loppa High were not preserved, and the 228 Ma time line was shifted up to overlap with the 165 Ma time line. However, interpreted seismic lines of similar orientation west of the Loppa High have sediments preserved between 228-165 Ma (e.g. Glørstad-Clark et al., 2011a). Indeed, the BMT input stratigraphy from the PETROBAR-07 study presented in figure 4.1 has a thin layer of Early Jurassic sediments mapped west of the Loppa High. As a result, it was decided to shift the 228 Ma time line downward within the TecMod input stratigraphy such that late post-rift sediments from 228-165 Ma were present along the entire profile, and are approximately the same as those mapped in figure 4.1. Once this was rectified, the corrected sections could be reloaded into TecMod for basin analysis.

Three stratigraphic sections along the extended PETROBAR-07 profile are used for investigation of the thermal history of the south-western Barents Sea:

1. The reference section (550 km long; figure 4.6 a, from x = 166 to x = 716 km) published in Clark et al. (2014)
2. The reference section (Clark et al., 2014) tied-in to the HB-3-96A interpretation by the author to the Knipovich Ridge (approximately 716 km long; figure 4.6a)
3. The same as section #2 (approximately 716 km long; figure 4.6b), but with a tapered lower sedimentary profile beneath the Vestbakken Volcanic Province, as suggested by Libak et al. (2012b)

The first section (section #1) used for analysis is the reference PETROBAR-07 profile (figure 4.6a, from x = 166 to x = 716 km). This 550 km long section was used to define a reference model from which more complex models could be compared, for example, models including continental breakup and/or magmatic underplating. The most suitable combination of erosion and isostatic parameters for basin reconstruction were defined and then kept constant for all subsequent models. Although much the PETROBAR-07 reference section

and models pertaining to it are covered extensively by Clark et al. (2014), and indeed most of the data derives from their study, a review is undertaken to understand the interplay between rifting, isostasy, and erosion in this area.

The second section (section #2) is approximately 716 km long, running from the Knipovich Ridge in the west to the Finnmark Platform in the east (figure 4.6a). The continent-ocean boundary was set at x = 152 km, based on the mapped position of the COB along seismic line HB-3-96A (figure 4.2). The base of the sedimentary succession below the Vestbakken Volcanic Province averages 12km, and is relatively flat, as mapped by Clark et al. (2014). Sediments from 320-65 Ma follow an arbitrary 65 Ma horizon west of the COB.

The third section (section #3), identical to section #2, but with a westward-trending tapered sedimentary profile below the Vestbakken Volcanic Province (figure 4.6b). This was inspired by the interpretation of the nearby BIS-2008 OBS line by Libak et al. (2012b). Libak et al. (2012b) proposed that the late Paleozoic-early Mesozoic sedimentary succession and upper continental crust below the Vestbakken Volcanic Province thin toward the COB in response the stretching prior to continental breakup (figure 4.5). This was simulated by progressively removing the lowermost stratigraphic units interpreted by Clark et al. (2014) gradually toward the COB (see figure 4.6b).

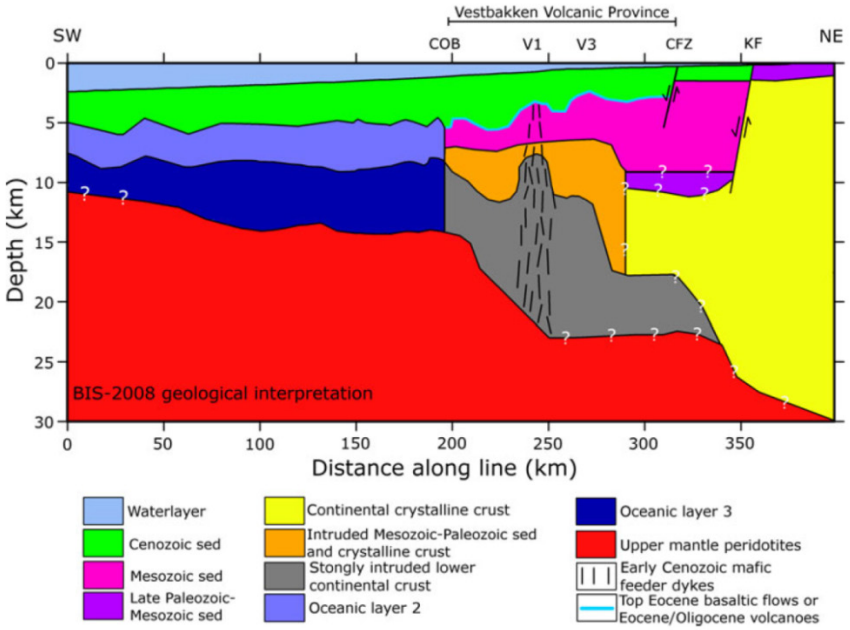

Figure 4.5. Geological interpretation of the Vestbakken Volcanic Province by Libak et al. (2012b), based on the BIS-2008 ocean-bottom seismic (OBS) line. Note the tapered structure of the Late Paleozoic-Early Mesozoic sedimentary succession and upper continental crust towards the COB. This implications on the thermal and burial history of such an interpretation are tested within the TecMod environment, with the input stratitgraphy presented in figure 4.6b.

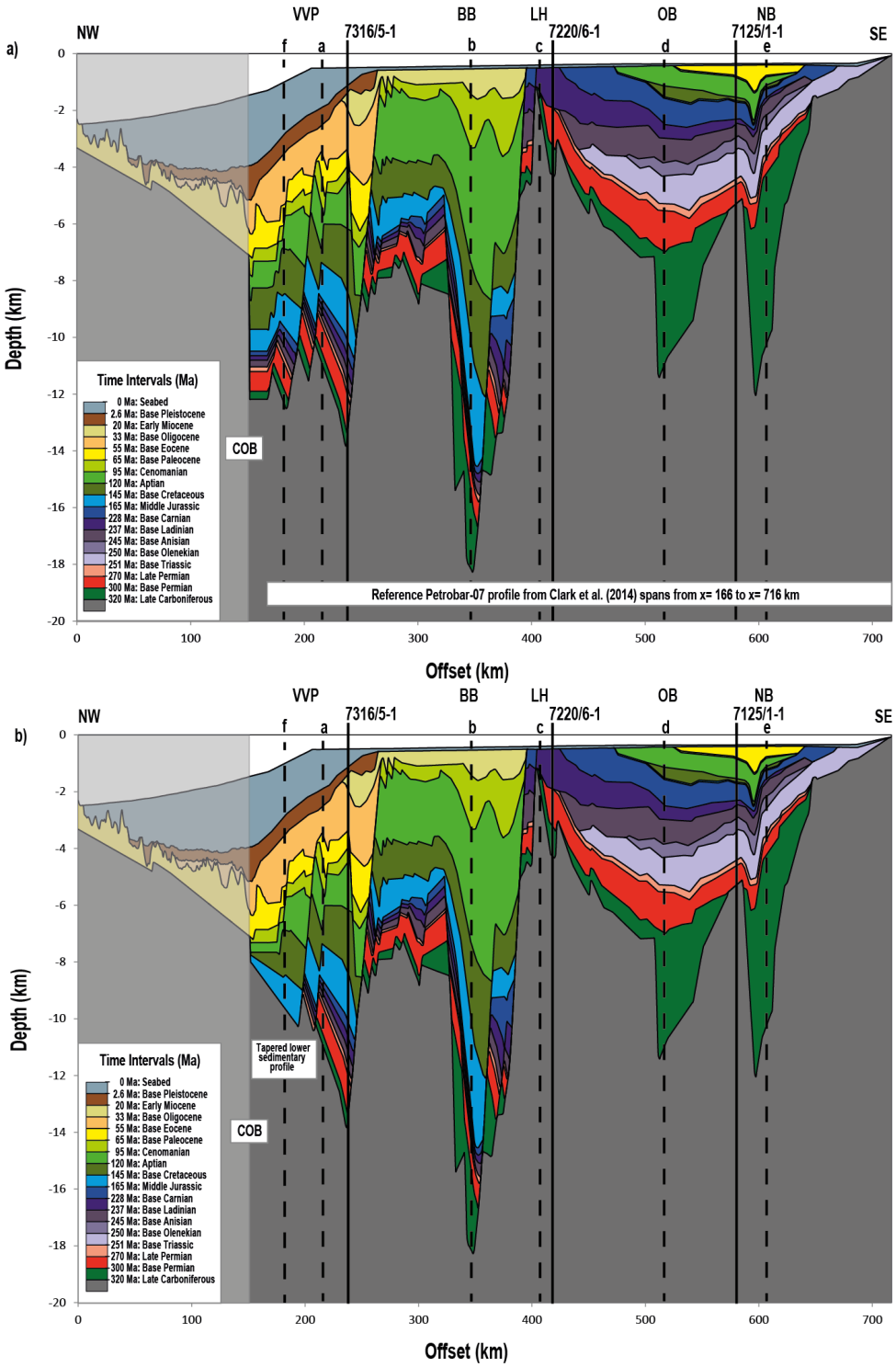

Figure 4.6. Input stratigraphic sections from the PETROBAR-07 profile (after Clark et al. 2014) integrated with the HB-3-96A interpretation in the oceanic domain toward the Knipovich Ridge (by the author). The reference section (Section #1) is 550 km long and spans from x = 166 km to x = 716 km in figure a. It is also shown in figure 4.1. a) Section #2: profile extending from the Finnmark Platform in the east through to continent-ocean boundary (COB), to the Knipovich Ridge. Note the flat base of the sedimentary succession below the Vestbakken Volcanic Province at 12 km depth. b) Section #3: profile identical to Section #2, but with a tapered Mesozoic-Paleozoic sedimentary succession toward the COB, as suggested by Libak et al. (2012b). The COB is located at x = 152 km. Some locations of 1D modelling results (pseudo-wells) for each section are shown as dashed lines (a-e); wells within the vicinity of the profile are indicated by solid lines. VVP – Vestbakken Volcanic Province; BB – Bjørnøya Basin; LH – Loppa High; OB – Ottar Basin; NB – Nordkapp Basin.

The new integrated profiles were then input into modelling software for analysis. Well data along the profiles were used for model calibration and analysis (see figures 4.1 and 4.6 for locations of wells). Sensitivity tests aimed at finding a single set of optimum inversion control parameters for all scenarios were undertaken. This process is discussed briefly in Appendix B. Once the optimum inversion control parameters for all scenarios were constrained, these remained constant for all model runs over the extended PETROBAR-07 and Loppa High profiles. The effect of different geological scenarios on the thermal history of the western Barents Sea can thereby be more easily determined.

Profile 2 – Loppa High

The stratigraphy defined for backstripping purposes in Glørstad-Clark et al. (2011a) was digitized using the Engauge Digitizer v4.1 open-source software package (http://digitizer.sourceforge.net/) and is presented in figure 4.7. It is oriented east-west, crossing the PETROBAR-07 profile on the Bjarmeland Platform (see figures 1.1 and 2.2). The Loppa High profile intersects the deep Tromsø Basin, Polheim Subplatform, Loppa High, and Bjarmeland Platform over a distance of 262 km. The stratigraphy published in Glørstad-Clark et al. (2011a) lacked present-day bathymetry, due to a systematic error encountered during data collection (S.A. Clark 2014, pers. comm. 25 Mar). So, using the extracted IBACO bathymetry profile data (figure 4.4b), each stratigraphic layer was shifted downward by 300 m (the average water depth along the profile), and the current bathymetric profile was overlain. The modified digitized profile, now combining accurate bathymetry and stratigraphic horizons was input into modelling software for analysis (figure 4.7). The horizon 360-320 Ma was applied to models only where specified, otherwise it is assumed to represent basement (same assumption was made in Clark et al. 2014).

4.2.2 Well Control Locations

Data from a series of wells drilled within the vicinity of the PETROBAR-07 extended and Loppa High profiles were used to verify and calibrate the models. The data used include vitrinite reflectance (R_o) and bottom hole and drill stem test (DST) temperature data (for well locations, see figures 1.1, 4.6 and 4.7, summarized in table 4.3). While the three well locations along the PETROBAR-07 extended profile are located within 4-12 km of the modelled profile, the Loppa High has only two wells located close to the modelled profile

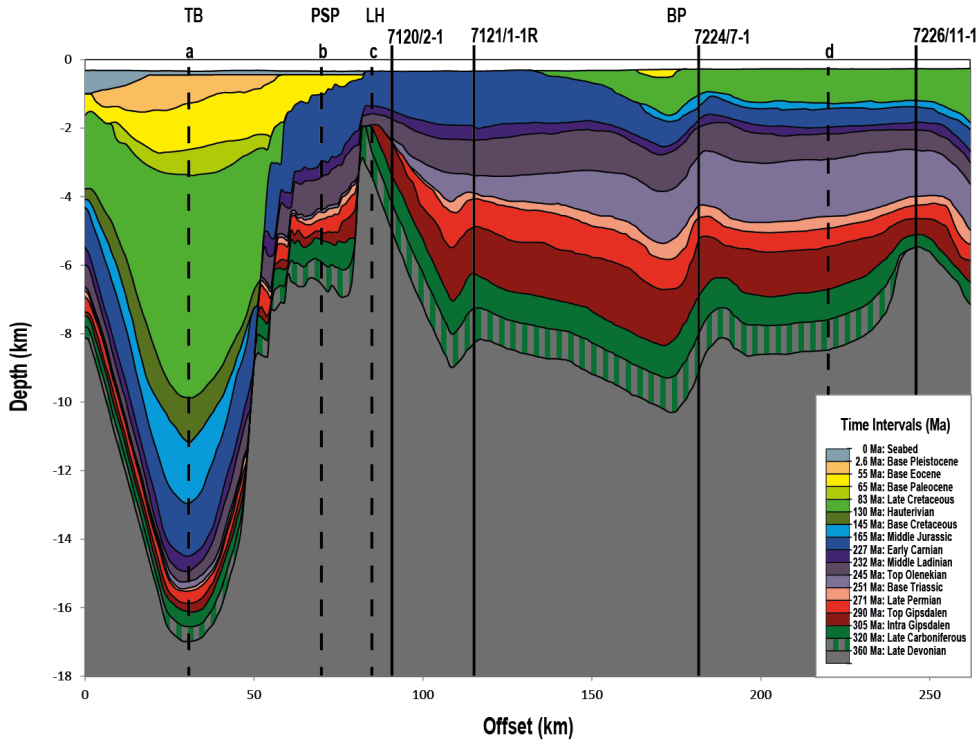

Figure 4.7. Input stratigraphic section from the Loppa High profile (Glørstad-Clark et al., 2011a). Combined with present-day bathymetry extracted from the IBACO Version 3.0, 500 m spaced grid (Jakobsson et al., 2012). Each stratigraphic horizon was shifted 300 m downward to accommodate for the overlying bathymetry before integrating the 2 datasets for input into modelling software. Location of wells used for model calibration are marked with solid lines, pseudo-wells with dashed lines. Note that wells 7120/2-1 and 7121/1-1R are located over 40 km south of the profile. The horizon from 360-320 Ma was only used in model runs where specified. TB – Tromsø Basin, PSP – Polheim Sub-platform, LH – Loppa High, BP – Bjarmeland Platform.

(7224/7-1 and 7226/11-1). The wells further west are located over 40 km south of theprofile, so their value as calibration points is somewhat limited. For reference, a typographic error in Glørstad-Clark et al. (2011a) was recognized in the description of well-tie locations. The easternmost well which lies in the vicinity of the profile is 7226/11-1 (not 7229/1-1 as previously published, which is located almost 100 km east of the Loppa High profile).

Table 4.3. Well locations and corresponding x-coordinate along the PETROBAR-07 extended and Loppa High modelled profiles. The vicinity of each well to the corresponding modelled profile is noted, 'close' being within 12 km, 'distant' being greater than 12 km. The two distant wells are located over 40 km south of the Loppa High profile.

Well Name	Profile	x-coordinate	Vicinity to profile
7316/5-1	PETROBAR-07 extended	238	Close
7220/6-1	PETROBAR-07 extended	419	Close
7125/1-1	PETROBAR-07 extended	579	Close
7120/2-1	Loppa High	90	Distant
7121/1-1 R	Loppa High	115	Distant
7224/7-1	Loppa High	181	Close
7226/11-1	Loppa High	246	Close

A series of pseudo-wells were also included along the profile for direct comparison with interpreted paleo-water depths by Clark et al. (2014) and Glørstad-Clark et al. (2011a), and near-margin analysis. These are shown in figures 4.6 and 4.7 (dashed lines).

4.2.3 Input parameters

TecMod Input Parameters

Each of the two stratigraphic profiles (from figures 4.6 and 4.7) were loaded into TecMod for analysis. The model data input process is similar to the workflow described in Clark et al. (2014). Rock properties were assigned to each stratigraphic layer. Here, assumptions regarding the lithology of each unit were made, choosing either the dominant lithology (e.g. limestone) or mixtures (e.g. 50% Sand, 50% Shale; see figure 4.8). Likewise, porosity-depth trends linked to mechanical compaction during burial were applied to each rock unit based on the assumed dominant lithology, while sand-shale mixtures were linearly interpolated based on their ratios. For simplicity, chemical compaction (diagenesis), and low-grade metamorphism were neglected (Clark et al. 2014).

The chronostratigraphic horizons mapped along profiles 1 & 2 are slightly different. For example, no sediments are preserved along the Loppa High profile between 25 Ma (assumed age of maximum burial) and 2.6 Ma. There are sediments preserved from this time period within the Vestbakken Volcanic Province along PETROBAR-07 profile. To reflect these differences, the basin infill properties, and rift phase timing and span have been adjusted to suit. These differences are summarized in figure 4.8. Kerogen-rich shales were assigned to 250-245 Ma and 150-145 Ma, representing Early Triassic and Late Jurassic source rocks. Rock properties assigned to each stratigraphic layer are presented in table 4.4.

Four discrete rift phases are defined from Carboniferous to present, facilitating the required accommodation space for the present-day stratigraphy. These are summarized in table 4.5. The rift phase interval is slightly different between profile 1 and profile 2 because the chronostratigraphic horizons are also different, and each rift phase must be bound by 2 stratigraphic surfaces in the TecMod basin model. The time frame of each rift phase is limited by the resolution of the input stratigraphy. Each rift phase must be bounded by an upper and lower stratigraphic horizon within the input data. So while Late Cretaceous extension is recognized in the south-west Barents Sea (e.g. Faleide et al., 1993b), the effects of this event is assumed to be included in the Paleocene-Eocene rift phase within all models.

Table 4.4. Rock properties assigned to the basin infill within the basin models for profile 1 (figures 4.1 and 4.6; Clark et al., 2014) and profile 2 (figure 4.7; Glørstad-Clark et al., 2011a).

Lithology	Density (kg/m3)	Thermal Exp. (1/K)	Rad. Heating (W/m3)	Heat Capacity (J/kg/K)	Grain Cond. (W/m/K)	Porosity	Inv.Comp. Length (1/km)
Water	1000	0	0	1000	1000	0	0
Peridotite	3340	3.2E-05	0	1000	3.5	0	0
Oceanic crust (Magmatic bodies)	2900	2.4E-05	0	1000	2	0	0
U. crust (Granite)	2700	2.4E-05	2E-06	1000	3	0	0
L. crust (Diabase)	2900	2.4E-05	2E-06	1000	3	0	0
Sandstone	2690	0	1E-06	1000	4.4	0.4900	0.27
Limestone	2600	0	1E-06	1000	2	0.4173	0.40
Shale	2720	0	1E-06	1000	1.5	0.6200	0.50
10ss90sh	2717	0	1E-06	1000	1.6704	0.6200	0.49
20ss80sh	2714	0	1E-06	1000	1.8602	0.6000	0.46
30ss70sh	2711	0	1E-06	1000	2.0716	0.5900	0.44
40ss60sh	2708	0	1E-06	1000	2.3069	0.5700	0.41
50ss50sh	2705	0	1E-06	1000	2.5690	0.5600	0.39
60ss40sh	2702	0	1E-06	1000	2.8609	0.5500	0.37
Shale (kerogen-rich)	2720	0	1E-06	1000	1.5	0.6200	0.50

Common model input parameters applied to this study are summarized in table 4.6. Flexural isostasy is applied through an effective elastic thickness (T_E) of 5 km and a corresponding necking depth of 15 km. As Clark et al. (2014) notes, these values are difficult to constrain and vary spatially and temporally, but are consistent with other published models for the Viking Graben and Vøring Basin (Fjeldskaar et al., 2004, 2009; Rüpke et al., 2008; Theissen & Rüpke, 2010).

Table 4.5. Rift phases defined with the basin models for profile 1 (figure 4.6; Clark et al. 2014) and profile 2 (figure 4.7; Glørstad-Clark et al. 2011).

Rift Phase	Rift Interval (Profile 1)	Rift Interval (Profile 2)
Carboniferous	320-300	320-305
Late Permian	270-251	271-251
Late Jurassic – Early Cretaceous	165-145	165-145
Paleocene – Early Eocene	65-55	65-55

The crustal and lithospheric thicknesses of the basin are also input into the models. These must be defined as constant at the initiation of rifting in the TecMod model. Post-Caledonian crust and lithosphere undoubtedly varied in thickness along our profile at rift initiation, but this geometry is unknown. An initial crustal thickness of 35 km (17.5 km upper crust, 17.5

km lower crust) and a total lithospheric thickness of 120 km, values which are also consistent with the previously published models mentioned above (Clark et al., 2014).

Other main forward model parameters include temperature boundary conditions of 5°C at the seafloor/atmosphere, and 1300°C at the Lithosphere/Asthenosphere. 2 μW/m3 radiogenic heat production in the crust. The numerical resolution of the finite element mesh was set at nx = 100 ny = 200.

As mentioned previously, the inversion control parameters, which define the extent of the inversion engine runs in TecMod, were optimized for a series of scenarios along the extended PETROBAR-07 profile, and then kept constant for all modelled scenarios in this study. They are presented in table 4.6. The idea being that each model can then be compared to another based on the geological input alone. Other assumptions include neglecting the effects of salt deposition and mobilization because it is difficult constrain in forward and reverse models. Volcanics are only considered in a model scenario where this is explicit. Episodic ice-loading during the Quaternary is also ignored, though this has previously been investigated by Cavanagh et al. (2006). Potential low-grade metamorphism in the deep Bjørnøya and Tromsø basins is also ignored.

Basin reconstructions are calibrated primarily by comparing the reconstructed stratigraphy with the input stratigraphy. Any significant errors were investigated and where possible, the model was adjusted. Thermal calibration data utilized include well data such as Vitrinite Reflectance and Bottom-Hole Temperature. Potential field free-air gravity data was extracted from each profile (and Bouger-corrected for the PETROBAR-07 extended profile only) based on publically-available data (Olesen et al., 2010; Kenyon et al., 2008) and compared to the computed gravity signature from TecMod.

Input erosion parameters

Erosion estimates for both the PETROBAR-07 (Clark et al., 2014) and Loppa High profiles (Glørstad-Clark et al. 2011a) were utilized within this study. These estimates were limited to the glacial-related erosion events in the Quaternary. As Clark et al. (2014) notes, erosion estimates of between 0 – 1000 m in the Tromsø Basin and 1000 – 1500 m in the Hammerfest Basin and Loppa High have been recorded. Within TecMod, erosion is handled by specification of a rate at which sediments will be eroded if located above an assigned level within a time and space range. For the reference and extended PETROBAR-07 profile within

Table 4.6. Input physical forward parameters and inversion control parameters used in this study. These parameters are the same for all modelled scenarios.

Model Parameter	Value	Units
Forward Parameters		
Lithosphere thickness	120	km
Upper crust	17.5	km
Lower crust	17.5	km
Top and bottom temperature	5 and 1300	ºC
e-fold length radiogenic heating (crust)	20	km
e-fold length correction	f(crust)	
Thermal conductivity (crust and mantle)	f(T)	W/m/K
Density (upper/lower crust and mantle)	2700/2900 and 3340	kgm^{-3}
Specific heat (upper/lower crust and mantle)	1000/1000 and 1000	J/kg/K
Thermal expansion co-efficient (crust and mantle)	2.4E-05 and 3.2E-05	K^{-1}
Radiogenic heat (crust)	2E-06	W/m^3
Matrix conductivity	f(T)	W/m/K
Pore fluid conductivity	f(T)	W/m/K
Effective conductivity	Geometric mean	W/m/K
Numerical resolution of finite element mesh (nx/ny)	200/100	
Effective elastic thickness (T_E)	5	km
T_E Boundary Conditions – Left (PETROBAR-07 only)	0	km
T_E Boundary Conditions – Right (PETROBAR-07 only)	5	km
Necking depth	15	km
Inversion Control Parameters		
Initial Guess		
Water Depth during syn-rift period for 1st forward simulation during inversion loops (W_{rift})	0	m
Isostatic adjustment co-efficient for crustal thinning (δ_{coeff})	0.9	
Inversion Engine		
δ_{up}	0.8	
β_{up}	0.4	
W_{up}	0.2	
W_{weight}	0.2	
Number of smoothers – water depth (W_{smooth})	1	
Number of smoothers - mantle thinning factor (β_{smooth})	2	
Accuracy		
Maximum number of iterations	15	
Maximum error	50	m

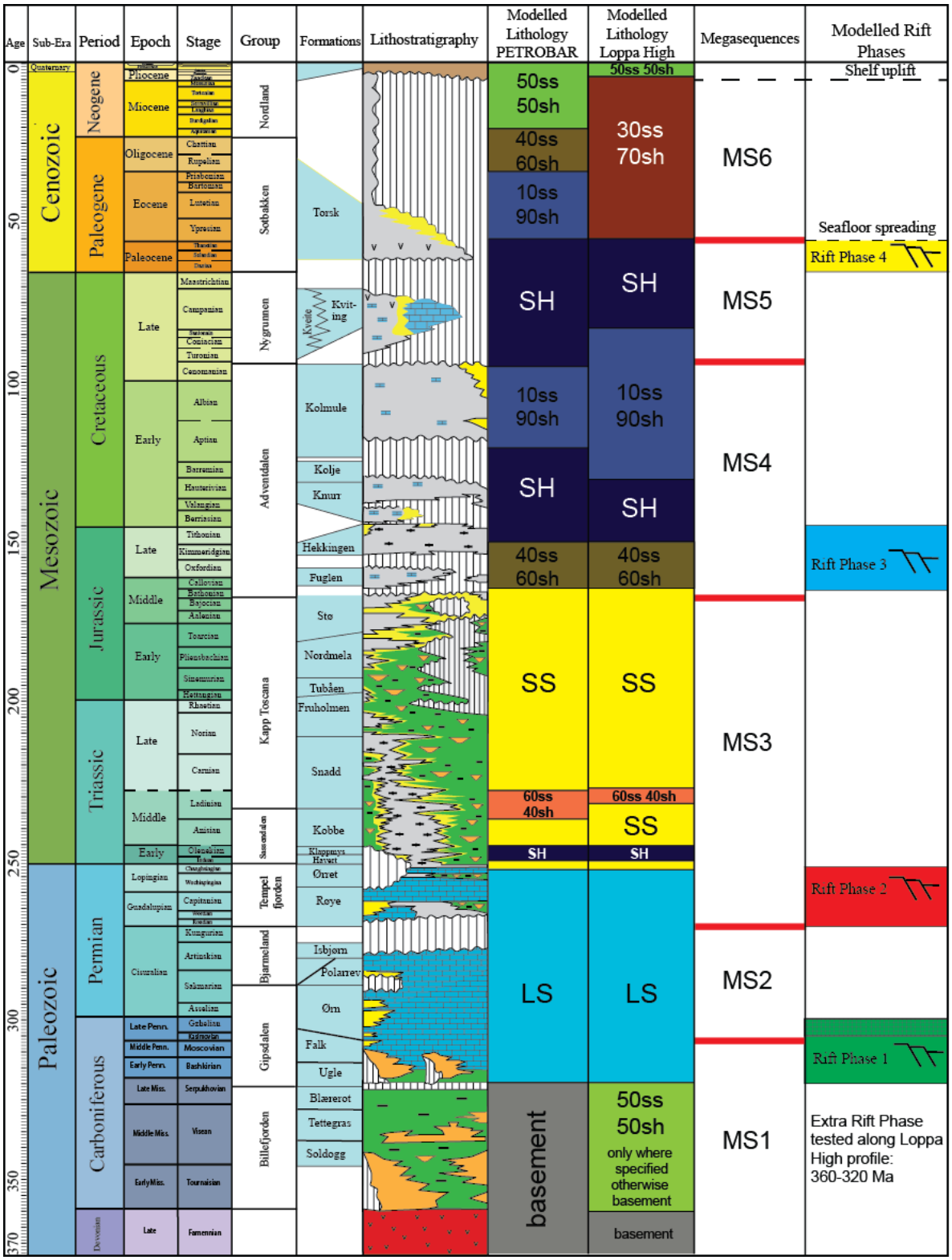

Figure 4.8. Lithostratigraphic column for the southwest Barents Sea. Modelled rift phases for the PETROBAR-07 profile (figure 4.6; Clark et al., 2014) and Loppa High profile (figure 4.7; Glørstad-Clark et al., 2011a) shown in the far right columns, spanning the duration of rifting in TecMod. Assigned lithostratigraphy for the 2 profiles is highlighted. Kerogen-rich shales were included between 250-245 Ma and 150-145 Ma. Lithostratigraphy key – basement: red; continental sand: orange; continental shales: green; carbonates: blue; marine sand: yellow; marine shale: gray; undifferentiated: brown. Time scale after Gradstein et al. (2004). Figure modified after Clark et al. (2014).

this study, the erosion level (400 m depth across most of the profile, deepening towards the shelf) and erosion rate (maximum 10 mm/yr from 5.3 – 2.6 Ma) are the same as those interpreted by Clark et al. (2014). This is shown in figure 4.9a. For the Loppa High profile, the erosion level is taken from the BMT backstripped stratigraphy at 2.6 Ma (300-400 m across most of the profile, deepening to 500 m in the western part of the Tromsø Basin; Glørstad-Clark et al., 2011a), while the erosion rate is maintained at 10 mm/yr from 5.3 – 2.6 Ma (figure 4.9b).

In order to erode sediments, they first need to be deposited. Because the erosion algorithm is part of the forward model in TecMod, and the inversion engine is working to fit the modelled stratigraphy to the input stratigraphy, sediments that need to be eroded according to the geological understanding of a basin are sometimes never deposited within TecMod. To rectify this, deposition of sediments can be forced by specifying the thickness of sedimentation required through a time and space range. Within this study, various amounts of forced deposition thicknesses were applied to the PETROBAR-07 and Loppa High profiles to optimize the fit with interpreted erosion events and paleo-water depth trends. The final optimized forced deposition input was consistent with the work of Clark et al. (2014). The deposition of 1 – 1.5 km of sediments was forced across most of both profiles between 120 Ma to 5.3 Ma to ensure they were available to be eroded during the Plio-Pleistocene erosion event. The maximum of forced deposition is located over the Loppa High, tapering to the NW toward the Vestbakken Volcanic Province and shelf. The optimized forced deposition inputs for both profiles are presented in figure 4.10.

Input parameters for serpentinization analysis within TecMod

Serpentinization of the upper mantle can be assessed using a kinematic basin modelling workflow within TecMod. Serpentinization involves the transformation of fosterite (Mg end-member of olivine) to serpentine and brucite with the addition of water. It is important to quantify because the petrophysical changes in the rock are exothermic, result in a volume change of up to 40% (for total transformation), a decrease in density, and a significant decrease in seismic wave speed. Serpentinization may cause anomalous subsidence and heat flow patterns, and the lower strength of serpentinized rocks can focus strain partitioning within rift zones. The integrated serpentinization routine found in TecMod is described extensively in Rüpke et al. (2013). Serpentinization reactions are dependent on mantle

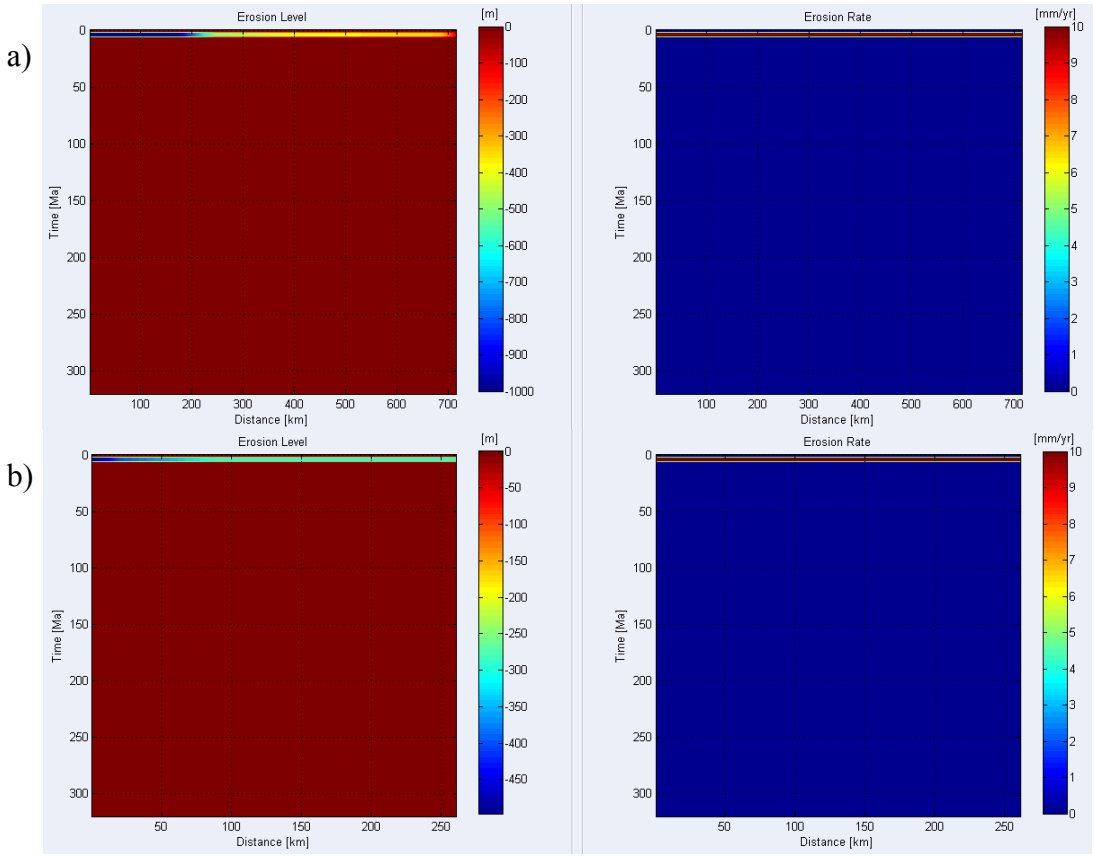

Figure 4.9. Erosion inputs into TecMod, limited to the time span 5.3-2.6 Ma. The level and rate above which erosion is activated in time and space is shown for a) The extended PETROBAR-07 profile and b) The Loppa High profile. The rate at which erosion takes place above the specified level is constant for both profiles, 10 mm/yr.

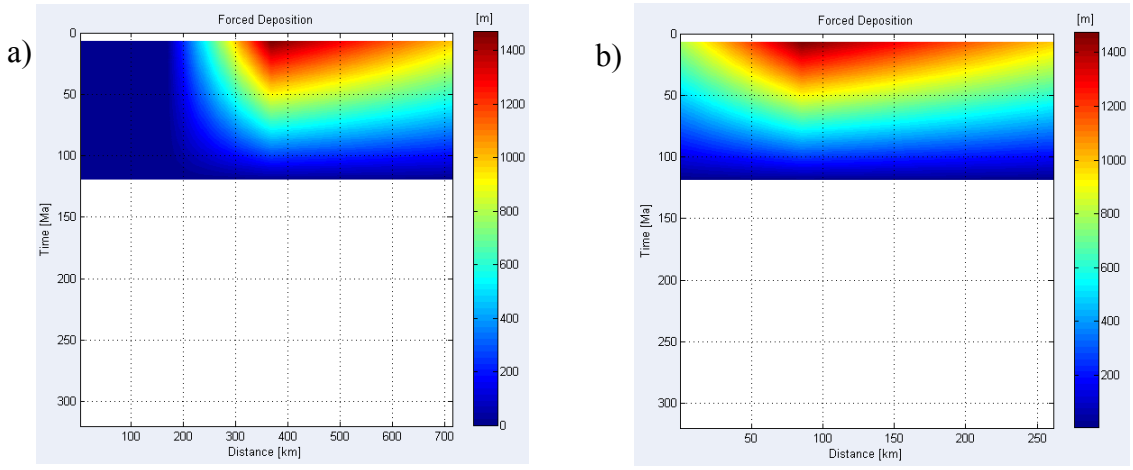

Figure 4.10. Forced deposition inputs to compensate for the Plio-Pleistocene erosion event shown in figure 4.10. Approximately 1 – 1.5 km sediment thicknesses were forced across most of the profile, with a maxima over the Loppa High, tapering toward the NW. a) PETROBAR-07 extended profile; b) Loppa High profile.

rheology, extension rate, fluid availability, and temperature. TecMod resolves the onset, extent, and consequences of mantle serpentinization by:

- Constraining the conditions under which the entire crust becomes brittle. Complete crustal embrittlement is required to facilitate the introduction of hydrous fluids into the mantle. Computation of the brittle and ductile yield stresses within the 2D model allows determination of where the brittle yield stress is lower than the ductile yield stress through the crust, and thus isolate where serpentinization reactions may occur;
- Estimating serpentinization reaction kinetics. The rate and extent of serpentinization is estimated based on published temperature-dependent fosterite-serpentine conversion rates. Changes in density of the uppermost mantle associated with serpentinization are also computed;
- Computing the change in temperature associated with the fosterite – serpentine transformation (with a latent heat of 2.9×10^5 J/kg, a 300°C increase in temperature can be expected following complete transformation) and integrating the result along discrete time steps into TecMod's heat transfer balance equations, which already cover heat advection, heat diffusion, and radiogenic heat production.

Input serpentinization parameters for the western Barents Sea models presented in this study are mostly the same as those published in Rüpke et al. (2013) and are listed in table 4.7. Rock properties for the sediments, crust and mantle are the same as those listed in table 4.4.

Table 4.7. Serpentinization input parameters for TecMod models run within this thesis. These are similar to those used in Rüpke et al. (2013).

Serpentinization Model Parameters	**Value**	**Units**
General Parameters		
Serpentinization rate (A)	1E-013	1/s
Thermal stability limit of serpentine	550	ºC
Fraction of magnetite	10	%
Maximum amount of serpentinization	20	%
Fraction of crust brittle for serpentinization	100	%
Brittle Rheology		
Pore pressure ratio	0.36	
Type of faulting	0.75	km
Ductile Rheology		
Sediment rheology	Wet quartzite	*TecMod inbuilt rheological estimates*
Upper crustal rheology	Wet quartzite (Aggregate also tested)	
Lower crustal rheology	Aggregate	*Based on composition, detailed in Rüpke et al. 2013*
Igneous body rheology	Aggregate	
Mantle rheology	Dry olivine	
Details		
Rate law	f(T)	
Rate constant (b)	0.00025	$1/K^2$
Rate constant (c)	540	K
Serpentine density	2550	kg/m^3
Magnetite density	5200	kg/m^3
Substepping synrift	10000	yrs
Substepping postrift	50000	yrs
Grid refinement below Moho	7000	m
Latent heat of reaction	290000	J/kg

5. Results

Automated basin reconstructions along the two profiles studied (PETROBAR-07 extended and Loppa High) were performed using TecMod v2014.1 for a series of scenarios. The input vs modelled stratigraphy was checked for each scenario. The distribution of crustal thinning factors in time and space were analyzed. The thermal history of the basin was investigated by examining the computed basement heat flow through time and temperature history in time and space, calibrated against vitrinite reflectance and bottom-hole temperature measurements from well data. Computed paleo-water depths were assessed. Gravity signatures from reconstructed profiles were compared to measured free-air and Bouger gravity data to assess their validity. Modelled crustal sections and thinning factors (β) distributions together with input vs modelled stratigraphy convergence for all scenarios are presented in Appendix A.

5.1 The Reference Model – PETROBAR-07 and Loppa High profiles

Reference models are required along the PETROBAR-07 and Loppa High profiles to allow for comparison with more detailed models, for example models incorporating continental breakup together with magmatic underplating and/or serpentinization. The reference PETROBAR-07 profile relates to the input stratigraphy as presented in figure 4.1, as published by Clark et al. (2014). The PETROBAR-07 reference profile is 550 km long and limited to basins underpinned by continental crust. The Loppa High reference profile is presented in figure 4.7, and is limited to sediments from 320 Ma to present.

The reference models account for the strength of the lithosphere and thereby the lateral extent of isostatic compensation, through an effective elastic thickness (T_E) input of 5 km. The geometric balance between lithospheric thinning from above (where lithosphere is replaced by water and sediments), and thinning from below (where lithosphere is replaced by upwelling asthenosphere) is defined by applying a necking depth of 15 km. These are the same parameters as those applied by Clark et al. (2014).

Late Cenozoic erosion is also applied. As discussed in chapter 4, erosion is simulated at the Plio-Pleistocene boundary, between 5.3 – 2.6 Ma. This is done by applying a maximum rate

of erosion of 10 mm/yr down to approximately 400 m water depth across most of the profile, deepening toward the shelf (see figure 4.9). Forced deposition of various thicknesses of sediments was applied to ensure that erosion could actually take place in the Pliocene. Without the forced deposition function applied, most of the sediments on the seabed are too deep to be eroded in the Pliocene. The deposition of 1 – 1.5 km of sediments is forced across the most of the profile (maximum over the Loppa High, tapering in the NW through the Vestbakken Volcanic Province) from 120 Ma to 5.3 Ma to ensure they are available to be eroded later (figure 4.10). Once again, these are similar erosion and forced deposition inputs as those described in Clark et al. (2014).

The convergence of the modelled stratigraphy to the input stratigraphy is good (approximately 5%) for the reference models along both profiles. A 350 m error in the fit for sediments over the Loppa High is observed, consistent with the results of Clark et al. (2014). But the overall fit for all scenarios is better than that published in Clark et al. (2014), with less iterations required to meet an acceptable convergence. This is the result of the improved inversion engine in TecMod v2014.1.

Elevated levels of crustal stretching are modelled over the deep Bjørnøya and Tromsø basins. A maximum cumulative β factor of 4.1 is modelled over the Bjørnøya Basin (figure 5.1a) and 3.4 over the Tromsø Basin (figure 5.1f). Maximum stretching along both profiles occurs during the Late Jurassic – Early Cretaceous rift phase, but this stretching is focused solely over the deep basins, and is absent from the Bjarmeland Platform further east. This is in contrast to the forward modeling results of Clark et al. (2014) along the PETROBAR-07 profile. The reason for the difference is the updated inversion engine in TecMod v2014.1 and different inversion control parameters applied, which have improved the modelled stratigraphy fit to the input stratigraphy. Elevated β-factors are modelled during the Carboniferous rift phase (light green lines; figure 5.1 b and g), especially over the Bjarmeland Platform along both profiles, including the Ottar and Nordkapp Basins along the PETROBAR-07 profile. So, as identified by Clark et al. (2014), the forward-modelling approach still creates some accommodation space for later rift phases during the earliest rift phase.

A trend can be seen in the β-factor distributions which reflects our current understanding of the evolution of the south-west Barents Sea, with the main axis of extension slowly migrating westward until eventual continental breakup. The basins and platform areas in the

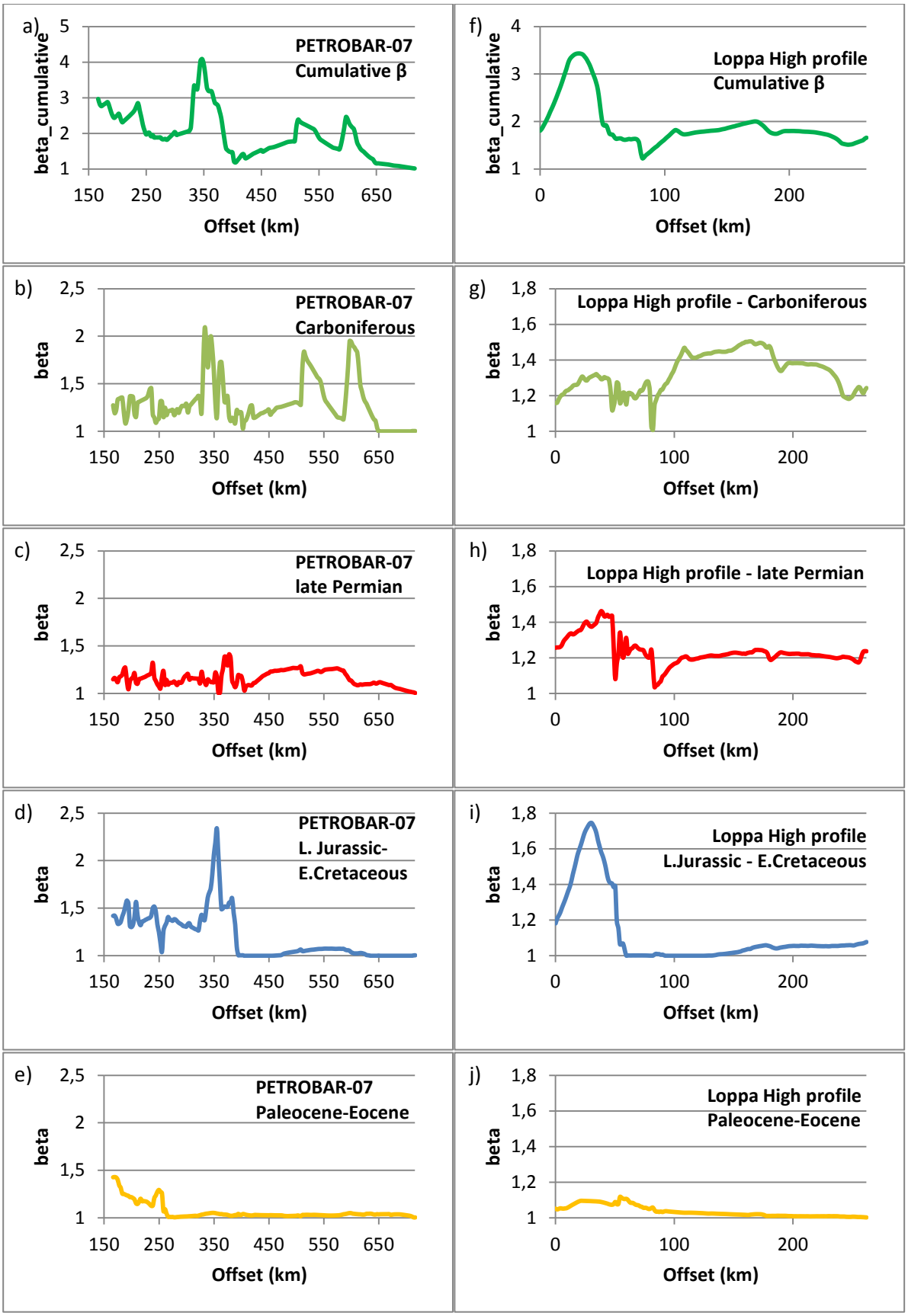
a)
PETROBAR-07
Cumulative β
beta_cumulative
Offset (km)
b)
PETROBAR-07
Carboniferous
beta
Offset (km)
c)
PETROBAR-07
late Permian
beta
Offset (km)
d)
PETROBAR-07
L. Jurassic-
E.Cretaceous
beta
Offset (km)
e)
PETROBAR-07
Paleocene-Eocene
beta
Offset (km)
f)
Loppa High profile
Cumulative β
beta_cumulative
Offset (km)
g)
Loppa High profile - Carboniferous
beta
Offset (km)
h)
Loppa High profile - late Permian
beta
Offset (km)
i)
Loppa High profile
L.Jurassic - E.Cretaceous
beta
Offset (km)
j)
Loppa High profile
Paleocene-Eocene
beta
Offset (km)

Figure 5.1. (previous page) Crustal stretching factors (β-factors) calculated from reference models along the PETROBAR-07 reference profile (a-e, left) and the Loppa High profile (f-j, right). The top graphs (a + f) represent the cumulative β-factors calculated along each profile, while graphs b-e (PETROBAR-07) and g-j (Loppa High profile) represent the β-factors calculated for the individual modelled rift phases. Note the maximum period of stretching over the deep Bjørnøya and Tromsø Basins occurred during the Late Jurassic – Early Cretaceous rift phase.

east, including the Nordkapp and Ottar Basins were the main focus of extension during the Carboniferous (light green lines; fig 5.1). Diffuse, low-magnitude rifting ensued during the late Permian inferred rift event (red lines; fig 5.1). Slowly, the main axis of extension migrated westward toward the Bjørnøya and the Tromsø basins in the Late Jurassic-Early Cretaceous (blue lines; fig 5.1). And finally, immediately prior to continental breakup, elevated levels of stretching are recorded within 100 km of the margin in the Vestbakken Volcanic Province (yellow line; fig. 5.1e).

TecMod varies water depths as a fitting parameter, so comparison of the modelled water depths to interpreted values is an important part of model evaluation (Clark et al., 2014). Computed paleo-water depth outputs from TecMod reference models are compared with interpreted paleo-water depths from Clark et al. (2014) and Glørstad-Clark et al. (2011a). These are provided in figures 5.2 (PETROBAR-07 profile) and figure 5.3 (Loppa High profile). Their estimates are based on clinoform relationships from seismic sequence stratigraphy studies. In general, the modelled reference water depths (green lines) along the Bjørnøya and Tromsø basins are much deeper (probably unrealistic) during the Jurassic rift event when compared with the interpreted depths (purple lines; figure 5.2 and 5.3) from Clark et al. (2014) and Glørstad-Clark et al. (2011a).

Upon inspection of the paleo-water depth trends, the Loppa High and Polheim-Sub-platform are subject to syn-rift flank uplift during the late Permian rift phase, resulting in an island forming from 270-260 Ma. Syn-rift flank uplift on the Loppa High is also observed during the Jurassic rift phase along the PETROBAR-07 profile (figure 5.2), but is mostly static along the Loppa High profile (figure 5.3). Following the Late Jurassic-Ealy Cretaceous rift phase, late post-rift subsidence is calculated in both the reference models, but the forced deposition feature in TecMod fills the Loppa High from 120 Ma ensuring it remains at or above sea level until the Quaternary glacial period, which is largely in agreement with our current knowledge. If the forced deposition feature is turned off, the basin remains underfilled, and too deep for subsequent Plio-Pleistocene erosion (not shown). So, without

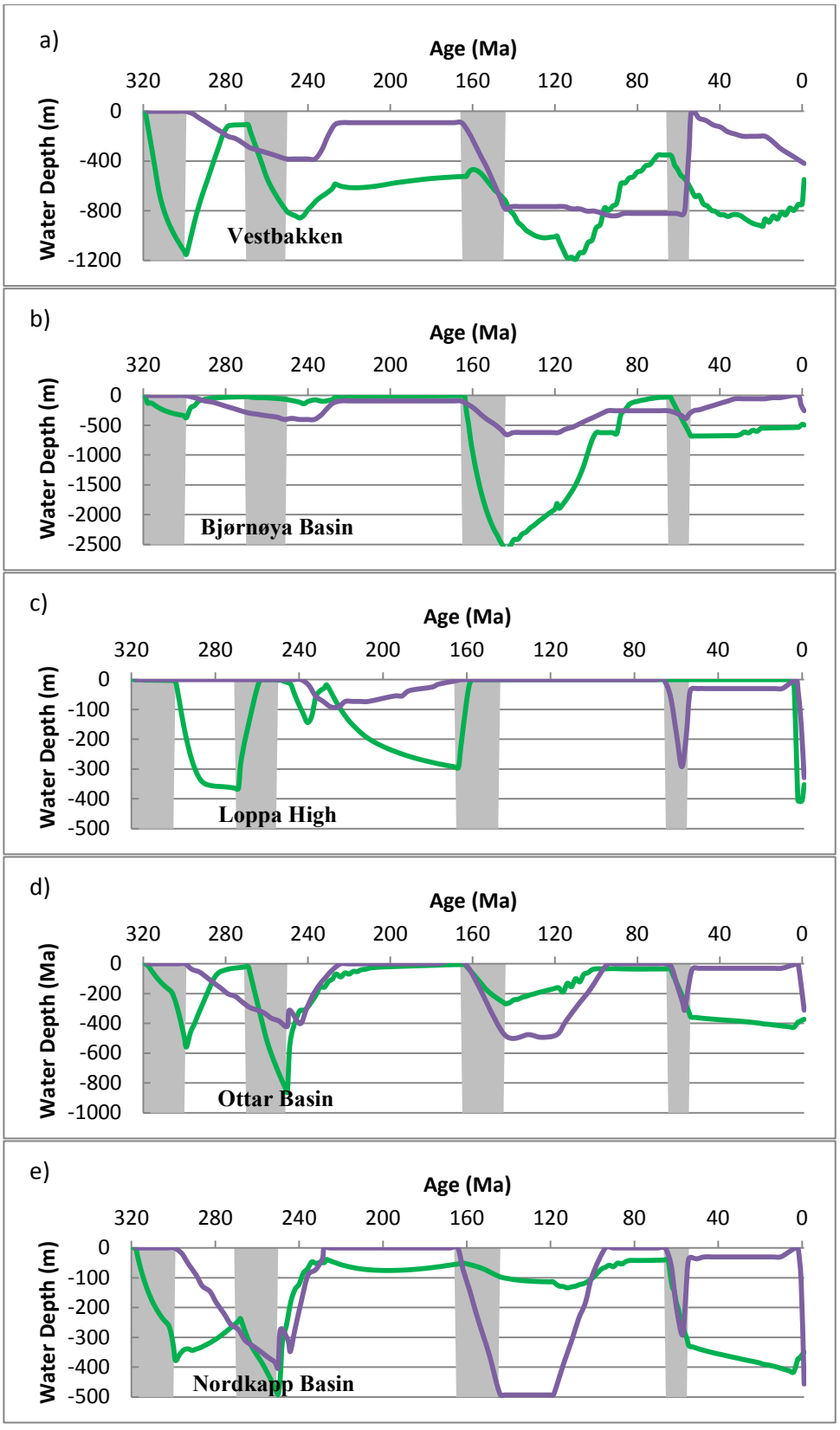

Figure 5.2. (previous page) Water depths over time for five pseudo-well locations (see figure 4.1 and 4.6a for pseudo-well locations a-e) along the PETROBAR-07 reference profile Green line – reference model applying flexural isostasy with erosion, purple line – interpreted water depths (Clark et al., 2014). Grey shaded areas represent modelled rift phases. Note the flexural models predict deeper basins and more elevated structural highs.

forced deposition and erosion applied to our models, TecMod computes water depths which are too deep during the Cenozoic such that erosion never has the opportunity to take place.

One problem recognized by Clark et al. (2014) in their TecMod outputs was the consistent, deep water depths in the Carboniferous and Permian of the Bjørnøya Basin. Considering deposition of limestones and evaporates is thought to have dominated the sediment infill throughout the south-west Barents Sea (Gudlaugsson et al. 1998; Larssen et al. 2002), shallow water depths are required. The reference models produced in this study over the Bjørnøya and Tromsø Basins exhibit shallow water depths during the Late Carboniferous and Permian, Again, this result is related to the improved fitting feature in the TecMod inversion engine and the application of optimized inversion control parameters.

Along the PETROBAR-07 reference profile, significant amounts of erosion (500 – 700 m) are modelled over the Loppa High and east of the Nordkapp Basin (figure 5.4a). Erosion-induced uplift is of the order of 200 m. However, very little erosion could be modelled over the Ottar (figure 5.2d) and Nordkapp basins (figure 5.2e), and west of the Loppa High through the Bjørnøya Basin (figure 5.2b) and Vestbakken Volcanic Province (figure 5.2a), because the assigned erosion level was above the modelled paleo-water depth.

Along the Loppa High profile (figure 5.4b), 400-500 m of erosion is modelled consistently from the Polheim Sub-platform (figure 5.3b) and Loppa High (figure 5.3c), eastward along the Bjarmeland Platform (figure 5.4b). Approximately 100-200 m of erosion is modelled through most of the Tromsø Basin (figure 5.3a). Similar amounts of erosion-induced uplift (200 m) were observed along the most eroded parts of the profile (e.g. Loppa High). Along both profiles, the amount of erosion modelled is within the limits, or less than published estimates (e.g. 0 – 1000 m erosion estimate in the Tromsø Basin; Riis & Fjeldskaar, 1992).

The reference models seem to match some general estimates of the topographic movement of the Selis Ridge/Loppa High, without capturing the total complexity of its evolution. The models exhibit deep water levels in basin depocenters (especially during the Late Jurassic-Early Cretaceous rift phase) and shallower water levels along basement highs. Incorporating forced deposition and erosion ensure that sufficient sedimentary fill is available on basement highs in the late Cenozoic for erosion to take place, a process that is important for petroleum system development in the south-western Barents Sea.

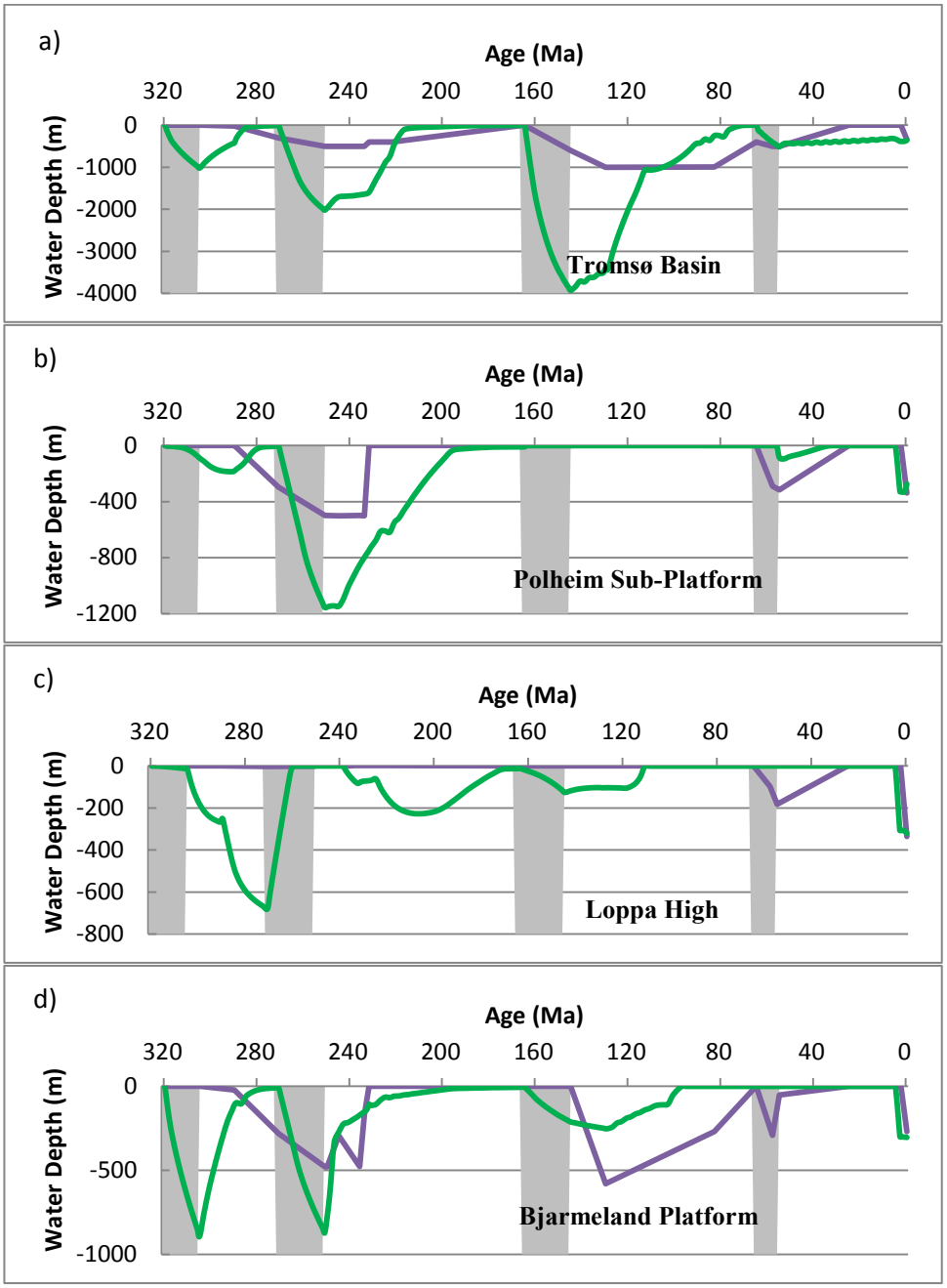

Figure 5.3. Water depths over time for four pseudo-well locations (see figure 4.7 for pseudo-well locations a-e) along the Loppa High profile for different isostatic and erosion conditions. Green line – reference model applying flexural isostasy with erosion, purple line – interpreted water depths (Glørstad-Clark et al., 2011a). Grey shaded areas represent modelled rift phases. Again, note the flexural models predict deeper basins and more elevated structural highs.

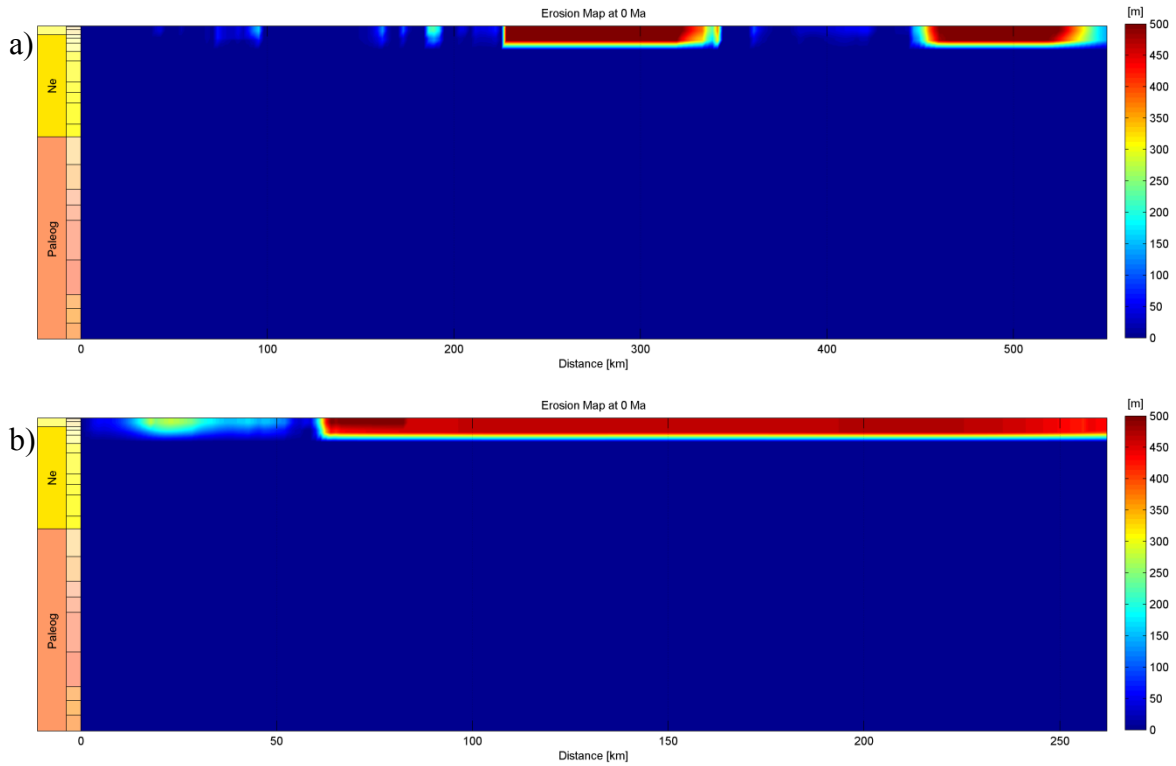

Figure 5.4. Erosion map through time (from 65-0 Ma) showing the amount of erosion computed for the reference models. a) PETROBAR-07 reference profile. b) Loppa High profile.

Summary – reference models

The reference models capture, to some extent, our current understanding of the topographic evolution of basement highs along the present-day Loppa High. However, they exhibit unrealistic water depths during the Late Jurassic-Early Cretaceous rift phase. The models incorporate forced deposition and erosion to ensure that the late Cenozoic history of the basement highs within the south-west Barents Sea is respected. The PETROBAR-07 reference model consists of the same data input as that published in Clark et al. (2014), specifically the input stratigraphy (though a horizon from 228-165 Ma was inserted west of the Loppa High, as discussed in chapter 4.2.1) and erosion/forced deposition estimates. But the inversion engine has been improved in TecMod since the work of Clark et al. (2014), and the inversion control parameters chosen for this study are different, so the results are slightly different. These case models along the PETROBAR-07 and Loppa High profiles will act as a reference to compare modelled outputs from all other scenarios within this study.

5.1.1 Model fit to well data – Reference models

Vitrinite reflectance (R_o), bottom hole temperature, and Drill Stem Test (DST) temperature measurements were acquired from the Norwegian Petroleum Directorate for 3 wells located within 12 km of the PETROBAR-07 profile (figure 4.1 and 4.6 for well locations), and 4 wells with 45 km of the Loppa High profile (figure 4.7 for well locations). Figures 5.5 and 5.6 show the temperature measurements plotted against the modelled geotherms from the PETROBAR-07 and Loppa High models respectively. Figures 5.7 and 5.8 show the R_o measurements plotted against the modelled R_o trends from the PETROBAR-07 and Loppa High profiles respectively.

Well control points show reasonable correlation for both the PETROBAR-07 and Loppa High reference models when comparing against most of the bottom hole and DST temperatures, but with considerable variation at wells 7316/5-1, 7215/1-1 (figs 5.5a and c) and 7226/11-1 (fig 5.6d). Bottom hole mud temperature measurements are not necessarily in equilibrium with the formation temperature, so the observed variability may be a function the measurement, not the validity of the model.

The vitrinite reflectance values also show good correlation with two wells intersecting the PETROBAR-07 profile (figs 5.7 b and c), but poor correlation with the well in the Vestbakken Volcanic Province (7316/5-1, fig 5.7a). This is probably due to the absence of igneous intrusives and extrusives in the reference model (Clark et al., 2014). For the Loppa High profile (figure 4.7), wells located close to the profile (fig 5.8c - 7224/7-1 and fig 5.8d - 7226/11-1) show good correlation, however the more distant wells (figs 5.8a and b, located near the Loppa High) show discrepencies.

5.1.2 Gravity analysis – Reference Models

Free-air anomaly and Bouger-corrected gravity is extracted from the TecMod density distribution for both the PETROBAR-07 (green lines; fig 5.9) and Loppa High (red line; fig 5.10, free-air anomaly only) profiles and compared with observed data from satellite altimetry (Kenyon et al., 2008) and ship tracks (Olesen et al., 2010). While the calculated gravity from the TecMod profile follows the general fluctuations in the observed gravity (dashed purple line), the amplitude of the observed gravity is far more intense, suggesting more advanced lateral density variations in the western Barents Sea than the models capture.

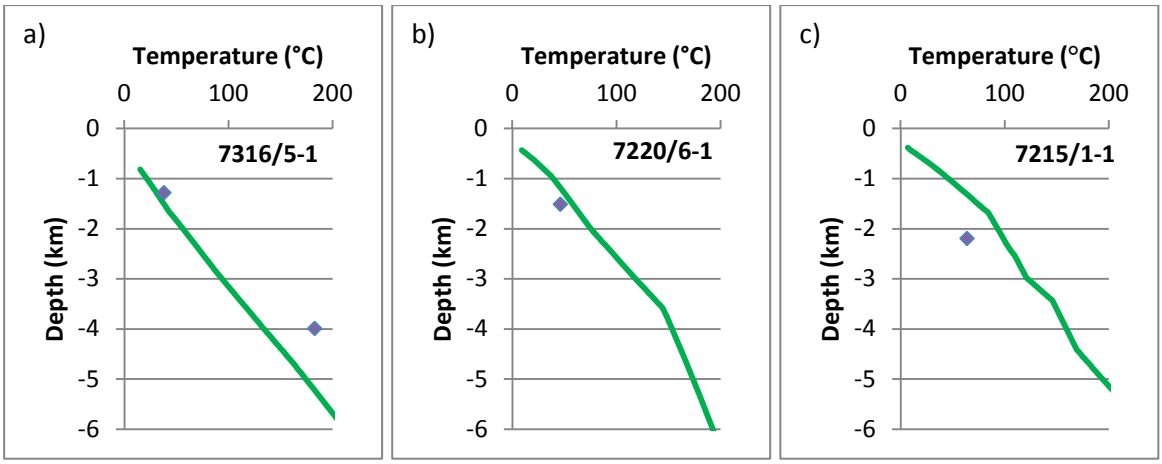

Figure 5.5. Geotherms extracted from the PETROBAR-07 reference model (green line) plotted against well temperature data from bottom-hole measurements and Drill Stem Tests (purple points). For well locations, see fig 4.6.

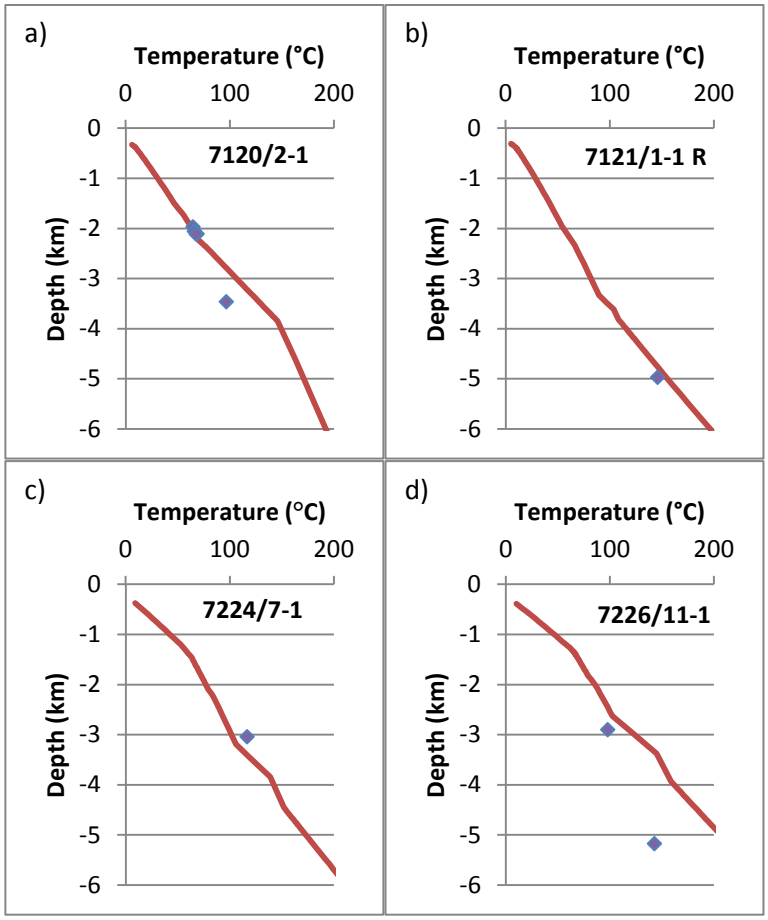

Figure 5.6. Geotherms extracted from the Loppa High reference model (red line) plotted against well temperature data from bottom-hole measurements and Drill Stem Tests (purple points). For well locations, see fig 4.7.

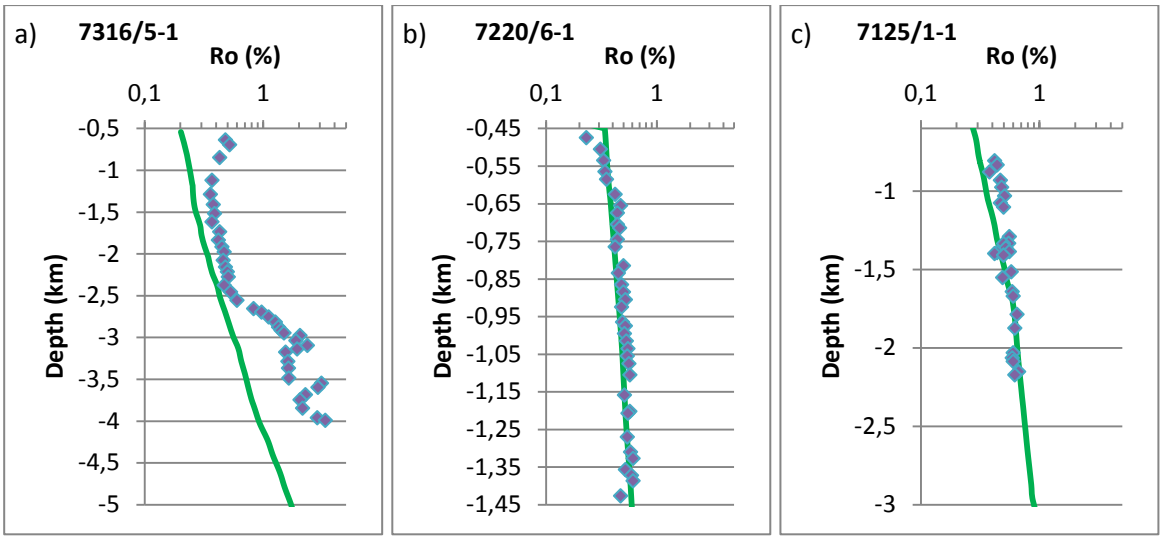

Figure 5.7. Vitrinite reflectance (R_o) trends extracted from the PETROBAR-07 reference model (green line) plotted against R_o data from three wells (purple points). For well locations, see figs 4.1 and 4.6.

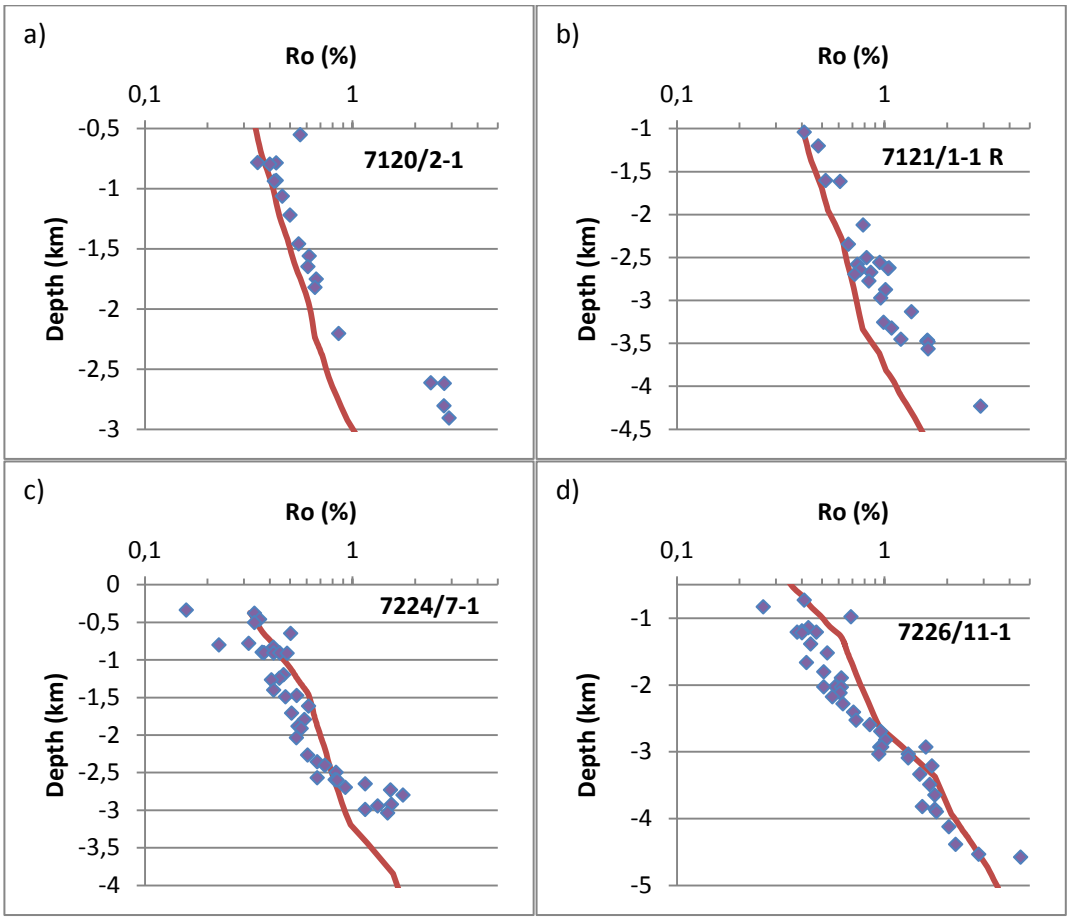

Figure 5.8. Vitrinite reflectance (R_o) trends extracted from the Loppa High reference model (red line) plotted against R_o data from three wells (purple points). For well locations, see figure 4.7.

PETROBAR-07 modelled gravity profiles were corrected by -43.4 mGal to fit with models incorporating continental breakup with a mid-ocean ridge (MOR).

Comparisons between the observed free-air anomaly profile (Keynon et al., 2008) and the calculated free-air anomaly based on the TecMod density distribution show very little correlation along the Loppa High profile (figure 5.10). This is partly because modelling is 2D and lateral density changes in the third dimension (especially near the Veslemøy High) are not taken into account in the gravity modelling.

Upon inspection of the calculated free-air gravity and Bouger-gravity anomalies in figures 5.9 and 5.10, the deep Bjørnøya Basin and Tromsø Basin have a relatively flat signature, or low-amplitude gravity low, while the observed data coincides with a high-amplitude gravity low. In the models, the Bjørnøya and Tromsø basins display little lateral density variation in the crust, while the actual basins are associated with strong lateral density variations in the crust (e.g. Barrère, 2010). In the sediments, lateral density variations may also be present which are not captured by the models. Density changes in sediments result from overpressure of deep-buried sequences. Alternatively, smectite-illite transformations, quartz cementation, and/or low-pressure metamorphism of the deep sediments have significantly altered the density of the sediments in the basin deep compared to the flanks.

5.2 Continental breakup, magmatic underplating, and sill intrusion models

A series of scenarios were modelled along the PETROBAR-07 extended profile progressively testing the thermal and isostatic implications of continental breakup (and seafloor spreading), breakup with emplacement of an underplate below the Vestbakken Volcanic Province, and breakup with sill intrusions within the sediments of the Vestbakken Volcanic Province. For the scenario including only breakup (without underplating or igneous events), two input stratigraphies were modelled to test the effect of a flat (figure 4.6a) and tapered (figure 4.6b) lower sedimentary succession below the Vestbakken Volcanic Province toward the COB. All models including magmatic underplating and sill intrusions employ the input stratigraphy in figure 4.6a, modified after Clark et al. (2014).

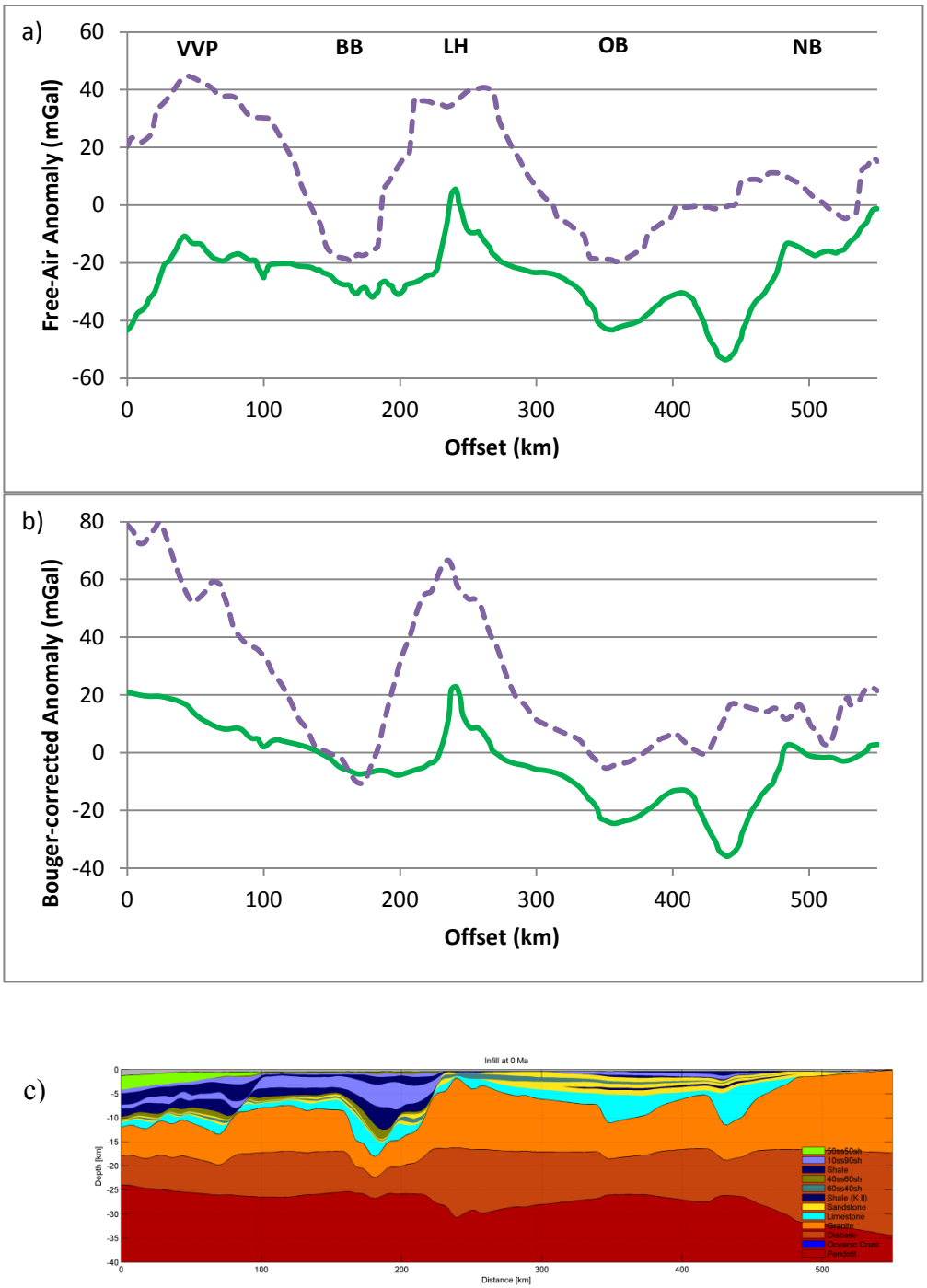

Figure 5.9. Gravity extracted from the density distribution of PETROBAR-07 reference model (green line) compared to the observed gravity anomaly data (purple dashed line). The modelled gravity profiles have been shifted by -43.3 mGal to fit with modelled breakup scenarios with a MOR. a) Free-air corrected gravity anomaly (Kenyon et al. 2008); b) Bouger-corrected gravity anomaly with 2200 kgm^{-3} water-sediment replacement (Olesen et al. 2011 c) Crustal section of the PETROBAR-07 reference model.. VVP – Vestbakken Volcanic Province, BB, Bjørnøya Basin, LH – Loppa High, OB – Ottar Basin, NB – Nordkapp Basin.

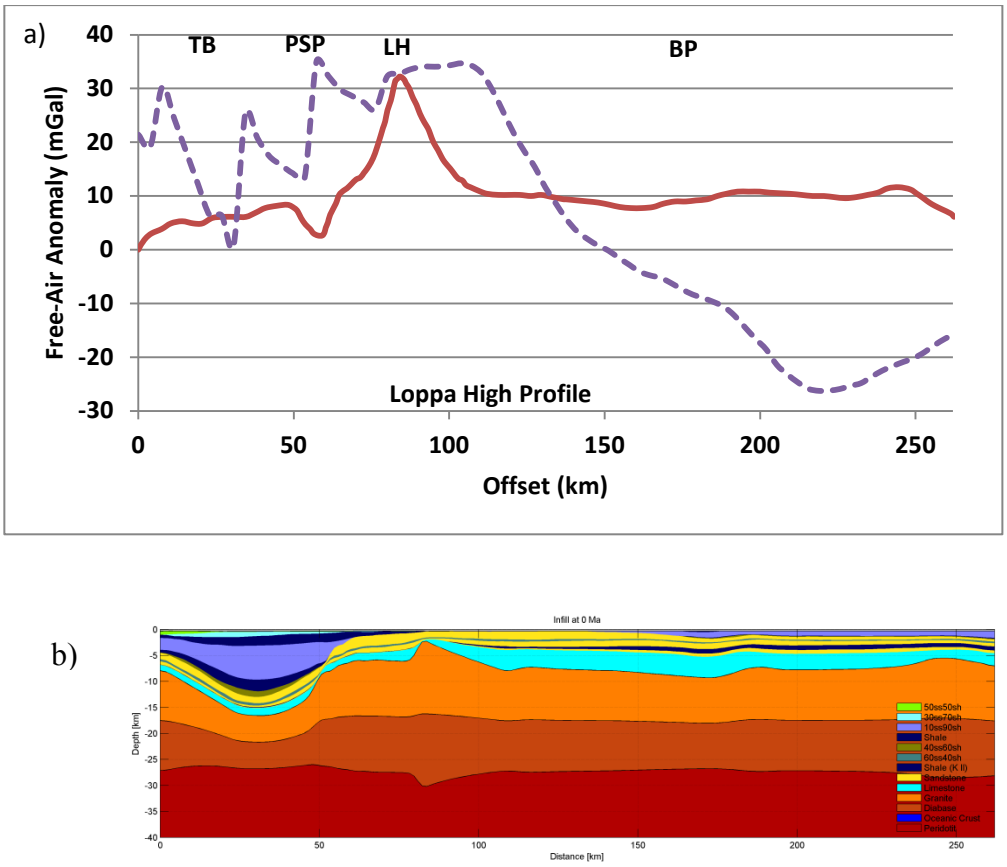

Figure 5.10. a) Free-air gravity anomaly data computed from the density distribution output from TecMod (red line) compared to the observed free-air anomaly data from satellite altimetry (purple dashed line) along the Loppa High profile (Kenyon et al. 2008). TB – Tromsø Basin; PSP – Polheim Sub-Platform; LH – Loppa High; BP – Bjarmeland Platform. b) Crustal section of the Loppa High reference model.

All models including continental breakup, underplating, and sill intrusion had similar fits between the input and modelled stratigraphy. Stratigraphy comparisons and the crustal configuration for each scenario are provided in Appendix A. The fit between the input and modelled stratigraphy is good for all scenarios east of the COB, identical to the PETROBAR-07 reference scenario. The seabed and Base Pleistocene horizons display relatively good fits in the oceanic crustal domain west of the COB. But the Early Miocene (20 Ma) is not well reproduced west of the COB. The modelled top of the oceanic crust is considerably deeper than the interpreted top of basaltic volcanic flows, but is consistent with oceanic crustal depths estimated by Clark et al. (2013) based on gravity and magnetic modelling.

5.2.1 Continental breakup and seafloor spreading – PETROBAR-07 profile

The position and timing of continental breakup along the sheared western Barents Sea margin is well studied, based on primarily on interpretations of paleomagnetic and potential field geophysical data (Faleide et al., 1991, 1993, 2008; Breivik et al., 1998, 1999, 2003; Engen et al., 2008; Libak et al., 2012a, 2012b). The position of the continent-ocean boundary (COB) used in this study was mapped accurately based on comprehensive gravity and seismic studies by Breivik et al. (1999); Libak et al. (2012a, 2012b); and Clark et al. (2013). The models incorporating continental breakup simulate replacement of continental crust by oceanic crust west of the COB. The spreading axis is assigned to the left side of the modelling domain. Lithospheric temperatures are set to mantle values at the spreading axis (1300 ºC). A spreading velocity of 0.55 $cm.yr^{-1}$ is used, consistent with published accounts (Faleide et al., 2008). Faleide et al. (2008) reported the timing of final lithospheric breakup at 55-54 Ma along the Norwegian margin. This is synchronous with the end of the final rifting episode between 65-55 Ma. All modelled breakup scenarios are therefore set at 55 Ma. The 55 Ma time line west of the COB (in the oceanic domain) simply represents the top of basaltic flows of indiscriminate age, and is ignored by the TecMod algorithm.

The thickness of oceanic crust formed as a result of seafloor spreading is optimized to provide the best reconstructed fit of Cenozoic stratigraphy. The input oceanic crustal thickness is 14 km within models where breakup is included, with a density of 2900 kgm^{-3}.

In order to simulate the isostatic effect of continental breakup, it is necessary to assume different boundary conditions on each side of the modelling domain in TecMod. While on the eastern side (right) of the PETROBAR-07 profile is underpinned by strong continental lithosphere, the seaward side (left) is weak at a plate boundary. The flexural boundary condition on the seaward boundary is therefore assigned to approach a broken plate scenario, with T_E = 0 km, whereas the eastern flexural boundary condition remains at T_E = 5 km (table 4.5). This is the same conditions as applied to the left side of the PETROBAR-07 reference model (section 5.1). This approach is similar to the work of Rüpke et al. (2010) along the Ghana transform margin.

Results – PETROBAR-07 profile with flat basement structure

Using an input stratigraphy (figure 4.6a) modified from Clark et al. (2014), crustal stretching factors (β) are significantly higher for the Paleocene-Eocene rift event adjacent to the COB (figure 5.11b). This, in turn, equates to a significantly higher cumulative β-trend at the COB, approaching β = 4. Otherwise, the Late Jurassic-Early Cretaceous, late Permian, and Carboniferous rift phase β-distributions are very similar to the reference model (figure 5.11a).

The paleo-water depths (figure 5.12, blue line) are comparable to the reference scenario (green line) across most the profile, except within the Vestbakken Volcanic Province. Within 30 km (x=182km; pseudo-well 'f') and 64 km (pseudowell 'a'; x=216km) east of the COB, the water depths are average 600 m and 100 m deeper (respectively) prior to the Paleocene-Eocene rift phase for the breakup scenario. During the final rift phase, approximately 250 m of subsidence is modelled. This is followed by 200-600 m of uplift in the near-margin basin (within 75 km of the COB) associated with continental breakup. Breakup-related uplift is a response to the simulated broken-plate boundary condition ($T_E = 0$) applied to the left side of the model. A thermal uplift effect associated with lateral heat flow from the spreading ridge is also a minor contributor. At 86 km (well 7316/5-1; x=238km) from the COB, there are no obvious differences in the paleo-water depth trends between the breakup and reference scenarios, implying limited flexural related to continental breakup.

The effect of continental breakup on the heat distribution within the basin is most obvious close to the COB (30km east; figure 5.13a – blue line), resulting in a 5-6 mW/m^2 increase in heatflow at 55Ma. 64 km from the COB (figure 5.13b), a 2 mW/m^2 heatflow increase is computed. On the other hand, the reference model (green line) and the breakup model with a flat basement structure (blue line) experience significant sediment blanketing effects from sediments deposited between 320-165 Ma near the margin, suppressing the basement heatflow trends. The thermal effects of continental breakup are not recorded greater than 75 km from the COB (figure 5.13 c).

Results – PETROBAR-07 profile with tapered lowermost stratigraphy

Using an input stratigraphy (figure 4.6b) inspired by Libak et al. (2012b), modelled β-factors are much lower for the Carboniferous (green line), late Permian (red line) and Late Jurassic-Early Cretaceous (blue line) rift phases close the COB (figure 5.11c). This is because the

upper Paleozoic and lower Mesozoic sediments were progressively removed from the input stratigraphy toward the COB in an attempt to simulate interpretations by Libak et al. (2012b), so no rift-induced subsidence is required to provide accommodation space for sediment deposition. Approximately 80 km eastward of the COB, the β-factor trends converge and are identical.

Paleo-water depths are significantly deeper close (30 km east) to the COB (yellow line; pseudo-well 'f'; x=182km) for the tapered section compared to the flat basement profile below the Vestbakken Volcanic Province (figure 5.12). The tapered section model (yellow line) show consistent deepening from rift initiation at 320 Ma to the Late Jurassic-Early Cretaceous rift event at 165 Ma, resulting in a 1500 m difference in water depth computed in the Early Jurassic. Further away from the COB, the difference reduces considerably. At 64 km east of the COB (pseudo-well 'a'; x=216km), only a maximum of 200 m difference in water depths are computed in the Carboniferous. At 86 km east of the COB (well 7316/5-1; x=238km) the paleo-water depth trends are identical.

The near-margin (30 km from COB; x=186km) basement heatflow history (yellow line; figure 5.13) is much higher after the initial Carboniferous rift phase (300 Ma) compared to the reference model and the breakup-model with a flat basement structure (figure 5.13a). This is due to the basement being exposed to the overlying seawater column from 320-165 Ma. No sedimentation had taken place because no sediments of this age were mapped along the input stratigraphy. Further east, the differences in heatflow diminish. 64 km from the COB (x=216km), only very minor heatflow differences are observable after 55 Ma (fig 5.13b).

Summary

The models incorporating breakup and seafloor spreading alter the thermal and subsidence history of sediments close to the COB (e.g. within 30-75 km). Further away from the COB, the effect is negligible. Two models incorporating breakup were run with different stratigraphic profiles below the Vestbakken Volcanic Province. The relatively flat layered sequence (Clark et al., 2014) exhibits similar trends in crustal thinning, paleo-water depths, and heat flow prior to breakup when compared with the reference model. The tapered sequence (Libak et al., 2012b) exhibits significantly deeper paleo-water depths, subdued crustal thinning factors, and higher basement heat flow, close to the COB.

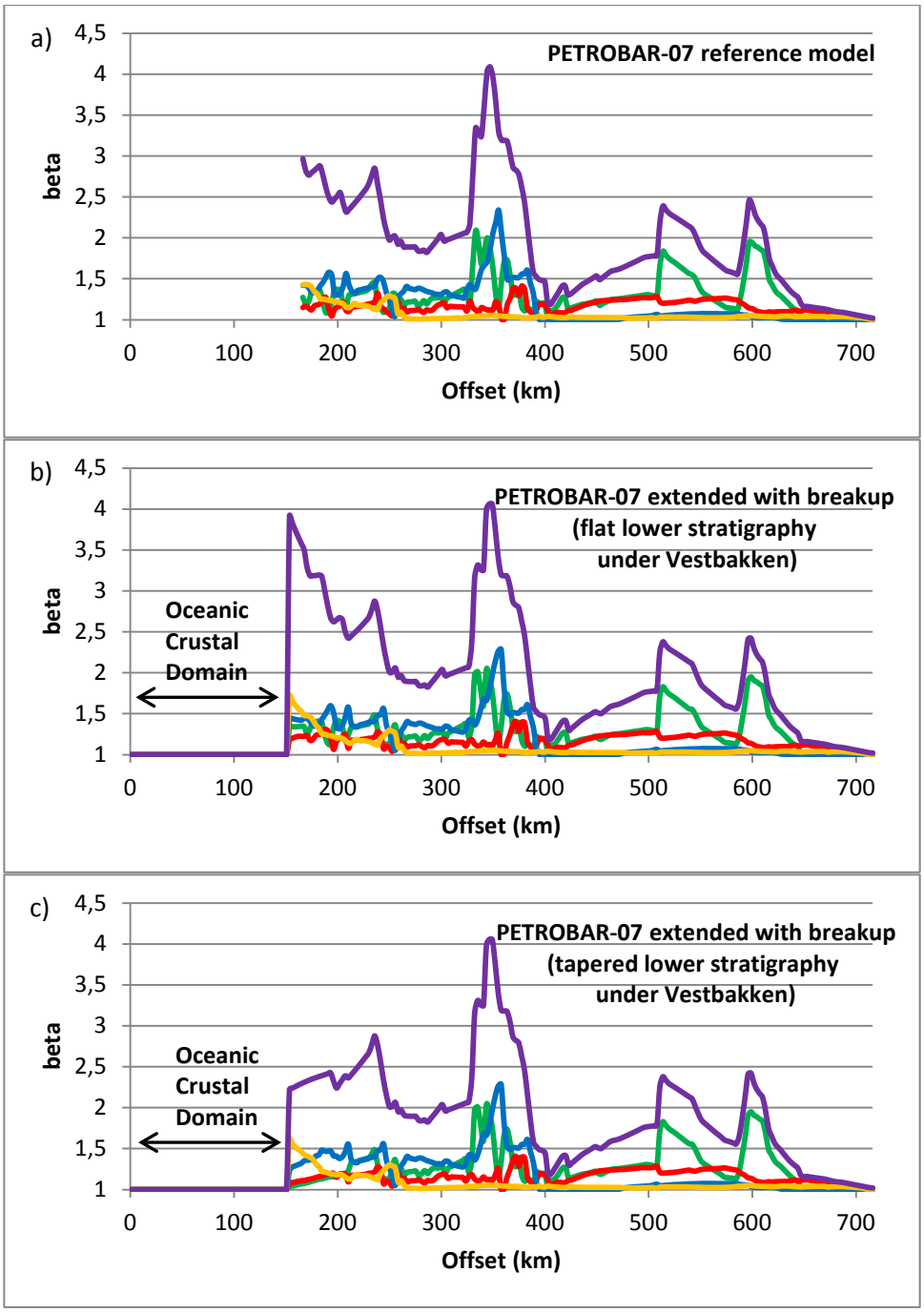

Figure 5.11. Crustal stretching factors (β) for computed for three models along the PETROBAR-07 extended profile. (a) PETROBAR-07 reference profile. (b) PETROBAR-07 extended profile incorporating continental breakup and a flat lower sedimentary succession as mapped by Clark et al. (2014). (c) PETROBAR-07 extended profile incorporating continental breakup and a tapered lower sedimentary succession as proposed by Libak et al. (2013b). 320-300 Ma rift phase –green line; 271-251 Ma rift phase – red line; 165-145 Ma rift phase – blue line; 65-55 Ma rift phase; yellow line; cumulative β – purple line.

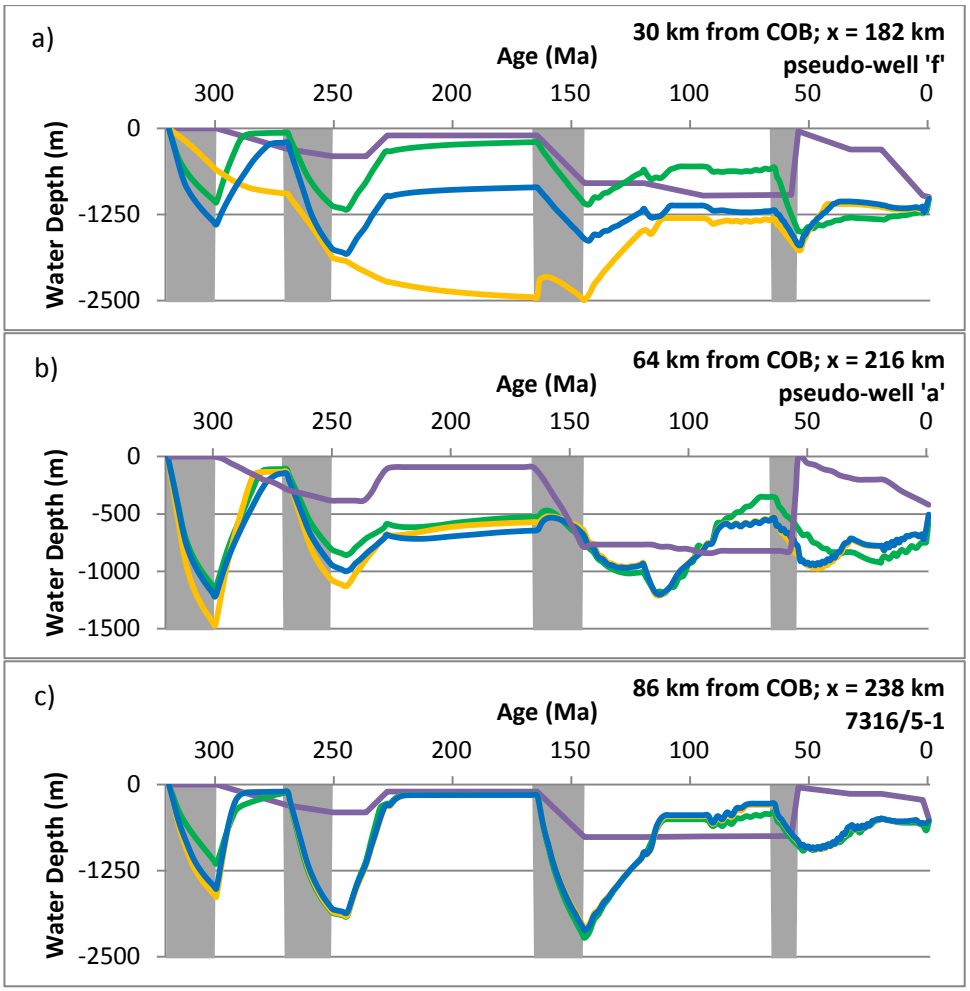

Figure 5.12. Calculated and interpreted water depths over time for three pseudo-well locations located in the Vestbakken Volcanic Province at different distances from the COB along the PETROBAR-07 extended profile. Green line – reference model, blue line – model incorporating breakup with a flat lower stratigraphy, orange line – model incorporating breakup and a tapered lower sedimentary succession, purple line – interpreted water depths (Clark et al., 2014). Grey shaded areas represent modelled rift phases. Note the tapered lower stratigraphic profile toward the COB produces significantly deeper water depths close to the COB. Breakup-induced uplift is observed close to the COB (figures a + b), but not distal to the COB (figure c).

For models including magmatic underplating and sill intrusion below the Vestbakken Volcanic Province, the flat-layered stratigraphic sequence as mapped by Clark et al. (2014) will be used as the input stratigraphy (figure 4.6a).

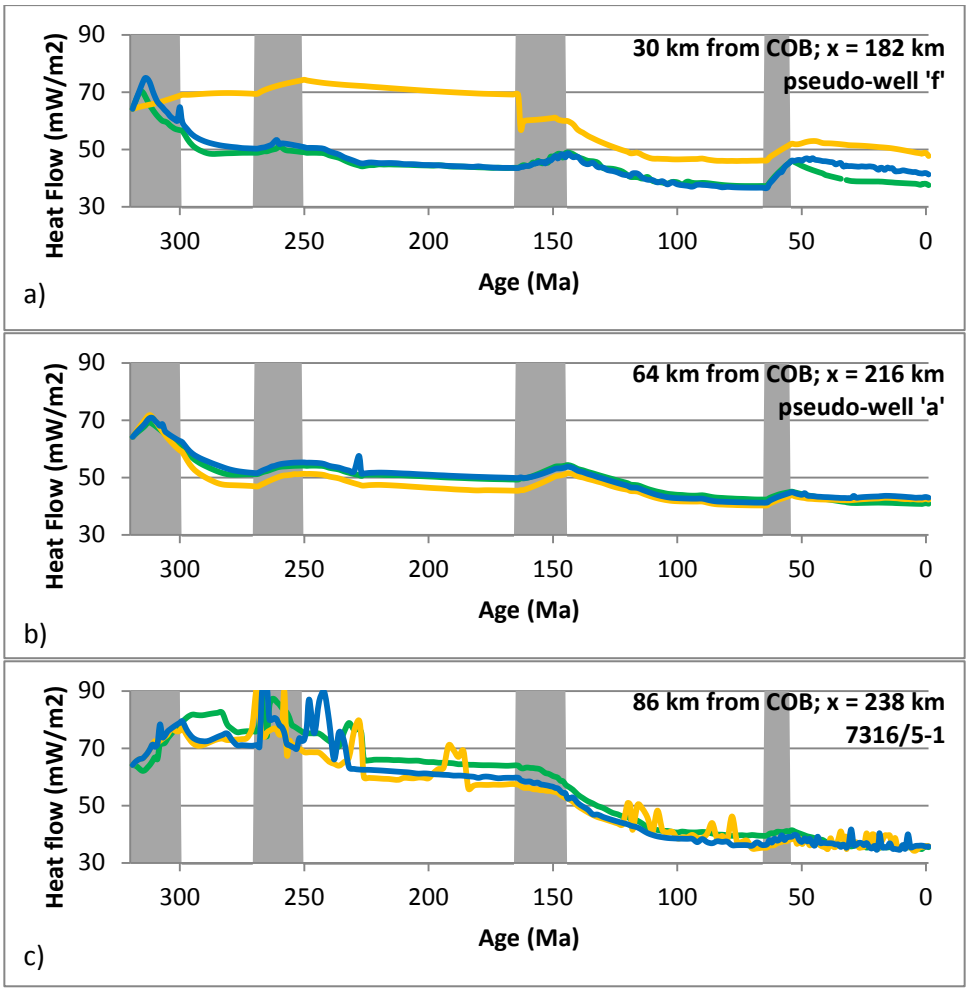

Figure 5.13. Basement heat flow data versus time for 3 well and pseudo-well locations located in the Vestbakken Volcanic Province at different distances from the COB along the PETROBAR-07 extended profile. Green line – reference model, blue line – model incorporating breakup with a flat lower stratigraphy, yellow line – model incorporating breakup and a tapered lower sedimentary succession. Note the thermal effect of continental breakup (post 55 Ma) close to the COB (figure a), with higher heatf low values compared to the reference model (green line). Very minor thermal effect is recorded 64km from the COB (fig b). Further away, no thermal effect is seen (fig c).

5.2.2 Continental breakup with magmatic underplating – PETROBAR-07 profile

A 5 km thick magmatic underplate was inserted under the Vestbakken Volcanic Province at 60 Ma (in the middle of the final rifting event from 65-55 Ma). The underplating event may have occurred closer to the time of breakup (55 Ma), but was moved back to 60 Ma for modelling considerations, so the effect of breakup and underplating could be measured independently. A potential magmatic underplate below the Vestbakken Volcanic Province was identified through seismic interpretation of deep crustal transects by Faleide et al.

(1991). They mapped an upper reflector at ~ 17 km depth interpreted as the top of an underplated crustal unit, and a lower reflector at ~ 22-23 km depth interpreted as the Moho. The lower crustal body may comprise of several lower crustal intrusions instead of a single 5 km thick magmatic lens. Velocity inversion models by Libak et al. (2012b) provide evidence for a heavily intruded lower continental crust below the Vestbakken Volcanic Province (see figure 4.5), rather than a massive underplate. Clark et al. (2013) did not identify a lower crustal body below the Vestbakken Volcanic Province, but the ray coverage in this area was poor, so it cannot be ruled out. Nevertheless, modelling a massive underplated body below the Vestbakken Volcanic Province is a reasonable assumption, because it provides insight into the effect that emplacement and cooling of melt at the base of the crust has on the thermal history of the overlying basin.

The density of the magmatic underplate is set to 2900 kgm^{-3} in the model. This is the same density as the oceanic crust. Unfortunately, TecMod currently does not support different input densities for oceanic crust and igneous events, so analysis of the isostatic implications of different underplate densities on our models was not carried out. Comparisons with P-T diagrams of dry MORB by Semprich et al. (2010) suggest a mafic underplate density of 3000 kgm^{-3} at approximately 20 km depth, consistent with the position of a potential magmatic underplate at 60 Ma. So, 2900 kgm^{-3} is probably a bit too light, but a reasonable estimate considering the limits imposed by the modelling software. The modelled underplate beneath the Vestbakken Volcanic Province is 90 km wide (x=152 to x=242km).

β-factor trends are only significantly different within the Vestbakken Volcanic Province when comparing between the reference (green line), breakup only (blue line), and breakup+underplate (magenta line) models (figure 5.14). Very little variation between models is observed east toward the Bjørnøya Basin. Generally, crustal thinning increases considerably toward the COB for the underplating scenario compared to the Breakup-only scenario. β-factors are considerably higher for the Carboniferous and late Permian rift phases, especially toward the COB. This is due to the extra uplift associated with underplating, which is compensated for in the model by more crustal stretching. The forward-modelling approach attributes higher stretching factors to the earliest rift phases, because it accounts for thinning of the crust and the basin. The extra stretching required to accommodate an underplate exacerbates this effect (e.g. Wangen et al., 2011). β-factors are only marginally higher for the underplate scenario during the Late Jurassic-Early Cretaceous

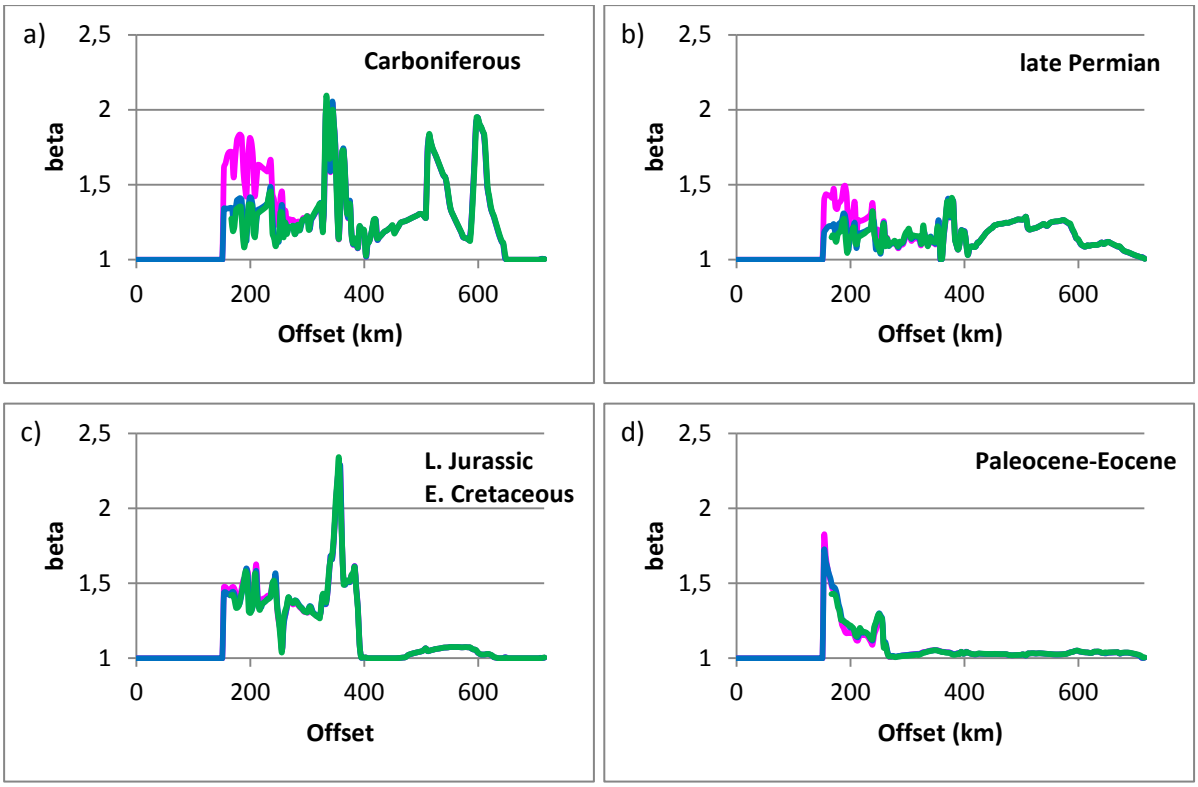

Figure 5.14. Crustal stretching factors (β) computed for four rift phases along the PETROBAR-07 extended profile, for models including no-breakup (green line – reference model), breakup-only (blue line), and breakup together with magmatic underplating below the Vestbakken Volcanic Province (magenta line). (a) Carboniferous rift phase, (b) late Permian rift phase (c) Late Jurassic-Early Cretaceous rift phase, (d) Paleocene-Eocene rift phase.

rift phase. During the Paleocene-Eocene rift phase, the breakup + underplate scenario shows slightly higher β-factors at the COB (1.81 vs 1.71).

Paleo-water depths are significantly deeper prior to underplate emplacement and breakup (magenta line) within the Vestbakken Volcanic Province (figure 5.15). Significant uplift is recorded at 60 Ma coinciding with the underplate emplacement. 1000 m uplift close to the COB (x=186km), 800 m uplift in the middle of the Vestbakken Volcanic Province (x=216km) and 600 m uplift near the eastern edge of the underplate (x=238km). Continental breakup from 55 Ma contributes to even more uplift (up to 500 m) due to the thermal and flexural response of the broken plate solution. Sub-aerial lavas are thought to occur within the Vestbakken Volcanic Province (purple line at 55 Ma in figure 5.15), but the models are unable to reproduce these shallow water depths, and remain below sea-level. It is clear, however, that the emplacement of a magmatic underplate has significant and permanent isostatic uplift effect. This is expected, due to the density contrast between the light gabbroic

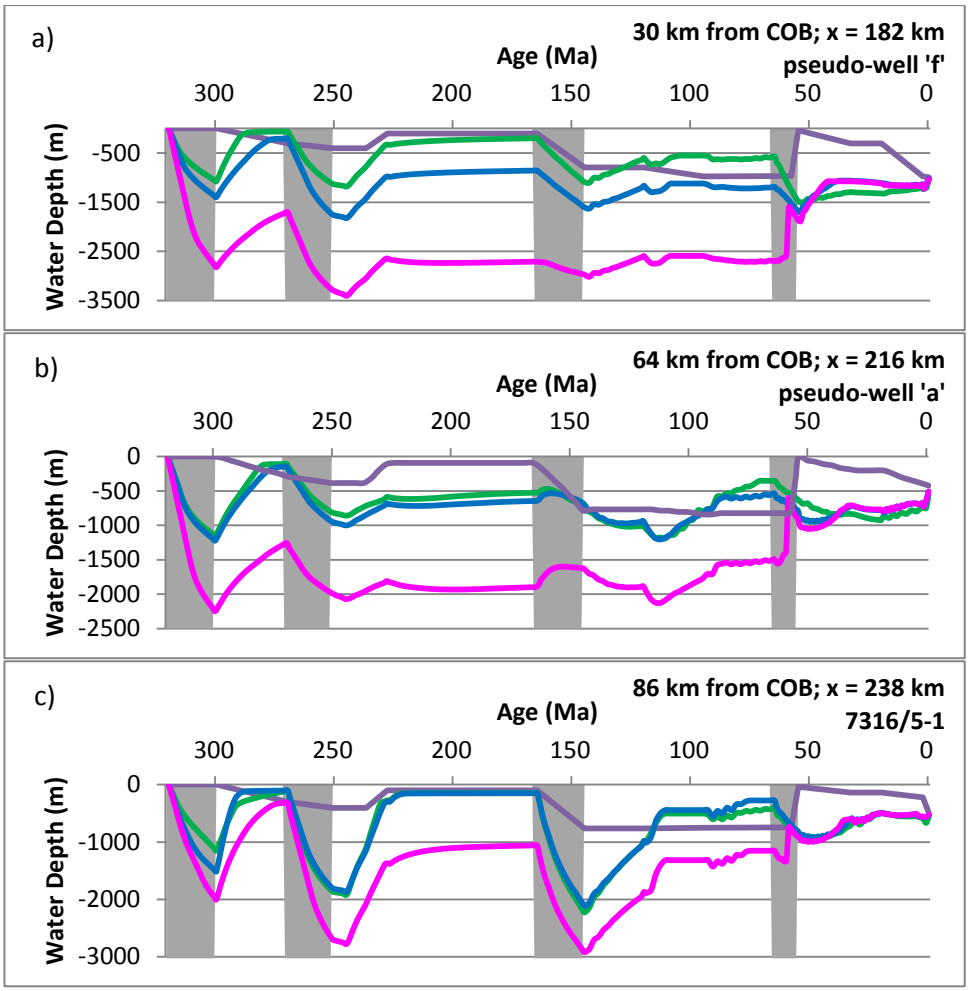

Figure 5.15. Calculated and interpreted water depths over time for three well and pseudo-well locations located in the Vestbakken Volcanic Province at different distances from the COB along the PETROBAR-07 extended profile. Green line – reference model, blue line – model incorporating breakup with a flat lower stratigraphy, magenta line – model incorporating breakup and magmatic underplating, purple line – interpreted water depths (Clark et al. 2014). Grey shaded areas represent modelled rift phases. Considerably deeper paleo-water depths calculated for the underplating scenario. Note the sharp isostatic uplift associated with underplate emplacement at 60 Ma.

underplate replacing the heavier mantle. These values are reasonable when compared to simple isostatic balance calculations. Assuming an underplate density (ρ_u) of 2900 kgm^{-3}, mantle density (ρ_m) of 3300 kgm^{-3}, water density (ρ_i) of 1000 kgm^{-3} and underplate thickness (s) of 5 km, 870 m uplift (U) can be calculated, where $U = s[(\rho_m-\rho_u)/(\rho_m-\rho_i)]$, comparable to the modelled solution.

The limit of the flexural response of the crust to the intrusion of the magmatic underplate is approximately 30 km east of its assigned right side (x =270 km). Further east, no difference is observable in paleo-water depth and subsidence trends for the reference, breakup-only, and breakup+underplate scenarios.

Within the Vestbakken Volcanic Province, basement heatflow is considerably higher during the Carboniferous rift event, and during emplacement of the underplate at 60 Ma (figure 5.16; magenta line). The high heatflow in the Carboniferous is related to the higher levels of crustal stretching modelled during this period, because following McKenzie (1978), the syn-rift heatflow increases by a factor of β following mechanical stretching and upwelling of the asthenosphere. This effect reduces with time, as the asthenospheric thermal anomaly cools, and from approximately 230 Ma the underplate scenario has less basement heat flow compared to the breakup only and reference scenarios due to less radiogenic heating from a thinned crust.

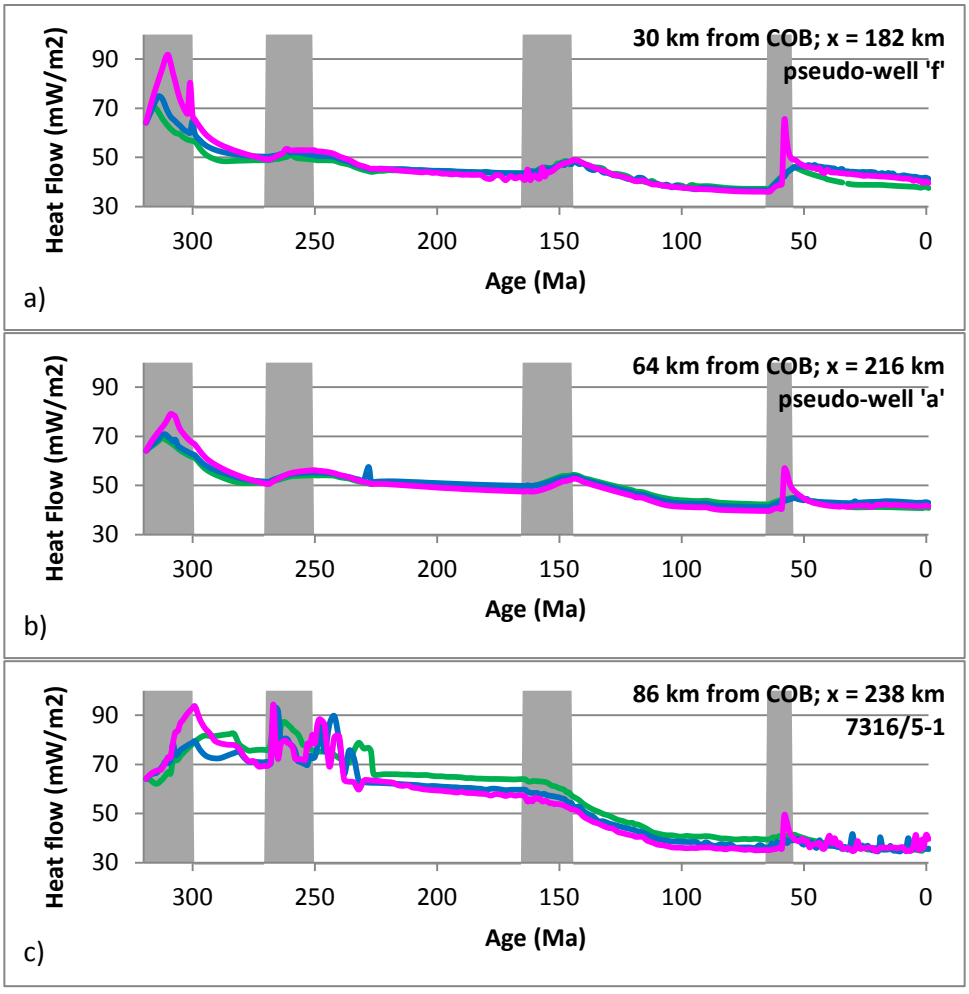

Figure 5.16. Basement heat flow data versus time for 3 well and pseudo-well locations located in the Vestbakken Volcanic Province at different distances from the COB along the PETROBAR-07 extended profile. Green line – reference model, blue line – model incorporating breakup with a flat lower stratigraphy, magenta line – model incorporating breakup and magmatic underplating. Grey shaded areas represent modelled rift phases. Note the peak in heatflow at 59 Ma associated with emplacement of the underplate. See text for details.

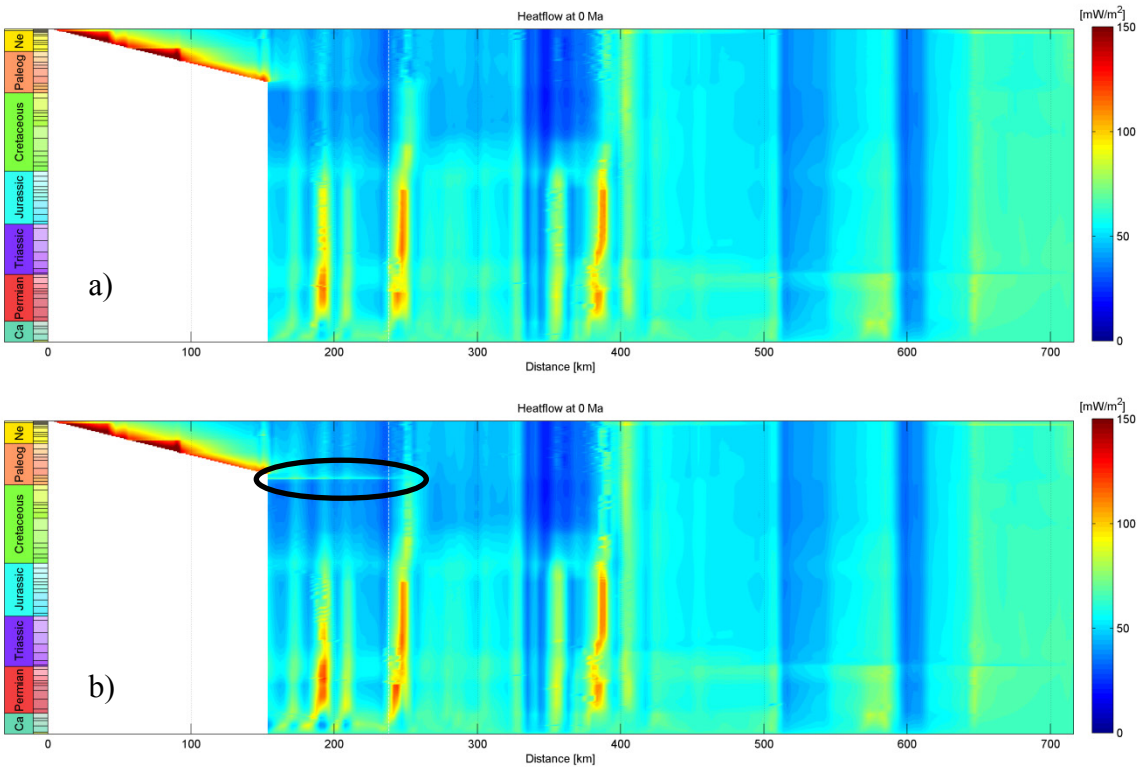

Figure 5.17. Heat flow versus time map a) Breakup-only scenario; b) Break and magmatic underplating scenario. Note the sharp increase in heat flow at 59 Ma following emplacement of the underplate, highlighted by black oval.

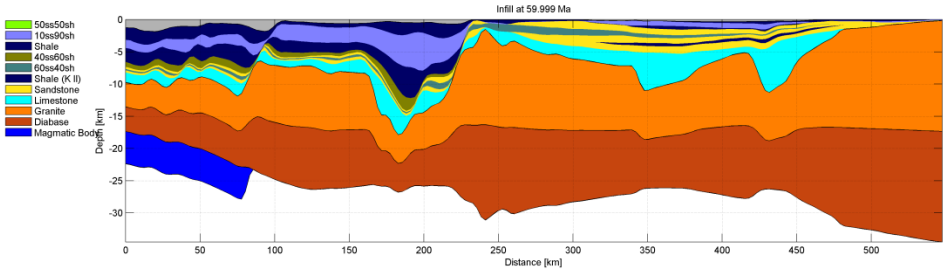

Figure 5.18. Crustal structure upon emplacement of the underplate at 59.9 Ma. Note the dip in the underplate, which encourages stronger thermal transients to the left of the model toward the COB compared to the deeper right side of the underplate toward the eastern limit of the Vestbakken Volcanic Province. This is due to elevated levels of stretching toward the COB prior to breakup. Lateral heat flow is limited to 10 km east of the right-hand side of the underplate.

A distinct peak in heatflow occurs 1 My after the emplacement of the underplate (figure 5.17), at 59 Ma, resulting in an 67% increase in heatflow within 30 km of the COB (figure 5.16a; pseudo-well ‘f’; x=182km). This effect diminishes away from the COB, averaging a 40% increase in heatflow 64km (figure 5.16b; pseudo-well ‘a’; x=216km) and 86 km (figure 5.16c; well 7316/5-1; x=238km) from the COB. This trend of lower heatflow away from the COB following underplating (but before continental breakup; 60-55 Ma) is due to the

eastward dip of the underplate (figure 5.18). The top of the underplate is shallower proximal to the COB and less exposed to heat dispersion effects, thereby delivering more heat to the overlying sediments close to the COB. Lateral heatflow from the right-side of the underplate is limited to approximately 10 km toward the Bjørnøya Basin (from x=242 to x=252 km, see figure 5.17b).

5.2.3 Continental breakup and underplating: Implications for source rock maturity

Present-day vitrinite reflectance trends versus depth show little variation between the reference, breakup, and breakup + underplating scenarios greater than 70 km from the COB (figure 5.19). Within 70 km of the COB, heat associated with opening of the North Atlantic Ocean and to a lesser extent magmatic underplating can be seen to have a minor effect on the present-day thermal maturity of sediments in the Vestbakken Volcanic Province. Adding breakup and underplating to the models does not provide enough thermal input to sediments that measured R_o values (based on 7316/5-1 well data) would suggest in the Vestbakken Volcanic Province (figure 5.19c). But sills and lava flows have been omitted from the model, and several sills were intersected in the 7316/5-1 well, so the increase in measured R_o values (figure 5.19c) may reflect local heat sources instead of heat from breakup and/or underplating

Despite the present-day maturity only showing minor variation, the thermal history of the sediments is distinctly different depending on the modelled scenario. This is highlighted by comparisons of computed vitrinite reflectance versus time plots (figure 5.20) for the PETROBAR-07 reference model, the breakup-only model, and the breakup + underplating model. These plots are derived from 50 km, 64 km, and 86 km east of the COB.

Late Jurassic (147 Ma) and potential Aptian/Albian (113 Ma) source rocks are utilized to investigate the effect of continental breakup and magmatic underplating on the thermal maturity of sediments in the Vestbakken Volcanic Province.

Late Jurassic source rocks (figure 5.20 a,b,c) incorporating breakup-only (blue line) shows similar R_o trends from 320-55 Ma. Close to the COB (fig 5.20a), a marked increase in maturity is apparent following seafloor spreading at 55 Ma. This effect diminishes away from the COB. The breakup+underplate scenario (magenta line) exhibits slower maturity

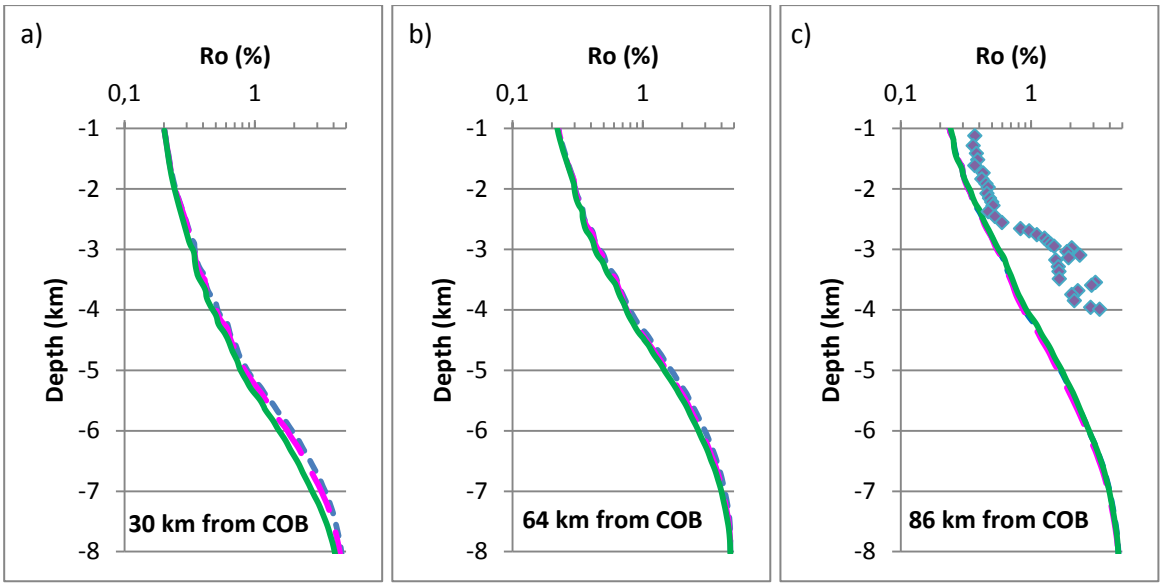

Figure 5.19. Present-day modelled vitrinite reflectance (R_o) trends along 3 pseudo-wells/wells in the Vestbakken Volcanic Province at different distances from the COB for different modelled scenarios. Green solid line – PETROBAR-07 reference model, blue short-dashed line – breakup only scenario, magenta long-dashed line – breakup + underplate scenario. Values plotted in purple in figure (c) represent R_o values measured in well 7316/5-1.The disparity between the modelled and measured Ro values in (c) may represent local heat input from sills, which were omitted from the model. Minor differences between the reference, breakup, and breakup+underplating models indicate that opening of the North Atlantic Ocean and underplating had only a minor effect on the present-day maturation history of sediments in the Vestbakken Volcanic Province.

prior to underplate intrusion and breakup, due to significantly higher amounts of crustal stretching from earlier rift phases, reducing the radiogenic heat input to the basin. Upon underplate intrusion, a sharp increase in R_o is observed, following the heat pulse associated with sudden cooling of the gabbroic melt below. All Late Jurassic source rocks in the Vestbakken Volcanic Province are overmature upon breakup.

The Aptian/Albian source rocks exhibit similar trends as the Late Jurassic source rocks, but the late Cenozoic thermal transients are much clearer. The effect of continental breakup (blue line) can be observed within 75 km of the COB (figure 5.20 d,e), but is negligible further away (figure 5.20 f). The thermal effect associated with underplating (magenta line) is less than that observed in the Late Jurassic source rocks. This is because the Aptian/Albian source rocks are located further up the sediment column, and heat dispersion is more pronounced. An interesting feature observable upon comparison of the breakup-only (blue line) versus breakup+underplate (magenta line) models is that while the underplate models show a sharp increase upon emplacement and cooling, the breakup-only models exhibit more advanced thermal maturity after approximately 30 Ma. This again is an effect related to the thinner crust within the underplate model. Once the thermal anomaly associated with the

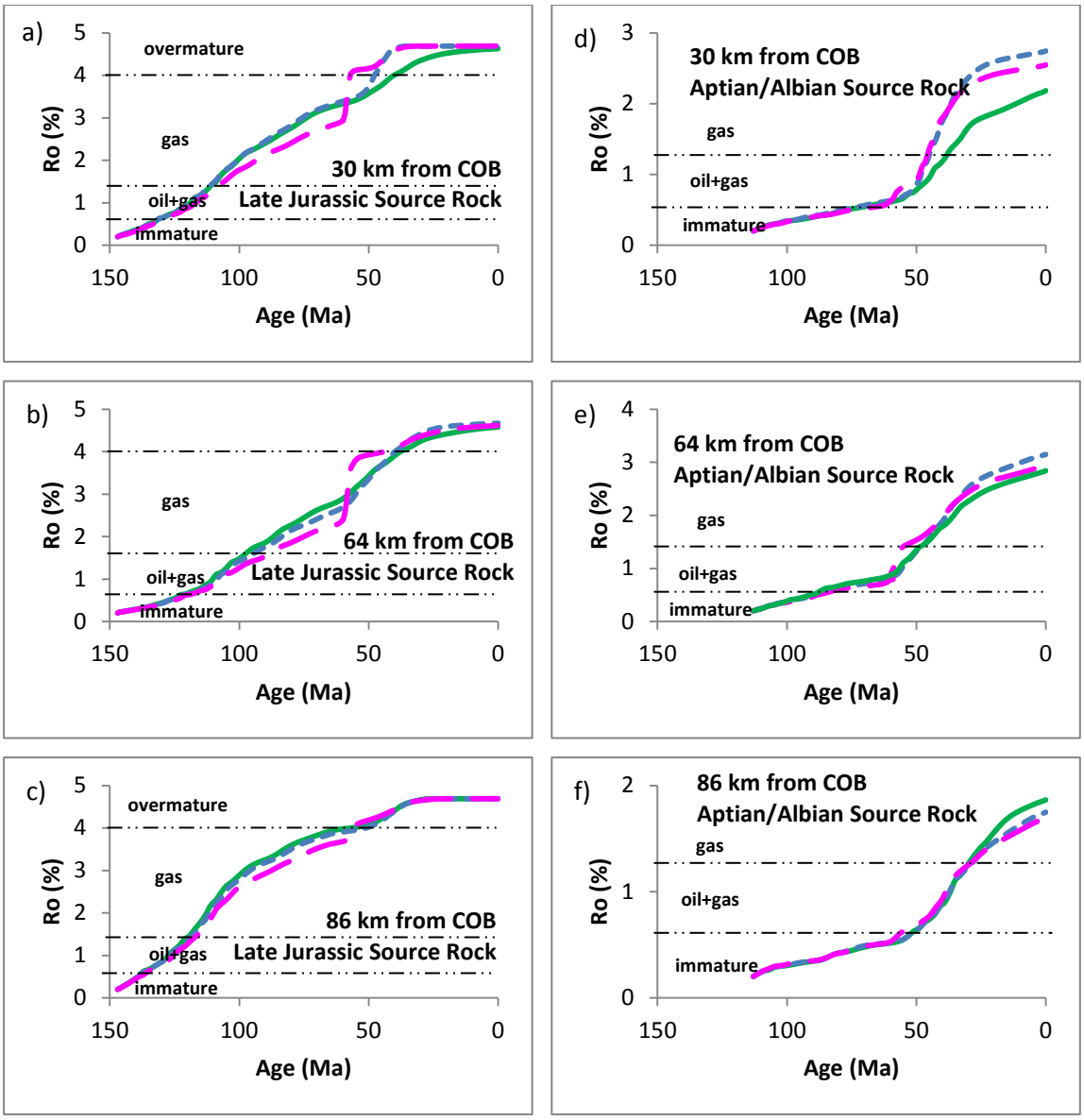

Figure 5.20. Source rock maturity (Late Jurassic and Aptian/Albian source rocks) and modelled vitrinite reflectance (R_o) for the PETROBAR-07 reference model (green line), breakup-only model (blue line) and breakup+underplate model (magenta line) along 3 wells and pseudo wells in the Vestbakken Volcanic Province. R_o maturity thresholds after Peters & Cassa (1994).

Paleocene-Eocene rift event and magmatic underplate has been removed, less radiogenic heating from the underlying thinned crust results in depressed thermal maturity for sediments modelled within the breakup + underplate scenario. Some simple forward models were also run to test whether the lower thermal conductivity of the underplate (2 W/m/K) was inhibiting heat conduction from the mantle (3.5 W/m/K) relative to the breakup-only and reference models, but these effects were minimal.

5.2.4 Continental breakup with sill intrusions – PETROBAR-07 profile

Based on gravity and magnetic modelling, Clark et al. (2013) interpreted an average 2 km thick sill within the middle sedimentary succession of the Vestbakken Volcanic Province. This body represents the main Eocene volcanic centre in the area. The thermal and isostatic implications of such an interpretation are tested here in TecMod. A series of sills together with an extrusive volcanic flow are inserted at different depths during the Paleocene-Eocene rift phase (table 5.2) and modelled together with continental breakup (no underplate). The sills and volcanic flow were assigned a density of 2900 kgm^{-3}, temperature of 1200ºC, and span 90 km within the Vestbakken Volcanic Province (x=152 to x=242km). They were emplaced at different time levels, before breakup, because emplacing them all simulataneously or emplacing them at 55 Ma together with breakup caused some modelling errors.

Table 5.2. Sill and extrusive flow inputs for the breakup with sill intrusion modelled scenario. See text for details.

Igneous event	Intrusion time (Ma)	Intrusion Level (Ma)	Average Sill Depth at 0 Ma (m)	Modelled thickness (m)
Sill	62	251	10000	220
Sill	61	228	9000	270
Sill	59	120	6500	220
Volcanic flow	56	-	4000	0-100

An interesting feature is that while 500 m thicknesses were defined for each sill in the TecMod forward input, TecMod restricts the thickness of each sill to achieve a good fit with the surrounding sediments. The depth of each sill varies according to the subsequent near-margin uplift associated with breakup and variable Cenozoic subsidence, but the average depth and thickness of the modelled sills at present-day is summarized in table 5.2.

Modelled paleo-water depths provide evidence of more subsidence (approx. 100 m) during the Paleocene-Eocene rift event when the sills and volcanic flow were emplaced (red line; figure 5.21) compared to the breakup-only model (blue line). To compensate for this extra subsidence, the inversion engine forces 100-200 m shallower paleo-water depths prior to the final rift event between 320-65 Ma. After breakup, the paleo-water depth trends are the same. Essentially, the higher density of the sills compared to the surrounding sediments enhance subsidence following the Paleocene-Eocene rift event.

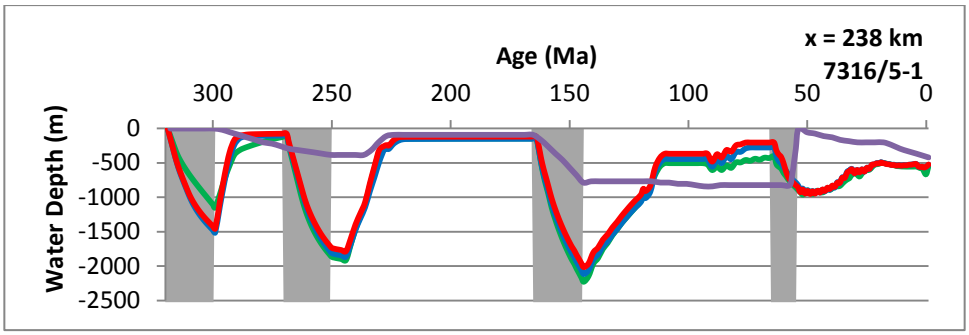

Figure 5.21. Calculated and interpreted water depths over time at well location 7316/5-1 located in the Vestbakken Volcanic Province along the PETROBAR-07 extended profile. Green line – reference model, blue line – model incorporating breakup, red line – model incorporating breakup with intrusion of sills and volcanic flows, purple line – interpreted water depths (Clark et al. 2014). Grey shaded areas represent modelled rift phases. Shallower water depths are modelled prior to sill intrusion and volcanic flows (red line) due to enhanced subsidence following cooling of gabbroic molten rock between 62-56 Ma.

β-factor trends are almost identical, but within the Vestbakken Volcanic Province cumulative β-factors are 3% less than the breakup only model (Appendix A). Again, the enhanced subsidence caused by the emplacement of heavier gabbroic sills requires less stretching-induced subsidence.

An average reduction of 10 mW/m^2 in basement heatflow is observed upon sill intrusion (figure 5.22). This may not be intuitive at first glance, considering the observed peak in heatflow coinciding with the modelled underplating scenario. However, the observed decrease in heatflow is related to the position of the sills relative to the basement. The sills are above the basement (in the sedimentary infill) and therefore project a negative flow of heat down to the basement (heat flow, q, is always positive upward towards the surface of the earth). An underplate, on the other hand, is below the basement, projecting a positive flow of heat upward toward basement. Therefore, sill intrusion has an immediate negative effect on the basement heat flow, but a positive effect on the surface heat flow. Following cooling of the sills and continental breakup, heat flow is consistently 1-2 mW/m^2 higher compared to the breakup-only scenario, due to the high thermal conductivity of the sills (2 W/m/K) compared to the surrounding sediment basin infill (1-1.5 W/m/K).

Sills have a significant effect on the thermal maturity of sediments adjacent to the intrusion. However, with increasing distance from the sill, the thermal effect diminishes. As can be seen in figure 5.23, thermal alteration of the sediments associated with heating from a sill intrusion spans over a distance equal or less than the thickness of the sill. Further than 1 sill thickness away from the intrusion, no thermal effect on sediment maturity is recorded. The

sills therefore only have a local effect the thermal maturity of the sediment basin infill. This is consistent with published 1-D modelling results (Wangen, 2010). However, it is not consistent with comments made in the Norsk Hydro Final Geochemical Report for well 7316/5-1, where the geologist recording the R_o measurement notes a thermal alteration aureole of 7:1, where 1 is the sill thickness and 7 is the number of equivalent sill thicknesses suffering alteration. They do note, however, that contamination from a high percentage of cavings in the drilled cuttings samples provides little confidence in such an estimate.

The modelled volcanic flow (less than 50 m thickness), has limited thermal effect on the surrounding sediments at the well location 7316/5-1 (figure 5.23; red line, 3.7 km depth). Only a very minor increase in R_o is modelled at 3739 m. Where the volcanic flow is modelled thicker, it has a more profound thermal effect on the adjacent sediments.

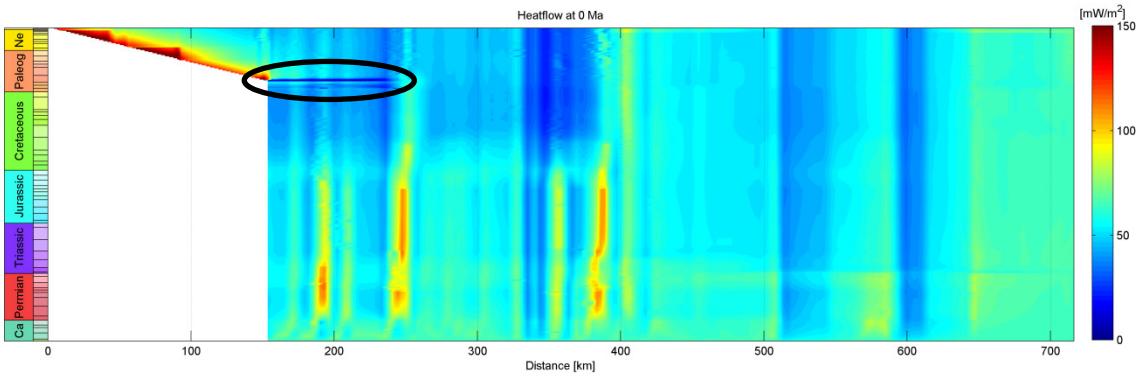

Figure 5.22. Basement heat flow versus time map for a breakup scenario with the intrusion of sills and volcanic flows from 62-56 Ma. Note the immediate negative effect sill intrusion and volcanic activity has on the heat flow at the basement, as heat from the igneous bodies are projected both upwards and downward upon cooling (highlighted with black oval). Once the sills are cooled and continental breakup is underway (after 55 Ma), heat flow increases and is elevated with respect to a model incorporating breakup-only (see figure 5.19a) due to the higher thermal conductivities of the sills compared to the surrounding sediments.

The model is unable to replicate the measured vitrinite reflectance trends from the 7316/5-1 well data (purple points; figure 5.23). But the modelled volcanic flow is located at 3850 m depth, whilst numerous sills from 5-44 m thick were intersected from 2953-3991 m depth in well 7316/5-1. This shows the number and thickness of sills and volcanic flows within the Vestbakken Volcanic Province is far more complex than modelled. However, it should be noted that the spread of elevated R_o measurements made on drilled cuttings from well 7316/5-1 may not be entirely representative of the in-situ thermal maturity of the sediment column due to poor sample integrity.

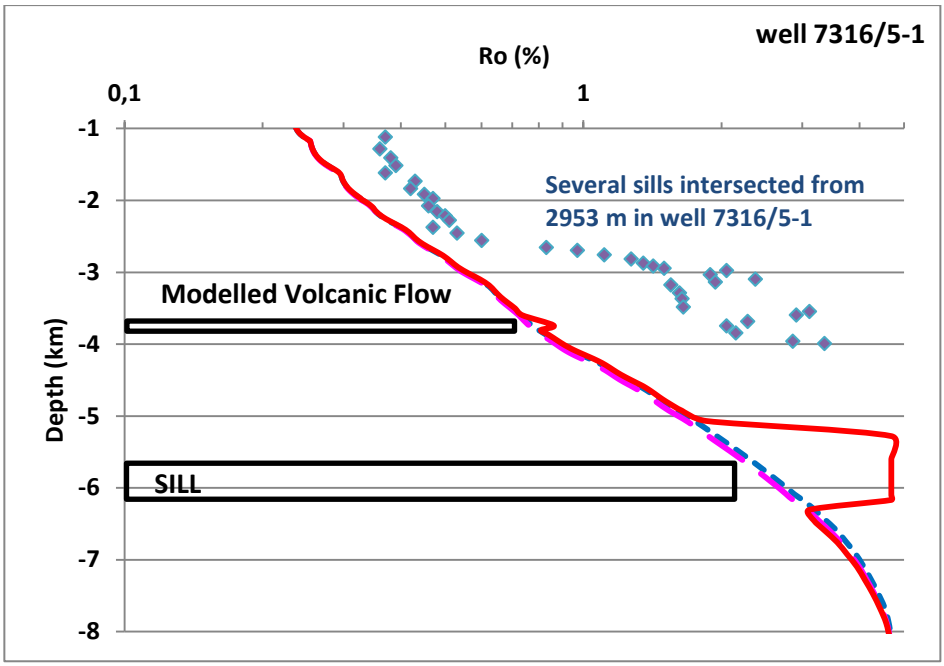

Figure 5.23. Vitrinite reflectance (R_o) data from the 7316/5-1 well (plotted in purple) in the Vestbakken Volcanic Province along the PETROBAR-07 profile for models including breakup-only (blue, short dashed line), breakup with underplating (magenta, long-dashed line), and breakup with sill intrusions and volcanic flows (red solid line) from 62-56 Ma. Values plotted in purple represent R_o measurements on samples from well 7316/5-1 and show marked disparity with modelled R_o trends. For well location, see fig 4.6. See text for discussion.

5.2.5 Gravity analysis: Continental breakup, underplating, and sill intrusion

Calculated gravity profiles extracted from TecMod for each model incorporating continental breakup, magmatic underplating, and sill intrusions are compared to the PETROBAR-07 reference model and the observed free-air gravity profile (Kenyon et al., 2008) and Bouger-corrected profile (Olesen et al., 2011) in figure 5.24.

All models show similar free-air and Bouger-corrected trends east of the Vestbakken Volcanic Province. Within the Vestbakken Volcanic Province, more variation is observed, owing to different thermal and isostatic histories inherent in the modelled scenarios. But these differences are only of a minor nature. The reference model (green line) shows slightly more variation along the profile than the models incorporating breakup (blue line). This is considered (1) an artefact of the resolution of the finite-element grid in TecMod and (2) different reference columns on the left-side of the grid. Both the breakup and reference models have 200 horizontal grid squares. However, the breakup-models are 166 km longer

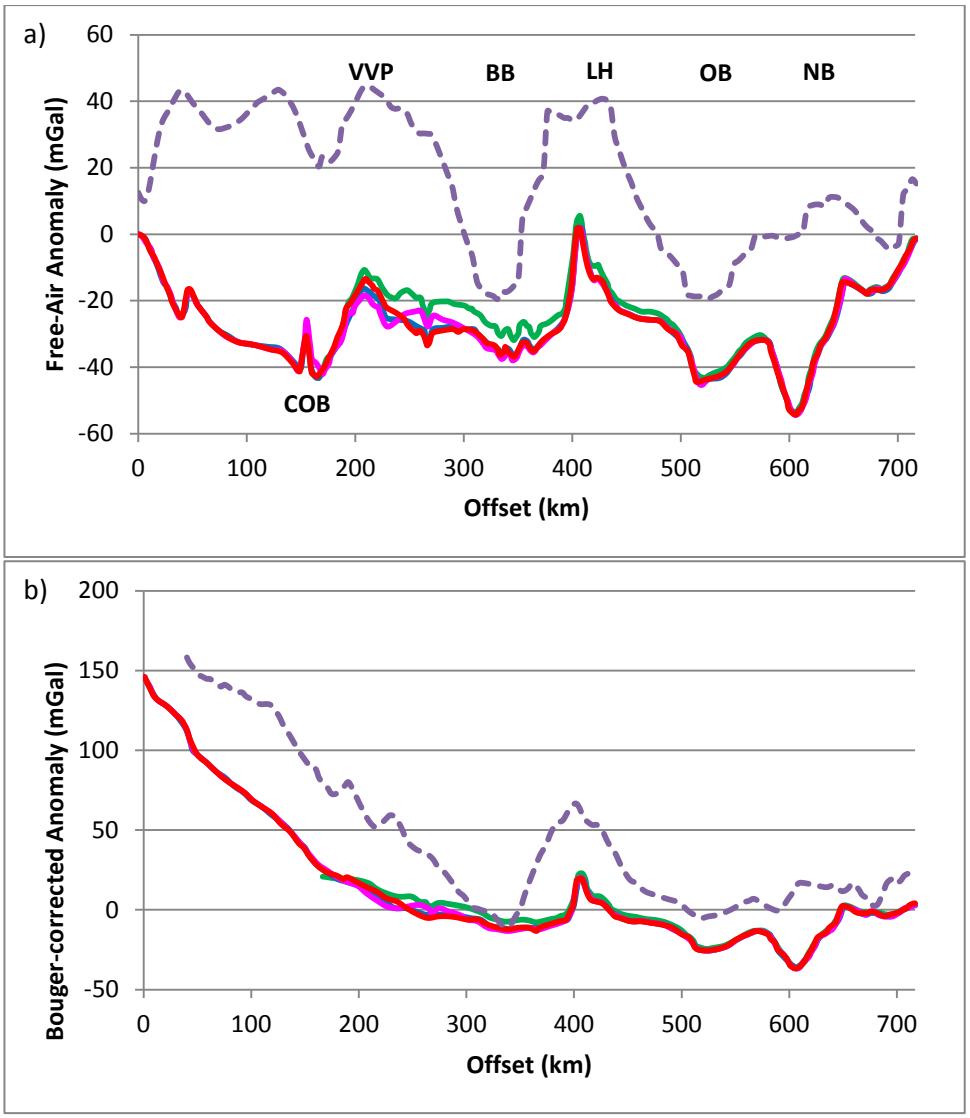

Figure 5.24. Gravity extracted from the density distribution of PETROBAR-07 extended models incorporating breakup (blue line), breakup+underplate (magenta line), and breakup+sill intrusion (red line) compared to the PETROBAR-07 reference model (green line) and the observed free-air anomaly data (purple dashed line). a) Free-air corrected (Kenyon et al., 2008), b) Bouger-corrected with 2200 kgm^{-3} water-sediment replacement (Olesen et al., 2011); c) Crustal section of the breakup-only model illustrating the oceanic crust, COB, basins, and basement highs for reference. VVP – Vestbakken Volcanic Province, BB, Bjørnøya Basin, LH – Loppa High, OB – Ottar Basin, NB – Nordkapp Basin, COB – Continent-Ocean boundary at x =152 km.

than the reference model, so the grid resolution is coarser for breakup-models, and the same degree of density variation may not have been captured. Within the TecMod gravity calculation, the reference-model has its assumed reference column 16 km east of the COB, while breakup models have a reference column at the spreading ridge. The reference-model has been shifted downwards by -43.3 mGal to fit with the right-side of the breakup models.

Within the Vestbakken Volcanic Province, the breakup+underplate scenario (magenta line) is slightly elevated relative to the breakup-only model (blue line) east of the edge of the underplate (x= 242-300 km). Above the underplate (x= 152-242 km), the gravity signature is comparatively lower for the underplate scenario. This is because the underplate is lighter (2900 kgm^{-3}) than the surrounding peridotite mantle (3340 kgm^{-3}). The gravity from the sill models (red line) exhibits an elevated trend over the Vestbakken Volcanic Province compared to the breakup-only scenario (blue line), due to the higher density of the sills relative to the surrounding sediments.

5.2.6 Serpentinization – PETROBAR-07 profile

Published accounts of interpreted mantle serpentinization beneath the deep basins (e.g. Bjørnøya Basin) of the western Barents Sea are found within a study of North Atlantic Cretaceous Basins by Lundin & Doré (2011). They identified a number of high-velocity crustal bodies beneath Cretaceous basins around the North Atlantic rim, often with coinciding sedimentary seaward-dipping reflectors (figure 5.25). They proposed that elevated levels of extension (hyperextension) during the Jurassic-Cretaceous rift-phase results in a situation where the crust has been sufficiently thinned to cause coupling between the lower and upper crust. This coupling permits brittle faults to penetrate the entire crust and, thereby, hydrate the upper mantle (Rüpke et al., 2013). Hydration of the mantle spurred serpentinization of dunite at and below the Moho. The new workflow created by Rüpke et al. (2013), and integrated into TecMod by the same workers, provides an excellent opportunity to test the hypothesis of Lundin & Doré (2011).

The serpentinization algorithm was run for all scenarios. A wet quartzite rheology was chosen for the sediments and upper crust, clinopyroxene/plagioclase aggregate rheology for the lower crust, and dry olivine rheology for the mantle. Modelled sub-Moho temperatures

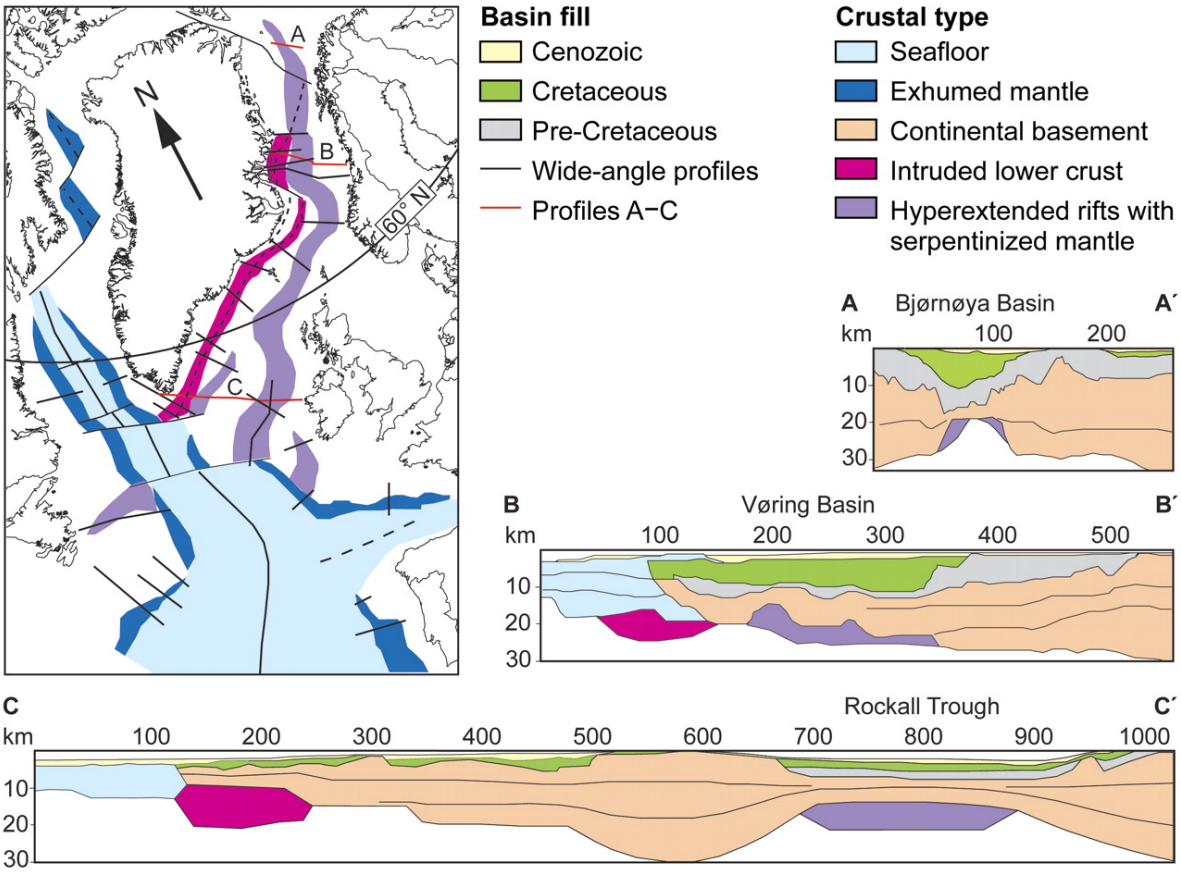

Figure 5.25. Early Eocene plate reconstruction (ca. 53 Ma) revealing interpreted chain of hyperextended Early Cretaceous rift basins, oblique line of northeast Atlantic breakup and associated underplated areas. Note the mauve coloured serpentinized lower crustal bodies preserved under the flanks of the Bjørnøya Basin (after Lundin & Doré, 2011).

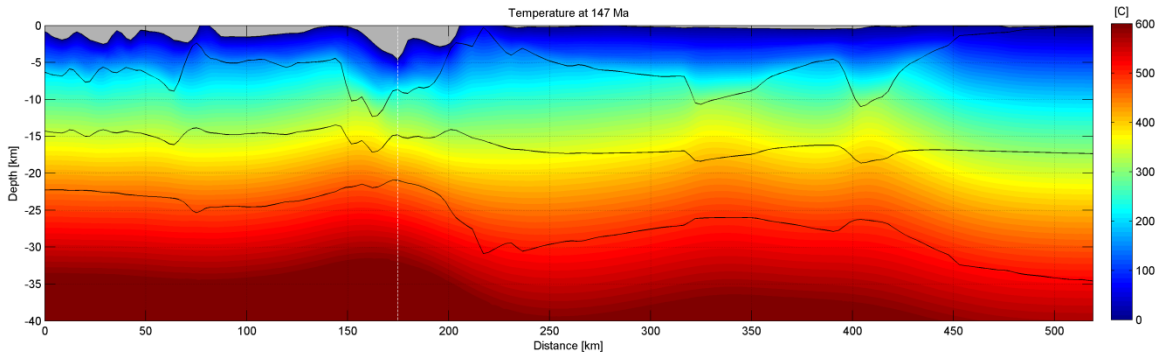

Figure 5.26. Temperature field at 147 Ma for the breakup-only scenario, during the end of the Late Jurassic rift phase. Contours highlight the seabed, basement, upper-lower crust transition, and the moho (top to bottom). Sub-moho temperatures are at 450 °C below the position of most intense stretching during the Late Jurassic (x = 175 km, marked by while dotted line), below the thermal stability limit for the fosterite → serpentine. So, the temperatures were low enough for serpentinization to occur if hydrous fluids are able to penetrate the crust.

are low enough to permit serpentinization reactions during the Late Jurassic-Early Cretaceous rift phase (figure 5.26). But, the entire crust does not couple in the way described by Lundin & Doré (2011), preventing brittle faults to penetrate the entire crust (figure 5.27) and, thereby, hydrate the upper mantle. Serpentinization tests were also carried out on the Loppa High profile, with similar results under the deep Tromsø Basin. Serpentinization cannot be resolved within any of the models.

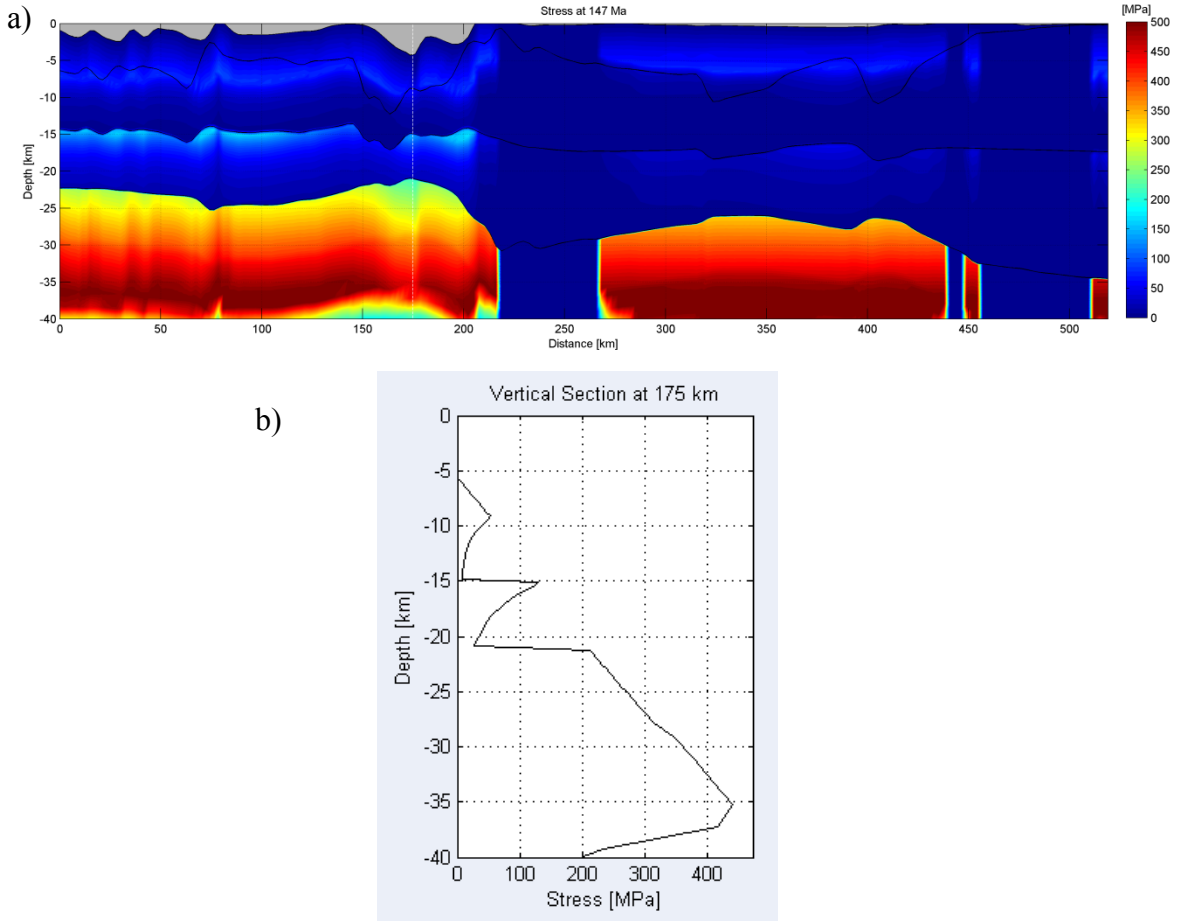

Figure 5.27. a) Differential stress field at 147 Ma for the breakup-only scenario. The sediments and upper crust were assigned a wet quartzite rheology, the lower crust and aggregate rheology, and the mantle a dry olivine rheology. b) Differential stress profile at x = 175 km. Note loss of strength corresponding with viscous flow observed at the sediment-crust interface (basement, 9 km depth) and the upper-lower crust interface (15 km depth). Viscous flow in the lower crust inhibits hydration of the mantle and serpentinization.

6. Discussion

6.1 Breakup and magmatic underplating

The thermal and isostatic implications of continental breakup and magmatic underplating below the Vestbakken Volcanic Province require further analysis. It has already been noted that continental breakup causes an elevated level of thermal maturity in sediments (from R_o calculations) approximately 70 km away from the COB. In contrast, the heat from emplacement of a magmatic underplate is offset by higher levels of crustal stretching required in rift phases prior to 60 Ma, such that present-day thermal maturity of sediments for a scenario with underplating and without underplating is almost the same. This indicates that the temperature maximum (T_{max}) experienced by sediments in the Vestbakken Volcanic Province was caused by heat from continental breakup and Cenozoic burial, and the thermal impact of magmatic underplating is not preserved until present. Further modelling shows that increasing the thermal conductivities of sediments within the Vestbakken Volcanic Province does not modify this conclusion.

The PETROBAR-07 models produced within this study have thick, low-conductivity shales between 4-8 km depth in the Vestbakken Volcanic Province (figure 6.1a). The thermal conductivities of the shales are k = 1.5 W/m/K at reference temperature, but the effective conductivity decreases to 1 W/m/K at 6 km depth due the temperature-dependency of matrix and pore-fluid conductivities. Sensitivity tests on the TecMod PETROBAR-07 extended model were undertaken by increasing the thermal conductivity of the shale and 10%SS-90%SH units to 2.1 W/m/K (then corrected for temperature effects on the pore fluid and matrix). The temperature corrections on the effective thermal conductivity (k) of the shale represent a reduction from k = 2.1 W/m/K at reference temperature to k = 1.33 W/m/K at 8 km depth (figure 6.1b). This temperature dependency of the effective conductivity of sediments, constrained through the input grain and pore-fluid conductivities therefore have a significant effect on thermal maturity modelling.

The TecMod sensitivity test with higher input thermal conductivity of shales (figure 6.1b) resulted in lower present-day maturity than the breakup-underplate model. This is illustrated with a graph of the R_o modelled through time for a Jurassic source rock 30 km east of the COB (figure 6.2a). Increasing the thermal conductivity (red line) results in a decrease in the

temperature gradient through the sediments and thereby reducing the maturity profile. This is because higher thermal conductivies result in lower basin temperatures due to reduced blanketing effects (figure 6.2b; Theissen & Rüpke, 2010). Higher heat conduction through the shales does not have a significant impact on the amount of heat conducted up to the Jurassic source rock. A similar 1% increase in R_o values following cooling of the underplate is observed, compared to the scenario with shale k = 1.5 W/m/K. Despite the increased heat conduction in the shales, the thermal effect related to underplating still does not represent the

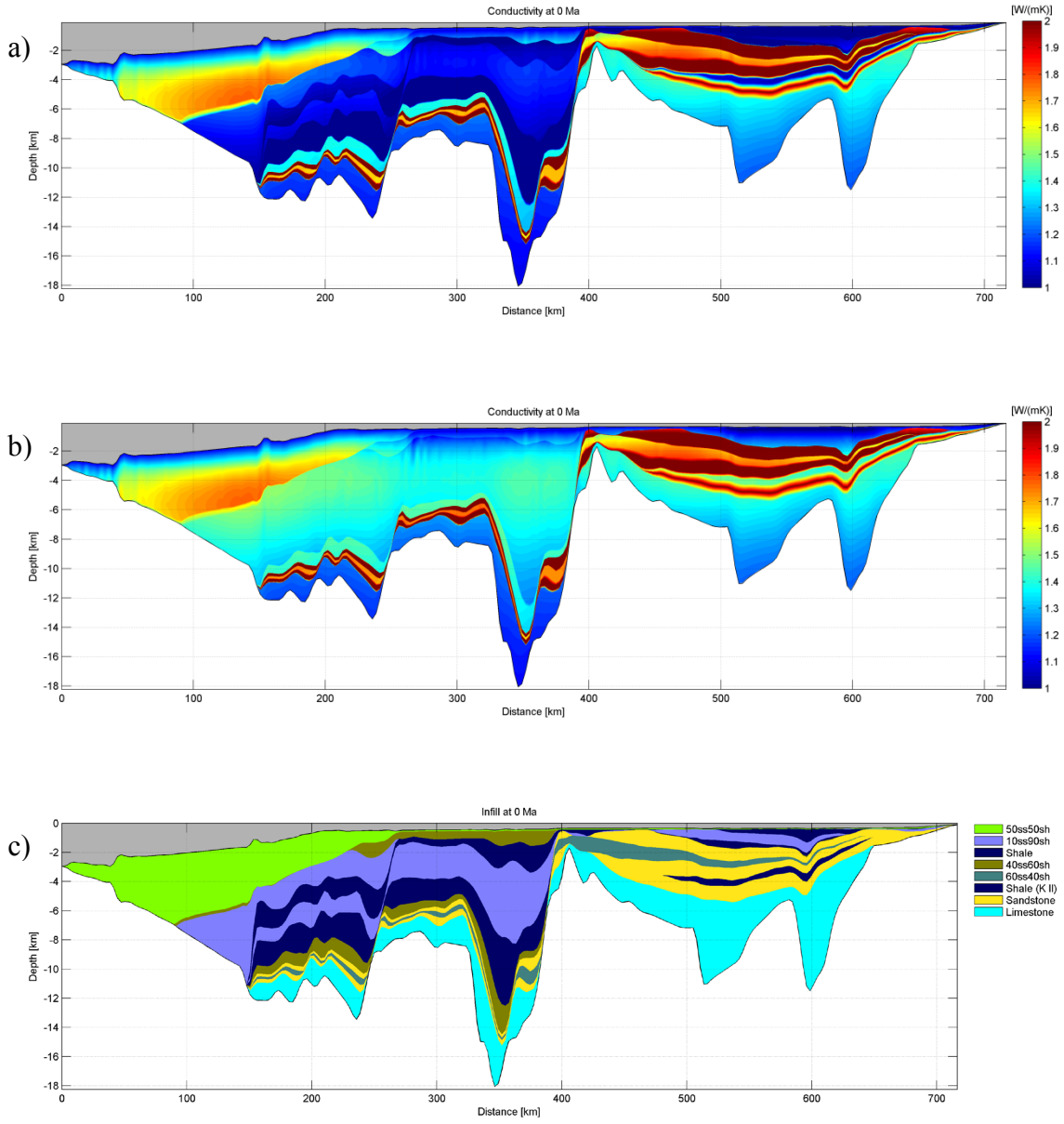

Figure 6.1. Modelled thermal conductivities for the breakup+underplate model with shales and silty shales (10% SS : 90% SH) (a) k = 1.5 W/m/K at reference temperature (default model) and (b)) k = 2.1 W/m/K at reference temperature in a sensitivity test. The geology of the sedimentary infill is provided in (c).

T_{max} experienced by the overlying sediments, and the present-day R_o trends remain unchanged. Underlying Permian-Carboniferous limestones at 11-12 km depth have very low effective conductivities of 1.2 W/m/K which remain a barrier to heat flow from the basement (see figures 6.1a + b).

Increasing the underplate thickness within the TecMod models also results in an increase in the heat pulse from the underplate on the overlying sediments, but since the seismic data constraint indicates an underplate of 5-6 km is most likely (e.g. Faleide et al., 1991), then such a proposition is largely irrelevant for this study.

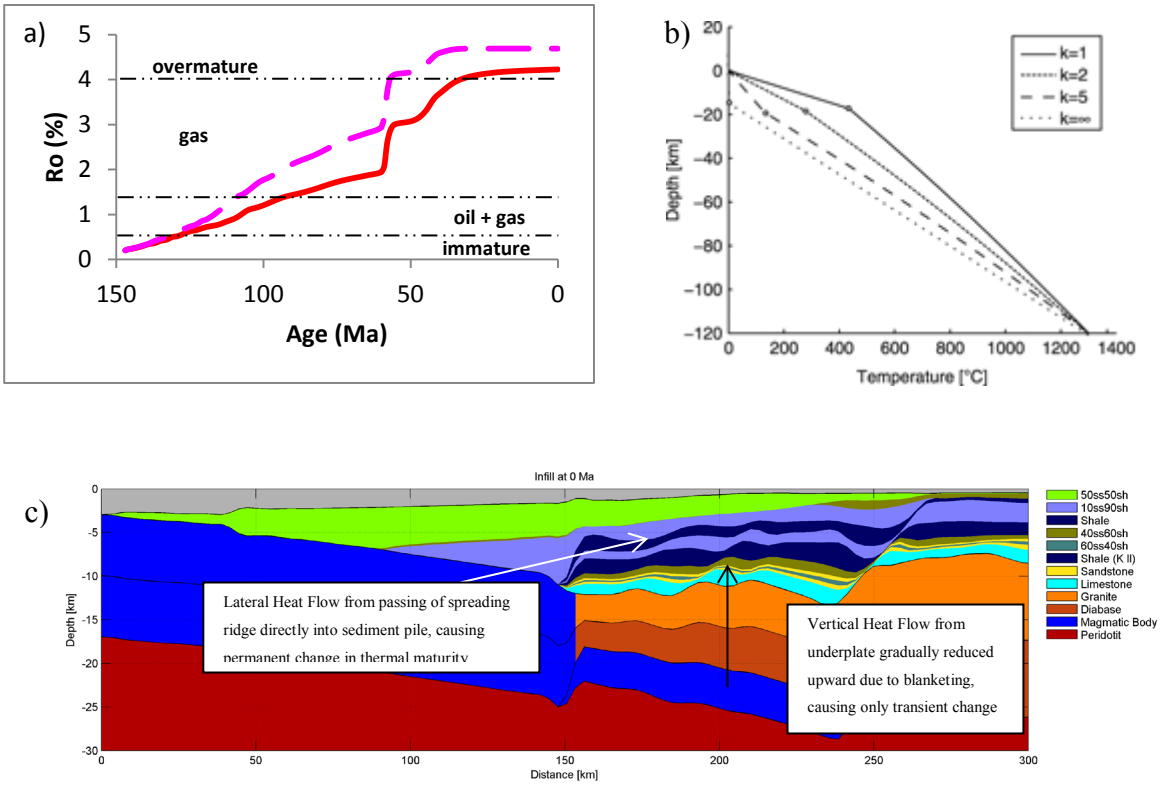

Figure 6.2. a) Thermal history of a Jurassic source rock in the Vestbakken Volcanic Province along pseudo-well 'a', 30 km from the COB for models incorporating breakup and underplating. Pink dashed line – model with shales and silty shales k =1.5 W/m/K; red solid line – model with shales and silty shales k= 2.1 W/m/K. Both scenarios show a 1% increase in R_o following the emplacement and cooling of an underplate at 60 Ma. Increasing the thermal conductivity of shales decreases the overall thermal maturity of sediments in the basin. b) Effect of increasing grain thermal conductivity of sediments with on a 1-D model with constant temperature boundary condition (as per TecMod). Circles mark the sediment-basement interface. The lower the sediment conductivity, the higher the thermal gradient in the sediments, and the lower the basement heat flow. This depression in basement heat flow is one effect of sediment blanketing and results directly from the fixed temperature boundary conditions at the top and bottom of the lithosphere. (after Theissen & Rüpke, 2010). c) Crustal structure along PETROBAR-07 extended profile illustrating the effective lateral heat flow from the passing of the spreading ridge away from the COB, and the dissipated vertical heatflow from the underplate which is blanketed by low conductivity shales and limestones from 6-10 km depth.

The models assume the underplate is a massive body at the base of the crust. If, instead, the lower crustal body below the Vestbakken Volcanic Province is heavily intruded lower continental crust, as interpreted by Libak et al. (2013), then the isostatic response to the magmatic event will be different, because the gabbroic sills should have similar densities to the surrounding crust. But volume will still need to be created in the lower crust for the sills to intrude through higher β-factors. Also, heat flow up to the overlying sediment column associated with cooling of a sill swarm in the lower crust should be similar to the cooling of a massive underplate, so the assumption of a massive underplate implicit in the models here can be applied to more complex scenarios.

Essentially, the reason why the modelled present-day thermal maturity of sediments in the Vestbakken Volcanic Province remains unchanged by magmatic underplating is because higher levels of crustal stretching in earlier rift phases, and low effective thermal conductivities of thick, deeply buried Jurassic and Cretaceous shale sequences and Permian-Carboniferous carbonates. The higher levels of stretching prior to underplating reduce the radiogenic heat budget from the crust, resulting in slower maturity during the Cenozoic compared to scenarios neglecting underplating. Meanwhile, the deeply-buried shales and limestones depress basement heat flow and thereby thermal conduction of the heat pulse from cooling of a magmatic underplate. Increasing the input thermal conductivity of the shales by 70% (from 1.5-2.1 W/m/K) in a sensitivity test does not result in a significant change in the thermal effect from the underplate, but does reduce the temperature gradient through the sediments due to less blanketing. Conversely, continental breakup provides a lateral heat flow from the spreading ridge (represented by the COB) directly into the adjacent sedments without heat dispersion through the continental crust and lowermost sediments within the Vestbakken Volcanic Province and is therefore measurable in the present-day thermal model through R_o trends (figure 6.2c).

Other basin modelling studies of magmatic underplating along the Vøring Basin in the Norwegian Sea do indeed record a permanent increase in the thermal maturity of sediments following underplating (ignoring breakup). Wangen et al. (2011b) performed forward modelling (without an inverse-scheme like TecMod) on a transect through the Vøring Basin and calculated the effect of magmatic underplating on the thermal maturity of sediments above. A permanent thermal effect on the overlying sediments was recorded. They employ a thicker underplate (7 km), assume constant sediment conductivities (2 W/m/K), and ignore the temperature-dependency of grain and pore-fluid conductivity compared with this study.

Along the same transect in a complementary study, Wangen et al. (2011a) agreed with the results published in this study with regards to stretching factors. Elevated stretching factors are required in the rift phases prior to underplating to facilitate the sudden uplift and Cenozoic subsidence and achieve a reasonable fit between the modelled and input stratigraphy.

Fjeldskaar et al. (2003) and Fjeldskaar et al. (2009) also reported on a series of backstripping models along profiles in the Vøring Basin, applying thermal conductivities to sediments according to an in-house database. They modelled a permanent thermal effect on sediments overlying a magmatic underplate. However, the backstripping approach ignores thinning of the sediments, and thereby underestimates sedimentation rates and blanketing effects (e.g. Theissen & Rüpke, 2010). Interestingly, they applied different thermal conductivity inputs for sediments with "low porosity" (φ=0.13) and "high porosity" (φ=0.5). In their study, a shale, for example, was assigned a thermal conductivity of 2.1 W/m/K in a low porosity environment (deep buried sediments), and 1.2 W/m/K in a high porosity environment (shallow sediments). Fjeldskaar et al. (2009) then corrected these thermal conductivity inputs according to the temperature profile, based on a correction factor (α), a somewhat different approach than the calculation of an effective conductivity from the geometric mean of the grain and matrix conductivities in TecMod.

6.2 Comparing cumulative beta factors

Cumulative β-factors from models along the PETROBAR-07 extended profile are compared with β-factors derived from observed crustal thickness (figure 6.3) along the profile from velocity inversion studies (Clark et al., 2013). The observed values are based on assumed thinning of the crust relative to an idealized 35 km original crustal thickness. The dark grey swath reflects calculated uncertainty in the velocity inversion results, and the light grey swath reflects local uncertainty of up to 5 km of high velocity sedimentary rocks included within the interpreted uppermost crystalline crust (Clark et al., 2014).

Within all the underplate models produced within this study, β-factors are calculated excluding the underplate. Within a seismic velocity inversion study (e.g. Clark et al., 2013) a magmatic underplate, or heavily intruded continental crust, may be included as part of the crust within a velocity inversion, so any elevated levels of stretching required to accommodate the underplate may not be observable. The "observed" β-factors calculated by

Clark et al. (2013) are from the top of the Moho, so any underplate would be included as a part of the crust in their calculations (S.A. Clark 2014, pers. comm. 20 Oct). Consequently, the elevated β-factors calculated for a modelled scenario incorporating breakup+underplating will be much higher than "observed" β-factors based on crustal thickness with an underplate at the base of the crust. This effect can be observed in figure 6.3, with anomalously higher modelled β-factors close to the COB for the breakup+underplate model (purple dashed line). As mentioned previously, Clark et al. (2013) did not identify an underplate below the Vestbakken Volcanic Province, but ray coverage was poor in this area, so the results are inconclusive. The value of a comparison between β-factors based on crustal thickness and β-factors based derived from forward basin modelling for the identification of an underplate is therefore dubious unless the velocity inversion can distinguish between the top of underplate (or heavily intruded continental crust) and Moho. But the comparison adds value by providing a first-pass calibration check of the β-factors derived from modelling.

As mentioned in chapter 5.2.2, the distribution of β-factors along the PETROBAR-07 profiles for different models (reference, breakup, and breakup + underplate models) is identical east of the Vestbakken Volcanic Province. Modelled cumulative β-factors east of the Vestbakken Volcanic Province mostly agree with the work of Clark et al. (2014), peaking at approximately β=4 over the deep Bjørnøya Basin (figure 6.3). In the far east of the profile, around the Nordkapp Basin, the modelled β-factors are consistent with the crustal thickness estimates. Between the Loppa High and Nordkapp Basin (around the Ottar Basin), modelled β-factors suggest a crust thinner than observed, suggesting a more complex mechanism than simple lithospheric thinning (Clark et al., 2014). Below the Ottar Basin, the lower crust shows almost no thinning (based on velocity modelling), yet up to 10 km of subsidence has been created to accommodate the overlying sediments. Depth-dependent thinning, phase changes, or thermal downwelling in the mantle have been proposed as possible explanations for this discrepancy (Clark et al., 2014). Depth-dependent thinning could occur through asymmetric extension by simple shear mechanisms (e.g. Wernicke model; figure 3.4b). This would require a detachment or series of detachments through the crust. Gernigon et al. (2014) proposed reactivation of crustal structures inherited from a Caledonian thrust within a pre-Permian extensional system across the Bjarmeland Platform (including the Ottar Basin). If these detachments facilitated further extension through the Permian, subsidence mechanisms would follow creating the necessary accommodation space for thick Permian sedimentary successions in the Ottar Basin. But the model of Gernigon &

Brönner (2012) and Gernigon et al. (2014) may also represent Devonian extension (following orogenic collapse) instead of Carboniferous rifting (J.I. Faleide, 2014, pers. comm. 28 Nov).

Within the Vestbakken Volcanic Province, β-factors derived from models incorporating the reference case, breakup, and breakup+underplating depart from each other significantly, especially toward the COB. The model accounting for breakup departs from the reference model approximately 70 km from the COB, with a maximum β of almost 4 at the COB. This implies the flexural uplift associated with passing of the spreading centre is limited to 70 km from the COB. Similar estimates have been made in studies along the Ghana transform margin (Rüpke et al., 2010). The underplate model exhibits much higher β-factors, with a maximum of over 6 at the COB. Interestingly, the lateral extent of the intruded underplate is 90 km east of the COB, while the β-factors departs from the reference and breakup-only models 120 km east of the COB. This means that the flexural (and to lesser extent, thermal) uplift associated with underplating is not only limited to the area directly above the magmatic body, but also up to 30 km east of it.

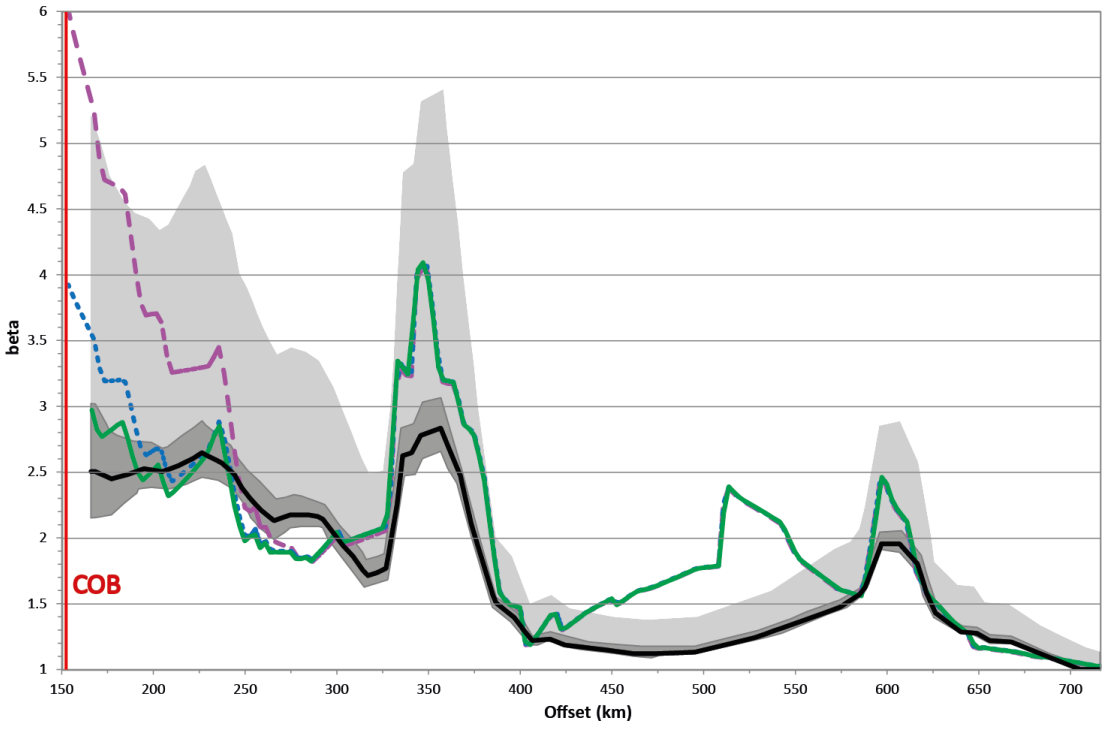

Figure 6.3. β-factors based on crustal thickness (black line) together with uncertainty in the velocity inversion results (dark grey swath), and local uncertainty of up to 5 km of high-velocity sedimentary rocks included in the uppermost crystalline crust (after Clark et al. 2013). These are overlain by modelled cumulative β-factors from PETROBAR-07 profile within this study for reference (green solid line), breakup (blue dotted line), and breakup+underplate (purple dashed line) cases in TecMod. The COB is located at x = 152 km, marked by red line.

6.3 Uplift and Erosion

The south-west Barents Sea has been subjected to significant periods of uplift and erosion since Permian time. Within the basin models produced within this study, some uplift around the Loppa High is noted during the late Permian rift phase and after the Late Jurassic-Early Cretaceous rift phase, primarily in response to rift-flank flexure. Glørstad-Clark et al. (2011a) identified a series of uplift and erosional events during the Permian and Triassic during the development of the Selis Ridge (paleo-Loppa High). They suggest that the rift-flank uplift may be the result of depth-dependent thinning. The models published here, and in Clark et al. (2014), suggest low levels of crustal stretching during the late Permian rift phase. The models show that some of the uplift can be resolved by accounting for the flexural behavior of the basement high (with a 15 km necking depth), but as previously mentioned simple-shear mechanisms may have also played a role, which are not resolved within the TecMod pure-shear model. Deep-mantle processes and far-field stresses probably contributed to the complexity of uplift patterns in this period. Indeed, in-plane stresses associated with late Permian buckling of the lithosphere in the adjacent East Barents Sea basin, as suggested by Gac et al. (2012; 2013; 2014) may have also played a part in the anomalous vertical movements in the western Barents Sea. And finally, the downwelling of hot asthenosphere associated with the impingement of the Siberian Traps mantle plume on the crust from 251-250 Ma may have contributed to sag-basin features recognized east of the Loppa high during the same period. So while some first-order features of uplift during the late Permian period can be resolved with a basin modelling approach, the complexity of the uplift features, and their longevity, require more integrated studies.

As recognized by Clark et al. (2014), inversion of the Late Triassic basin, which formed the Loppa High during the Late Jurassic-Early Cretaceous rifting event, can also be resolved, to some degree, by rift-flank uplift in the models. But the inversion was complex, and was probably influenced by compression along the northern periphery of the Loppa High (Glørstad-Clark et al., 2011a). The high β-factors during the Jurassic rift phase within the adjacent Bjørnøya and Tromsø Basins contributed significantly to the observed uplift.

Clark et al. (2014) interpreted 800 m of Paleocene-Eocene uplift, 50 km east of the COB within the Vestbakken Volcanic Province. Uplift of the Vestbakken Volcanic Province is resolved by models incorporating continental breakup and continental breakup + magmatic underplating. The flexural and thermal uplift associated with continental breakup and the

passing of the spreading ridge is up to 500 m, tapering away from the COB. The uplift associated with emplacement of a 5 km magmatic underplate (2900 kgm^{-3}) density below the lowermost crust in the Vestbakken Volcanic Province at 60 Ma results in up to 1000 m uplift (pseudo-well 'a'; dashed magenta line in figure 6.4). The isostatic/flexural uplift is the dominant contributor to total uplift. Following Allen & Allen (2013), the underplate and crust are assigned a volumetric coefficient of thermal expansion $\alpha = 2.4 \times 10^{-5}$ K^{-1} and the excess temperature of the underplate is 750°C compared to the surrounding temperature, so the surface uplift due to thermal effects is 0.018 times the underplate thickness, that is 90 m for a 5 km thick underplate. The results from a model incorporating continental breakup together with underplating are comparable to uplift estimates by Clark et al. (2014).

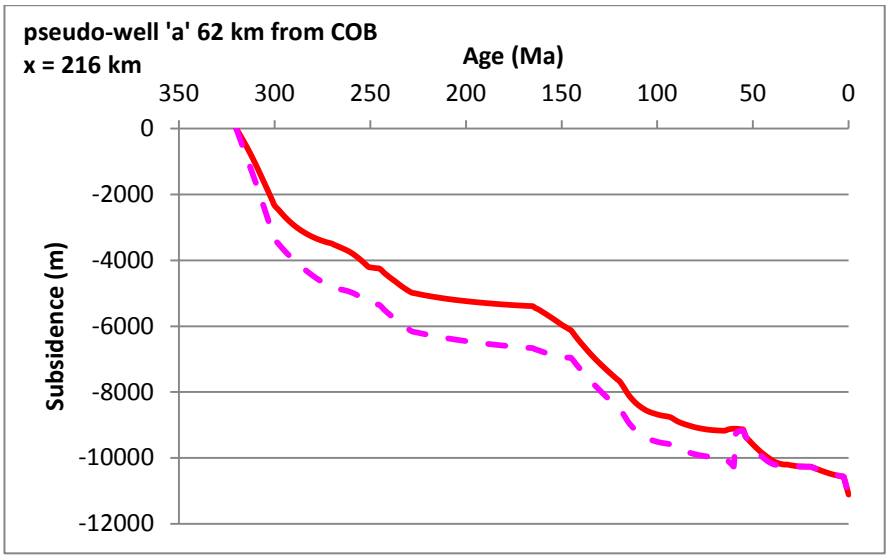

Figure 6.4. Subsidence curves at pseudo-well location'a' along the PETROBAR-07 profile, 64 km east of the COB. Red solid line – subsidence from TecMod model incorporating continental breakup only; magenta dashed line – subsidence from TecMod model incorporating continental breakup and a 5 km thick underplate (2900 kgm^{-3} density) below the Vestbakken Volcanic Province. Note the 1000 m of uplift modelled upon emplacement of the underplate at 60 Ma, comparable to 800m of interpreted relative uplift by Clark et al. (2014).

The Neogene was characterized by uplift and erosion of the shallow Barents Sea shelf. The extensive uplift and erosion has been documented by several workers (Wood et al., 1989; Vorren et al., 1991; Riis & Fjeldskaar, 1992; Faleide et al., 1996; Riis, 1996; Dimakis et al., 1998; Glørstad-Clark et al., 2011a) and erosion estimates range between 0-1000 m in the Tromsø Basin (Riis & Fjeldskaar, 1992) and 1000-1500 m in the Hammerfest Basin and Loppa High (Berglund et al., 1986; Wood et al., 1989). Based on seismic mapping, Glørstad-Clark et al. (2011a) estimated maximum burial for the Barents shelf at 25 Ma, followed by 1200 m uplift over the Loppa High, 1000 m of uplift over the Bjarmeland Platform to the

east, and 500 m over the Tromsø Basin to the west. This uplift and erosion was incorporated into their backstripping model. Within the TecMod models in this study, no such uplift can be reproduced, despite significant amounts of erosion applied at the Plio-Pleistocene boundary. This is unfortunate because the uplift and erosion from Eocene to recent has had a profound effect on the distribution of hydrocarbons in the present-day Barents Sea. If TecMod had the ability to include some known uplift estimates into the inversion this may provide a solution to this problem, and may be the focus for future releases (D. Schmid 2014, pers. comm. 29 Aug). As it stands, this technology is yet to be developed for commercial distribution.

6.4 Gravity from TecMod

The free-air and Bouger corrected gravity anomaly computed from the density distribution within TecMod follows the general trends found in the observed gravity anomaly data from satellite altimetry and ship-track sources, but the amplitude of calculated gravity anomalies is significantly less than the observed. The reason for this discrepancy is most likely a function of the lack of lateral density variation in the crust within the models. All models assume a homogeneous crust, with density varying only as a function of temperature. Within the Barents Sea, the crustal structure is complex, made up of stacked Caledonian nappes of varying age and composition (Barrère et al., 2009, Marello et al., 2013; Gernigon et al., 2014). Within each nappe package (allochthon) the composition also varies as a function of the degree of metamorphism (dependent on pressure-temperature conditions and fluid availability) and the protolith stratigraphy. These factors in the basement combine to create more lateral density variation than is captured within the TecMod models with an assumed homogeneous crust (figure 6.5a).

Clark et al. (2013) were able to capture some of the density variation within the crust by forward gravity modelling (not basin modelling approach) along the PETROBAR-07 profile. Polygons were assigned with different densities based on lateral velocity changes. This provided a good fit between the modelled and observed Bouger-corrected gravity anomaly (figure 6.5b).

Basin models commonly assume the density of the rocks in the mantle only change with temperature. However, many studies have been published showing mantle rocks may change their mineral assemblage due to changes in pressure (e.g. during rifting), and their density is

therefore also pressure-dependent (Podladchikov et al., 1994; Kaus et al., 2005; Simon & Podladchikov, 2008; Semprich et al., 2010). Some sensitivity tests were also run to determine whether accounting for phase-changes in the mantle (specifically garnet-spinel and spinel-plagioclase transitions) would have an effect on the overall density distribution and gravity output from TecMod. The P-T-dependent phase-change model of Kaus et al. (2005) was applied to the mantle rocks in TecMod. The phase-change models showed very little deviation from the models assuming mantle density is only temperature-dependent, confirming the lateral density variations observed in the gravity data must be from within the crust.

a)

b)

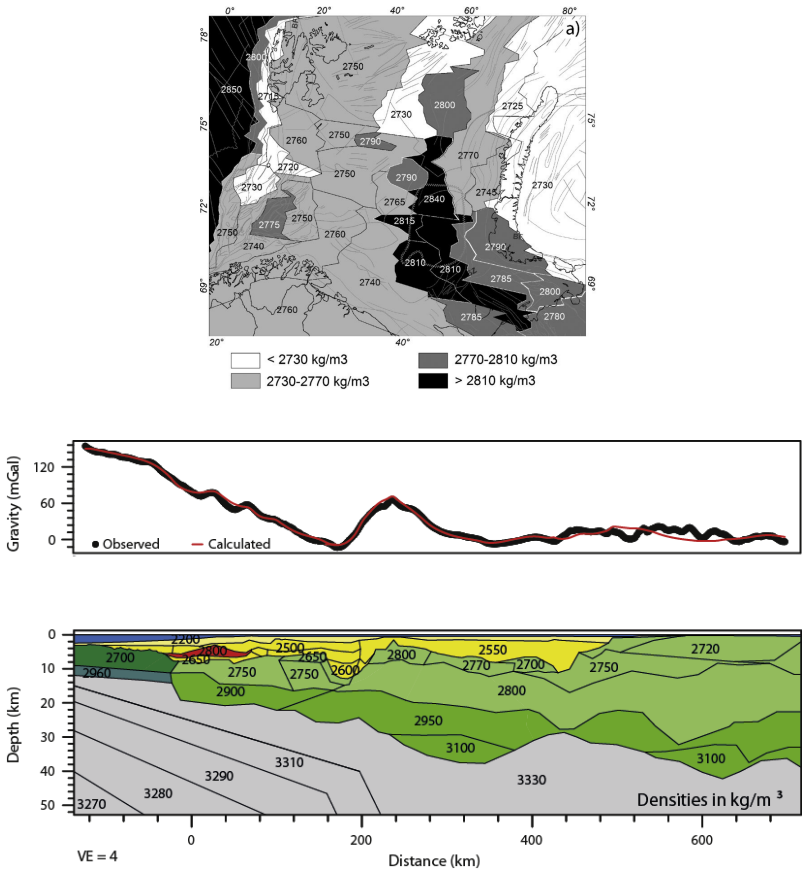

Figure 6.5. a) A density distribution map of the upper crust throughout the Barents Sea based on gravity modelling (Marello et al. 2013). b) Observed bouger-corrected gravity data, compared to the calculated bouger-corrected gravity anomaly from a forward gravity model along the PETROBAR-07 profile and out towards the Knipovich Ridge (Clark et al. 2013). Notice in both figures the lateral density variations captured in the basement due to changes in composition, whereas crustal densities are assumed to be only a function of temperature using a basin modelling approach (e.g. TecMod).

6.5 Correlation with recent discoveries

6.5.1 7220/11-1 Alta Discovery

Located on the southern boundary of the Loppa High, approximately 30 km south of the Loppa High profile (Glørstad-Clark et al., 2011a) is the 7220/11-1 Alta discovery. It is located approximately along the same line-of-strike as the 7120/2-1 well (x = 90 km), which has been used for well data calibration against the Loppa High model in this study (shown in figures 1.1 and 4.7), but the Alta discovery is about 9 km NNE of the 7120/2-1 well and therefore closer to the modelled profile. With initial estimates of up to 300 million barrels of oil (400 million barrels oil equivalent including gas), this is a significant find by Lundin Norway AS in Permian reservoir carbonates (Ørn Formation/Gipsdalen Group; www.npd.no), and can be linked with their earlier 7120/1-3 Gohta discovery in the same formation. What can the Loppa High model within this study say about the discovery? Where are mature source rocks on the eastern flank of the Loppa High?

Oil was encountered at around 2 km depth within Ørn Formation karstified carbonates (290-305 Ma; dark brown unit in figure 6.6a). There are reports in the media that Lundin have measured oil seeping up to the seafloor along fractures and faults over the Loppa High, indicative of an active petroleum system, with oil expulsion from source rocks continuing to this day (Taraldsen & Qvale, 2014). The trap appears to be a stratigraphic unconformity (red shaded area, figure 6.6b), with an Early Triassic shale acting as the seal (basal Kobbe Formation). The Loppa High reference model indicates that Ørn Formation sediments are within the oil window. But there are no reports on the published record of Gipsdalen Group source rocks. Petroleum geochemistry studies on the 7120/2-1 well by Pestman et al. (2011) suggest the oil shows observed in Permian carbonates may derive from Ørret Formation (Tempelfjorden Group) source rocks, which date between approximately 250 and 258 Ma. A continuous permeable carrier bed directly below the Ørret source rock interal was also suggested by Pestman et al. (2011) in order to provide the necessary migration pathway to the Loppa High. Within the Loppa High reference model, these Ørret Formation source rocks (black shaded area, figure 6.6b) are within the oil (R_o – 0.7-1.0; main oil: x =95-104 km) and condensate windows (R_o – 0.7-1.0: late oil: x = 95-140 km). According to our model, the Ørret Formation sediments closest to the Loppa High have been charging the area with hydrocarbons since Jurassic time until present day (figure 6.6c), confirming both the

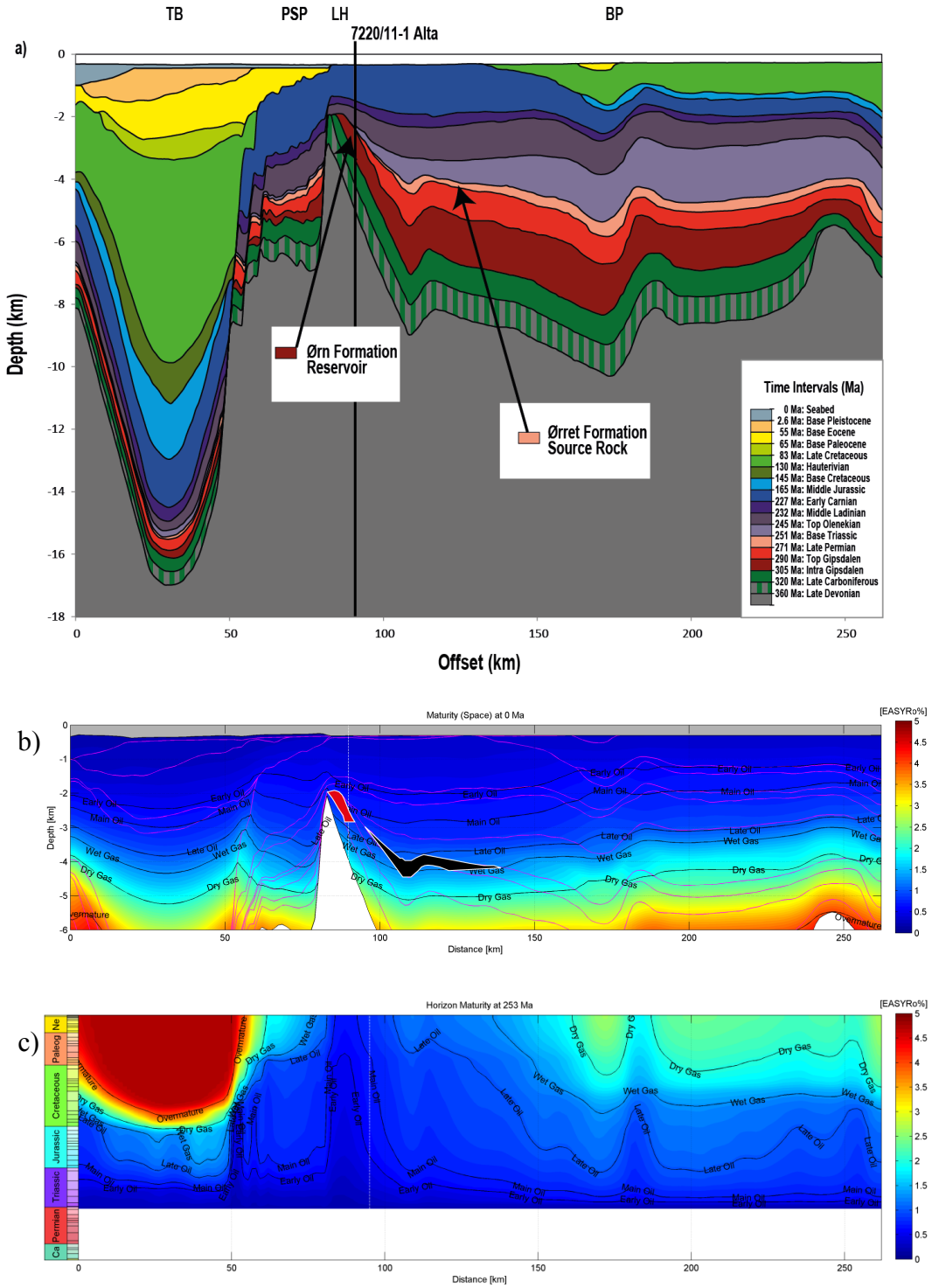

Figure 6.6. Maturation history of Ørret Formation source rocks (deposited 253 Ma) near the 7220/11-1 Alta discovery on the Loppa High. a) Proposed Permian play model on the Loppa High and Bjarmeland Platform, consisting of a Late Permian source rock, migration pathway along a permeable carrier bed directly below the Ørret Formation source rock interval, and unconformity trap by truncation of the Ørn Formation (karstified limestone) by Kobbe Formation (shale). b) Present-day thermal maturity of sediments along the Loppa High profile from the Loppa High reference model in TecMod. Black contours represent different phases of hydrocarbon generation, while pink contours represent formation time lines from the stratigraphic input into the model. Notice the Ørret Formation source rocks are still within the oil-condensate window (black shaded area), continuously delivering hydrocarbons to the Loppa High. The reservoir is shaded in red. c) Thermal history of the same source rock interval. The white dotted line shows the projected well position along the profile. The source rocks have been charging the Loppa High with hydrocarbons since Jurassic time.

validity of the model and the huge potential within this recently discovered petroleum system.

6.5.2 7319/12-1 Pingvin Technical discovery

The 7319/12-1 well discovered a 15 m gas column in reservoir sands belonging to the early Paleocene Torsk Formation or Late Cretaceous Kveite Formation. The well was located on the eastern flank of the Bjørnøya Basin, and although non-commercial (5-20 billion m^3 gas; 30-120 million barrels oil equivalent), it proves an active petroleum system is present in the Bjørnøya Basin for the first time (NPD, 2014). The discovery is located 19 km north of the PETROBAR-07 profile, approximately along the same line of strike as coordinate x = 358 km in figure 6.7. The trap appears to lie within a Cretaceous-Paleocene anticline towards the eastern flank of the Bjørnøya Basin. Where are the source rocks located within this petroleum system?

As mentioned in chapter 2, the highest quality source rocks studied in the western Barents Sea are Late Jurassic shales in the Hekkingen Formation. These source rocks are overmature in the Bjørnøya Basin before the Late Cretaceous-Paleocene trap is formed. So, the source rock must be younger. Norsk Hydro intersected some prospective source rocks of Aptian age (upper Kolje Formation) in the Hammerfest Basin in well 7122/2-1. These Aptian source rocks were cored and contained the highest hydrogen indexes (and therefore higher hydrocarbon-generating potential) in the well (typically 300-500 mg HC/gTOC), even compared to the underlying Hekkingen Formation source rocks (NPD Factpages, 2014). For PETROBAR-07 models produced within this study, Early Aptian source rocks (123 Ma) are gas mature from approximately 100 Ma to 17 Ma on the eastern flank of the Bjørnøya Basin (x = 376 km). Upon gas expulsion from the source rock interval, the gas could have migrated along the western boundary fault of the Bjørnøyrenna Fault Complex, and fed into the Late Cretaceous-Paleocene anticlinal trap (following the pink arrow in figure 6.7a). Shale in the Torsk Formation is the most attractive seal. Modelling suggests that the Late Cretaceous-Paleocene play in the Bjørnøya Basin is no longer active, since the source rocks have been overmature for the past 20 Ma (figure 6.7b and c).

Alternatively, like in the 7316/5-1 well in the Vestbakken Volcanic Province, the gas may also be biogenic in origin, perhaps from shallower Late Cretaceous shales in the Kolmule Formation.

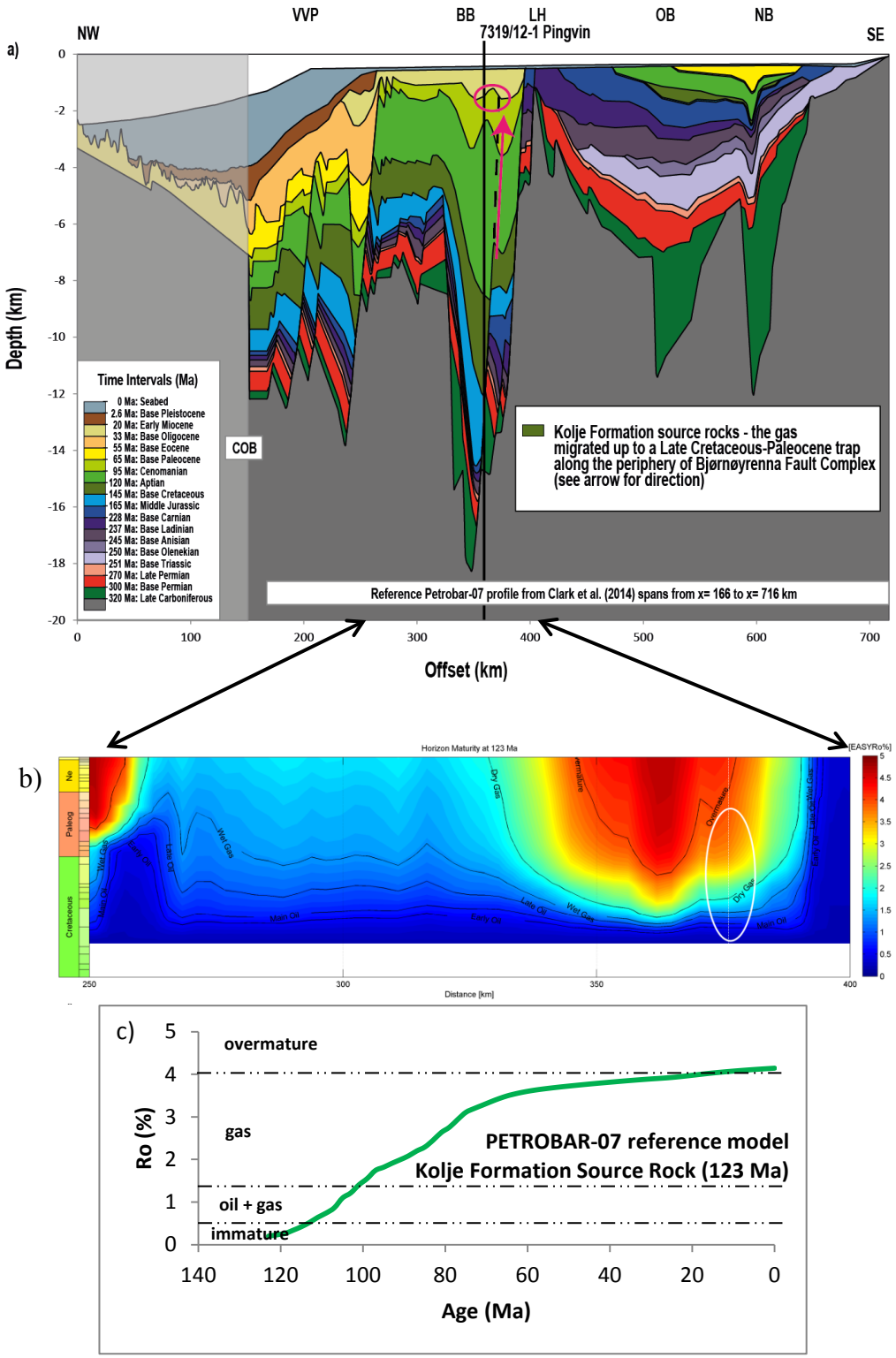

Figure 6.7. Maturation history of Kolje Formation source rocks (deposited 123 Ma) near the 7319/12-1 Pingvin technical discovery in the Bjørnøya Basin. a) Proposed Late Cretaceous-Paleocene play model in the Bjørnøya Basin, consisting of Early Aptian source rock, migration pathway along the western boundary fault of the Bjørnøyrenna Fault Complex, and anticlinal trap in Kveite or Torsk Formation sandstones. b) Horizon maturity section for 123 Ma source rocks from PETROBAR-07 TecMod reference model. Y-axis spans from 0-145 Ma. Notice the source rocks are only mature for an extended period of time on the eastern flank of the Bjørnøya Basin (marked by white ellipse). c) Thermal history of the same source rock interval on the eastern flank of the basin at x = 376 km, marked by dotted white line in (b).

6.6 Sensitivity tests

A series of sensitivity tests on the Loppa High profile (figure 4.7) and the PETROBAR-07 extended profile (figure 4.6a) were conducted to quantify some of the uncertainty inherent within the models presented as a part of this study. Crustal thicknesses prior to rifting are assumed to be 35 km within all models. Thicker (40 km) and thinner (30 km) initial crustal thickness inputs are modelled along the Loppa High profile and compared to the reference case to measure the implications on thermal history of the overlying sediments. Another assumption in the models presented is that rift initiation occurs at 320 Ma. But early Carboniferous sediments have been intersected by wells drilled on the Loppa High (e.g.7120/2-1), and early Carboniferous to Devonian sediments are known to occur on both Bjørnøya (Harland et al., 1997; Worsley et al., 2001) and Svalbard (Gjelberg & Steel, 1981; Steel & Worsley, 1984; Worsley, 2008).

An extra sedimentary horizon is added to the input stratigraphy along the Loppa High profile from 360-320 Ma, as mapped by Glørstad-Clark et al. (2011a). An extra rift phase is required to accommodate this sedimentary package from 360-320 Ma. The effect of these additions to the model is compared to the Loppa High profile reference case.

The sensitivity of the serpentinization algorithm to different upper crustal rheologies is tested within TecMod. The models presented so far have assumed a wet quartzite rheology for the upper crust, and clinopyroxene-plagioclase aggregate rheology for the lower crust. For simplicity, Rüpke et al. (2013) assumed an aggregate rheology for both the upper and lower crust within their serpentinization models, which has a much higher viscous yield than wet quartzite in the upper crust. They were able to embrittle the entire crust within their models along the Vøring margin. The same model setup is therefore run along both the PETROBAR-07 and Loppa High profiles to determine whether serpentinization can be established beneath the deep Bjørnøya and Tromsø Basins during the Late Jurassic to Early Cretaceous rift phase as suggested by Lundin & Doré (2011).

6.6.1 Varying crustal thicknesses – Loppa High Profile

The sensitivity of the model to varying initial crustal thicknesses was tested on the Loppa High profile. The default initial crustal thickness for all models in this study is 35 km (17.5 km upper/lower crust), consistent with Clark et al. (2014). In this study, models with 30 km (15 km upper/lower crust, blue line in figures) and 40 km thick crust (20 km upper/lower

crust, green line in figures) were tested along the Loppa High profile, and compared to the reference (35 km crust, red line in figures) model. The fit of each model to well data (R_o and bottom hole temperature) and free-air anomaly gravity data was analyzed. The effect on the thermal history of sediments was also investigated.

The thinner the initial crustal thickness, the more iterations required to achieve a good fit. The 30 km crustal thickness scenario failed to reproduce the thin Late Cretaceous unit (83-65 Ma). A better fit along this horizon was achieved with 35 and 40 km initial crustal thicknesses.

Thinner crust at rift initiation demands higher crustal stretching (β) factors to provide the necessary amount of accommodation space and subsidence within the basins for sediment deposition (blue line, figure 6.8). Higher upper mantle temperatures are observed with thicker crust (green line) due to the deeper position of the moho and a higher contribution of radioactive heat from the crust. Basement heatflow is also significantly higher in the thick crust scenario, due mainly to the larger source of crustal radioactive heat.

There are negligible differences in paleo-water depths when comparing the scenarios with different crustal thicknesses (not shown), indicative that the stratigraphy fit is maintained by increasing the amount of crustal stretching required to provide the subsidence for subsequent basin infilling, rather than adjusting water depths.

Well control points show reasonable correlation for all scenarios when comparing bottom hole and DST temperatures (figure 6.9). The DST temperature measurement on well 7226/11-1 plots close to the modelled temperature fields at approximately 3 km depth, but the measured bottom hole temperature (near 5 km depth) is over 50 ºC less than the modelled temperature fields (figure 6.9c). The vitrinite reflectance values also show good correlation for the wells located close to the profile (7224/7-1 and 7226/11-1), however the more distant wells (>40 km south of the profile, near the Loppa High) deviate considerably from the observed temperatures (figure 6.10). The higher crustal thickness values correspond to high basement heatflow values which result in increasing the thermal maturity of sediments across the profile, evidenced by elevated R_o trends.

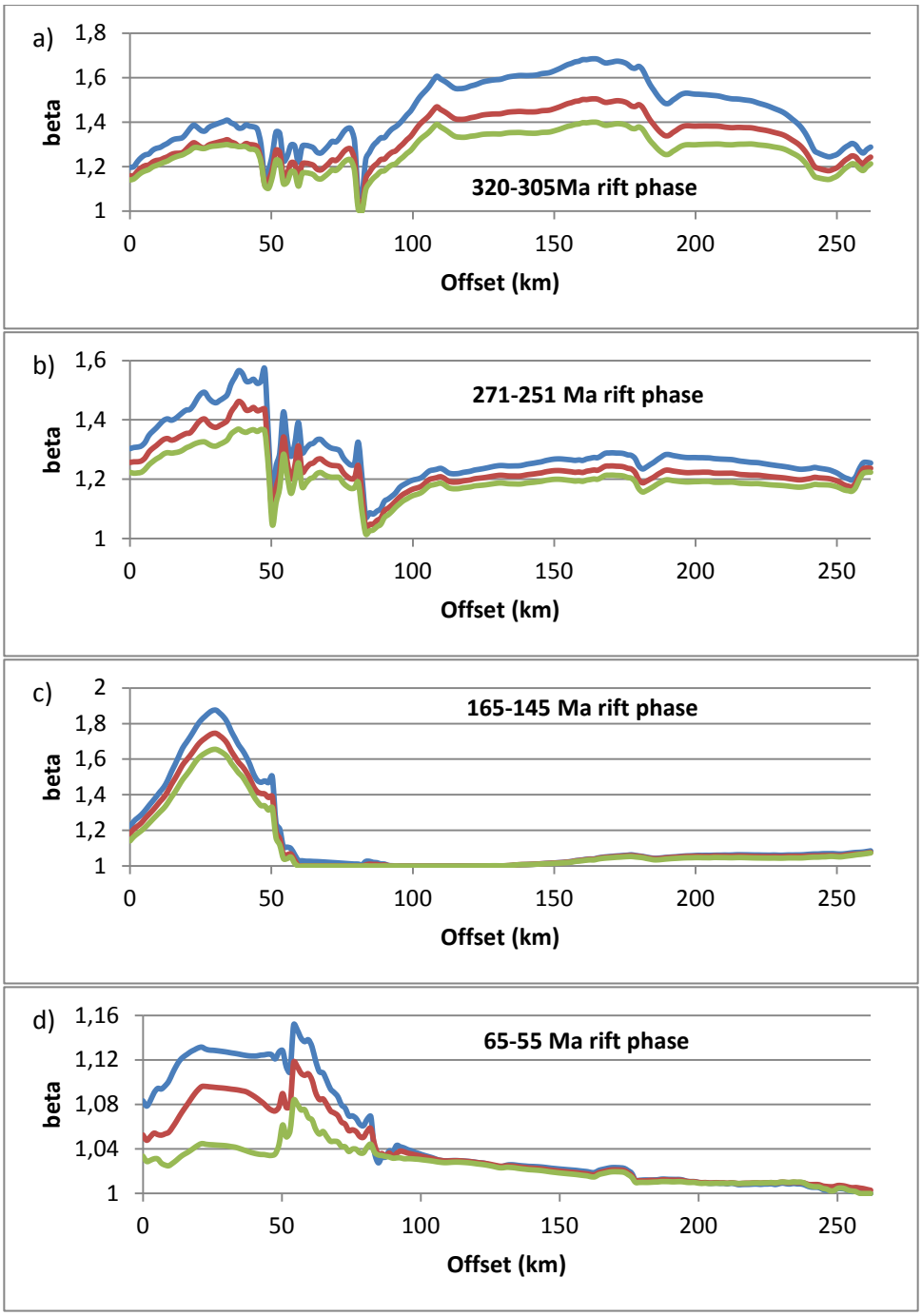

Figure 6.8. Calculated crustal stretching factors (β) across the Loppa High profile for (a) Carboniferous rift phase (320-300 Ma), (b) late Permian rift phase (270-250 Ma), (c) Late Jurassic-Early Cretaceous rift phase, and (d) Paleocene-Eocene rift phase. The sensitivity of the model to different pre-rift initial crustal inputs can be observed, 30 km initial crustal thickness (blue line), 35 km crustal thickness (red line), 40 km crustal thickness (green line). Note the thinner the intial crustal thickness input, the greater amount of crustal stretching required to create a specific amount of subsidence.

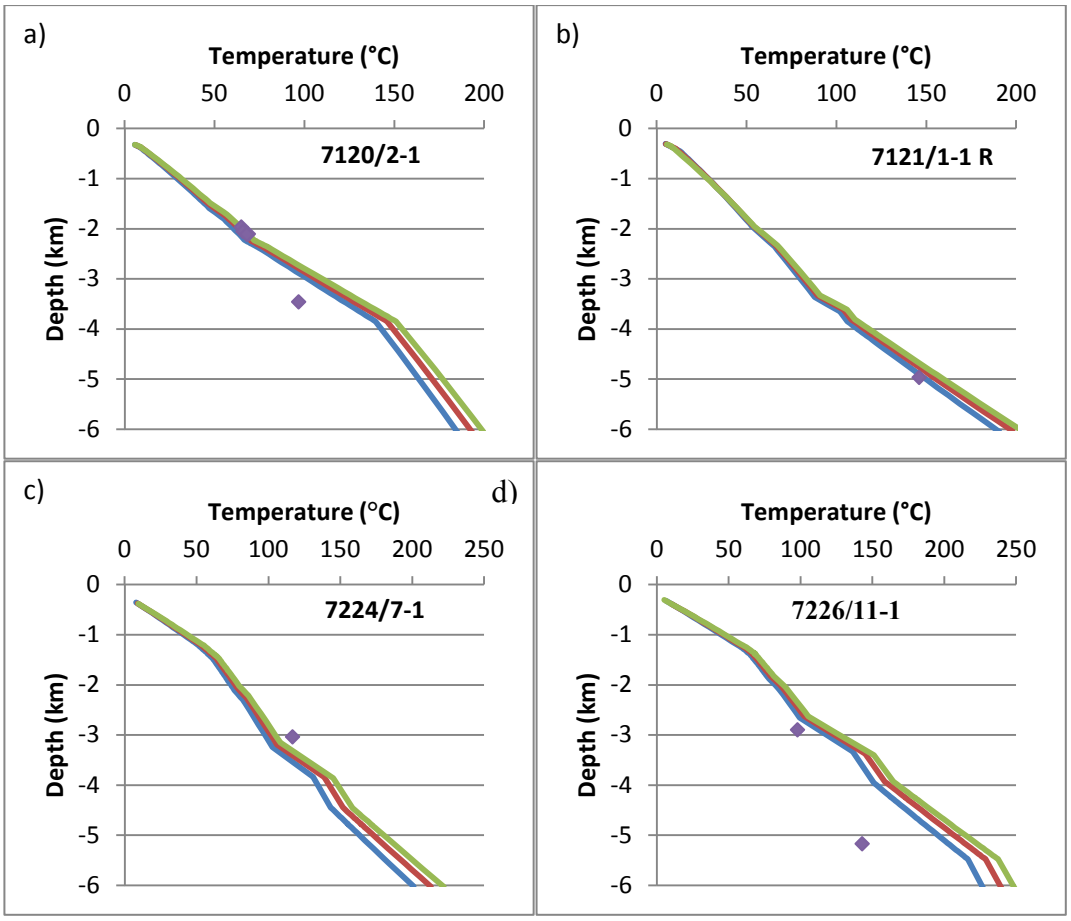

Figure 6.9. Modelled geotherms along the Loppa High profile with different initial crustal thickness inputs compared to well temperature data from bottom-hole measurements and Drill Stem Tests (DST). 30 km initial crustal thickness – blue line, 35 km initial crustal thickness – red line (this is also the reference crustal thickness), 40 km initial crustal thickness – green line; well temperature measurements – purple markers. For well locations, see fig 4.7.

Increasing the initial crustal thickness increases the wavelength of the dense lower crust and sub-Moho mantle contribution to the overall density distribution along the profile (figure 6.11). This in turn, weakens the calculated free-air gravity anomaly signature on the basement highs and platform areas. The contribution from the lower crust and mantle is also reduced in the deep basins (e.g. Tromsø Basin) with thicker pre-rift crust. Here, the lateral density variation is dominated by the sediments and upper crust, with steep basin flanks of relatively higher density which promote positive free-air gravity anomalies in the modelled basins containing a thick pre-rift crustal configuration (40km - green line, and 35km - red line). With a thin (30 km - blue line) pre-rift crust, the contribution from the lower crust and sub-Moho mantle reduce the influence of the lateral variation of the sediments and upper crust, resulting in a relatively flat gravity anomaly through the Tromsø Basin.

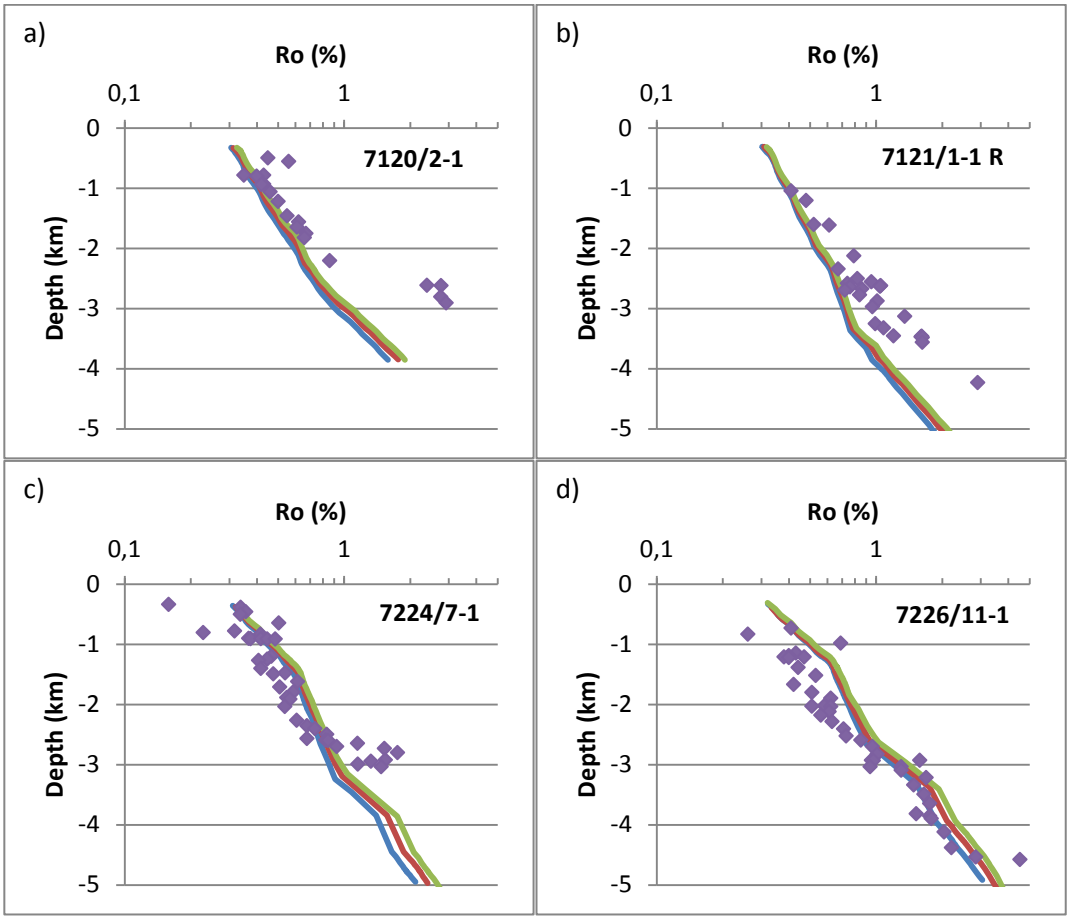

Figure 6.10. Vitrinite reflectance (R_o) data from four wells (plotted in purple) along the Loppa High profile for models with different crustal thicknesses. 30 km initial crustal thickness – blue line, 35 km initial crustal thickness – red line (this is also the reference crustal thickness), 40 km initial crustal thickness – green line. For well locations, see fig 4.7.

6.6.2 Early Carboniferous sediments and extra rift phase – Loppa High Profile

Early Carboniferous sediments (Billefjorden Group) have not been considered in the models produced so far. Instead, a general assumption has been made that any sediments older than 320 Ma are pre-rifting and therefore can be included in the models as basement. The sensitivity of this assumption is tested. Glørstad-Clark et al. (2011a) mapped a consistent horizon between 360-320 Ma across their profile. Recorded accounts of tectonic activity in the Barents Sea region exist in the literature, and evidence of pronounced rifting during the early Carboniferous, based on observations on Bjørnøya, Svalbard, and the Loppa High (Gabrielsen et al., 1990; Dengo & Røssland, 1992; Gudlaugsson et al., 1998). A sedimentary horizon comprising 50% sand, 50% shale (Billefjorden Group) was added to the input stratigraphy and an extra rift phase from 360-320 Ma (table 5.1) was input into TecMod for

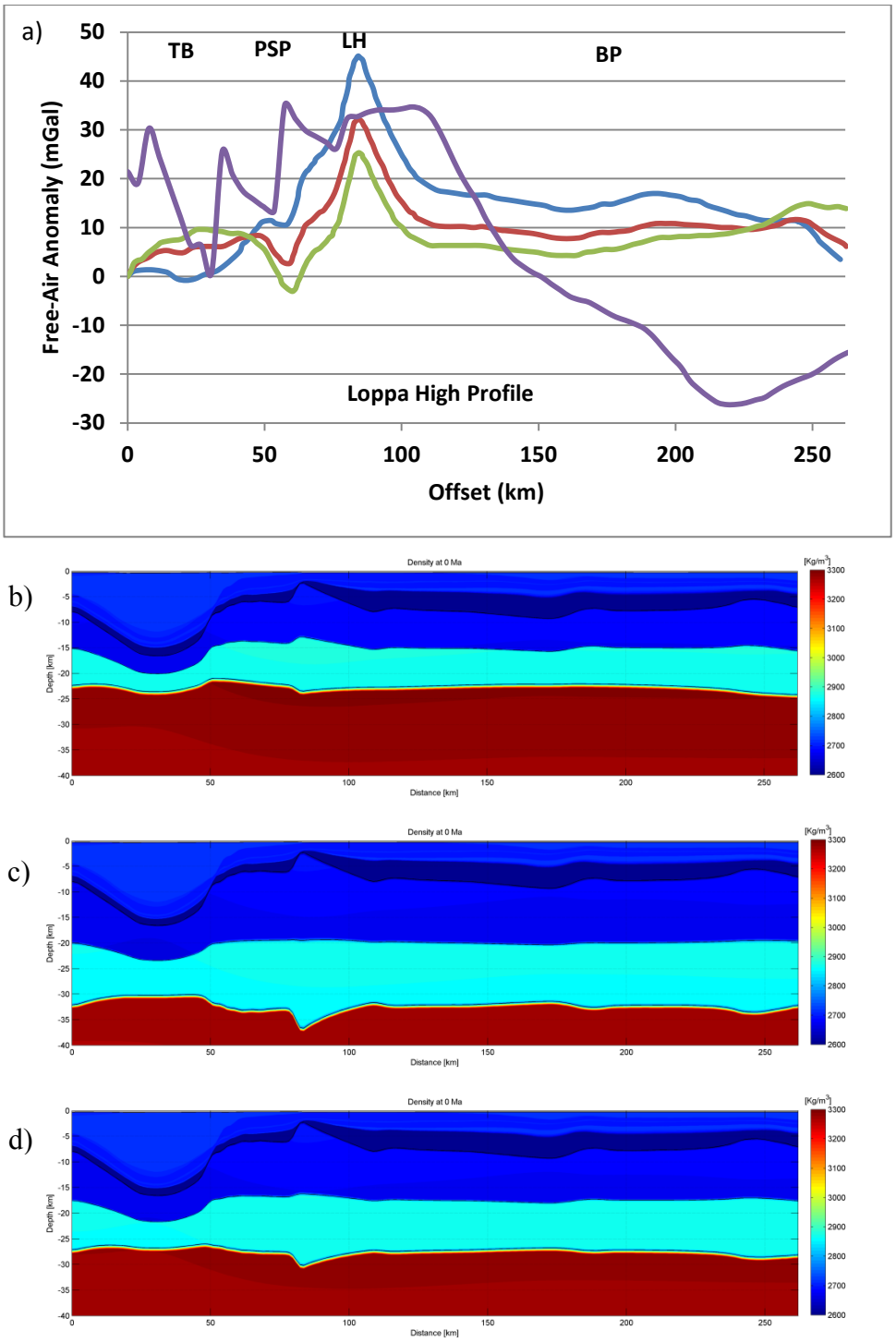

Figure 6.11. a) Free-air gravity anomaly data computed from the density distribution output from TecMod compared to the observed free-air anomaly data from satellite altimetry along the Loppa High profile (Kenyon et al., 2008). Different initial crustal thickness inputs are shown. 30 km initial crustal thickness – blue line, 35 km initial crustal thickness – red line (this is also the reference crustal thickness), 40 km initial crustal thickness – green line; observed free-air anomaly data – purple line. TB – Tromsø Basin; PSP – Polheim Sub-Platform; LH – Loppa High; BP – Bjarmeland Platform. TecMod computed density distributions for b) 30 km; c) 35 km; and d) 40 km initial crustal thickness along the Loppa High profile. See text for details.

analysis (interval mapped with striped green and grey colours in figure 4.7). A 35 km initial crustal thickness together with flexural isostatic condition and erosion were applied. No post-rift horizon is present following the 360 – 320 Ma event. Comparisons are made with the Loppa High reference model from 320 Ma.

The wells drilled further north on the Loppa High which are located close to the PETROBAR-07 profile (e.g. 7220/6-1) did not intersect Early Carboniferous sediments prior to drilling into basement, and as a result have not been mapped. Therefore no sensitivity test with early Carboniferous sediments was run on the PETROBAR-07 profile.

The fit between the modelled vs input stratigraphy is good, with almost identical fit within the same number of iterations (11) as the reference case (rift initiation at 320 Ma).

Table 5.1. Summary of rift phases for scenario with rift initiation from 360 Ma modelled along the Loppa High profile.

Rift Phase	Rift Interval (Loppa High Profile)
Early Carboniferous	360-320
Late Carboniferous	320-305
Late Permian	271-251
Late Jurassic – Early Cretaceous	165-145
Paleocene – Early Eocene	65-55

Stretching factors (β) for the last 4 rift phases (from 320-55 Ma) are all slightly less than the reference model, while cumulative stretching factors are higher (β=3.55; figure 6.12), resulting in generally thinner crust compared to the reference case.

The paleo-water depths show very high correlation between the 360 Ma and 320 Ma rift initiation models (not shown). The 360 Ma model is slightly shallower (30 m) during the Jurassic post-rift phase on the Loppa High and during the late Carboniferous (185 m) and late Permian (55 m) rift phases on the eastern Bjarmeland Platform.

Very small but notable differences in the present-day thermal maturity and vitrinite reflectance of sediments coinciding with drilled wells and pseudo-wells are measured between the reference case and the 360 Ma rift initiation scenario. The 360 Ma scenario reveals a slightly reduced thermal maturity profile through the sediment pile (blue dashed line; figure 6.13). The modelled thermal history of the Middle Triassic and Late Jurassic source rocks through time along wells and pseudo-wells also show very similar trends (figure 6.14). Within the Tromsø Basin there is almost no observable difference (not shown).

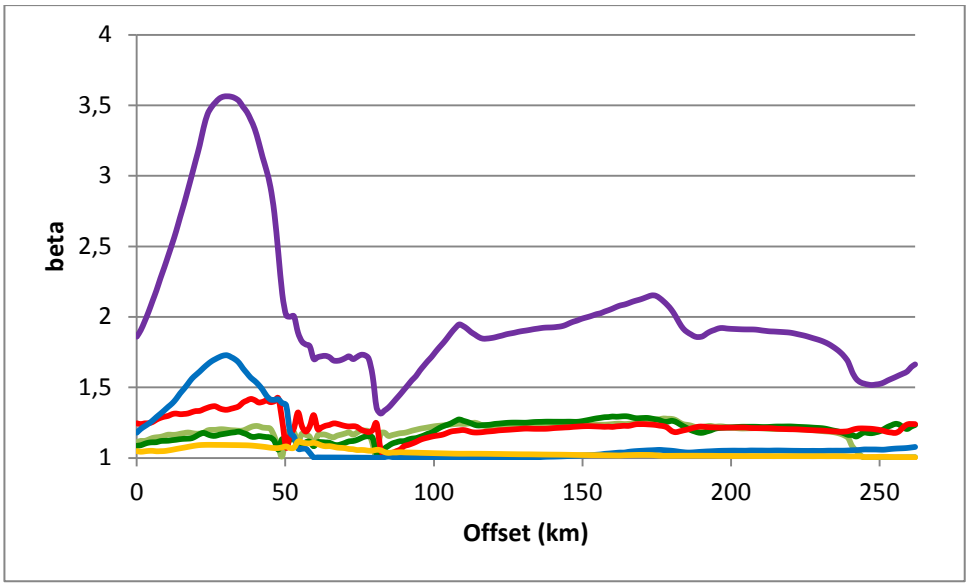

Figure 6.12. Crustal stretching factors (β) for five respective modelled rift phases for a basin with rift initiation at 360 Ma together with the computed cumulative β along the Loppa High profile. Comparisons with the reference model limited to 4 rift phases from 320 Ma can be made by referring to figures 5.1 and 5.5. 360-320 Ma rift phase – light green line; 320-300 Ma rift phase – dark green line; 271-251 Ma rift phase – red line; 165-145 Ma rift phase – blue line; 65-55 Ma rift phase; yellow line; cumulative β – purple line.

No difference is observed at well 7226/11-1 either, because the 360 Ma horizon is absent here. But on the Polheim Sub-Platform, Loppa High, and most of the Bjarmeland Platform it is clear that the 360 Ma rift initiation scenario has a slightly slower maturity profile compared to the reference case.

The reason for the minor difference in thermal histories of source rocks when rift initiation begins at 360 Ma (dashed lines) versus 320 Ma (solid lines) is clear upon inspection of the basement heatflow trends versus time along wells and pseudo-wells (figure 6.15). Less basement heatflow is computed for the 360 Ma rift initiation scenario because the crust is thinner, providing less radiogenic heat to the overlying sediments. This reduction in basement heatflow results in a slower thermal maturity profile for the sedimentary basement infill, except where the early Carboniferous (360 – 320 Ma) horizon is not present, for example in the east on the Samson Dome (well 7226/11-1 in figure 6.13d, and pink line - figures 6.14 and 6.15). At the 7226/11-1 well location the basement heatflow is high from 360-315 Ma due to the basement being exposed as a topographic high. Another interesting feature observed on the heatflow trends is the sharp increase over the Polheim Sub-Platform and Loppa High from 5-3 Ma, coinciding with Plio-Pleistocene glacial erosion event (figure 6.15).

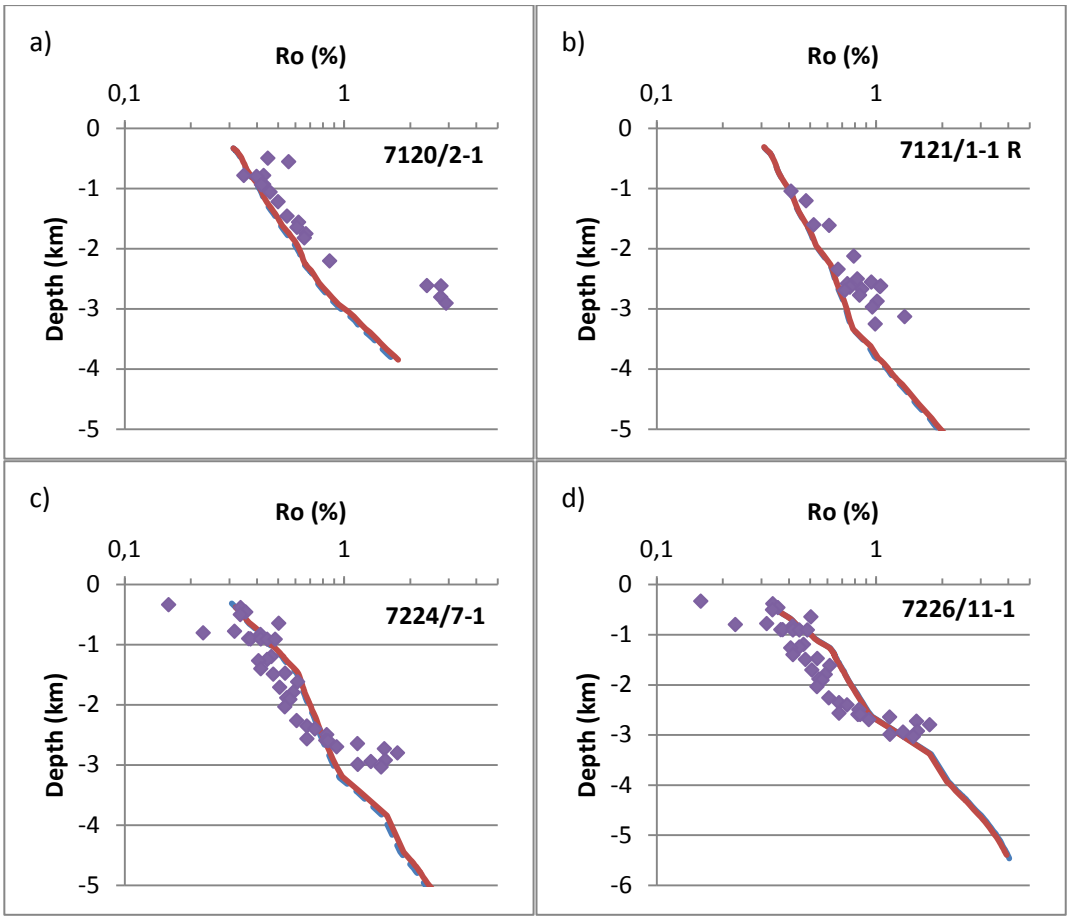

Figure 6.13. Vitrinite reflectance (R_o) data from four wells (plotted in purple) along the Loppa High profile for models with rift initiation at 360 Ma (blue line) and rift initiation at 320 Ma (red line; reference case). For well locations, see fig 4.7.

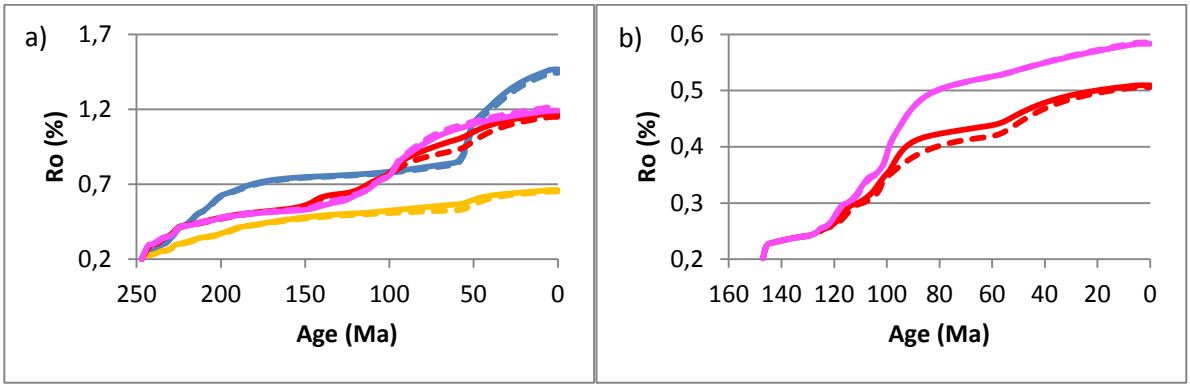

Figure 6.14. Modelled vitrinite reflectance (R_o) data versus time for (a) Triassic (247 Ma) and (b) Jurassic (147 Ma) source rocks along 4 well and pseudo-well locations along the Loppa High profile for models with rift initiation at 360 Ma (dashed lines) and rift initiation at 320 Ma (solid lines; reference model). Polheim Sub-Platform (pseudo-well 'b', x=70km) – blue line, well 7120/2-1 – yellow line; well 7224/7-1 – red line; well 7226/11-1 – pink line. See text for details. For well and pseudo-well locations, see fig 4.7.

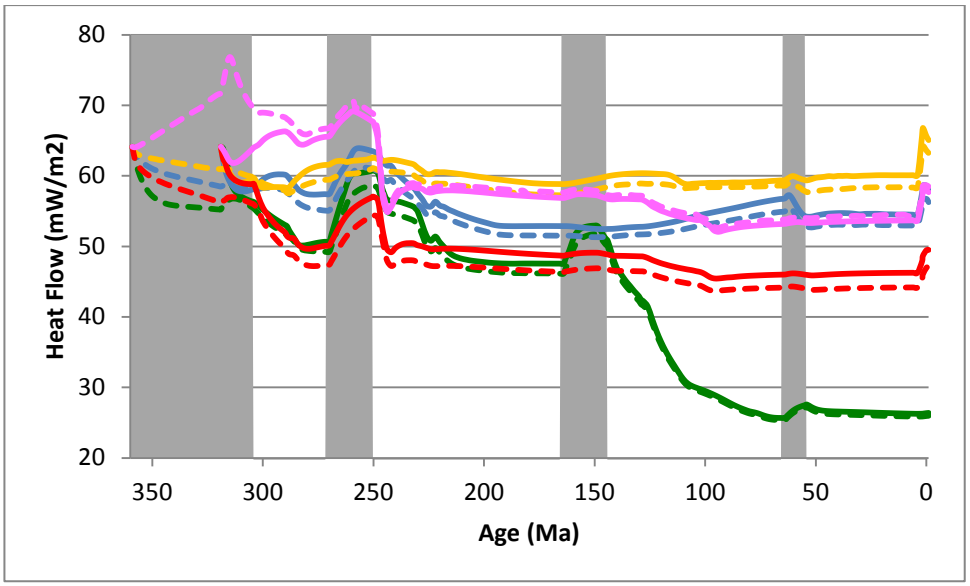

Figure 6.15. Basement heat flow data versus time for 4 well and pseudo-well locations along the Loppa High profile for models with rift initiation at 360 Ma (dashed lines) and rift initiation at 320 Ma (solid lines; reference model). Polheim Sub-Platform (pseudo-well 'b', x=70km) – blue line, well 7120/2-1 – yellow line; well 7224/7-1 – red line; well 7226/11-1 – pink line. Shaded grey areas represent modelled rift phases. See text for details. For well and pseudo-well locations, see fig 4.7.

Summary – Varying crustal thickness and adding Early Carboniferous sediments to model

The sensitivity of the models produced with varying crustal thicknesses and different ages of the rift initiation have been presented along the Loppa High profile. Thicker initial crust prior to rifting requires elevated β-factors to provide the necessary amount of subsidence for a good stratigraphic fit. The increase in basement heatflow associated with thicker crust increases the thermal maturity of sediments. The reference initial crustal thickness of 35 km produces a good fit to the input stratigraphy and the best fit with the crustal structure as proposed by Clark et al. (2013) based on velocity analysis along the PETROBAR-07 profile.

By adding early Carboniferous sediments and an extra rift phase (360-320 Ma), the β-factors for each individual rift phase are slightly lower, while the cumulative β-factor for the entire south-west Barents Sea is slightly higher than the reference model. Small differences in present-day thermal maturity indicators can be identified, but these differences are more pronounced when comparing modelled R_o trends through time. The 360 Ma rift initiation model results in less basement heatflow over time across most of the profile due to a more attenuated crust providing less radiogenic heat input. This slows the thermal maturity

gradients modelled in source rocks and results in a marginally longer time frame for source rocks in the oil/gas window.

6.6.3 Sensitivity of serpentinization algorithm to different upper crust rheologies

The sensitivity of the serpentinization algorithm to different upper crust rheologies was also tested, while keeping the lower crust rheology constant. Wet quartzite, dry quartzite, and aggregate (2-phase mafic aggregate of plagioclase and clinopyroxene; Tullis et al., 1991) rheologies for the upper crust were applied to the PETROBAR-07 and Loppa High serpentinization models. For a given strain rate ($\dot{\varepsilon}$) and temperature (T), and universal gas constant (R), the ductile yield stress is dependent on the material-based constants the prefactor (A), power law coefficient (n), and the exponential of the activation energy (E). For strain rates and crustal temperatures observed under normal conditions during rifting:

$$\sigma_{\text{viscous yield (Wet Quartzite)}} < \sigma_{\text{viscous yield (Dry Quartzite)}} < \sigma_{\text{viscous yield (Aggregate)}}.$$

$$\sigma_{vis} = \left(\frac{\dot{\varepsilon}}{A}\right)^{\frac{1}{n}} \exp\left(\frac{E}{nRT}\right)$$

Dry quartzites and aggregates are generally too strong to be deformed appreciably by viscous flow mechanisms at realistic upper crustal stresses (Paterson et al., 1989; Kohlstedt et al., 1995). So they should fail by brittle mechanisms. The composition of the lower crust was kept constant with an aggregate rheology (as in previous models), as this composition is most sensitive to brittle deformation.

The modelled results support the notion that changes in the upper crust rheology such that it is anhydrous (dry quartzite and aggregate) and mafic in composition (aggregate) significantly increase the viscous deviatoric stress yield and therefore promote potential brittle deformation down to the mantle. Despite this, assigning a dry quartzite or aggregate rheology to the upper crust along both the PETROBAR-07 and Loppa High profiles did not result in complete crustal embrittlement (figure 6.16).

Elevated levels of crustal thinning are modelled during the Late Jurassic-Early Cretaceous rift phase (β_{max} = 1.8 Tromsø Basin; β_{max} = 2.2 Bjørnøya Basin), but these levels of

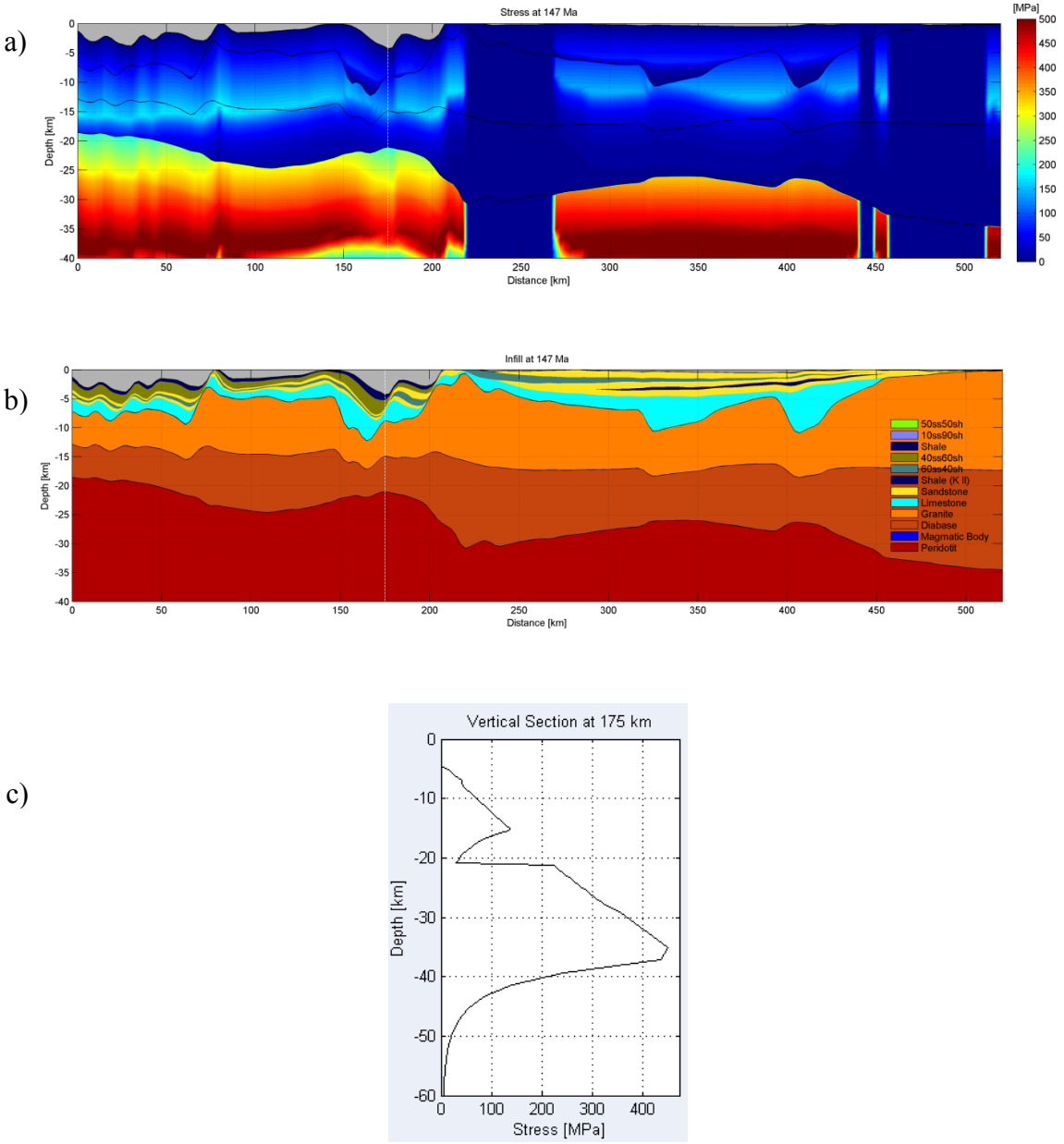

Figure 6.16. a) Differential stress map towards the end of the Late Jurassic rift phase (147 Ma) along the PETROBAR-07 profile. A serpentinization routine with aggregate upper and lower crustal rheologies is applied. b) Crustal structure at 147 Ma. c) Differential stress profile below the zone of most intense crustal thinning below the Bjørnøya Basin, shown with while dotted line in (a) and (b). Note rock weakening directly below the upper crust/lower crust interface (15 km) related to ductile/viscous flow mechanisms. No embrittlement of the lower crust is modelled and therefore no serpentinization is calculated.

stretching are below the minimum critical β-factor of 3 required for mantle serpentinization to occur (Perez-Gussinye & Reston, 2001; Rüpke et al., 2013). At the same time, elevated syn-rift sedimentation rates (up to 0.7 mm/yr) led to rapid filling of the deep Bjørnøya and

Tromsø basins during the Jurassic and Cretaceous. As illustrated by Rüpke et al. (2013), high sedimentation rates promote thermal blanketing of basins which result in elevated crustal and Moho temperatures. These higher temperatures support viscous deformation processes in the lower crust and thereby inhibit crustal-scale faulting and active serpentinization. The models presented in this study suggest that the blanketing effect also contributes to prevent mantle serpentinization. Therefore, high velocity lower crust beneath the Bjørnøya Basin is probably representative of a partially eclogitized Caledonian exhumed crustal root as proposed by Ritzmann & Faleide (2007) rather than pods of serpentinized mantle.

7. Summary and Conclusions

Using a basin modelling approach, the thermal history of sediments in the south-west Barents Sea has been constrained along two seismic profiles by accounting for the near-margin transient heat input from continental breakup and magmatic underplating. The likelihood of mantle serpentinization below the deep Bjørnøya and Tromsø basins has been tested. Gravity anomalies have been extracted from the modelled density distribution for each scenario and compared to observed data from satellite altimetry and ship-track surveys. The implications of the different modelled scenarios on the maturation of hydrocarbon source rocks have been investigated and petroleum systems analysis has been undertaken. The sensitivity of the forward-inversion scheme within TecMod was tested by adjusting the pre-rift initial crustal thickness and including early Carboniferous sediments into the input stratigraphy. The following conclusions are drawn:

1. Including Paleocene-Eocene continental breakup and a 5 km thick magmatic underplating into a forward model requires elevated levels of crustal stretching to compensate for the associated uplift. The crustal stretching factors (β) for scenarios including breakup and underplating are elevated relative to a scenario ignoring these effects (reference case) in the Vestbakken Volcanic Province (VVP) during the Carboniferous, late Permian, and along the COB during the Paleocene-Eocene.
2. Both continental breakup and magmatic underplating clearly alter the thermal history of sediments within the VVP. Continental breakup has a permanent effect on the hydrocarbon maturation of source rocks in the VVP, observable along R_o trends. Magmatic underplating has only a transient effect, with no permanent change in hydrocarbon maturation indicies. Magmatic underplating is offset by higher levels of crustal stretching in earlier rift phases, which reduces the volume of radiogenic-heat-generating crust. Low thermal conductivities of deeply-buried shales and limestones in the VVP also act as a barrier to heat conduction through the sediment column, reducing the potentially much higher increase in measurable maturation that otherwise could occur following cooling of an underplate.
3. Measured elevated vitrinite reflectance (R_o) from the 7316/5-1 well in the VVP cannot be reproduced in models including continental breakup, underplating, or multiple sill intrusions. The distribution of sills and extrusives within the Vestbakken Volcanic Province is far more complex than captured in the models.

4. Serpentinization of sub-Moho mantle peridotite below the deep Bjørnøya and Tromsø basins during the Late Jurassic-Early Cretaceous rift phase cannot be resolved within the basin modelling workflow applied here. At the rift-maxima, β-factors of up to 2.2 are modelled, together with elevated syn-rift sedimentation rates (0.7 mm/yr). The amount of crustal stretching is insufficient, and the syn-rift sedimentation rates are too high to induce complete crustal embrittlement and any potential serpentinization. This is in contrast to an earlier, qualitative study of seismic velocity anomalies around to North Atlantic rim by Lundin & Doré (2011).
5. Modelled gravity anomalies follow the general fluctuations in the observed data along the PETROBAR-07 profile. The observed anomaly amplitude is much higher than the modelled, a function of lateral crustal density variations in the Barents Sea not captured in a basin modelling workflow with assumed homogeneous crust. Unfortunately, along the Loppa High profile, probable 3-D effects in the observed data related to some nearby out-of-plane basement highs result in very little correlation between modelled and observed gravity anomalies.
6. Recent hydrocarbon discoveries on the Loppa High (7220/11-1 Alta) and Bjørnøya Basin (7319/12-1 Pingvin) have been analysed within the context of the models produced within this study. The Alta discovery is an extensive, active petroleum system that has been mature since Jurassic time. The Pingvin discovery petroleum system is probably no longer active, overmature for the past 20 Ma.
7. Applying thicker initial pre-rift crust in a sensitivity test results in elevated β-factors, basement heatflow, and hydrocarbon maturity trends. Adding early Carboniferous sediments to the input stratigraphy (360-320 Ma) requires higher β-factors to provide the necessary extra accommodation space. This, in turn, reduces basement heatflow and slows source-rock maturity.

Future work could be focussed on further understanding the mutual effects of continental breakup and magmatic underplating on sediments in the Vestbakken Volcanic Province by a backstripping approach. Uplift and erosion events are more easily resolved using a backstripping approach, so it would be interesting to apply recently published uplift and erosion estimates by Henriksen et al. (2011b) and Baig et al. (2014), and then comparing the results with the work published in this study and the work of Clark et al. (2014). Any future improvements to the TecMod engine with regards to including fixed uplift and erosion estimates would also be worthwhile trialling within a study.

8. References

Airy, G.B. (1855). On the Computation of the Effect of the Attraction of Mountain-Masses, as Disturbing the Apparent Astronomical Latitude of Stations in Geodetic Surveys. Philosophical Transactions of the Royal Society of London, 145, 101-104.

Al-Hajeri, M. M., Al Saeed, M., Derks, J., Fuchs, T., Hantschel, T., Kauerauf, A., Neumaier, M., Schenk, O., Swientek, O., Tessen, N., Welte, D., Wygrala, B., Kornpihl, D. & Peters, K. (2009). Basin and petroleum system modeling. Oilfield Review, 21(2), 14-29.

Allen, P. A. & Allen, J. R. (2013). Basin analysis: Principles and application to petroleum play assessment (3rd Edition). John Wiley & Sons, Chichester. 619pp.

Baig, I., Faleide, J.I., Mondol, N.H. & Jahren, J. (2014). Uplift/erosion estimates and uncertainties on the Norwegian Barents Shelf. In: Eriksen, S. Haflidason, H., Olesen, O., Schiellerup, H. & Husås, A.M (eds.) Arctic Days 2014, NGF Abstracts and Proceedings, No 2, 2014, p11.

Barrère, C., Ebbing, J. & Gernigon, L. (2009). Offshore prolongation of Caledonian structures and basement characterisation in the western Barents Sea from geophysical modelling. Tectonophysics, 470(1), 71-88.

Barrère, C. (2010). Integrated geophysical modelling and tectonic evolution of the western Barents Sea. [Ph.D. thesis]: Trondheim, Norwegian University of Science and Technology, 185 p.

Berglund, L., Augustson, J., Færseth, R., Gjelberg, J. & Ramberg-Moe, H. (1986). The Evolution of the Hammerfest Basin. In: Spencer, A. (ed.) Habitat of Hydrocarbons on the Norwegian Continental Shelf, Graham & Trotman, London, 319-338.

Breivik, A. J., Gudlaugsson, S. T. & Faleide, J. I. (1995). Ottar Basin, SW Barents Sea: a major Upper Palaeozoic rift basin containing large volumes of deeply buried salt. Basin research, 7(4), 299-312.

Breivik, A.J., Verhoef, J. & Faleide, J.I. (1999). Effect of thermal contrasts on gravity modeling at passive margins: Results from the western Barents Sea. Journal of Geophysical Research, 104, 15293-15311.

Breivik, A.J., Mjelde, R., Grogan, P., Shimamura, H., Murai, Y., Nishimura, Y. & Kuwano, A. (2002). A possible Caledonide arm through the Barents Sea imaged by OBS data. Tectonophysics 355, 67-97.

Bruvoll, V., Breivik, A. J., Mjelde, R., & Pedersen, R. B. (2009). Burial of the Mohn-Knipovich seafloor spreading ridge by the Bear Island Fan: Time constraints on tectonic evolution from seismic stratigraphy. Tectonics, 28(4). TC4001.

Burnham, A. K. & Sweeney, J. J. (1989). A chemical kinetic model of vitrinite maturation and reflectance. Geochimica et Cosmochimica Acta, 53(10), 2649-2657.

Carstens, H. (2013). Gamle ideer – ny teknologi. GEO magasinet 7, 40-45.

Cavanagh, A. J., Di Primio, R., Scheck-Wenderoth, M., & Horsfield, B. (2006). Severity and timing of Cenozoic exhumation in the southwestern Barents Sea. Journal of the Geological Society, 163(5), 761-774.

Clark, S. A., Faleide, J. I., Hauser, J., Ritzmann, O., Mjelde, R., Ebbing, J., Thybo, H. & Flüh, E. (2013). Stochastic velocity inversion of seismic reflection/refraction traveltime data for rift structure of the southwest Barents Sea. Tectonophysics, 593, 135-150.

Clark, S. A., Glørstad-Clark, E., Faleide, J. I., Schmid, D., Hartz, E. H. & Fjeldskaar, W. (2014). Southwest Barents Sea rift basin evolution: comparing results from backstripping and time-forward modelling. Basin Research, 26, 550-566.

Dengo, C.A. & Røssland, K.G. (1992). Extensional tectonic history of the western Barents Sea. In: Larsen, R., Brekke, H., Laresen, B., Talleraas, E. (eds.), Structural and Tectonic Modelling and Its Application to Petroleum Geology. Elsevier, Amsterdam, 91-107.

Dimakis, P., Braathen, B.I., Faleide, J.I., Elverhoi, A. & Gudlaugsson, S.T. (1998). Cenozoic Erosion and the Preglacial Uplift of the Svalbard-Barents Sea Region. Tectonophysics, 300, 311-327.

Doré, A. G. (1991). The structural foundation and evolution of Mesozoic seaways between Europe and the Arctic. Palaeogeography, Palaeoclimatology, Palaeoecology, 87, 441-492.

Doré, A. G., & Jensen, L. N. (1996). The impact of late Cenozoic uplift and erosion on hydrocarbon exploration: offshore Norway and some other uplifted basins. Global and Planetary Change, 12(1), 415-436.

Ehrenberg, S. N. (2004). Factors controlling porosity in Upper Carboniferous–Lower Permian carbonate strata of the Barents Sea. AAPG bulletin, 88(12), 1653-1676.

Eidvin, T., Goll, R. M., Grogan, P., Smelror, M., & Ulleberg, K. (1994). En stratigrafisk undersøkelse av øvre del av brønn 7316/5-1 (Bjørnøya Vest). NPD Contribution 38, 91 pp.

Eidvin, T., Goll, R. M., Grogan, P. A. U. L., Smelror, M. & Ulleberg, K. (1998). The Pleistocene to Middle Eocene stratigraphy and geological evolution of the western Barents Sea continental margin at well site 7316/5-1 (Bjørnøya West area). Norsk Geologisk Tidsskrift 78, 99-124.

Engen, Ø., Faleide, J. I. & Dyreng, T. K. (2008). Opening of the Fram Strait gateway: a review of plate tectonic constraints. Tectonophysics, 450(1), 51-69.

Faleide, J.I., Gudlaugsson, S.T., & Jacquart, G. (1984). Evolution of the western Barents Sea. Marine and Petroleum Geology 1, 123-150.

Faleide, J. I., Gudlaugsson, S. T., Eldholm, O., Myhre, A. M. & Jackson, H. R. (1991). Deep seismic transects across the sheared western Barents Sea-Svalbard continental margin. Tectonophysics, 189(1), 73-89.

Faleide, J.I., Vågnes, E. & Gudlaugsson, S.T. (1993a). Late Mesozoic-Cenozoic evolution of the southwestern Barents Sea. In: Parker, J.R. (ed.), Petroleum Geology of Northwest Europe, Proceedings of the 4th Conference. The Geological Society of London, London, 933-950.

Faleide, J.I., Vågnes, E. & Gudlaugsson, S.T. (1993b). Late Mesozoic-Cenozoic evolution of the south-western Barents Sea in a regional rift-shear tectonic setting. Marine and Petroleum Geology 10, 186-214.

Faleide, J.I., Solheim, A., Fiedler, A., Hjelstuen, B.O., Andersen, E.S. & Vanneste, K. (1996). Late Cenozoic evolution of the western Barents Sea-Svalbard continental margin. Global and Planetary Change 12, 53-74.

Faleide, J.I., Tsikalas, F., Breivik, A.J., Mjelde, R., Ritzmann, O., Engen, O., Wilson, J. & Eldholm, O. (2008). Structure and evolution of the continental margin off Norway and Barents Sea. Episodes 3, 82-91.

Faleide, J.I., Bjørlykke, K. & Gabrielsen, R.H. (2010). Geology of the Norwegian Continental Shelf. In: Bjørlykke K. (ed.), Petroleum Geoscience: From Sedimentary Environments to Rock Physics. Springer-Verlag, Berlin, 467-499.

Fiedler, A., & Faleide, J. I. (1996). Cenozoic sedimentation along the southwestern Barents Sea margin in relation to uplift and erosion of the shelf. Global and Planetary Change 12, 75-93.

Fjeldskaar, W., Johansen, H., Dodd, T. A. & Thompson, M. (2003). AAPG/Datapages Discovery Series No. 7, Multidimensional Basin Modeling, Chapter 6: Temperature and Maturity Effects of Magmatic Underplating in the Gjallar Ridge, Norwegian Sea.

Fjeldskaar, W., Ter Voorde, M., Johansen, H., Christiansson, P., Faleide, J. I. & Cloetingh, S. A. P. L. (2004). Numerical simulation of rifting in the northern Viking Graben: the mutual effect of modelling parameters. Tectonophysics, 382 (3), 189-212.

Fjeldskaar, W., Helset, H. M., Johansen, H., Grunnaleite, I. & Horstad, I. (2008). Thermal modelling of magmatic intrusions in the Gjallar Ridge, Norwegian Sea: implications for vitrinite reflectance and hydrocarbon maturation. Basin Research, 20(1), 143-159.

Fjeldskaar, W., Grunnaleite, I., Zweigel, J., Mjelde, R., Faleide, J. I. & Wilson, J. (2009). Modelled palaeo-temperature on Vøring, offshore mid-Norway—The effect of the Lower Crustal Body. Tectonophysics, 474(3), 544-558.

Fowler, C.M.R. (2005). The Solid Earth: An Introduction to Global Geophysics (2nd Edition). Cambridge University Press, Cambridge, 695pp.

Gabrielsen, R. H. (1984). Long-lived fault zones and their influence on the tectonic development of the southwestern Barents Sea. Journal of the Geological Society, 141(4), 651-662.

Gabrielsen, R.H. Færseth, R.B., Jensen, L.N., Kalheim, J.E. & Riis, F. (1990). Structural Elements of the Norwegian Continental Shelf: The Barents Sea Region. Oljedirektoratet (NPD) Bulletin 6, 47pp.

Gabrielsen, R.H., Grunnaleite, I. & Ottesen, S., (1993). Reactivation of fault complexes in the Loppa High area, southwestern Barents Sea. In : Vorren, T.O., Bergsager, E., Dahl-Stamnes, Ø.A., Holter, E., Lie, E and Lund, T.B. (eds.): Arctic Geology and Petroleum Potential, Proceedings of NPF conference: "Arctic geology and petroleum potential", 15-17 August 1990, Tromsø. Norwegian Petroleum Society (NPF), Special Publication No.2, pp 631-641.

Gac, S., Huismans, R. S., Podladchikov, Y. Y. & Faleide, J. I. (2012). On the origin of the ultradeep East Barents Sea basin. Journal of Geophysical Research: Solid Earth (1978–2012), 117(B4).

Gac, S., Huismans, R. S., Simon, N. S., Podladchikov, Y. Y. & Faleide, J. I. (2013). Formation of intracratonic basins by lithospheric shortening and phase changes: a case study from the ultra-deep East Barents Sea basin. Terra Nova, 25(6), 459-464.

Gac, S., Huismans, R. S., Simon, N. S., Faleide, J. I. & Podladchikov, Y. Y. (2014). Effects of lithosphere buckling on subsidence and hydrocarbon maturation: A case-study from the ultra-deep East Barents Sea basin. Earth and Planetary Science Letters, 407, 123-133.

GeoModelling Solutions, (2014). TecMod2D 2014.1 Manual (unpublished).

Gernigon, L. & Brönner, M. (2012). Late Palaeozoic architecture and evolution of the southwestern Barents Sea: insights from a new generation of aeromagnetic data. Journal of the Geological Society, 169(4), 449-459.

Gernigon, L., Brönner, M., Roberts, D., Olesen, O., Nasuti, A. & Yamasaki, T. (2014). Crustal and basin evolution of the southwestern Barents Sea: From Caledonian orogeny to continental breakup. Tectonics, 33(4), 347-373.

Gjelberg, J. G. & Steel, R. J. (1981). An outline of Lower-Middle Carboniferous sedimentation on Svalbard: effects of tectonic, climatic and sea level changes in rift basin sequences. In: Kerr, J.W. & Furgusson, A.J. (eds) Geology of the North American Borderlands. Can. Soc. Petrol. Geol. Mem. 7, 543-561.

Glørstad-Clark, E., Faleide, J. I., Lundschien, B. A. & Nystuen, J. P. (2010). Triassic seismic sequence stratigraphy and paleogeography of the western Barents Sea area. Marine and Petroleum Geology, 27(7), 1448-1475.

Glørstad-Clark, E., Clark, S.A., Faleide, J.I., Bjørkesett, S.S., Gabrielsen, R.H. & Nystuen, J.P. (2011a). Basin dynamics of the Loppa High area, SW Barents Sea: A history of complex vertical movements in an epicontinental basin. In: Glørstad-Clark, E. (2011). Basin analysis in the western Barents Sea area: The interplay between accommodation space and depositional systems. PhD thesis, University of Oslo, Oslo, 91-147.

Glørstad-Clark, E., Birkeland, E. P., Nystuen, J. P., Faleide, J. I. & Midtkandal, I. (2011b). Triassic platform-margin deltas in the western Barents Sea. Marine and Petroleum Geology, 28(7), 1294-1314.

Gradstein, F. M., Ogg, J. G. & Smith, A. G. (eds.). (2004). A geologic time scale 2004 (Vol. 86). Cambridge University Press, Cambridge. 610 pp.

Gudlaugsson, S.T., Faleide, J.I., Johansen, S.E. & Breivik, A.J. (1998). Late Palaeozoic structural development of the south-western Barents Sea. Marine and Petroleum Geology 15, 73-102.

Hallam, A. (2001). A review of the broad pattern of Jurassic sea-level changes and their possible causes in the light of current knowledge. Palaeogeography, Palaeoclimatology, Palaeoecology, 167(1), 23-37.

Harland, W. B., Geddes, I. & Doubleday, P. A. (1997). Southern Svalbard: Bjørnøya and submarine geology. In: Harland, W.B., Anderson, L.M. & Manasrah, D. (eds.) The Geology of Svalbard. Geological Society, London, Memoirs, 17(1), 209-226.

Hartz, E. H., Martinsen, B. B., Øverli, P. E., Lie, H., Ditcha, E. M., Schmid, D. W. & Medvedev, S. (2013). Newly Discovered Giant Oil Fields of North Sea - The Role of

Fractured Basement Highs. In: Abstracts of the First EAGE/SBGf Workshop 2013, Rio de Janeiro - Fractures in Conventional and Unconventional Reservoirs.

Henriksen, E., Ryseth, A. E., Larssen, G. B., Heide, T., Rønning, K., Sollid, K. & Stoupakova, A. V. (2011a). Tectonostratigraphy of the greater Barents Sea: implications for petroleum systems. Geological Society, London, Memoirs, 35, 163-195.

Henriksen, E., Bjørnseth, H. M., Hals, T. K., Heide, T., Kiryukhina, T., Kløvjan, O. S., Larssen, G.B., Ryseth, A.E., Rønning, K., Sollid, K. & Stoupakova, A. (2011b). Uplift and erosion of the greater Barents Sea: impact on prospectivity and petroleum systems. Geological Society, London, Memoirs, 35(1), 271-281.

Hjelstuen, B. O., Elverhøi, A. & Faleide, J. I. (1996). Cenozoic erosion and sediment yield in the drainage area of the Storfjorden Fan. Global and Planetary Change, 12(1), 95-117.

Hjelstuen, B. O., Eldholm, O. & Faleide, J. I. (2007). Recurrent Pleistocene mega-failures on the SW Barents Sea margin. Earth and Planetary Science Letters, 258(3), 605-618.

Huismans, R. S. & Beaumont, C. (2008). Complex rifted continental margins explained by dynamical models of depth-dependent lithospheric extension. Geology, 36(2), 163-166.

Jakobsson, M., Mayer, L.A., Coakley, B., Dowdeswell, J.A., Forbes, S., Fridman, B., Hodnesdal, H., Pedersen, R., Rebesco, M., Schenke, H.-W., Zarayskaya, Y., Accettella, A.D., Armstrong, A., Anderson, R.M, Bienoff, P., Camerlenghi, A., Church, I., Edwards, M., Gardner, J.V., Hall, J.K., Hell, B., Hestvik, O.B., Kristoffersen, Y., Marcussen, C., Mohammed, R., Mosher, D., Ngheim, S.V., Pedrosa, M.T., Travaglini, P.G. & Weatherall, P. (2012). The International Bathymetric Chart of the Arctic Ocean (IBCAO) Version 3.0, Geophysical Research Letters 39, L 12609

Jarvis G.T. & McKenzie, D.P. (1980). Sedimentary basin formation with finite extension rates. Earth and Planetary Science Letters 48, 42-52.

Jebsen, C. & Faleide, J.I. (1998). Tertiary rifting and magmatism at the western Barents Sea margin (Vestbakken volcanic province): III international conference on Arctic margins, ICAM III; abstracts; plenary lectures, talks and posters, pp. 92.

Johansen, S.E., Ostisty, B.K., Birkeland, O., Fedorovsky, Y.F., Martirosjan, V.N., Christensen, O.B., Cheredeev, S.I., Ignatenko, E.A. & Margulis, L.S. (1992). Hydrocarbon potential in the Barents Sea region: play distribution and potential, In: Vorren T.O., Bergsager E., Dahl-Stamnes Ø.A., Holter E., Johansen B., Lie E., & Lund T.B. (eds.), Arctic Geology and Petroleum Potential, 273–320. NPF Special Publication 2, Elsevier, Amsterdam.

Kaus, B. J., Connolly, J. A., Podladchikov, Y. Y. & Schmalholz, S. M. (2005). Effect of mineral phase transitions on sedimentary basin subsidence and uplift. Earth and Planetary Science Letters, 233(1), 213-228.

Kenyon, S., Forsberg, R. & Coakley, B. (2008). New Gravity Field for the Arctic. Eos, Transactions American Geophysical Union, 89 (32), 289-290.

Klett, T. R. & Pitman, J. K. (2011). Geology and petroleum potential of the East Barents Sea Basins and Admiralty Arch. Geological Society, London, Memoirs, 35(1), 295-310.

Knies, J., Matthiessen, J., Vogt, C., Laberg, J. S., Hjelstuen, B. O., Smelror, M., Larsen, E. Andreassen, K., Eidvin, T. & Vorren, T. O. (2009). The Plio-Pleistocene glaciation of the Barents Sea–Svalbard region: a new model based on revised chronostratigraphy. Quaternary Science Reviews, 28(9), 812-829.

Knutsen, S.-M., Augustson, J. H. & Haremo, P. (2000). Exploring the Norwegian part of the Barents Sea – Norsk Hydro's lessons from nearly 20 years of experience. In: Ofstad, K., Kittilsen, J. E. & Alexander-Marrack, P. (eds): Improving the Exploration Process by Learning from the Past. NPF Special Publication 9, Elsevier, Amsterdam, 99-112.

Kohlstedt, D. L., Evans, B. & Mackwell, S. J. (1995). Strength of the lithosphere: Constraints imposed by laboratory experiments. Journal of Geophysical Research: Solid Earth (1978–2012), 100(B9), 17587-17602.

Kusznir, N.J. Karner, G.D. & Egan, S. (1987). Geometric, thermal, and isostatic consequences of detachments in continental lithosphere extension and basin formation. In: Beaumont, C. & Tankard, A.J. (eds.) Sedimentary Basins and Basin Forming Mechanisms. Mem. Can. Soc. Petrol. Geol. 12, 185-203.

Kusznir, N. J., Marsden, G. & Egan, S. S. (1991). A flexural-cantilever simple-shear/pure-shear model of continental lithosphere extension: applications to the Jeanne d'Arc Basin, Grand Banks and Viking Graben, North Sea. Geological Society, London, Special Publications, 56(1), 41-60.

Kusznir, N. J., Roberts, A. M. & Morley, C. K. (1995). Forward and reverse modelling of rift basin formation. Geological Society, London, Special Publications, 80(1), 33-56.

Kusznir, N.J., Hunsdale, R., Roberts, A.M. & SIMM team. (2005). Norwegian margin depth-dependent stretching. In: Dore, A.G. & Vining, B.A. (eds.) Petroleum geology: North-west Europe and global perspectives - Proceedings of the 6th Petroleum Geology Conference: Geological Society of London, Petroleum Geology Conferences Ltd. 767-786.

Kvarven, T., Hjelstuen, B. O. & Mjelde, R. (2014). Tectonic and sedimentary processes along the ultraslow Knipovich spreading ridge. Marine Geophysical Research, 35(2), 89-103.

Laberg, J. S. & Vorren, T. O. (1996). The Middle and Late Pleistocence evolution and the Bear Island Trough Mouth Fan. Global and Planetary Change, 12(1), 309-330.

Larssen, G.B., Elvebakk, G., Henriksen, L.B., Kristensen, S.E., Nilsson, I., Samuelsberg, T.J., Svånå, T.A., Stemmerik, L. & Worsley, D. (2002). Upper Palaeozoic lithostratigraphy of the Southern Norwegian Barents Sea. Oljedirektoratet (NPD) Bulletin 9. 76 pp.

Libak, A., Eide, C. H., Mjelde, R., Keers, H. & Flüh, E. R. (2012a). From pull-apart basins to ultraslow spreading: Results from the western Barents Sea Margin. Tectonophysics, 514, 44-61.

Libak, A., Mjelde, R., Keers, H., Faleide, J. I. & Murai, Y. (2012b). An integrated geophysical study of Vestbakken Volcanic Province, western Barents Sea continental margin, and adjacent oceanic crust. Marine Geophysical Research, 33(2), 185-207.

Macdonald, K. C. (1982). Mid-ocean ridges: Fine scale tectonic, volcanic and hydrothermal processes within the plate boundary zone. Annual Review of Earth and Planetary Sciences, 10, 155.

Makhous, M. & Galushkin, Y.I. (2005). Basin analysis and modeling of the burial, thermal and maturation histories in sedimentary basins. Technip, Paris. 383pp.

Marcussen, Ø., Faleide, J. I., Jahren, J. & Bjørlykke, K. (2010). Mudstone compaction curves in basin modelling: a study of Mesozoic and Cenozoic Sediments in the northern North Sea. Basin Research v. 22, p. 324-340.

Marello, L., Ebbing, J. & Gernigon, L. (2013). Basement inhomogeneities and crustal setting in the Barents Sea from a combined 3D gravity and magnetic model. Geophysical Journal International, 193(2), 557-584.

McCarthy, K., Rojas, K., Niemann, M., Palmowski, D., Peters, K. & Stankiewicz, A. (2011). Basic petroleum geochemistry for source rock evaluation. Oilfield Review, 23(2), 32-43.

Mørk, A., Dallmann, W.K., Dypvik, H., Johannesen, E.P., Larsen, G.B., Nagy, J., Olaussen, S., Pcelina, T.M. & Worsley, D. (1999). Mesozoic lithostratigraphy. In: Dallmann, W.K. (Ed.), Lithostratigraphic Lexicon of Svalbard. Review and Recommendations for Nomenclature Use. Upper Paleozoic to Quaternary Bedrock. Norsk Polarinstitutt, Tromsø, pp. 127-214.

NASA (2014). http://visibleearth.nasa.gov/view.php?id=67852 (retrieved 28/01/2014).

NPD (2012). http://www.npd.no/en/Topics/Geology/Geological-plays/ (retrieved 15/05/2014).

NPD (2014). http://factpages.npd.no (last retrieved 20/11/2014).

Nyland, B., Jensen, L. N., Skagen, J. L., Skarpnes, O. & Vorren, T. (1992). Tertiary uplift and erosion in the Barents Sea: magnitude, timing and consequences. In: Larsen, R.M., Brekke, H., Larsen, B.T. & Talleraas, E. (eds.), Structural and Tectonic Modelling and its Application to Petroleum Geology. Norwegian Petroleum Society, Special Publication 1, 153-162.

Nøttvedt, A., Cecchi, M., Gjelberg, J.G., Kristensen, S.E., Lonoy, A., Rasmussen, A., Rasmussen, E., Skott, P.H. & van Veen, P.M. (1993). Svalbard-Barents Sea correlation: a short review. In: Vorren, T., Bergsager, E., Dahl-Stamnes, Ø., Holter, E., Johansen, B., Lie,

E., Lund, T. (Eds.), Arctic Geology and Petroleum Potential. Norwegian Petroleum Society (NPF), Special Publication, vol. 2. Elsevier, Amsterdam, 363-375.

Ohm, S. E., Karlsen, D. A., & Austin, T. J. F. (2008). Geochemically driven exploration models in uplifted areas: Examples from the Norwegian Barents Sea. AAPG bulletin, 92(9), 1191-1223.

Olesen, O., Brönner, M., Ebbing, J., Gellein, J., Gernigon, L., Koziel, J., Lauritsen, T., Myklebust, R., Sand, M., Solheim, D. & Usov, S. (2010). New aeromagnetic and gravity compilations from Norway and adjacent areas - methods and applications. In: Geological Society, London, Petroleum Geology Conference Series, 7, pp. 559–586.

Paterson, M. S. (1989). The interaction of water with quartz and its influence in dislocation flow-an overview. In: Karato, S.-I. & Toriumi, M. (eds.) Rheology of Solids and of the Earth, Oxford University Press, New York, 107-142.

Pedersen, J.H. & Karlsen, D.A. (2005). Assessment of oils and source rocks from the Norwegian Barents Sea Region. In: AAPG (2005), Exploring energy systems, global roundup: Annual Meeting, Calgary, Alberta, Canada, June 19-22, Abstracts Volume (AAPG Search and Discovery Article #90039): http://www.searchanddiscovery.com/abstracts/html/2005/annual/abstracts/pedersen02.htm (accessed March 7, 2014).

Perez-Gussinye, M., and Reston, T.J. (2001). Rheological evolution during extension at nonvolcanic rifted margins: Onset of serpentinization and development of detachments leading to continental breakup. Journal of Geophysical Research: Solid Earth, 106(B3), 3961–3975.

Pestman, P. Tur, N., Esteban, M., Polo, T., Sanchez, A., Tiwary, D., Tocco, R., Tritlla, J. & Vayssaire, A. (2011). Charge and Leakage Analysis Integrating Different Scales: From Fluid Inclusions to Seismic Attributes, Loppa High, Barents Sea, Norway. Extended Abstracts: AAPG 2011 International Conference & Exhibition, Milan, Italy. AAPG Search and Discovery Article #10377.

Peters, K.E. & Cassa, M.R. (1994). Applied Source Rock Geochemistry. In: Magoon, L.B. & Dow, W.G. (eds.): The Petroleum System – From Source to Trap. The American Association of Petroleum Geologists, Tulsa, AAPG Memoir, 60, 93-120.

Podladchikov, Y. Y., Poliakov, A. N. B. & Yuen, D. A. (1994). The effect of lithospheric phase transitions on subsidence of extending continental lithosphere. Earth and Planetary Science Letters, 124(1), 95-103.

Pratt, J.H. (1855). On the attraction of the Himalaya Mountains and of the elevated regions beyond them upon the plumb-line in India. Philosophical Transactions of the Royal Society of London, 145, 53-100.

Reston, T. (2007). Extension discrepancy at North Atlantic nonvolcanic rifted margins: Depth-dependent stretching or unrecognized faulting?. Geology, 35(4), 367-370.

Riis, F. & Fjeldskaar, W. (1992). On the magnitude of the Late Tertiary and Quaternary erosion and its significance for the uplift of Scandinavia and the Barents Sea. In: Larsen, R.M., Brekke, H., Larsen, B.T. & Talleraas, E. (eds.) Structural and Tectonic Modelling and Its Application to Petroleum Geology, Vol. 1, Elsevier, Amsterdam, 163–185.

Riis, F. (1996). Quantification of Cenozoic Vertical Movements of Scandinavia by Correlation of Morphological Surfaces with Offshore Data. Global and Planetary Change, 12, 331-357.

Ritzmann, O. & Faleide, J.I. (2007). Caledonian basement of the western Barents Sea. Tectonics 26, 417-435.

Roberts, D., & Gee, D. G. (1985). An introduction to the structure of the Scandinavian Caledonides. In: Gee, D.G. & Sturt, B.A. (eds.) The Caledonide orogen – Scandinavia and Related Areas. Wiley, Chichester, 55-68.

Roberts, D. (2003). The Scandinavian Caledonides: event chronology, palaeogeographic settings and likely modern analogues. Tectonophysics, 365(1), 283-299.

Rodrigues Duran, E., di Primio, R., Anka, Z., Stoddart, D. & Horsfield, B. (2013). 3D-basin modelling of the Hammerfest Basin (southwestern Barents Sea): A quantitative assessment of petroleum generation, migration and leakage. Marine and Petroleum Geology, 45, 281-303.

Rowley, D. B. & Sahagian, D. (1986). Depth-dependent stretching: A different approach. Geology, 14(1), 32-35.

Royden, L. & Keen, C. E. (1980). Rifting process and thermal evolution of the continental margin of eastern Canada determined from subsidence curves. Earth and Planetary Science Letters, 51(2), 343-361.

Rüpke, L. H., Schmalholz, S. M., Schmid, D. W., & Podladchikov, Y. Y. (2008). Automated thermotectonostratigraphic basin reconstruction: Viking Graben case study. AAPG Bulletin 92, 309-326.

Rüpke, L. H., Schmid, D. W., Hartz, E. H. & Martinsen, B. (2010). Basin modelling of a transform margin setting: structural, thermal and hydrocarbon evolution of the Tano Basin, Ghana. Petroleum Geoscience 16, 283-298.

Rüpke, L. H., Schmid, D. W., Perez-Gussinye, M. & Hartz, E. (2013). Interrelation between rifting, faulting, sedimentation, and mantle serpentinization during continental margin formation—including examples from the Norwegian Sea. Geochemistry, Geophysics, Geosystems 14, 4351-4369.

Ryseth, A., Augustson, J. H., Charnock, M., Haugerud, O., Knutsen, S. M., Midbøe, P. S., Oppsal, J.G. & Sundsbø, G. (2003). Cenozoic stratigraphy and evolution of the Sørvestsnaget Basin, southwestern Barents Sea. Norwegian Journal of Geology, 83(2), 107-130.

Rønnevik, H.C. (1981). Geology of the Barents Sea. In: Illing, L.V. & Hobson, G.D. (eds) Petroleum Geology of the Continental Shelf of north-West Europe, vol 2, Heyden, London, 395-406.

Rønnevik, H.C & Jacobsen, H.P. (1984). Structural Highs and Basins in the western Barents Sea. In: Spencer, A.M. (ed.), Petroleum Geology of North European Margin. Norw. Petrol. Soc., Graham and Trotham, London, 19-32.

Schmoker, J. W. & Halley, R. B. (1982). Carbonate porosity versus depth: a predictable relation for south Florida. AAPG Bulletin, 66(12), 2561-2570.

Sclater, J. G. & Christie, P. (1980). Continental stretching: An explanation of the post-Mid-Cretaceous subsidence of the central North Sea Basin. Journal of Geophysical Research: Solid Earth (1978–2012), 85(B7), 3711-3739.

Semprich, J., Simon, N. S. & Podladchikov, Y. Y. (2010). Density variations in the thickened crust as a function of pressure, temperature, and composition. International Journal of Earth Sciences, 99(7), 1487-1510.

Simon, N. S. & Podladchikov, Y. Y. (2008). The effect of mantle composition on density in the extending lithosphere. Earth and Planetary Science Letters, 272(1), 148-157.

Smelror, M., Petrov, O. V., Larssen, G. B., & Werner, S. C. (2009). Geological history of the Barents Sea. Norges Geol. undersøkelse, 1-135.

Solbu, Ø.H. (2013). Seismic Interpretation of the Continent-Ocean Boundary along the Senja Margin and the Vestabkken Volcanic Province, SW Barents Sea. (Masters thesis). Norges teknisk-naturvitenskapelige universistet (NTNU), Intstitutt for petroleumsteknologi og anvendt geofysikk. 93 pp.

Spencer, A. M., Embry, A. F., Gautier, D. L., Stoupakova, A. V. & Sorensen, K. (2011). An overview of the petroleum geology of the Arctic. Geological Society, London, Memoirs, 35, 1-15.

Steckler, M. S. & Watts, A. B. (1978). Subsidence of the Atlantic-type continental margin off New York. Earth and Planetary Science Letters, 41(1), 1-13.

Steel, R. J. & Worsley, D. (1984). Svalbard's post-Caledonian strata—an atlas of sedimentational patterns and palaeogeographic evolution. In: Spencer, A. (ed.) Petroleum geology of the North European margin (pp. 109-135). Graham & Trotman, London.

Stüwe, K. (2007). Geodynamics of the lithosphere: an introduction (2nd edition). Springer, Berlin. 493pp.

Taraldsen, L. & Qvale, P. (2014). Den som ler sist, ler best. Teknisk Ukeblad 16.10.2014, 14-15.

Theissen, O. (2013). Petroleum systems of the Barents Sea. In: Abstracts of the 3P Arctic Conference & Exhibition. The Polar Petroleum Potential. AAPG Search and Discovery Article #90177.

Theissen, S. & Rüpke, L. H. (2010). Feedbacks of sedimentation on crustal heat flow: New insights from the Vøring Basin, Norwegian Sea. Basin Research 22, 976-990.

Tullis, T. E., Horowitz, F. G. & Tullis, J. (1991). Flow laws of polyphase aggregates from end-member flow laws. Journal of Geophysical Research: Solid Earth (1978–2012), 96(B5), 8081-8096.

van Koeverden, J. H., Karlsen, D. A., & Backer-Owe, K. (2011). Carboniferous non-marine source rocks from Spitsbergen and Bjørnøya: comparison with the western arctic. Journal of Petroleum Geology, 34(1), 53-66.

Vening Meinesz, F.A. (1941). Gravity over the Hawaiian Archipelago and over the Madeira area: conclusions about the Earth's crust. Proceedings of the Koninklijke Nederlandse Academie van Wetenschappen 44, 1-12.

Vorren, T.O., Richardsen, G., Knutsen, S.-M. & Henriksen, E. (1991). Cenozoic Erosion and Sedimentation in the Western Barents Sea. Marine and Petroleum Geology, 8, 317-340.

Wangen, M. (1995). The blanketing effect in sedimentary basins. Basin Research 7, 283-298.

Wangen, M. (2010). Physical principles of sedimentary basin analysis. Cambridge University Press, Cambridge, 527pp.

Wangen, M., Mjelde, R. & Faleide, J. I. (2011a). The extension of the Vøring margin (NE Atlantic) in case of different degrees of magmatic underplating. Basin Research, 23(1), 83-100.

Wangen, M., Mjelde, R. & Faleide, J. I. (2011b). Modelling thermal transients from magmatic underplating — an example from the Vøring margin (NE Atlantic). Computational Geosciences, 15(4), 771-788.

Watts, A.B. & Ryan, W.B.F. (1976). Flexure of the lithosphere and continental margin basins. Tectonophysics, 36(1), 25-44.

Watts, A.B., Karner, G.D. & Steckler, M.S. (1982). Lithospheric flexure and the evolution of sedimentary basins. Philosphical Transactions of the Royal Society, London. 305, 249-281.

Watts, A. B. (2001). Isostasy and Flexure of the Lithosphere. Cambridge University Press. Cambridge, United Kingdom. 458 pp.

Wernicke, B. (1985). Uniform-sense normal simple shear of the continental lithosphere. Canadian Journal of Earth Sciences 22, 108-125.

Wilhelms, A., Larter, S. R., Head, I., Farrimond, P., Di-Primio, R. & Zwach, C. (2001). Biodegradation of oil in uplifted basins prevented by deep-burial sterilization. Nature, 411(6841), 1034-1037.

Wood, R.J., Edrich, S.P. & Hutchison, I. (1989). Influence of North Atlantic Tectonics on the Large-Scale Uplift of the Stappen High and Loppa High, Western Barents Shelf. In: Tankard, A.J. & Balkwill, H.R. (eds.) Extensional Tectonics and Stratigraphy of the North Atlantic Margins, American Association of Petroleum Geologists Memoir No. 46, 559-566.

Worsley, D., Agdestein, T., Gjelberg, J. G., Kirkemo, K., Mork, A., Nilsson, I., Olaussen, S., Steel, R.J. & Stemmerik, L. (2001). The geological evolution of Bjornoya, Arctic Norway: implications for the Barents shelf. Norsk Geologisk Tidsskrift, 81(3), 195-234.

Worsley, D. (2008). The post-Caledonian development of Svalbard and the western Barents Sea. Polar Research, 27(3), 298-317.

Ziegler, P. A. (1988). Evolution of the Arctic-North Atlantic and the western Tethys. American Association of Petroleum Geologists Memoir No. 43. AAPG, Tulsa, 198 pp.

9. Appendix A

Crustal Structure and Thinning (β) distributions together with Input vs. Modelled Stratigraphy Fit for all Modelled Scenarios

PETROBAR-07 models (modified after Clark et al. 2014)

PETROBAR-07 Reference Model: Flexural Isostasy and Erosion

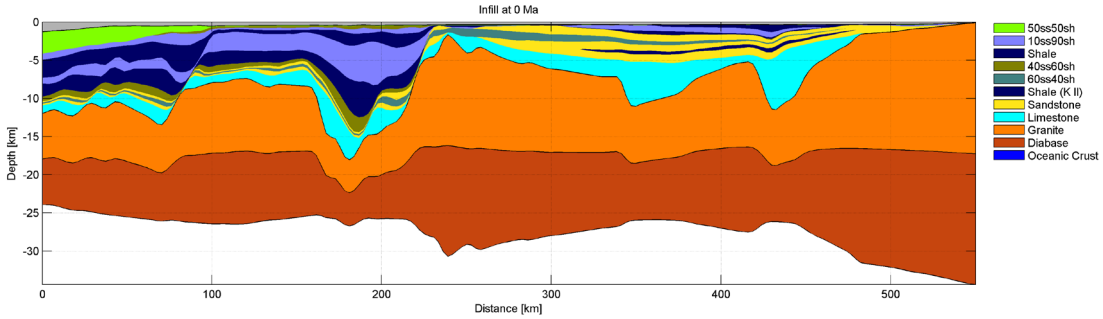

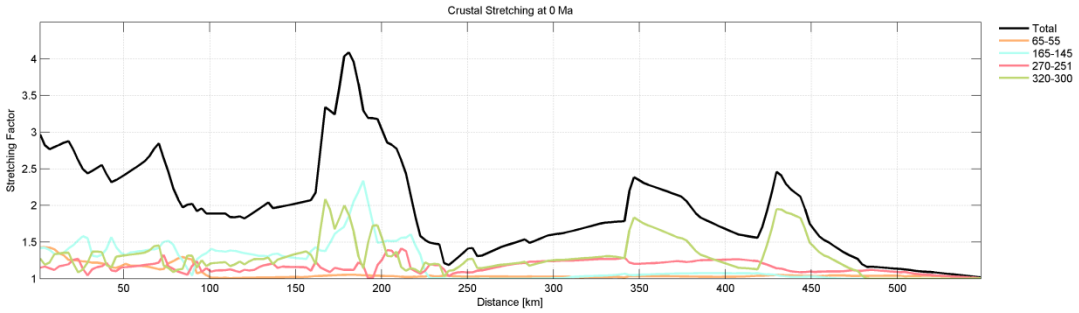

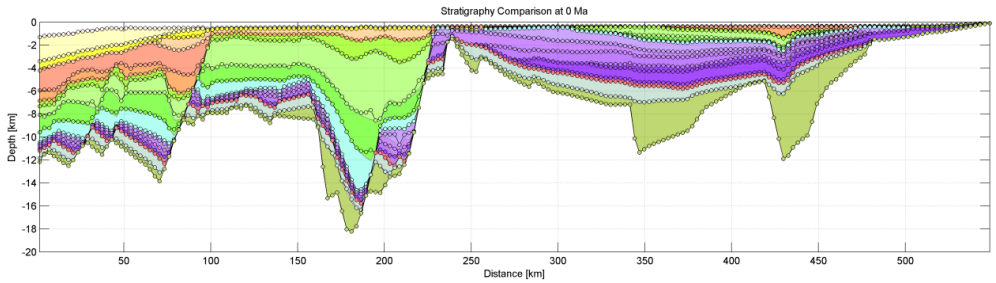

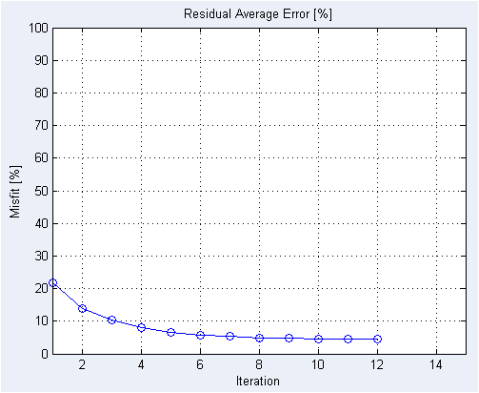

PETROBAR-07 Breakup-only, with flat lower stratigraphy below Vestbakken Volcanic Province (modified from Clark et al. 2014).

All PETROBAR-07 models from this stage forward have a flexural isostatic condition applied together with erosion/forced deposition.

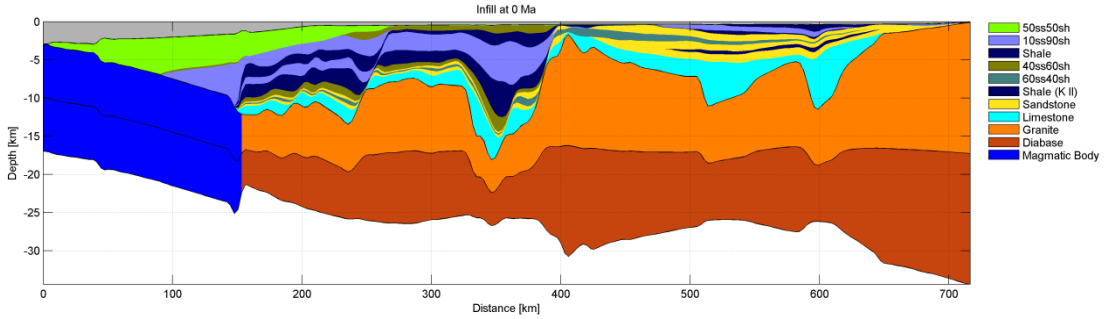

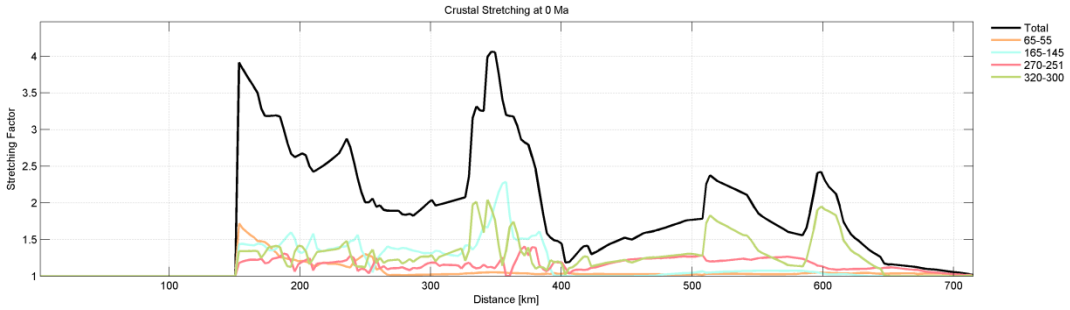

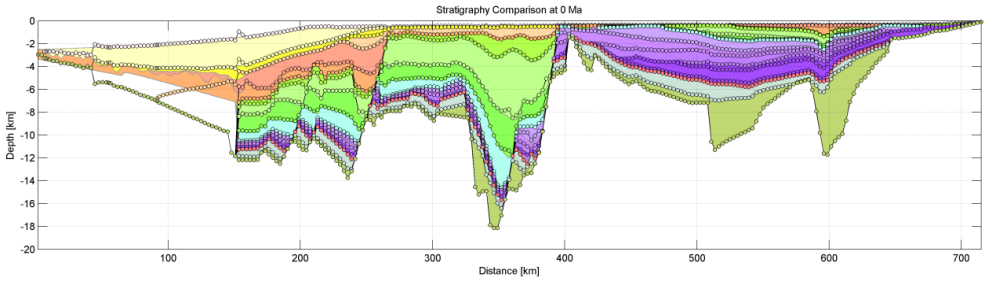

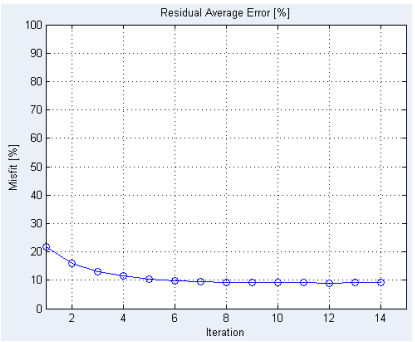

PETROBAR-07 Breakup only, with tapered lower stratigraphy below Vestbakken Volcanic Province (inspired by Libak et al. 2012b)

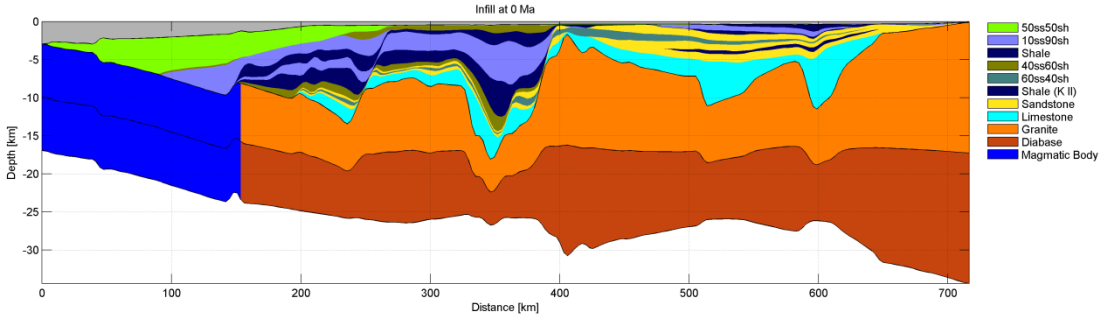

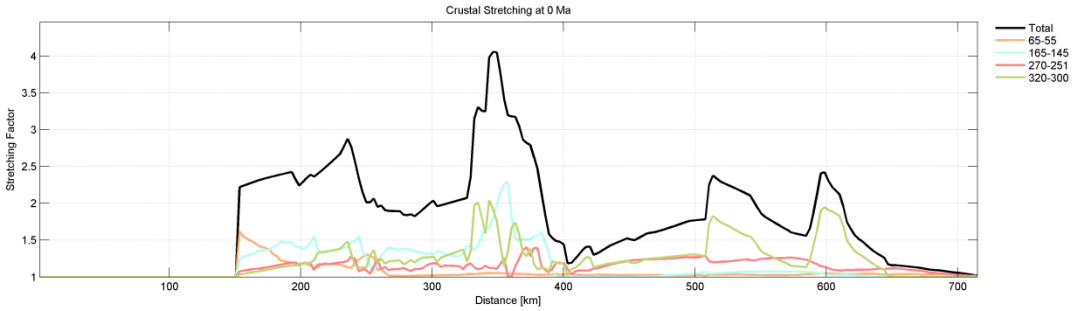

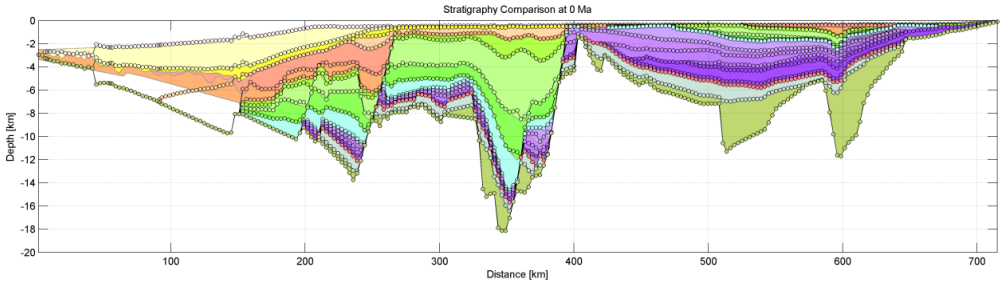

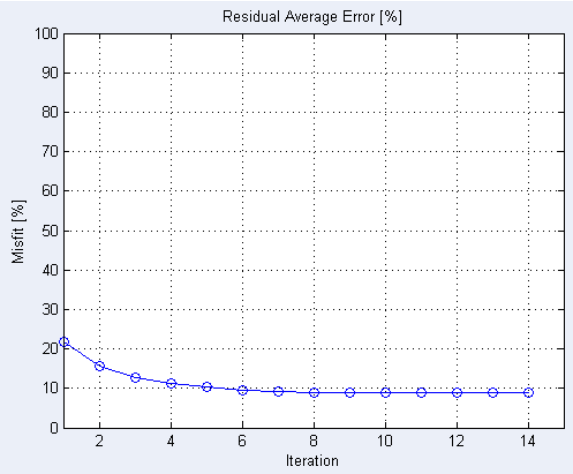

PETROBAR-07 Breakup with magmatic underplating

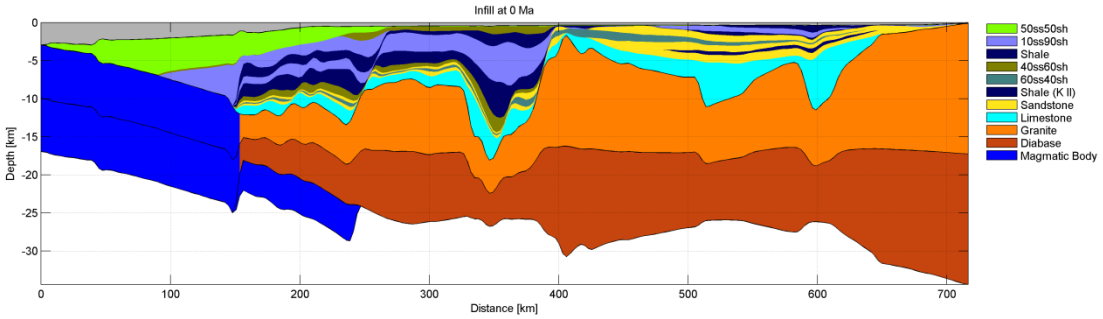

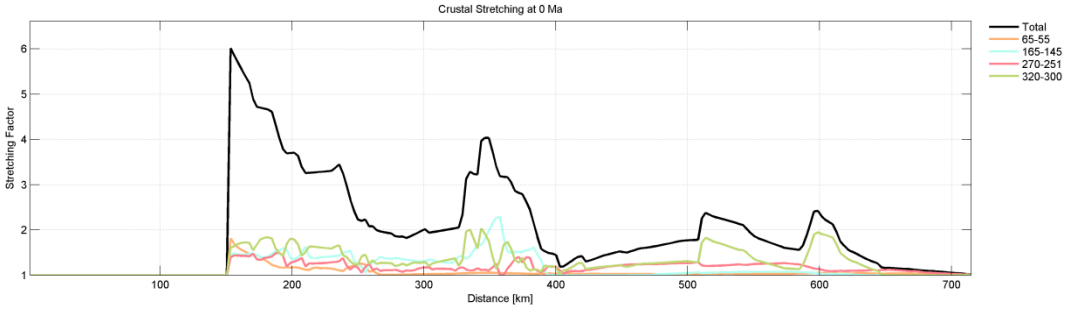

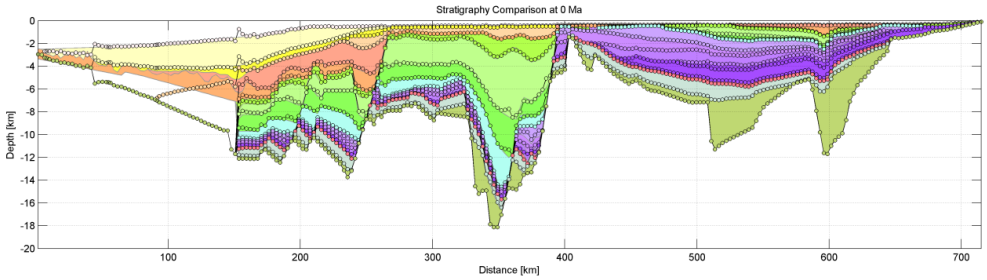

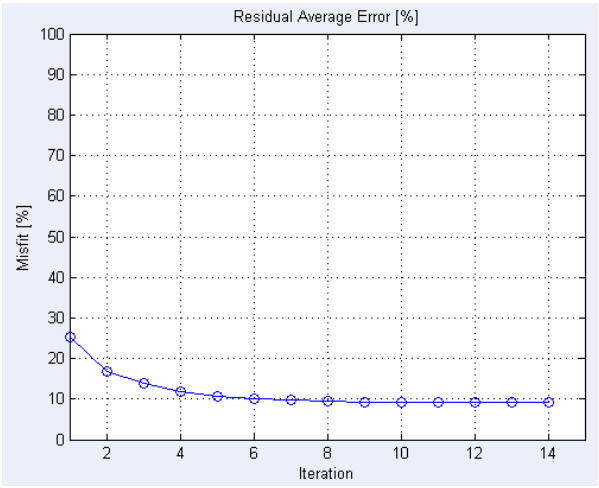

PETROBAR-07 Breakup with sill intrusion and volcanic flows

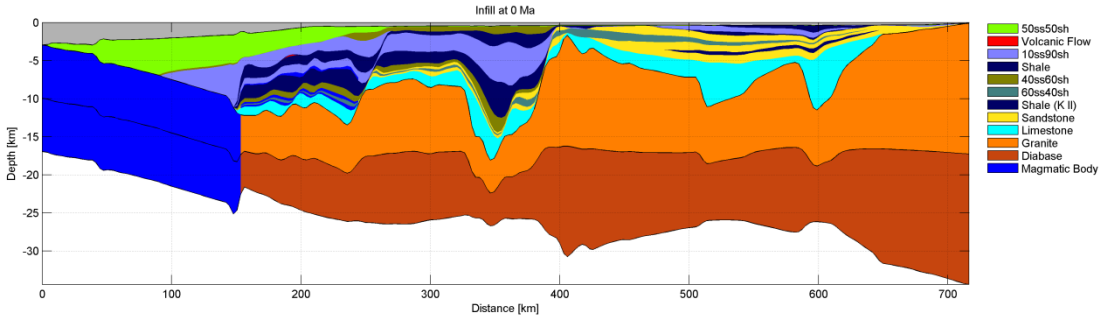

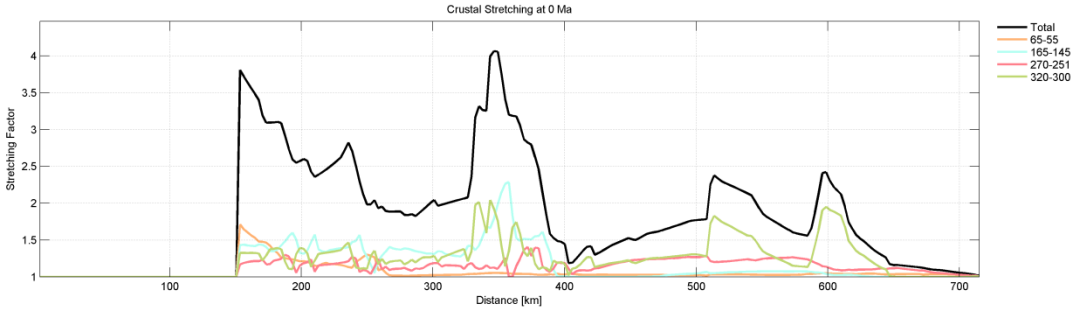

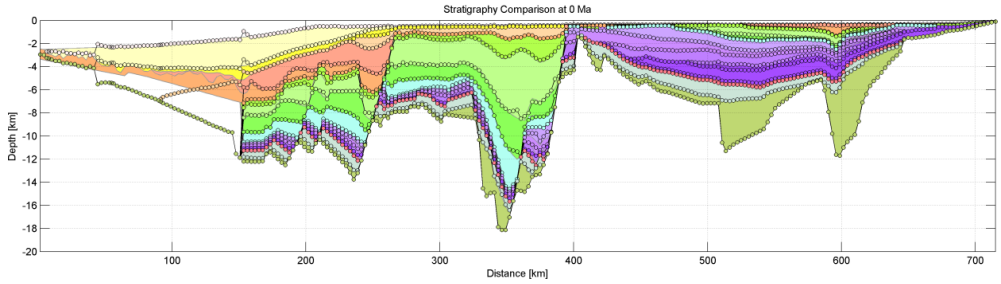

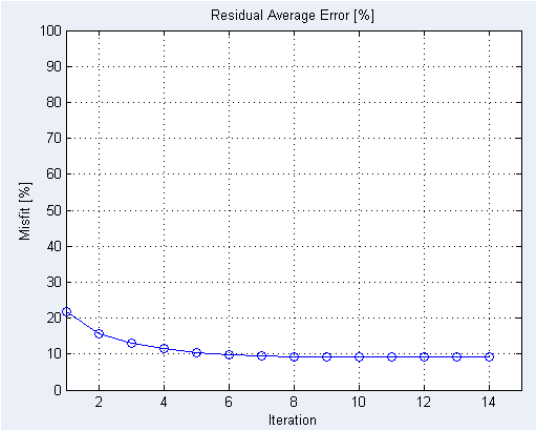

Loppa High Models (after Glørstad-Clark et al. 2011a)

Loppa High Reference Model: flexural isostasy and erosion (35 km crustal thickness)

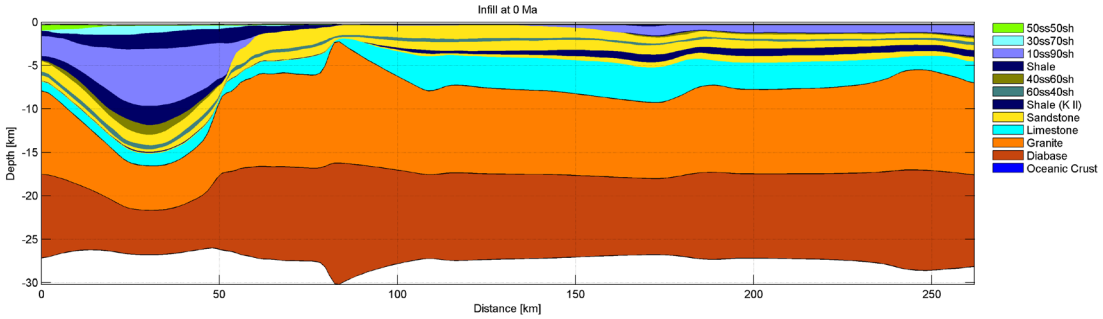

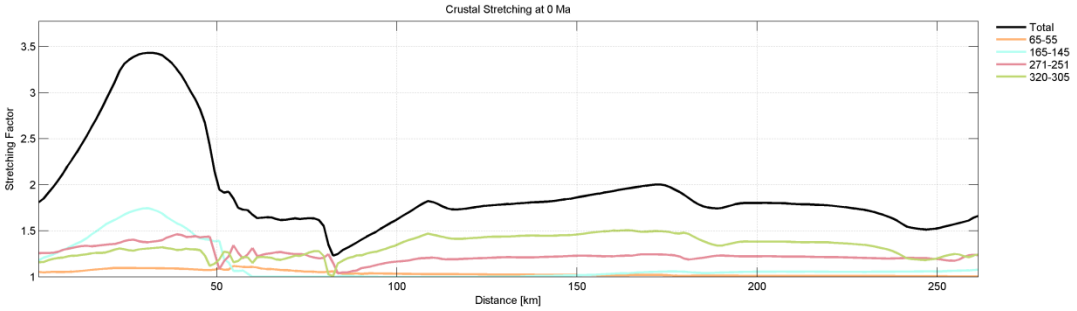

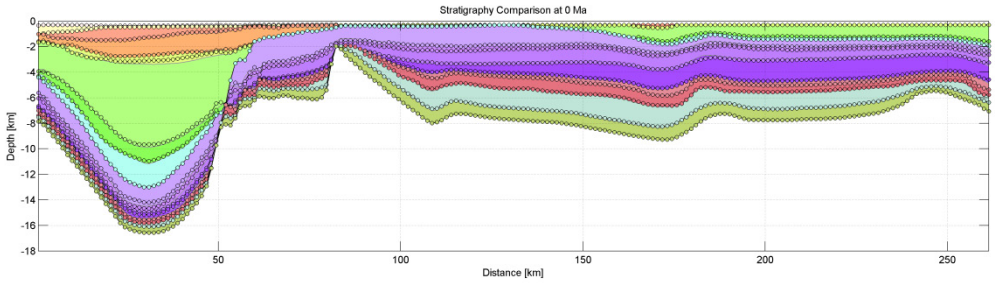

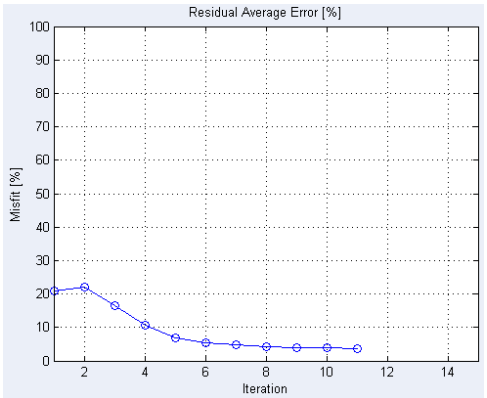

Loppa High with 30 km crustal thickness

All Loppa High models from this stage forward have a flexural isostatic condition applied together with erosion/forced deposition.

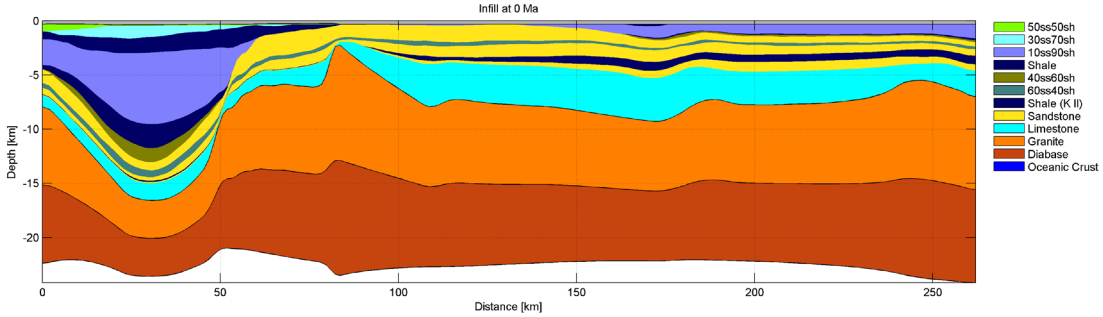

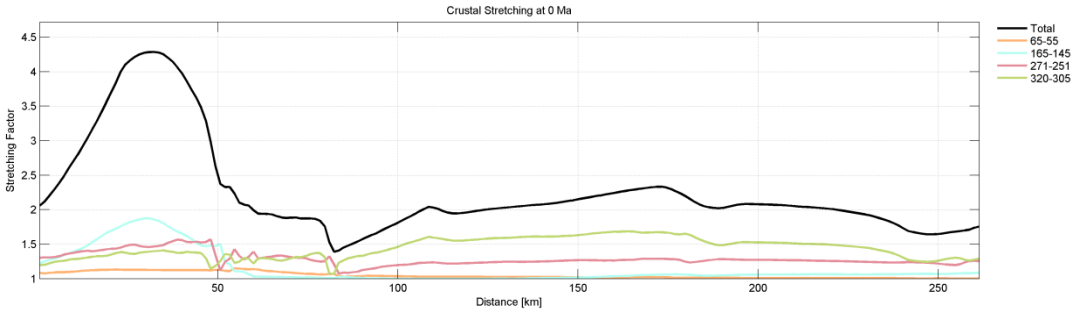

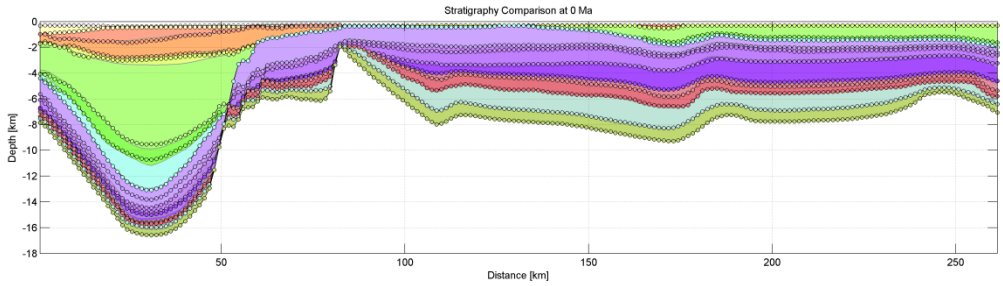

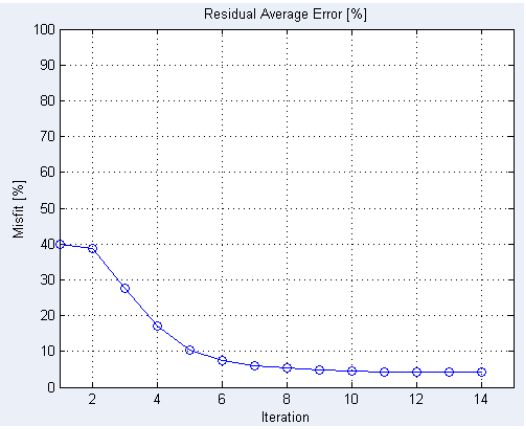

Loppa High with 40 km crustal thickness

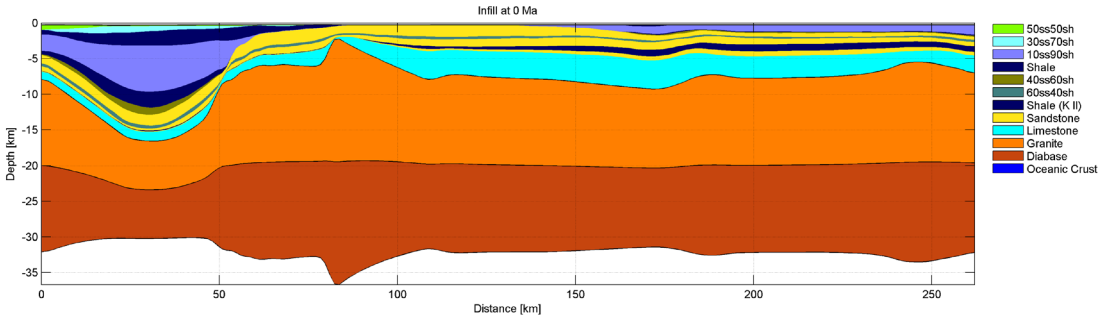

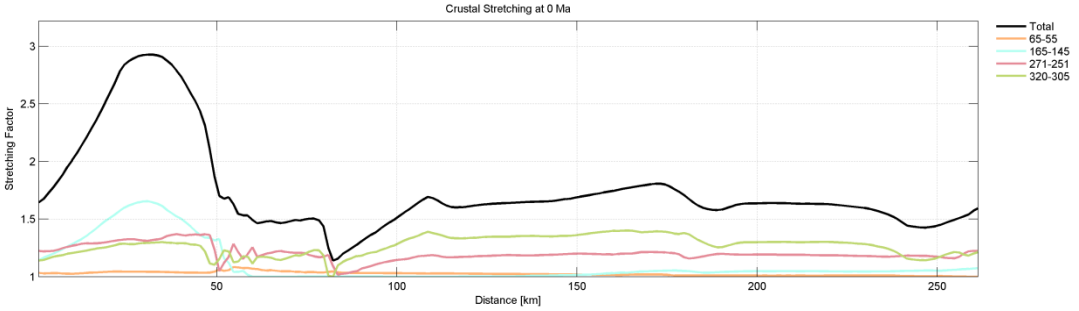

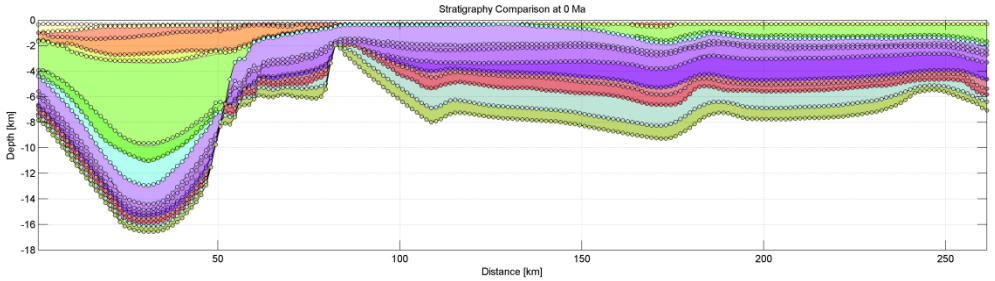

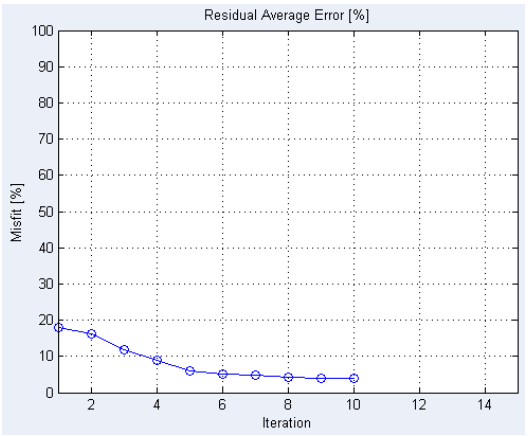

Loppa High with extra sedimentary sequence and rift phase from 360-320 Ma

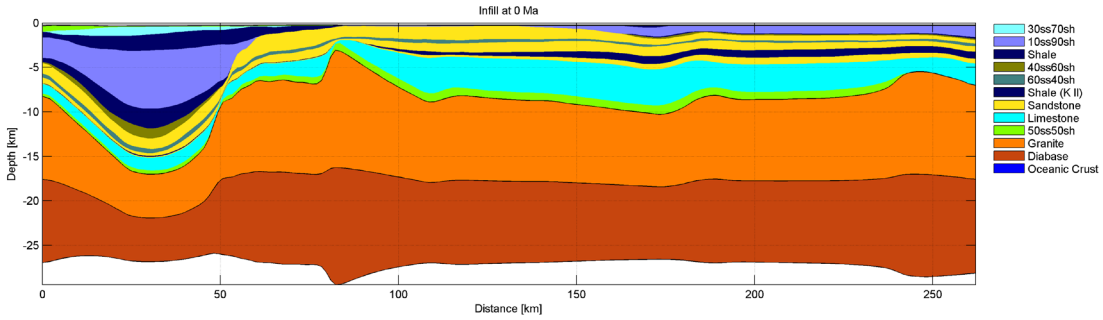

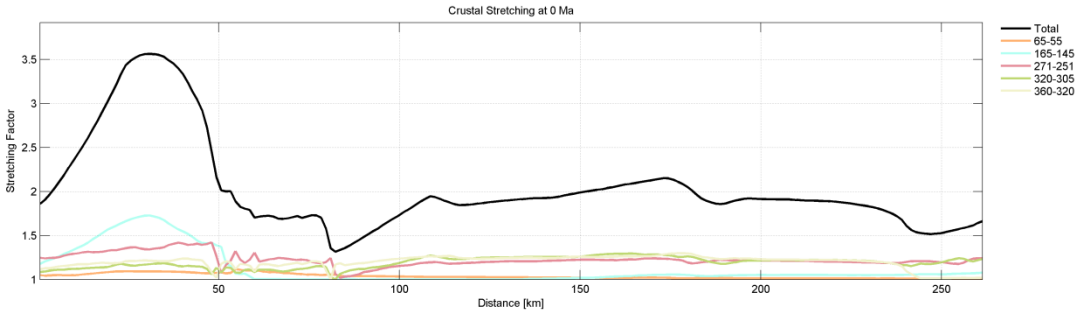

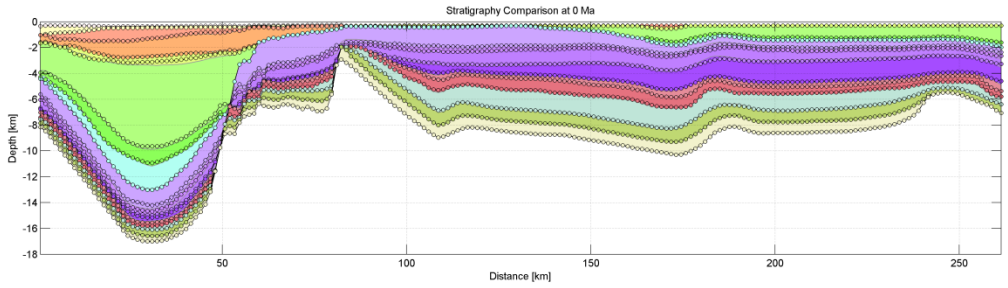

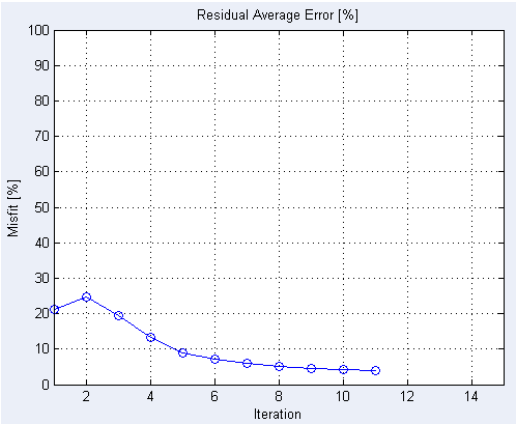

10. Appendix B

Inversion Tests

An optimum set of inversion control parameters were determined by performing a series of sensitivity tests. The motive was to find a reasonable set of inversion control parameters which could be kept constant for all modelled scenarios such that comparisons could be made on the geological input alone. This involved step-wise increasing or decreasing the main parameters to determine which set provide the best calculated fit with the observed stratigraphy and estimated paleo-water depths. Checks were also performed on all geologically modelled scenarios to determine whether the inversion engine could support each set of control parameters tested.

As described in chapter 3, the inversion control parameter which governs the method by which the modelled stratigraphy is fit to the input stratigraphy is W_{weight}. $W_{weight} = 0$ tells the inversion engine to only update sedimentation rates, so that the thickness of sedimentary layers is fitted. This method is known to be effective in exactly reproducing the input stratigraphy. Assigning a value of $W_{weight} = 1$ updates only paleowater depths values to fit the stratigraphy, which is more robust but results in inferior fits. TecMod can use both methods simultaneously by assigning the weighting function W_{weight} to between 0 and 1 (GeoModelling Solutions, 2014). A number of inversion runs with $W_{weight} = 0$ were performed along the PETROBAR-07 reference profile. Good fits with the observed stratigraphy were achieved within about 7 iterations. However, when more complex geological scenarios were chosen, including continental breakup, the inversion engine would stall and was unable to compute a solution. Increasing the W_{weight} to 0.2 solved this issue while maintaining a good stratigraphic fit with reasonable stretching factors and paleo-water depths.

The δ_{coeff} value of 0.9 was chosen to provide sufficient convergence along the uppermost sediments and seabed of the passive margin of the PETROBAR-07 extended profile. Higher values of δ_{coeff} resulted in inferior fits.

The W_{rift} value defines the water depth at the onset of rifting. Comparing $W_{rift} = 0$ m with $W_{rift} = 100$ m, the convergence between the modelled and input stratigraphy is nearly identical, as are the stretching factors. However, the reconstructions with $W_{rift} = 100$ m are slightly deeper than the reconstructions with $W_{rift} = 0$ m. The reconstructed paleo-water depths from the $W_{rift} = 0$ m scenario were in better agreement with the interpreted paleo-water depths described by Clark et al. (2014) based on sequence stratigraphy relationships.

Otherwise, default inversion control parameters within TecMod were used, as described in table 4.6.